№1, 2026

ISSN 2706-977X

MATERIAL AND MECHANICAL ENGINEERING TECHNOLOGY

Material and Mechanical Engineering Technology | MMET

Editorial board of the journal

Content

Zhumabekov A.T., Sakhapov R.L., Suyunbayev S.M., Karsakova A.Zh, Sinelnikov K.A. Justification of the Effectiveness of Developing and Using a Mobile Overpass…….....3
Tursunov N.K., Saidirakhimov A.A. Research of the Influence of Chemical Composition on the Mechanical Characteristics of Cast Parts for Freight Car Bogies…….....14
Nurzhanova O.A., Zharkevich O.M., Bakenov A.A., Berg A.S., Zakirov K. Strength Assessment of a New Adaptive Tooling Design……...23
Makhmudova Sh. Modeling and Analysis of Interactions in the Rotor–Bearing–Housing System under Variable Loads……...31
Pak D., Pak Yu., Ibragimova D., Matonin V., Tebayeva A.Studying Radiation-Radon Safety of Building Materials and Residential Buildings of the Karaganda Region ……...37
Raghavendra S., Kumar A.R., Manjunatha K.N., Suresh S., Shivaramakrishna A. Effect of Nickel Content on Tensile, Hardness Properties and Dry Sliding Wear Behaviour of Austempered Ductile Iron…….....46
Akhmediyev S.K., Filippova T.S, Oryntayeva G.Zh., Tazhenova G.D Stability of a Cantilever Rod with Variable Bending Stiffness ……56
Oda Z.A., Radhi N.S. A Review of Modeling and Preparation of Functionally Graded Materials for Bone Tissue Engineering…….....62
Ashkeyev Z.A., Andreyachshenko V.A., Abishkenov M.Zh., Kamarov A.U. Stress State and Contact Pressure during Asymmetrical Rolling of Thick Sheets……...72
Modi Y. K. Comparative Mechanical Performance of Cylindrical and Cuboid Pore Geometries in Additively Manufactured ABS BoneScaffolds…….81
Yunusov S.Z., Kasimova D. A. Influence of the Seed Shaft Parameter of the Linter Machine on the Dynamics and Load of the System…….89
Fan Z., Wen B., Reshetnikova O.S, Li J., He X. Determination and Optimization of Working Parameters of a Sheep House Feeding Device Based on the Discrete Element Method…….98
Abdullayev S., Bakyt G., Yelshibekov A., Jakupov N., Duisembayeva B. The Reliability and Durability of Welded Joints in Steel Rails: a Methodology for Process Control at Modern Rail Welding Facilities……...107
Černašėjus O., Rutė M., Černašėjienė R., Užtupis S., Valasevičius A. The Effect of Laser Post-Processing on NiCrMoSiBFeCuC Thermally Sprayed Coatings……120

DOI 10.52209/2706-977X_2026_1_3 IRSTI 55.43.03 UDC 625.72(574.3)=111

Justification of the Effectiveness of Developing and Using a Mobile Overpass

Zhumabekov A.T.[1], Sakhapov R.L.[2], Suyunbayev S.M.[3], Karsakova A.Zh[1], Sinelnikov K.A.*[1]
[1]Abylkas Saginov Karaganda Technical University, Karaganda, Kazakhstan
[2]Kazan (Volga region) Federal University, Kazan, Russia
[3]Tashkent State Transport University, Tashkent, Uzbekistan
*corresponding author

Abstract. The article discusses the development and research of a mobile overpass as an engineering solution in the field of mechanical engineering and transport technology. It describes the design features of the overpass: the load-bearing span integrated into a two-axle wheeled chassis, the tensioning mechanism, and the suspension system, which ensure reliability and stability under dynamic loads. The technological advantages of the design are shown: mobility, quick installation without major construction, modularity, and the possibility of repeated use in various operating conditions. Based on preliminary engineering calculations and analysis of transport loads, the strength and operational reliability of the structure when moving passenger cars and light-duty vehicles is justified. The use of reinforced guide elements and a spatial truss scheme minimizes deformation and evenly distributes loads. The economic analysis confirms the efficiency of the proposed overpass's installation and operation, demonstrating a total annual saving exceeding 18 million tenge, primarily through reduced fuel consumption and minimized vehicle idling time. The results of the study confirm the feasibility of introducing mobile overpasses as an effective engineering solution that ensures the maintenance of transport links during major repairs and reconstruction of roads. The design combines manufacturability, mobility, and operational reliability, which opens up prospects for its widespread use in Kazakhstan's transport infrastructure.

Keywords: mobile overpass design; mobile overpass installation technology; utility network repair; traffic capacity of mobile overpass; mobile overpass installation efficiency.

Introduction.

Modern cities face complex transport problems associated with the growth in the number of cars, congestion on the road network, and environmental degradation. In Kazakhstan, urbanization and the increase in the number of cars are leading to regular traffic jams, fuel overconsumption, and longer travel times. In Karaganda, for example, the average travel time is about 32 minutes, which is close to the national average of 34.7 minutes. Such values indicate a high load on the urban road network, since an interval of 30–45 minutes in transport statistics is considered an indicator of severe congestion and traffic jams [1]. As a result, this negatively affects the efficiency of the transport system, increases socio-economic costs, and exacerbates the environmental situation [2].

The problem becomes particularly acute during periods of repair and road works on utility networks and road surfaces. Such work is often accompanied by lane closures, speed restrictions, and the redistribution of traffic flows. As a result, traffic capacity is reduced several times over [3]. Practice shows that during major repairs, the intensity of traffic jams increases sharply. Drivers are forced to use detour routes that are not designed for high traffic, which leads to congestion on secondary streets. This increases travel time, reduces the average speed of traffic flow, contributes to an increase in road accidents, and leads to additional emissions of harmful substances into the atmosphere [4,5].

When repairing urban underground utilities (heating networks, water pipes, communication cables, and power lines), traffic is also disrupted and diverted to other roads [6]. In this case, the mileage of cars increases, the intensity of traffic on detour routes increases, which leads to additional fuel consumption and greater air pollution [7]. Air pollution from nitrogen oxides, carbon monoxide, soot, and fine particulate matter (PM2.5 and PM10) causes an increase in the number of respiratory and cardiovascular diseases, including asthma, bronchitis, chronic obstructive pulmonary disease, ischemic heart disease, and stroke [8,9]. Children, the elderly, and people with chronic diseases, whose lung function deteriorates and whose immunity weakens, are particularly vulnerable to these effects [10,11].

Thus, traffic congestion caused not only by the growth in the number of vehicles but also by repair works is becoming one of the key transport problems. The overload of the urban road network during major repairs requires not only organizational measures but also the development of mobile engineering structures that ensure the continuity of traffic flow.

The development and application of a mobile overpass is proposed, designed to maintain uninterrupted traffic movement in areas where repair works and reconstruction of utility networks are carried out without complete closure of the roadway [12,13].

The mobile overpass considered in this study is part of a comprehensive research program conducted at the Department of Transport Equipment and Logistics Systems aimed at reducing the overall environmental load of the urban transport system. In addition to the development of mobile overpasses, this research also addresses methods of exhaust gas purification [14] through the introduction of innovative technologies for cleaning exhaust gases in car mufflers [15] and provides practical recommendations for improving air quality in urban environments. The combined application of

these approaches — ensuring continuity of traffic flows and reducing vehicle emissions by — is expected to produce a significant integrated environmental and transport effect.

This article focuses on the development and justification of a mobile overpass [16] as an engineering transport solution that combines mobility, manufacturability, and operational reliability.

The purpose of the study is to justify the need to develop and use a mobile overpass and to prepare specific proposals for its operation to reduce traffic congestion and optimize traffic flow.

To achieve this goal, the following tasks were set:

– analysis of the effectiveness of existing infrastructure solutions (traffic light control, detour routes, public transport priority, intelligent transport systems);

– justification of the need to develop and use a mobile overpass, with a description of its design and installation technology;

– assessment of the economic and environmental efficiency of the proposed solution;

– preparation of practical recommendations for the operation of a mobile overpass using the example of a selected street section in the city of Karaganda.

The scientific novelty of the research lies in the development of a methodology for assessing the effectiveness of the proposed solution in the urban transport system. In particular, it presents a system of criteria that allows assessing the economic feasibility, environmental sustainability, and logistical efficiency of the proposed solution in conditions of road network congestion.

The practical significance of the work lies in the fact that the proposed solution will reduce traffic congestion, reduce average delays, and ensure annual savings in time and fuel for motor vehicles on the road. The methodology and results of the study can be applied in the planning of transport projects by local authorities, as well as in the design of temporary and mobile infrastructure facilities.

1. Materials and methods

In global practice, a wide range of solutions are used to reduce traffic congestion and optimize traffic flow, each of which has its own advantages and limitations (Table 1).

Table 1. Key solutions for reducing traffic congestion and optimizing traffic flow

Solutions	Advantages	Disadvantages	Implementation time	Financial costs	Countries where it is used
Special lanes for public transport	Increases the speed of public transport and reduces delays	Infrastructure is not suitable on some streets	6–12 months	200–400 million tenge	Colombia (Bogotá), Turkey (Istanbul), China (Beijing)
Smart traffic light system	Regulates traffic in real time, prevents congestion	Expensive system, requires sensors and database	6–9 months	150–300 million tenge	Netherlands (Amsterdam), Russia (Moscow), Singapore
Limits parking time at stops	Public transport runs according to schedule	Constant monitoring of driver compliance is required	3 months	20–50 million tenge	Finland (Helsinki), Singapore, Japan
Introduction of one-way traffic or detour systems	Redistributes traffic flows at intersections, reduces congestion	For some directions, the length of the route increases	3–6 months	50–100 million tenge	Czech Republic (Prague), Spain (Barcelona), USA (New York)

According to Table 1, dedicated lanes for public transport increase its speed and reduce delays, but their implementation may not be possible on all streets due to the need to adapt the infrastructure. Intelligent traffic light systems allow real-time traffic control and prevent traffic jams, but require expensive sensors and a developed database. Limiting parking time at stops helps buses run on schedule, but it needs to be strictly enforced. Setting up one-way traffic or detour routes helps redistribute traffic flows, but it can make some trips take longer.

Analysis of these examples shows that in many countries, solving the problem of traffic jams requires a comprehensive approach that combines the development of public transport, the introduction of digital technologies, and changes in traffic management schemes. Such practices are also of interest to Kazakhstan, but their high cost and the need for constant monitoring and maintenance limit their widespread implementation.

Therefore, the solution requires a comprehensive approach that takes into account the characteristics of infrastructure and public transport and the introduction of mobile solutions. One such solution is the use of temporary mobile overpasses, which allow traffic to continue uninterrupted and reduce socio-economic losses during road works.

A mobile overpass is a temporary, quickly erected engineering structure designed to organize traffic over congested or repaired sections of road [17,18]. Unlike the organizational measures listed above, the developed mobile overpass is a mechanical structure with a focus on strength, reliability, and the ability to be used repeatedly under various loads .

From an engineering and design point of view, the mobile overpass is a metal load-bearing system for the roadway, mounted on a two-axle wheeled chassis that acts as a running gea [19]. This design solution simultaneously ensures the transport of the module to the place of operation and its stable position during operation [20]. (Figure 1).

The load-bearing part of the overpass is designed for motor vehicle traffic and is made as a single-span structure without connecting elements. The span configuration allows it to cross trenches and obstacles up to 8 meters wide. The width of the roadway is 2.5 m, with a design load on the pavement of up to 3 t/m² . The design load of 3 t/m² corresponds to the passage of passenger cars and the majority of light-duty commercial vehicles with a gross vehicle weight up to 3.5 tons (category N1 according to UNECE classification). Thus, the overpass ensures safe operation for the entire spectrum of urban light transport without weight restrictions for this vehicle category.

Fig. 1 – Three-dimensional model of a modular overpass

Its key feature is high mobility: the overpass is transported on a special chassis or trailer and can be quickly delivered to the place of operation (Figure 2). Installation is carried out directly at the site of work by deploying the structure, which does not require capital construction and reduces installation time to a few hours (Figure 3).

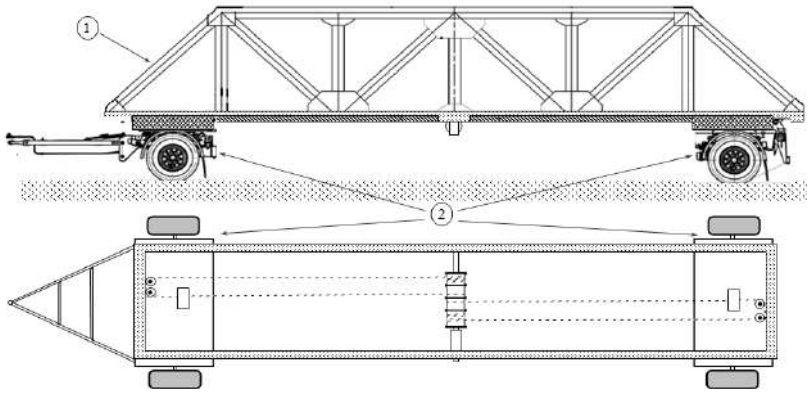

1 – supporting structure (platform) of the mobile overpass; 2 – movable suspension of the overpass.

Fig. 2 - Single-span modular overpass structure - transport position

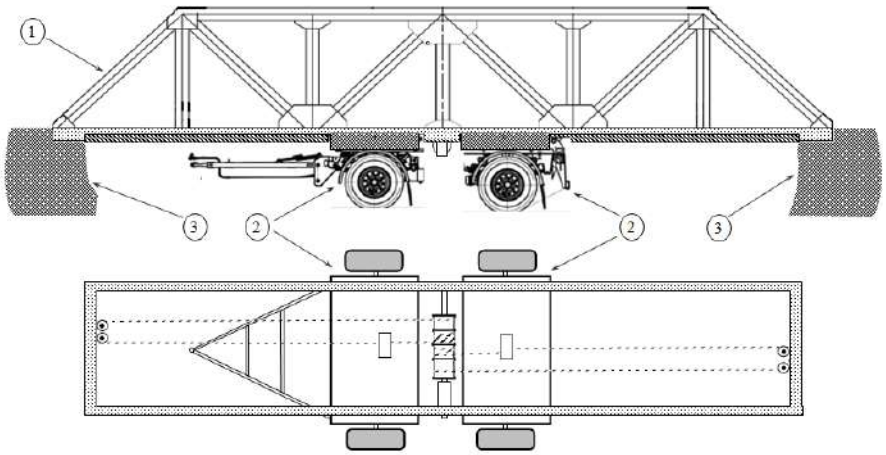

1 – supporting structure (platform) of the mobile overpass; 2 – movable suspension of the overpass; 3 – trench side.

Fig. 3 - Single-span modular overpass structure - in operational position above the trench

The presented structural diagram of the overpass ensures high operational reliability: the use of a spatial truss and reinforced guide elements allows for even load distribution and minimizes deformation.

The undercarriage of the overpass is equipped with a system of running wheels that can be in two positions: raised and lowered. In the transport position, the wheels are lowered, which allows the overpass to be moved to the installation site. After the structure is moved over the trench, the suspensions are moved using a special mechanism, transferring the overpass to bridge mode.

The position of the axle is adjusted by rotating a special drum that transmits force to the cable. When the tension of the cable is changed, the axle moves to the required position. The process of pulling or loosening the cable can be performed either manually or using an electric drive, which ensures high positioning accuracy. The electrical equipment of the mobile overpass is designed according to a single-wire DC power supply system with a nominal voltage of 24 V. Power is supplied either from the onboard electrical network of the towing vehicle or from an автономous аккумулятор battery mounted on the overpass frame. A separate independent circuit is provided for powering the electric motor of the axle movement drive (24 V). Such a power supply scheme allows the overpass to be installed and operated in locations without stationary electrical infrastructure while ensuring reliable operation of the tensioning and positioning mechanisms.

The running gear also includes cargo tie rods designed to connect to the towing vehicle, as well as suspension movement mechanisms. The latter ensure the correct installation of the structure on the supports, allowing this process to be carried out smoothly and safely.

To increase rigidity and operational reliability, a system of additional links connecting the front and rear axles is provided. This spatial arrangement prevents deformation and ensures the stability of the structure when subjected to dynamic loads during transportation.

An essential element of the structure is reinforced metal guide skids, which evenly distribute the load from the wheels to the supporting surface. This reduces the impact on the ground, allowing the overpass to be used even in areas with reduced bearing capacity without the risk of damage.

Thus, the running gear of the mobile overpass is a complex system that includes mechanisms for transportation, maneuvering, and installation. Design solutions aimed at increasing its strength and functionality ensure reliable operation of the overpass in various road and soil conditions.

The structure is designed to overcome trenches, repaired utilities, and temporarily closed road sections, ensuring the continuity of traffic flow even during large-scale reconstruction. During the operation of the mobile overpass, pedestrian movement across the repair zone is organized along temporary side walkways installed parallel to the overpass. This ensures complete separation of pedestrian and vehicle flows and increases overall safety during repair works.

An analysis of strength characteristics has shown that the mobile overpass is capable of functioning reliably under loads created by the movement of light and small-tonnage vehicles. The structure maintains the required level of rigidity and stability when exposed to dynamic factors. The spatial truss scheme ensures stability and uniform load distribution, while the presence of side barriers increases safety by eliminating the risk of vehicles veering off the road.

The economic efficiency of the mobile overpass is evident in the reduction of traffic jams, fuel consumption, and transport downtime. This achieves a significant socio-economic effect, especially in cities with heavy traffic. After the repair work is done, the overpass can be taken down and quickly moved to another spot, making it a flexible and versatile tool for temporarily organizing traffic and effectively managing traffic flows.

The study examines the main factors affecting the efficiency of traffic flows. The condition of Kazakhstan's road network remains one of the main factors contributing to transport problems: more than 40% of roads are in poor condition, and the lack of interchanges and bridges creates problem areas on the roads. Traffic management is also far from optimal: only about 15% of traffic lights are integrated into intelligent control systems, which limits the ability to regulate traffic flows and increases delays. The growth of the vehicle fleet further exacerbates the problem: by 2023, the number of registered vehicles exceeded 5 million, with about 60% of them being more than ten years old.

Urban development is also lagging behind the growth in car ownership: the density of the street and road network limits the possibilities for expansion, and the shortage of parking spaces is evident; for example, in Almaty, there are three cars for every parking space. The use of intelligent transport systems is still limited: only in Astana and Almaty do they cover about 30% of the territory, while in other cities such solutions are practically non-existent. The environmental component is also significant: the old, fuel-inefficient vehicle fleet accounts for up to 25% of the country's total pollutant emissions.

All these factors together create a systemic effect: worn-out roads, ineffective regulation, growth of the vehicle fleet, and weak integration of digital technologies lead to increased traffic jams, higher socio-economic costs, and a worsening environmental situation.

The above factors have an impact on key road sections in Karaganda. In particular, an analysis of the transport infrastructure and traffic at the intersection of Komissarova Street and Voinov-Internatsionalistov Street in Karaganda (Figure 4) revealed a number of key problems. Its strategic importance is due to the fact that this transport hub provides a direct connection to the railway station along Komissarova Street, provides access to the central district of the city (Mikhailovka) and the business center of Karaganda, and also serves the heavy traffic flows heading to large shopping and entertainment complexes, in particular City Mall. In addition, this intersection plays an important role in the transport

accessibility of cultural and leisure facilities, such as the city circus, as well as related infrastructure, including hotels, administrative buildings, and social institutions.

Fig. 4 – General view of the intersection of Komissarova and Voinov-Internatsionalistov streets

An analysis of the current traffic situation at the intersection of Komissarova Street showed that during rush hour, the load on the intersection reaches critical levels. In the morning (7:30–9:30 a.m.), there is heavy traffic, mainly from residential areas, including Mikhailovka, towards the railway station and the city center. The evening period (17:00–19:00) is characterized by the opposite direction of traffic: the main flow goes from the station and the center to the residential areas. During both time periods, the traffic intensity consistently exceeds the standard capacity of the intersection. This leads to the formation of long traffic jams several hundred meters long.

Measurements for the section under consideration were taken between August 18 and 24, 2024, over a full 24-hour period with one-hour intervals. Particular attention was paid to the morning and evening peak periods. To record the data, vehicles were counted manually by direction of travel: straight ahead, right, and left, at each of the approaches to the intersection.

The recorded value was 1,067 vehicles/hour, which exceeds the reference capacity of 1,000 vehicles/hour. The reference capacity value of 1000 vehicles/hour corresponds to the typical calculated capacity of a signalized urban intersection according to traffic engineering practice and methodologies presented in the Highway Capacity Manual (HCM). The distribution of traffic flows showed that the straight direction is predominant — up to 75% ($q_{straight}$= 800 vehicles/hour). The share of right-turn and left-turn flows was 13% ($q(_{right})$ = 134 cars/hour) and 12% ($q(^{left)}$= 133 cars/hour), respectively. The total flow at the turns reached 267 cars per hour.

If the total traffic flow q_c exceeds the standard capacity of intersection C, traffic jams and congestion are inevitable on the road section. In this case, the recorded value was 1,067 vehicles/hour, which exceeds the established standard of 1,000 vehicles/hour. Thus, the intersection of Komissarova Street and Voinov-Internatsionalistov Street is operating at overload, which confirms the presence of persistent traffic jams and highlights the need to implement additional engineering solutions to increase its capacity.

In addition, large-scale repair work is currently being carried out on the section under study, involving the replacement of underground utilities. These measures have significantly complicated the traffic situation: part of the roadway was completely blocked, which led to a reduction in the already limited number of lanes and a significant decrease in the capacity of the intersection (Figure 5).

Fig. 5 – Situation at the intersection of Komissarova Street and Voinov-Internatsionalistov Street during the overhaul of utilities

A telling example was the situation recorded in Karaganda from September 5 to 7, 2024, when traffic through the intersection of Komissarova Street and Voinov-Internatsionalistov Street was completely closed (Figure 6).

Fig. 6 – Fig. 6 – Traffic closure plan developed based on official municipal repair scheme

During this period, it was impossible to drive through the intersection, which exacerbated traffic jams and forced motorists to use detours.

In addition to organizational restrictions, the construction work itself was a complicating factor: pipelines were being replaced at the intersection, requiring significant intervention in the road structure (Figure 7).

Fig. 7 – Work on replacing utilities (pipelines)

The situation on site showed that the actual capacity of the intersection had decreased by more than half, which led to a forced redistribution of traffic flows to neighboring streets. However, the street network of the adjacent area is not designed for such high loads, which caused a chain reaction of traffic jams, increased transportation costs, and reduced overall traffic efficiency in the central part of the city. As a result, traffic restrictions in this area inevitably have a negative impact on the functioning of the entire urban transportation system.

In such conditions, the use of a mobile overpass appears to be the most rational engineering solution. Its installation will ensure continuity of traffic, redistribute transit traffic over the section under repair, and reduce the load on the intersection, while maintaining the stability of the city's transport links.

Unlike traditional traffic management methods (temporary detour schemes, installation of additional traffic light phases, widening of lanes at the expense of road shoulders), a mobile overpass provides physical separation of traffic flows and guarantees the preservation of traffic capacity on a critically important route.

A distinctive feature of this technology is its modularity and mobility. The structure can be erected in a very short time, without the need for large-scale earthworks or prolonged traffic closures. At the same time, standard low-frame chassis and prefabricated span structures can be used, which makes the project economically viable and technically realistic for urban conditions.

The socio-economic effect of the introduction of a temporary mobile overpass is evident in several key areas:

- reduction of transport costs by reducing travel time and fuel consumption;
- maintaining the stability of the city's transport system by redistributing traffic flows and eliminating congestion on the street and road network in residential areas;
- minimization of environmental damage by reducing emissions from cars stuck in traffic jams;
- increased safety for both drivers and pedestrians by eliminating intersections between traffic flows and repair work zones.

Thus, the introduction of a temporary mobile overpass at the intersection of Komissarova street and Voinov-Internatsionalistov street can be considered an innovative and strategically important solution capable of significantly improving the efficiency of Karaganda's transport system under restrictive conditions. Moreover, the mobile overpass can be reused in other parts of the city where similar capacity problems arise, ensuring its reusable value and quick return on investment.

2. Results and discussion

It is estimated that after the installation of the overpass, 90% of straight traffic will be redirected to the overpass, with only 10% remaining at the intersection (Figure 8).

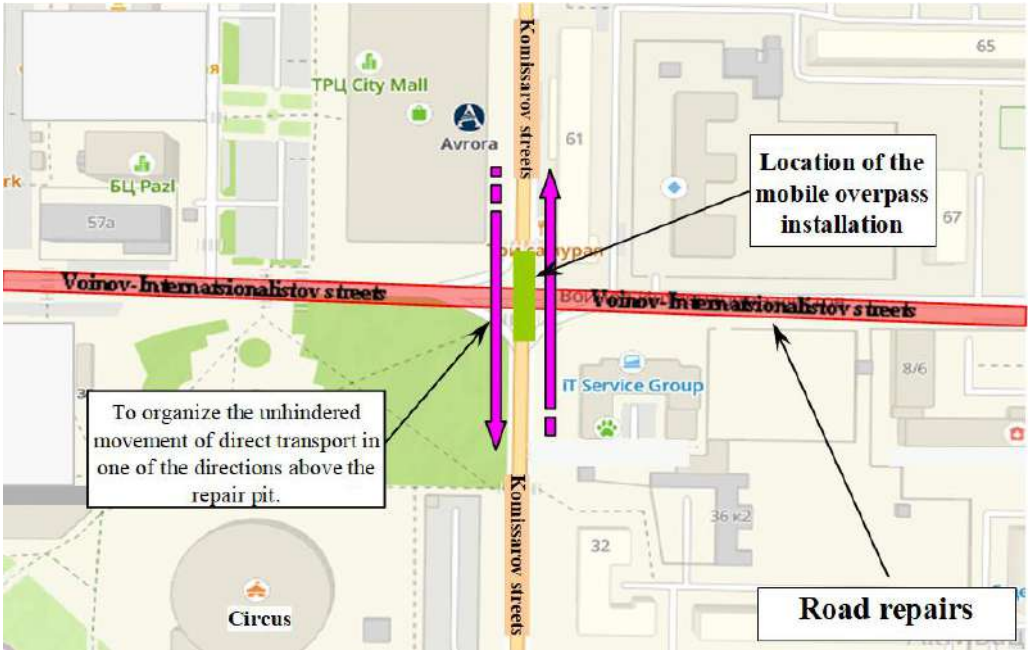

Fig. 8 – Proposed scheme for installing a mobile overpass to ensure continuity of traffic at the intersection in question

Then, if the straight flow initially was q_t =800 cars/hour, then the traffic flow ascending the overpass and remaining at the intersection will be:

$$q_{asen} = q_t \cdot n, car/hour \quad (1)$$

where q_t- the straight flow;

n - % of straight traffic, which will be redirected to the overpass or will be remained at the intersection.

$$q_{asen} = 800 \cdot 0{,}9 = 720\ car/hour$$

$$q_{rem} = 800 \cdot 0{,}1 = 80\ car/hour$$

And the total traffic flow after the overpass is installed will be:

$$q_{total} = q_{rem} + q_{on\ turns},\ \ car/hour \tag{2}$$

where $q_{on\ turns}$ - The share of right-turn and left-turn flows

$$q_{total} = 80 + (133{,}5 + 133{,}5) = 347\ \ car/hour$$

As a result of the redistribution of traffic flows, the total load on the intersection will decrease from 1,067 to 347 vehicles/hour, which is significantly lower than the standard capacity. This will eliminate the conditions for traffic jams. Consequently, after the installation of the mobile overpass, traffic will flow without congestion at the intersection of Komissarova Street and Voinov-Internatsionalistov Street during the calculated time intervals.

The average delay time for one vehicle at the intersection before and after the installation of the overpass was also considered:

$$d = \frac{0{,}5 \times c \times \left(1 - \frac{g}{c}\right)}{1 - X \times \frac{g}{c}},\ seconds. \tag{3}$$

where c - the traffic light cycle (84 s);

g - the duration of the green traffic light signal (35 s);

X - the load level

The load level is determined by the following equation:

$$x = \frac{g}{c}\ , \tag{4}$$

$$d_{before} = \frac{0{,}5 \cdot 84 \cdot \left(1 - \frac{35}{84}\right)}{1 - 1{,}067 \cdot \frac{35}{84}} = 25{,}74\ c.$$

Vehicle delay time at the intersection after the overpass installation:

$$d_{after} = \frac{0{,}5 \cdot 84 \cdot \left(1 - \frac{35}{84}\right)^2}{1 - \frac{347}{1000} \cdot \frac{35}{84}} = 16{,}71\ \ c$$

It is assumed that after the installation of the overpass, the average delay time for one vehicle at the intersection will be 16.71 s.

After the overpass is installed, the delay time for vehicles is reduced:

$$\Delta d = \ \ d_{before} - \ \ d_{before}\ \ \ hour \tag{5}$$

where d_{before} – vehicle delay time at the intersection before the overpass installation;

d_{after} – vehicle delay time at the intersection before the overpass installation.

$$\Delta d = 25.74 - 16.71 - 9.03\ c = 0.0025\ hour$$

Therefore, after the installation of the overpass, the average delay time for a single vehicle at the intersection will be reduced to **16.71 seconds**. Thus, compared to the initial value of **25.74 seconds**, the delay will be reduced by **9.03 seconds**, which is equivalent to approximately **0.0025 hours**.

Based on the calculations, a graph was drawn up describing the traffic flow at the intersection in question before and after the installation of the overpass (Figure 9).

The graph clearly demonstrates that redistributing traffic flow using an overpass reduces the load on the intersection and significantly reduces vehicle waiting times. This confirms the effectiveness of the proposed engineering solution in terms of both throughput capacity and reduction of socio-economic costs.

The effectiveness of installing the overpass was also assessed according to the following criteria:

- load reduction coefficient (traffic flow) per vehicle:

$$K_{lr} = \frac{q_{total(before)} - q_{total(after)}}{q_{total(before)}}$$

$$K_{lr} = \frac{1067 - 347}{1067} \cdot 100\% = 67{,}4\%$$

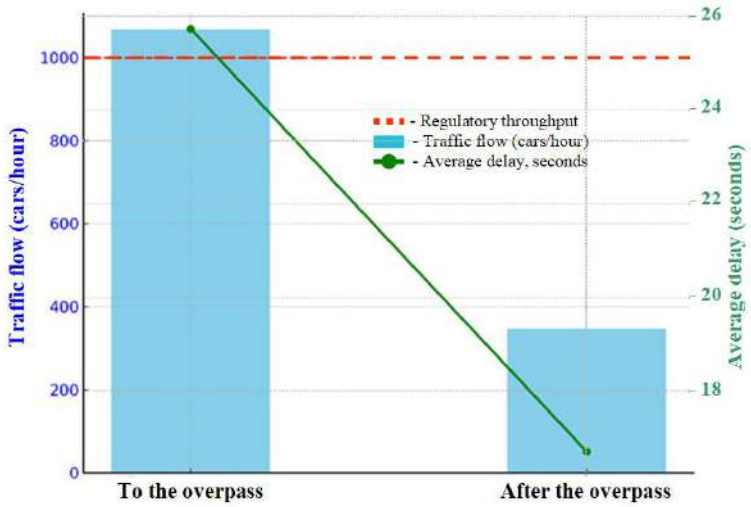

Fig. 9 - Graph describing the traffic flow at the intersection in question before and after the installation of the overpass

The load on the intersection after the installation of the overpass is reduced to 67.4%
- Intersection capacity (K_{ic}):

$$K_{ic} = \frac{C_{before}}{C_{after}} \quad (6)$$

$$K_{ic} = \frac{1067}{347} = 3{,}07$$

The capacity of the intersection will increase threefold after the installation of the overpass.
The economic efficiency of installing the overpass was assessed according to the following criteria:
- time savings at the intersection:

$$T_Y = \Delta d \cdot N_к \cdot C \quad (7)$$

where Δd – Is the reduction in vehicle delay time;
$N_к$ – number of cars, 1000 units;
C – price per hour of 1 driver's time 1500 tenge/hour.

Per day:

$$T_Y = 0.025 \cdot 1.000\ cars \cdot 1.500\ tenge/year = 3.750\ tenge$$

Per year:

$$T_Y = 3750 \cdot 365 = 1\,368\,750\ tenge/year$$

- Fuel savings:

$$\Delta Q = \Delta L \cdot R \cdot N \quad (8)$$

where ΔL = 2 km (reduction in traffic congestion)
R = 10 l/100 km = 0.1 l/km (fuel consumption)
N = 230 tg/l (fuel price)

The value ΔL = 2 km is based on field observations conducted during the closure of the intersection (September 5–7, 2024), where the average length of traffic congestion on detour routes recorded by visual measurements and GPS tracking exceeded 1.8–2.2 km.

Per day:

$$\Delta Q = 2 \cdot 0.1 \cdot 1000 = 200 \ \ l/day$$

Per year:

$$\Delta Q = 200 \cdot 230 \cdot 365 = 16\,790\,000 \ \ tenge/year$$

Total savings:

$$E_{year} = T_Y + \Delta Q$$

$$E_{year} = 1\,368\,750 + 16\,790\,000 = 18\,158\,750 \quad tenge/year$$

Thus, the calculations show that the installation of a mobile overpass at the intersection of Komissarova Street and Voinov-Internatsionalistov Street provides significant transport and economic benefits. The total load on the intersection is reduced by more than two-thirds – by 67.4 percent, which eliminates the conditions for traffic jams. At the same time, the effective throughput capacity increases 3.07 times thanks to the diversion of the main part of the direct traffic flow to the overpass. The average delay time for one car is reduced from 25.74 to 16.71 seconds, which corresponds to a reduction of almost nine seconds. In economic terms, this provides a tangible benefit: the annual time savings for drivers is estimated at 1.37 million tenge, and the reduction in fuel consumption due to the reduction of traffic jams by two kilometers allows for additional savings of about 16.8 million tenge per year. The total annual effect of installing the overpass is approximately 18.2 million tenge, which confirms the practical significance of implementing the proposed engineering solution.

Conclusion

The study confirmed the engineering and operational efficiency of the developed mobile overpass as an element of transport technology. The design, based on a metal support system integrated into a two-axle wheeled chassis, provides high mobility, strength, and stability under operational loads. The developed solutions for the suspension system, cable tensioning mechanism, and spatial truss scheme of the span section ensure reliability and durability of operation with short-term installation and dismantling.

Preliminary studies have confirmed that the overpass is capable of withstanding loads corresponding to the movement of light and small-tonnage vehicles, while maintaining structural rigidity and stability under dynamic loads. The use of reinforced guide rails and connecting elements minimizes deformation and allows the structure to be used in various road and soil conditions.

From an engineering point of view, the mobile overpass is an example of a high-tech mechanical engineering solution that not only allows traffic flows to be maintained during major repairs, but also allows the product to be reused multiple times at different sites. Its modularity, collapsible elements, and standardized components simplify production, transportation, and operation, which is especially important in the urban infrastructure of Kazakhstan.

Thus, the results of the study confirm the promising prospects for the development of mobile overpasses in the context of mechanical engineering and transport technology. The design combines mobility and technological efficiency with operational reliability, which makes it in demand both for temporary transport connections and for further improvement of engineering solutions in the field of road and construction technology.

References

[1] Ma M., Liu M., Li Z. Quantifying the Environmental Impact of Vehicle Emissions Due to Traffic Diversion Plans for Road Infrastructure Construction Projects: A Case Study in China //Sustainability, 2023, 15(10), 7825. https://doi.org/10.3390/su15107825

[2] Wang P., Zhang R., Sun S., Gao M., Zheng B., Zhang D., Zhang H. Aggravated air pollution and health burden due to traffic congestion in urban China //Atmospheric chemistry and physics, 2023, *23*(5), 2983-2996. https://doi.org/10.5194/acp-23-2983-2023

[3] Kim C., Butt A. A., Harvey J. T., Ostovar M. Environmental impacts from traffic on highway construction work zones: Framework and simulations. International //Journal of Sustainable Transportation, 2024, 18(8), 680-694. https://doi.org/10.1080/15568318.2024.2392624

[4] Hu X., Zheng M., Guo J., Chen X., Dai G., Zhao J., Long,B. Impact of lane-changing behavior on traffic emissions of road sections in multi-dimensional mixed traffic flow environment // Journal of the Air & Waste Management Association, 2023, *73*(5), 403-416. https://doi.org/10.1080/10962247.2023.2190180
[5] Bin Thaneya A., Horvath A. Exploring regional reduction pathways for human exposure to fine particulate matter (PM2. 5) using a traffic assignment model //Environmental Science & Technology, 2023, *57*(48), 19649-19662. https://doi.org/10.1021/acs.est.3c05594?urlappend=%3Fref%3DPDF&jav=VoR&rel=cite-as
[6] Wang B., Wang B., Lv B., Wang R. Impact of motor vehicle exhaust on the air quality of an urban city //Aerosol and Air Quality Research, 2022, 22(8), 220213.
[7] Askariyeh M. H., Venugopal M., Khreis H., Birt A., Zietsman J. Near-road traffic-related air pollution: Resuspended PM2. 5 from highways and arterials //International journal of environmental research and public health, 2020, *17*(8), 2851.
[8] Yessenbayeva A., Kadyrova I, Aukenov N., Shaimardanov N. Apsalikov B., Massabayeva M., Kazymov M., Shakhanova A., Mussazhanova Zh., Biomarkers of immunothrombosis and polymorphisms of IL2, IL6, and IL10 genes as predictors of the severity of COVID-19 in a Kazakh population //PLoS ONE, Vol. 18, Issue 6, 2023. – p. 61-67.
[9] Akhmaltdinova L., Sirota V., Babenko D., Zhumaliyeva V., Kadyrova I., Maratkyzy M., Ibrayeva A., Avdienko O. Proinflammatory cytokines and colorectal cancer – the impact of the stage //Wspolczesna Onkologia, Vol. 24, Issue 4, 2021. – p. 207-210.
[10] Esenbaeva G.T., Zhautikova S.B., Mindubayeva F.A., Kadyrova I.A. A method for predicting probability of stroke // Zhurnal Nevrologii i Psihiatrii imeni S.S. Korsakova, 2014, 3,51 – 54, {https://www.scopus.com/inward/record.uri?eid=2-s2.0-84905052170&partnerID=40&md5=b90780d360de8f3c3ea2cc6c51542d32}
[11] Kadyrova I.A., Mindubaeva F.A., Grjibovski A.M. Prediction of outcomes after stroke: A systematic review //Human Ecology (Russian Federation), Vol. 4, Issue 10, 2015 – p. 55 – 64
[12] Kadyrov A., Ganyukov A., Balabekova K. Development of constructions of mobile road overpasses // MATEC Web of Conferences, Vol. 108, Issue 16002, 2017 – p.1-4. DOI: 10.1051/matecconf/201710816002
[13] Kadyrov A.S., Ganyukov A.A., Amanbayev S.Sh., Bogdanova A.A. Development of Mobile Communal Overpasses Applied During Repairing of Urban Communal Networks // Material and Mechanical Engineering Technology, No. 3, 2023. – P.11-14. DOI 10.52209/2706-977X_2023_3_1
[14] Kabibollayev B.B., Kadyrov A.S., Kukesheva A.B., Karsakova A.Zh., Sinelnikov K.A. Environmental and Economic Feasibility of Implementing Electro-Impulse Mufflers on Motor Vehicles // Material and Mechanical Engineering Technology, Vol. 7, No. 3, 2025. – P. 99–110. DOI: 10.52209/2706-977X_2025_3_99.
[15] Kadyrov A., Warguła Ł., Kukesheva A., Dyssenbaev Y., Kaczmarzyk P., Klapsa W., Wieczorek B. Optimization of Vertical Ultrasonic Attenuator Parameters for Reducing Exhaust Gas Smoke of Compression–Ignition Engines: Efficient Selection of Emitter Power, Number, and Spacing //Applied Sciences, 2025, 15(14), 7870.
[16] Kadyrov A.S., Kukesheva A.B., Bakytov Y.S. Mobile Overpass with a Movable Foundation: Ensuring Trench Stability Under Traffic Loads //Material and Mechanical Engineering Technology, Vol. 7, No. 4, 2025. – P. 30–36. DOI: 10.52209/2706-977X_2025_4_29.
[17] Kadyrov A., Ganyukov A., Balabekova K. Development of constructions of mobile road overpasses // MATEC Web of Conferences, Vol. 108, Issue 16002, 2017 – p.1-4. DOI: 10.1051/matecconf/201710816002
[18] Kadyrov A.S., Ganyukov A.A., Amanbayev S.Sh., Bogdanova A.A. Development of Mobile Communal Overpasses Applied During Repairing of Urban Communal Networks // Material and Mechanical Engineering Technology, No. 3, 2023. – P.11-14. DOI 10.52209/2706-977X_2023_3_1
[19] Ganyukov A.A., Sinelnikov K.A., Kabikenov S.Zh., Karsakova A.Zh. Research and Calculation of the Deformed State of the Roadway Mobile Overpass // Material and Mechanical Engineering Technology, Vol. 6, Issue 3, 2024. - p. 88-95.
[20] Kadyrov A. A., Ganyukov, A. A., Balabekova K. G., Zhunusbekova Z. Z., Suleev B. D. Scientific and engineering bases for development of mobile overpasses //Material and Mechanical Engineering Technology, 2020, *2*(2), 7-13.

Information of the authors

Zhumabekov Aidar Temirgalievich, master of Technical Sciences, Abylkas Saginov Karaganda Technical University
e-mail: aidar_7478@mail.ru

Sakhapov Rustem Lukmanovich, d.t.s., professor, Kazan (Volga region) Federal University
e-mail: rusakhapov@gmail.com

Suyunbayev Shinpolat Mansuralievich, d.t.s., professor, Tashkent State Transport University
e-mail: shinbolat_84@mail.ru

Karsakova Akbope Zholaevna, PhD, Abylkas Saginov Karaganda Technical University
e-mail: karsakova84@mail.ru

Sinelnikov Kirill, PhD, Abylkas Saginov Karaganda Technical University
e-mail: coolzero7777@gmail.com

DOI 10.52209/2706-977X_2026_1_14 **IRSTI 55.43.09** **UDC 620.179.16**

Research of the Influence of Chemical Composition on the Mechanical Characteristics of Cast Parts for Freight Car Bogies

Tursunov N.K.*, Saidirakhimov A.A.
Tashkent State Transport University, Tashkent, Uzbekistan
* corresponding author

Abstract. This article presents the main factors influencing the mechanical properties of steel. The influence of the main chemical elements in the composition of steel on mechanical properties is shown and their role in obtaining a high complex of operational characteristics is explained. Laboratory data on chemical composition and mechanical properties of steel were analyzed. The possible effects of chemical elements on the formation of the non-metallic inclusions and microstructure are considered. Steel grade 20GL must possess high strength, plasticity, and impact toughness, which are crucial for cast parts of freight cars. In railway transport, the side frame and overhead beam are considered critical components are cast from 20GL grade steel. Improving the mechanical properties of this steel is the main task.

Key words: strength limit, relative elongation, impact toughness, chemical composition, non-metallic inclusions, microstructure.

Introduction

The mechanical properties of a material characterize its resistance to destruction, deformation, or behavior during the destruction process. These include hardness, plasticity, strength, elasticity, impact toughness, fatigue resistance (endurance), and others.

Strength is the ability of a material to resist destruction and deformation when compressed, stretched, twisted, and bent. Two strength characteristics are used: fluidity limit σ_T and strength limit σ_S [1].

Plasticity is the ability of metals and alloys to deform irreversibly (plastically) under external load without breaking down. The characteristics of plasticity are relative elongation and relative narrowing [1].

Impact toughness is the ability of metals and alloys to resist impact loads. For testing, samples of standard size according to GOST 9454-78 with a concentrator are used, the role of which is performed by a V-shaped incision [1].

High impact toughness (from 20 to 80 J/cm^2 for different groups of alloys) is characteristic of highly plastic single-phase metals and alloys, pure in impurities or heterogeneous in structure alloys with a small number of non-metallic inclusions or their optimal sizes and distribution. Alloying leads to a decrease in impact toughness. Impact toughness is increased by removing impurities that lead to the formation of fragile excess phases [2].

The impact toughness test is the main one due to the instability of this parameter, as impact toughness depends on many factors: chemical composition, heat treatment, microstructure, casting defects, etc. [3].

One of the main criteria for the quality of metal is its cold resistance, i.e., high plasticity and low-temperature viscosity. The quality level of the metal, i.e., its high mechanical properties and cold resistance, is determined by the degree of contamination with harmful impurities such as sulfur, phosphorus, oxygen, nitrogen, hydrogen, etc. At the same time, sulfur and phosphorus have the most negative effects - through non-metallic inclusions and through the enrichment of metal boundary volumes, which leads to the weakening of bonds at grain boundaries [4].

The main objectives of this work are analyzing the effect of key chemical elements on strength, plasticity, and impact toughness and determining methods for improving the mechanical performance of steel grade 20GL for freight car cast components. To achieve these objectives, the following tasks are performed: analyze the influence of key chemical elements on the strength, plasticity, and impact toughness of steel grade 20GL; investigate the relationship between chemical composition, microstructure, and non-metallic inclusions, and their effect on mechanical properties; develop practical recommendations for improving the mechanical properties of 20GL steel used in critical freight car components (side frame and overhead beam).

As expected results, the research will establish the dependence of the mechanical properties of 20GL grade steel, used for manufacturing critical components of freight car bogies, on its chemical composition and the level of harmful impurities.

It will also study the influence of sulfur and phosphorus on the steel's plasticity, impact toughness, and low-temperature resistance, which is caused by the formation of non-metallic inclusions and the development of intergranular brittleness.

1. Research method

The smelting processes were carried out in a six-ton induction crucible furnace of the Otto-Junker company (Fig. 1). Table 1 presents the technical characteristics of the ICF-6 induction crucible furnace [5], which is used at JSC "Foundry and Mechanical Plant" (Tashkent, Uzbekistan).

Fig. 1. – Induction crucible furnace

Table 1. Technical characteristics of ICF [5].

Parameter name	Norm
Capacity	6 t
Nominal power	4.8 MB•A
Current frequency	500 Hz
Internal diameter of the crucible	920 mm
Lining thickness	125 mm
Specific electricity consumption	505 kWh/t
Lining	Based on Al_2O_3

Metallographic studies were conducted on cast metal cross-sections (trifle-shaped samples) and after etching with a 3% HNO_3 solution in spirit (alcohol). The "Olympus BX 41M LED" modular microscope was used to determine the microstructure of the metal (Figure 2) in scientific-research laboratory of the Materials Science and Mechanical Engineering Department, Tashkent State Transport University.

Fig. 2. – Modular microscope "BX 41M LED"

Figure 3 shows the MSA optical emission spectrometer of the scientific-research laboratory of the Materials Science and Mechanical Engineering Department (Tashkent State Transport University), which was used to determine the chemical composition of steel.

Fig. 3. – Optical-emission spectrometer for chemical composition analysis

The chemical composition and mechanical properties of 20GL steel according to GOST 32400 2013 are presented in tables 2 and 3 [6].

Table 2. Chemical composition of 20GL steel, (% by mass.)

C	Si	Mn	Al	P	S	Cr	Ni	Cu	Fe
				no more than					
From 0.17 to 0.25 (-0.020)	From 0.30 to 0.50 (±0.10)	From 1.10 to 1.40 (±0.10)	From 0.020 to 0.060 (+0.005)	0.020 (+0.005)	0.020 (+0.005)	0.30 (+0.20)	0.30 (+0.30)	0.60	rest

Note! In brackets, the permissible deviations from the chemical composition of steel are indicated.

Table 3. Mechanical properties of 20GL steel

Fluidity limit, MPa	Strength limit, MPa	Relative elongation, %	Relative narrowing, %	Impact toughness, KCV^{-60}, kJ/m^2
no less than				
343	510	18	30	200

2. Results and discussion

The results of the analysis of samples for the chemical composition and mechanical characteristics of some 20GL steel alloys are considered. Figure 4 shows the dependence of mechanical characteristics on the carbon content in the steel.

From Figure 4, it can be seen that with an increase in the carbon content in cast steels, their strength increases, while plasticity and impact toughness decrease. With an increase in carbon from 0,19% to 0,25%, the relative elongation of steel significantly decreases from 30% to 24%, and the value of the strength limit slightly increases. An increase in carbon content in steel, accompanied by an increase in the proportion of perlite in the structure, leads to an increase in fluidity limit and strength limit and a decrease in plasticity.

The impact toughness level is decreasing imperceptibly. Perhaps this is due to the increase in the pearlite fraction in the steel.

Silicon is also introduced into steel to reduce its oxidation. Silicon enters the solid solution in ferrite, increasing the strength properties of steel.

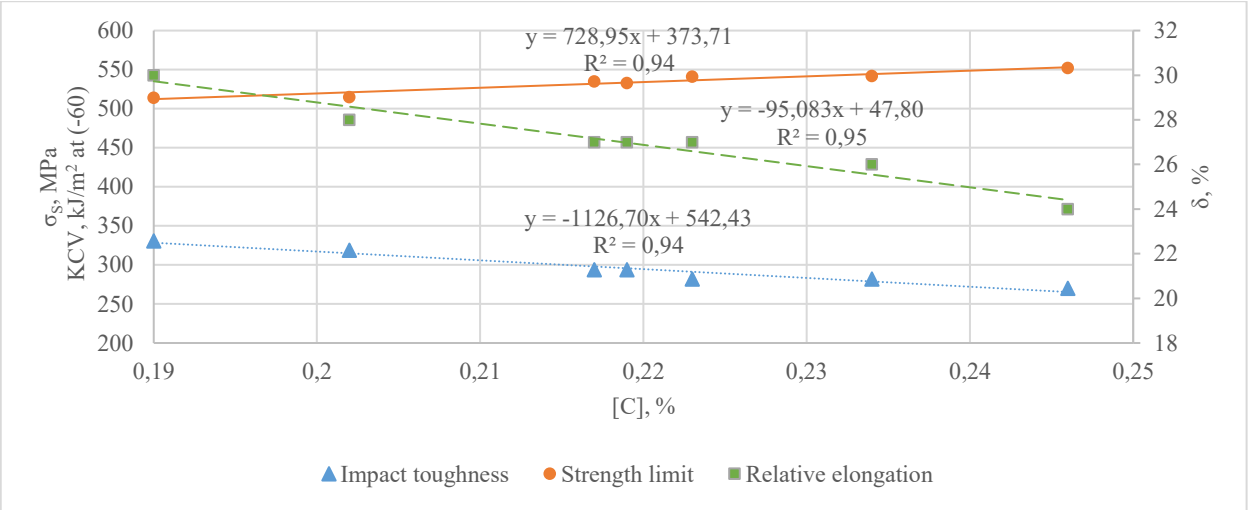

Fig. 4. - Dependence of mechanical properties on the carbon content

Figure 5 shows the dependence of mechanical characteristics on the silicon content in the steel.

From Figure 5, it can be seen that with an increase in the silicon content within the range of 0,33-0,46%, the value of relative elongation and impact toughness decreases insignificantly, while the strength limit increases.

Manganese is a technological additive that is introduced into steel for deoxidation and desulfurization - to eliminate the harmful effects of sulfur. Manganese is partially dissolved in ferrite and partially in cementite, where it replaces iron atoms. Manganese impurity slightly increases the strength of the steel.

Manganese and silicon can partially be part of non-metallic inclusions - complex oxides of the spinel type FeO·MnO, silicates $2FeO·SiO_2$, $2MnO·SiO_2$, etc. [7].

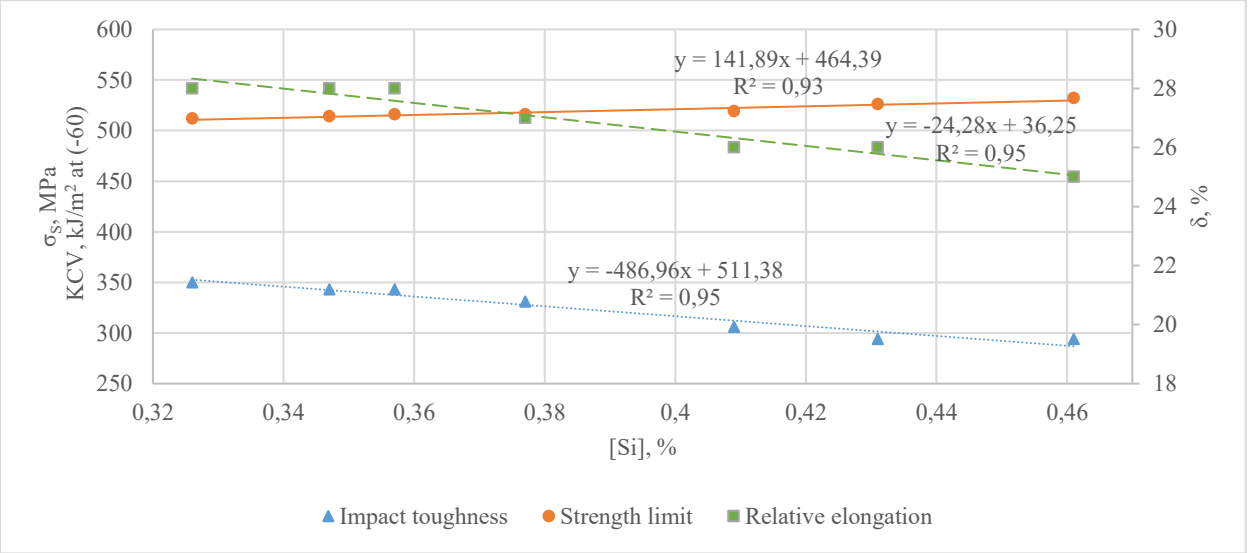

Fig. 5. – Dependence of mechanical properties on the silicon content

Figure 6 shows the dependence of mechanical properties on manganese content.

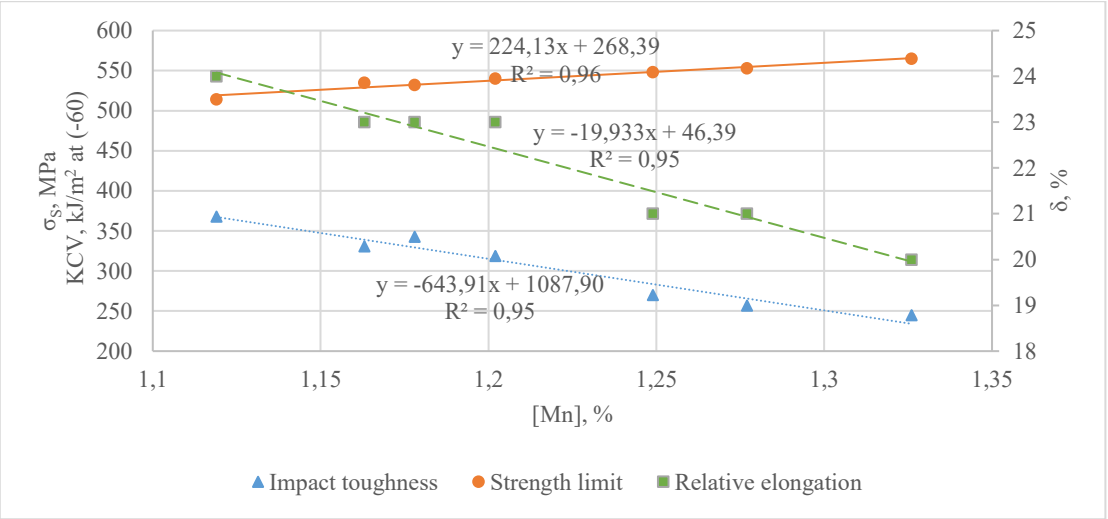

Fig. 6. – Dependence of mechanical properties on manganese content

From Figure 6, it can be seen that with an increase in manganese content from 1.1% to 1.35%, the relative elongation decreases. Manganese also leads to a decrease in impact toughness. However, it increases the strength limit of the steel.

Aluminum is the best deoxidizer, plays the role of deoxidizing and grinding grains, which increases the impact toughness and plasticity of steel. Additionally, nitrogen can be bound to nitrides (e.g., AlN), aluminum (approximately 0,05%) is introduced into the ladle before pouring to obtain hereditary fine-grained steel - dispersed particles of aluminum oxide and nitride inhibit the growth of austenite grains [7].

Figure 7 shows the dependence of aluminum's influence on the mechanical properties of steel.

From Figure 7, it can be seen that with high aluminum content, the level of mechanical characteristics of steel reaches high values. When oxidized with aluminum, the aluminum content should be at the highest level according to GOST 0,04-0,06%. Aluminum has no apparent harmful effect on the mechanical properties of steel.

Phosphorus, being a harmful impurity, significantly reduces the properties of steel. With an increase in the phosphorus content, the strength, brittleness, and cold-breaking threshold increase, while simultaneously reducing the plasticity and viscosity of the steel [8].

Phosphorus influences the properties of the metal matrix, while sulfur influences the properties of the metal matrix through sulfides. The brittleness of phosphorus is enhanced by the action of the third element. Carbon and manganese displace phosphorus from the solution to the grain boundaries, significantly weakening the intergranular bonds and leading to a decrease in plasticity and viscosity [4].

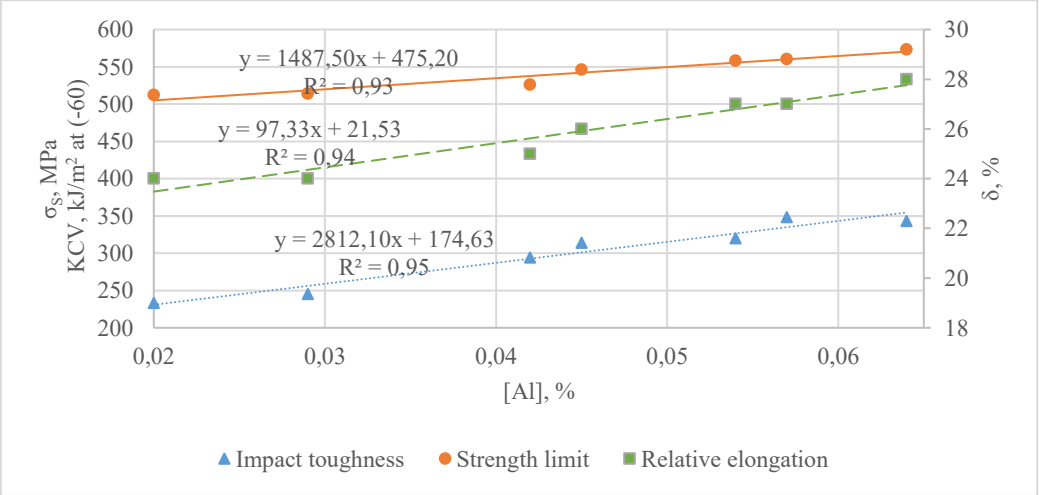

Fig. 7. – Dependence of mechanical properties on the aluminum content

The harmful effects of phosphorus are related to the peculiarities of the iron-phosphorus phase diagram. Phosphorus dissolves in austenite up to 0,2%, and in ferrite even more, and significantly strengthens the solid solution. The plastic properties of steel, especially at low temperatures, significantly decrease due to the release of very fine phosphide segregations along the grain boundaries. The damage from phosphorus is always observed in grain boundary brittleness, which reduces impact toughness [9].

Sulfur dissolved in steel acts similarly to phosphorus, and non-metallic inclusions are released at the boundaries of primary grains (when oxidized by aluminum), weakening the metallic bond and reducing viscosity and plasticity indicators [4].

The large radius of the sulfur atom (0,104 nm) compared to the iron atom leads to an increase in strength and loss of plasticity due to the stressed state in the iron lattice [4].

Figure 8 shows the influence of the total sulfur and phosphorus content on the mechanical properties of steel.

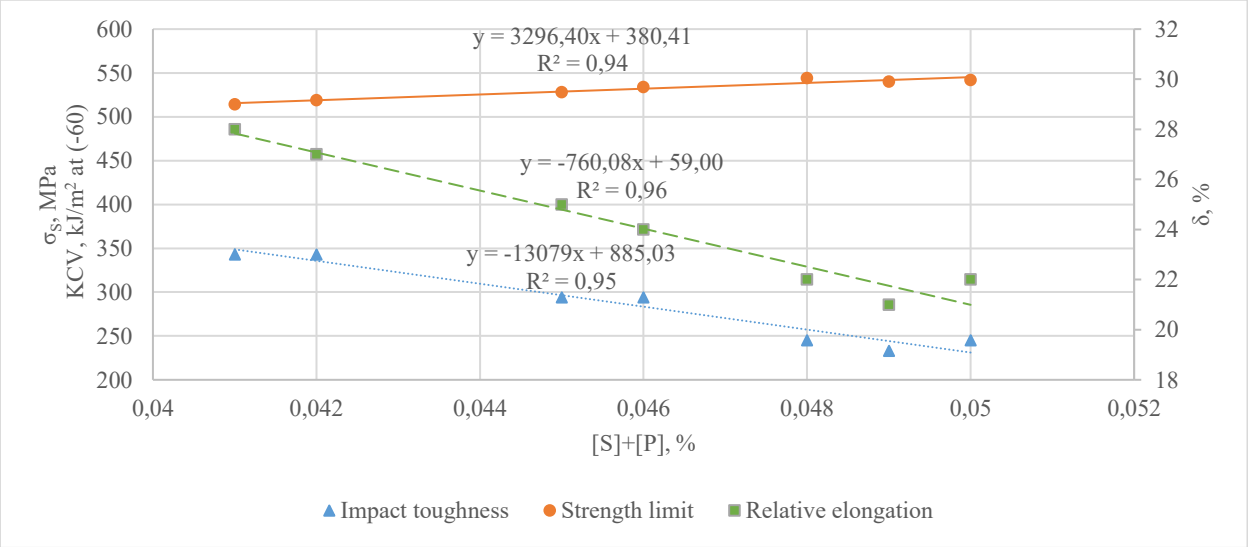

Fig. 8. – Influence of sulfur and phosphorus on the mechanical properties of steel

As can be seen from Figure 8, sulfur and phosphorus are harmful impurities, significantly reducing impact toughness and relative elongation. Especially, the impact toughness decreases from 350 KJ/m^2 to 230 KJ/m^2 with an increase in the total sulfur and phosphorus content from 0,040% to 0,050%.

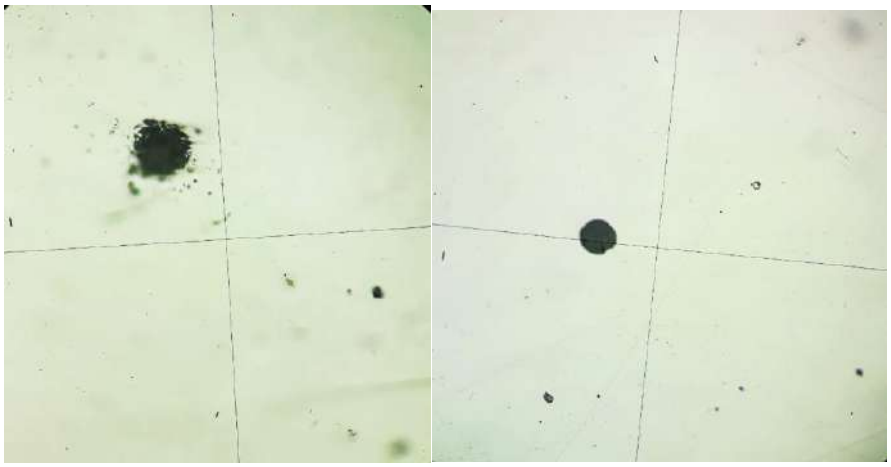

Fig. 9. – Non-metallic inclusions in 20GL steel

Figure 9 shows non-metallic inclusions in 20GL steel. The main part of oxide inclusions (endogenous inclusions) is formed as a result of oxidation during the addition of reducing agents and cooling of liquid steel (pre-crystallization) and during its crystallization (crystallization) [10].

Stress concentration causes a volumetric stress state, inclusions worsen the plasticity (relative elongation and relative narrowing) and impact toughness. The strongest inclusions affect the impact toughness, which is especially sensitive to stress concentrators and metal cuts [10].

Increased sulfur content leads to steel contamination with non-metallic inclusions, mainly sulfides. For this reason, the decrease in plasticity and impact toughness with increasing sulfur content is explained not only by metal contamination with non-metallic inclusions but also by changes in the solubility of sulfur present in the solution, which will enrich the boundary areas of austenite and ferrite grains during steel cooling, leading to metal brittleness at positive and low temperatures [4].

Sulfides are the main type of inclusions. The type or form of sulfide inclusions separation is determined by the degree of deoxidation (content of residual aluminum and oxygen) of the steel [11].

When the amount of [O] in the metal is 0,02%, only globular sulfides (type 1) are formed, at 0,01-0,02% - sulfides of type 1 and 2, and when [O] is less than 0,01%, only sulfides of type 2 are formed [11].

Type 1 - small globular sulfides and oxysulfides that are separated in steels in the branches of austenite dendrites as droplets of a high-sulfur liquid during separate or cooperative monothetic transformation. These droplets, upon further cooling, solidify as manganese sulfide or oxysulfide inclusions. This type of inclusion is characteristic of steels containing low aluminum concentrations.

Type 2 is characteristic of well-deoxidized steels, but containing low concentrations of excess aluminum. Such sulfides lead to a sharp weakening of intergranular bonds and a significant decrease in the plastic and viscous properties of steel, which plays the role of films located along the grain boundaries.

Type 3 - edged, anchor-shaped, and dendritic sulfides formed under conditions of separate eutectic crystallization with a further increase in aluminum content. They reduce the quality of steel to a lesser degree than type 2 inclusions, but still deteriorate the properties of the metal to a greater extent than type 1 inclusions.

To obtain type 1 sulfides, it is necessary to have a critical amount of aluminum in the steel. However, this is not enough to obtain a dense metal with a fine-grained structure. Therefore, to make a high-quality metal, it is necessary to introduce a supercritical amount of aluminum into the steel.

Elongated inclusions are dangerous because, under the influence of external loads, stress concentration occurs around these sulfides, resulting in microcracks. Inclusions with a size of 5-10 μm are especially dangerous [11].

Deoxidation solely by aluminum does not ensure the favorable forms and topography of non-metallic inclusions, and consequently, the physical and mechanical properties of steel. Therefore, complex modification is used, where elements are introduced along with aluminum for globulation and more disoriented distribution of oxidesulfide formations. The most promising in this direction are alkaline-earth and rare-earth metals (AEM and REM). These elements have a beneficial effect on the mechanical and operational properties of steel due to their high deoxidizing ability, refining effect, and globularization of non-metallic inclusions. However, the application of these elements is effective after preliminary oxidation with aluminum [12].

Figure 10 shows the microstructure of 20GL steel after heat treatment.

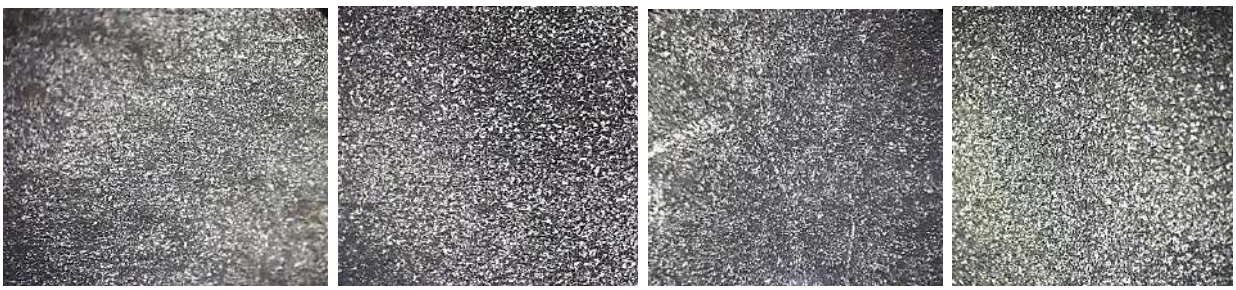

Fig. 10. – Microstructure of 20GL steel after normalization and tempering (x100)

The microstructure is homogeneous, ferrite-pearlite, fine-grained, with a uniform distribution of structural components. The grain score according to GOST 5639-82 is 8-9, which is permissible according to GOST 32400-2013 (not lower than 8) [13].

Ferrite is a soft, plastic component of the structure. The properties of ferrite primarily depend on its carbon content, alloying elements, and grain size. Carbon and nitrogen, which form solid solutions with iron, provide the most significant effect of ferrite hardening, which is mainly due to their strong interaction with dislocations and hardening of the latter [14-16].

Alloying elements, which form solid substitution solutions with iron, strengthen ferrite less than carbon and nitrogen.

Substitution elements and, to a greater extent, embedding elements increase the temperature of the viscous-fragile transition T_{cr}, which characterizes the steel's tendency to fragile destruction.

The strength of ferrite is greatly influenced by the size of its grain. With the grinding of ferrite granules simultaneously with additional hardening, the viscous-fragile transition temperature decreases [17-19].

Thus, grinding ferrite granules is an effective strengthening method, as it simultaneously reduces the tendency for brittle destruction.

The viscosity of steels with a ferrite-carbide structure increases when pearlite colonies and ferrite grains are ground. These structural parameters significantly depend on the size of the austenitic grain. Therefore, to obtain a high degree of mechanical properties during heat treatment, a fine austenitic grain is sought [20-22].

Conclusions

This research was conducted as part of the scientific and innovative projects of Tashkent State Transport University, commissioned by JSC “Foundry and Mechanical Plant” (Tashkent, Uzbekistan).

As a result of the conducted research, it was established that the mechanical properties of 20GL grade steel used for critical parts of freight car bogies significantly depend on its chemical composition and the level of contamination with harmful impurities. Particularly significant influence is exerted by sulfur and phosphorus, which deteriorate the plasticity, impact toughness, and cold resistance of steel due to the formation of non-metallic inclusions and inter-crystallite brittleness. Increasing the carbon and silicon content contributes to an increase in strength characteristics, but is accompanied by a decrease in plasticity and viscosity indicators. The addition of aluminum positively affects the dispersion strengthening, deoxidation, and grinding of grain, thereby increasing the complex of mechanical properties. The most critical indicator characterizing steel reliability is impact toughness, as it is most sensitive to the presence of casting defects, microstructural changes, and stress concentrators. Tests show that a steel structure with minimal harmful impurities and an optimal alloying system provides a high level of strength and operational reliability. Thus, effective management of the chemical composition and modification technology of steel allows for obtaining optimal mechanical characteristics necessary for reliable and safe operation of rolling stock parts.

References

[1] Maletkina T.Yu. Mechanical properties of metals and alloys and methods for their determination: methodological instructions. / Comp. - Tomsk: State University Publishing House, 2015. - 27 p.

[2] Novikov I.I., Zolotorevsky V.S., Portnoy V.K. Metallology: textbook. In 2 vols. Fundamentals of Metal Science / 2nd ed., revised. - M.: Publishing House. MISiS House, 2014. - 496 p.

[3] Pavlov A.V., Kveglis L.I., Romanova A.A., Rakhadilov B.K., Zhilkashinova A.M. Investigation of 20GL steel castings for compliance with the technical requirements of railway transport. 66 Innovations in Science / Collection of articles based on materials of the XLVII International Scientific Practical Conf. No. 7 (44). Novosibirsk: SibAK Publishing House, 2015. - 150 p.

[4] Lunev V.V., Averin V.V. Sulfur and phosphorus in steel// Metallurgy, 1988. - 256 p.

[5] Tursunov N.K., Semin A.E., Sanakulov E.A. Research of dephosphorization and desulfurization processes during the smelting of 20GL steel in an induction crucible furnace //Collected Works. Moscow – Elektrostal, 2016, - P. 272-276.

[6] GOST 32400-2013 Side frame and overhead beam of cast railway freight cars.

[7] Novikov I.I., Zolotorevsky V.S., Portnoy V.K. [et al.] Metallology: textbook. In 2 vols. Heat treatment. Alloys / 2nd ed., revised. - M.: Publishing House. MISiS House, 2014. - 528 p.

[8] Semin A.E., Alpatov A.V., Kotelnikov G.I. Modern Problems of Metallurgy and Materials Science: Practicum. - M.: Publishing House, MISIS House, 2015. - 56 p.

[9] Semin A.E., Tursunov N.K., Kosyrev K.L. Innovative production of high-alloy steel and alloys: theory and technology of steel smelting in induction furnaces: textbook. - M.: Publishing House NITU "MISIS," 2017. - 166 p.

[10] Povolotsky D.Ya., Roshchin V.E., Ryss M.A., Stroganov A.I., Yartsev M.A. Electrometallurgy of steel and ferroalloys - Textbook for universities. 2nd ed., revised and expanded. - M.: Metallurgy, 1984. - 568 p.
[11] Sheshukov O.Yu., Yermakova V.P., Smirnova V.G., Nekrasov I.V., Marshuk L.A. Technological parameters of melting and microstructure of 20GL steel in cast and heat-treated state //Collected Works. Moscow – Elektrostal, 2016, P. 152-157.
[12] Durynin V.A., Solntsev Yu.P. Research and improvement of production technology to increase the resource of steel products from large coils of critical purpose. - SP6.: KHIMIZDAT, 2006. - 272 p.
[13] GOST 5639-82 Steels and alloys. Methods for identifying and determining grain size.
[14] Smirnov M. A., Schastlivtsev V. M., Zhuravlev L.G. Fundamentals of Thermal Processing of Steel: Textbook/ O-75 - M.: Science and Technology, 2002. - 519 p.
[15] Rakhimov U., Tursunov N., Urazbayev T., Bakhteev E., Omonov I. Development of a technology for producing cast iron in an induction crucible furnace, modification in a ladle and casting in a system of casting molds Vibroengineering Procedia, Vol. 60, 2025. - P. 416–423/
[16] Toirov O., Tursunov N., Kuchkorov L. Development of resource-saving composition of sand-clay mixtures for steel castings with improved physical and chemical characteristics //Vibroengineering Procedia, Vol. 58, 2025. - P. 277–282
[17] Tursunov N., Saidirakhimov A., Toirov O. Experimental and theoretical study of the efficiency of solid slag mixtures for desulfurization of 20GL steel under conditions of induction crucible melting //Vibroengineering Procedia, Vol. 58, 2025. - P. 283–290, May
[18] Bekmurzaev N., Nurmetov K., Alimukhamedov S. Creation of a wear-resistant bimetallic coating for the track treadmill of a crawler //Vibroengineering Procedia, 2025, Vol. 60, pp. 370–377
[19] Valieva D., Yunusov S., Tursunov N. Study of the operational properties of the bolster of a freight car bogie //E3S Web of Conferences, 401, 05017 2023
[20] Toirov O., Tursunov N. Research of the influence of the technological parameters of the steelmaking process on the design and defect formation of large-sized castings for freight cars //Vibroengineering Procedia, Vol. 58, 2025. - P. 271–276
[21] Toirov O., Tursunov N. Efficiency of using heat-insulating mixtures to reduce defects of critical parts //E3S Web of Conferences 401, 05018, 2023
[22] Urazbayev T., Tursunov N., Tursunov T. Steel modification modes for improving the cast parts quality of the rolling stock couplers //AIP Conf. Proc. 3045, 060015, 2024

Information of the authors

Tursunov Nodirjon Kayumjonovich, DSc, professor, Tashkent State Transport University
e-mail: u_nadir@mail.ru

Saidirakhimov Azizjon Azim ugli, PhD student of “Materials Science and Mechanical Engineering” Department, Tashkent State Transport University
e-mail: azizsaidrahimov94@gmail.com

DOI 10.52209/2706-977X_2026_1_23 **IRSTI 55.03.14** **UDC 621.8**

Strength Assessment of a New Adaptive Tooling Design

Nurzhanova O.A.[1], Zharkevich O.M.[1*], Bakenov A.A.[1,2], Berg A.S.[1], Zakirov K.[1,3]
[1]Abylkas Saginov Karaganda Technical University, Karaganda, Kazakhstan
[2] Maker LLP, Karaganda, Kazakhstan
[3] KazTechInstrument LLP, Astana, Kazakhstan

Abstract. This article discusses the current scientific and technical challenge of improving the efficiency of processing complex spatial shapes of body and thin-walled parts in small-batch production. Traditional tooling often does not provide the required rigidity and flexibility, which leads to vibrations and deformations of workpieces. The authors propose an innovative design for adaptive tooling, a distinctive feature of which is the use of a polymer concrete base and a matrix of telescopic pins positioned by stepper motors. The main focus of the work is on evaluating the strength and load-bearing capacity of the new design using the finite element method (FEM) in the Ansys Discovery 2024 R2 software package. During simulation modeling, the behavior of the system under the influence of a significant static load of 100,000 N was investigated. S275N steel was used for the pins and epoxy-based polymer concrete for the frame. The analysis results showed high rigidity of the system. The maximum displacements were only 4.53 μm and were localized at the tops of the pins, without exceeding the elastic deformation zone. The study of equivalent stresses according to Mises confirmed that the peak values (4.58 MPa) are many times lower than the yield strength of steel (237 MPa). The use of polymer concrete is justified by its ability to effectively dampen vibrations and ensure geometric stability at low levels of internal stresses. It has been established that the critical value of the coefficient ($n > 1.5$) is reached at loads exceeding 550–600 kN, which is equivalent to a workpiece weight of more than 56 tons. Thus, the developed tooling is a promising solution for precision machining of heavy and complex parts, combining adaptability, vibration resistance, and high load-bearing capacity.

Keywords: displacements, stresses, safety factor, pins, polymer concrete

Introduction

Modern trends in mechanical engineering, such as product clustering and the transition to small-batch production with a wide range of products, place increased demands on the flexibility of technological processes [1, 2]. A particular challenge is the clamping of complex spatial shapes for machining of body, cast, and thin-walled parts [3]. Housing parts occupy a special place in mechanical engineering, instrument making, and aviation technology, as they are characterized by complex spatial geometry, the presence of thin-walled elements, covers, stiffening ribs, and internal cavities [4, 5].

Their processing is associated with a number of technological problems that require solutions and experimental design proposals. These problems include:

- high flexibility and low rigidity of housing parts, which leads to deflection and vibration during machining. These phenomena reduce dimensional accuracy and surface quality [6, 7];
- the complexity of fixing parts with complex geometry, especially thin-walled elements and covers, where traditional fixtures do not provide reliable fastening without deformation [8, 9];
- the need for individual tooling for each product series, which increases costs and setup time. According to research, the cost of designing and manufacturing fixtures can be up to 10-20% of the total cost of the production system [10, 11];
- the influence of thermal and dynamic loads, since metal bases of fixtures are subject to thermal deformation and do not dampen vibrations well, which reduces process stability [12, 13];
- limited capabilities of existing universal systems, since modular and reconfigurable fixtures often remain highly specialized and do not provide adaptation to complex-shaped body parts [14, 15].

The development of a new tooling design allows for the fastening of products with various geometries, tolerances, and accuracy requirements, which is particularly relevant for machine-building industries with small and medium-scale production [16].

Strength assessment based on the finite element method is an important stage in modern mechanical engineering design [17]. The transition from traditional analytical calculations to digital testing in software packages such as Ansys Discovery allows engineers to study the behavior of complex assemblies in detail long before the first prototype is manufactured. The use of FEM analysis allows the stiffness of the system to be assessed under the influence of high and varied technological loads [18]. The FEM method allows the distribution of internal forces that tend to return the structure to equilibrium to be visualized. Analysis of equivalent stresses according to Mises makes it possible to identify the most loaded elements. The use of modern software packages allows for the effective combination of materials with different physical and mechanical properties [19]. Comparing the physical and mechanical properties of different materials in a single design in a digital environment helps to justify their use. Strength calculations allow the safety margin of the design to be determined. Modeling also helps to construct a graph of the safety factor as a function of the applied force, which allows predicting the maximum capabilities of the equipment: for example, determining the weight of the workpiece at

which the structure will transition from the elastic deformation zone to the critical zone. Strength calculations allow determining the strength margin of the structure. Modeling also helps to determine the dependence of the safety factor on the applied force, which allows predicting the maximum capabilities of the equipment [20].

Thus, strength assessment using the FEM method at the design stage allows:

- eliminating the risk of residual deformations;
- reducing the cost of manufacturing expensive specialized fixtures and visualizing stress concentration points in order to improve the design;
- evaluate the versatility of designs that can automatically adapt to the complex geometry of workpieces.

The purpose of this article is to conduct an FEM analysis to evaluate the strength of an innovative design for technological equipment and determine its load-bearing capacity under the intense loads of modern production.

1. Materials and methods

The adaptive technological equipment under development with a polymer concrete-based pin table (Figure 3) forms a support surface for the specific geometry of the cover, reduces vibration, and ensures versatility when processing body parts.

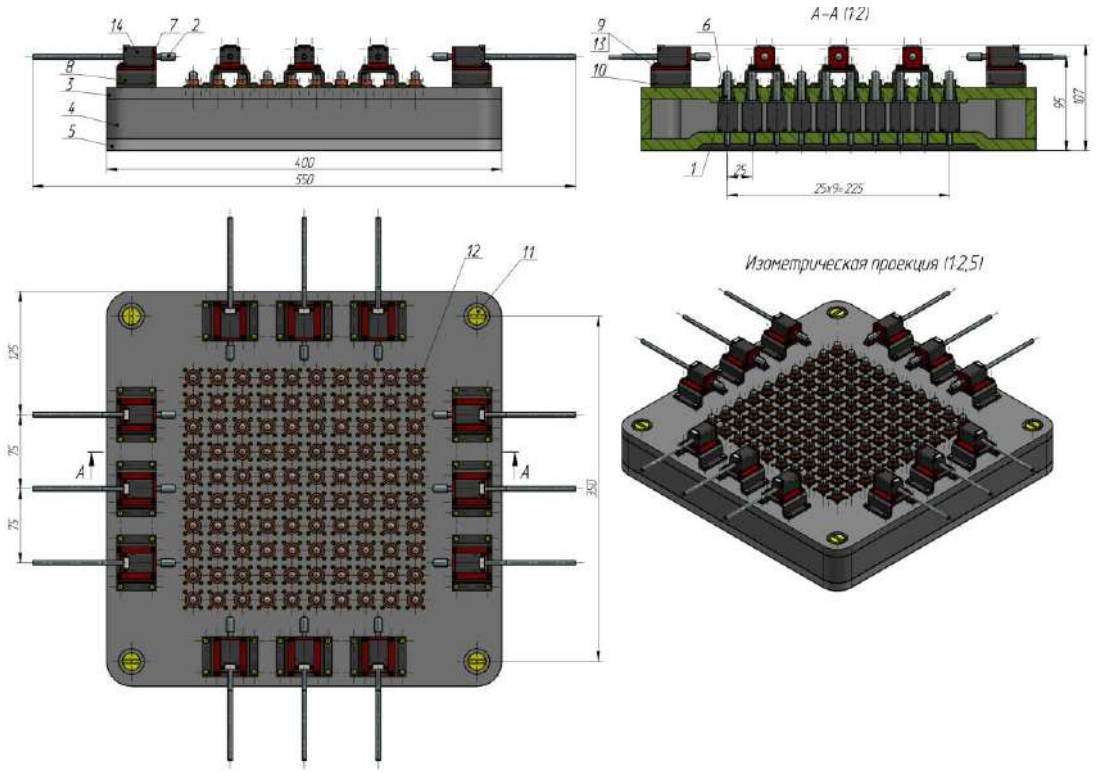

1 – screw assembly; 2 – screw assembly; 3 – top plate; 4 – wall; 5 – bottom plate; 6 – guide; 7 - holder; 8 - stand; 9 – M2 bolt; 10 – M3 bolt; 11 – A.M12 screw; 12 - A.M2 screw; 13 – M2 nut

Fig.3. - Adaptive tooling with a pin table

The design of the adaptive technological equipment includes:

- a polymer concrete base, which provides high vibration resistance and low thermal deformation compared to metal counterparts;
- a matrix of telescopic pins located in the working area of the table (400×550 mm), allowing the formation of a support surface according to the geometry of the part being fixed;
- a drive mechanism that moves the pins with stepper motors and ensures positioning accuracy and the possibility of automatic readjustment.
- a modular assembly that simplifies maintenance and replacement of individual elements.

Adaptive tooling was modeled using Ansys Discovery 2024 R2 software.

Adaptive tooling modeling was performed in several stages:

- creation of a 3D model of adaptive tooling (Figure 4);
- selection of material and specification of physical and mechanical properties for S275N steel pins, as well as upper and lower plates of Polymer concrete (epoxy-based) tooling (Table 1);

- fastening of the equipment with a sliding screw thread (Figure 5);
- applying load across the entire surface of the fixture pins (Table 2, Figure 6);
- creating contact connections - 202 contact pairs.

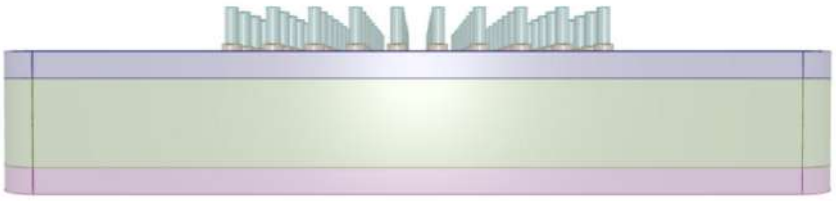

Fig. 4 – 3D model of adaptive process equipment with a pin table

Table 1. Materials Structural steel, S275N

Parametr	Value	Value
Material	Structural steel, S275N	Polymer concrete (epoxy-based)
State	Solid	Solid
Density	7850 kg/m³	2460 kg/m³
Young's modulus	$2{,}1 \cdot 10^{11}$ Pa	$3{,}5 \cdot 10^{10}$ Pa
Poisson's ratio	0,305	0,22
Shear modulus	$8{,}05 \cdot 10^{10}$ Pa	$1{,}43 \cdot 10^{10}$ Pa
Bulk modulus	$1{,}79 \cdot 10^{11}$ Pa	$2{,}08 \cdot 10^{10}$ Pa
Tensile yield strength	$2{,}37 \cdot 10^{8}$ Pa	$2 \cdot 10^{7}$ Pa
Tensile ultimate strength	$4{,}23 \cdot 10^{8}$ Pa	$3 \cdot 10^{7}$ Pa
Thermal expansion coefficient	$1{,}2 \cdot 10^{-5}$ 1/°C	$1{,}4 \cdot 10^{-5}$ 1/°C
Thermal conductivity	50,4 W/m·K	1,2 W/m·K
Specific heat	0,479 kJ/kg.C	0,9 kJ/kg.C
Embodied energy	2,02e7 J/kg	2,8e7 J/kg
CO_2 footprint	2,03 kg/kg	2,5 kg/kg
Potential to recycle	True	False
Description	Structural steel, S275N, normalized Data compiled by Ansys Granta, incorporating various sources including JAHM and MagWeb. ANSYS, Inc. provides no warranty for this data.	Polymer concrete (epoxy-based), mineral aggregate bonded with thermosetting resin. Data compiled from manufacturer datasheets, academic literature, and engineering handbooks. Typical values for structural and machine-base applications. ANSYS, Inc. provides no warranty for this data.
Class	Metals - ferrous	Composites
Subclass	Microalloy and high strength steels	Polymer matrix composites – mineral filled

Table 2. Application of loadings

Name	Total force	Remote
Remote Distributed Force 2	100000 N	0,0375 m

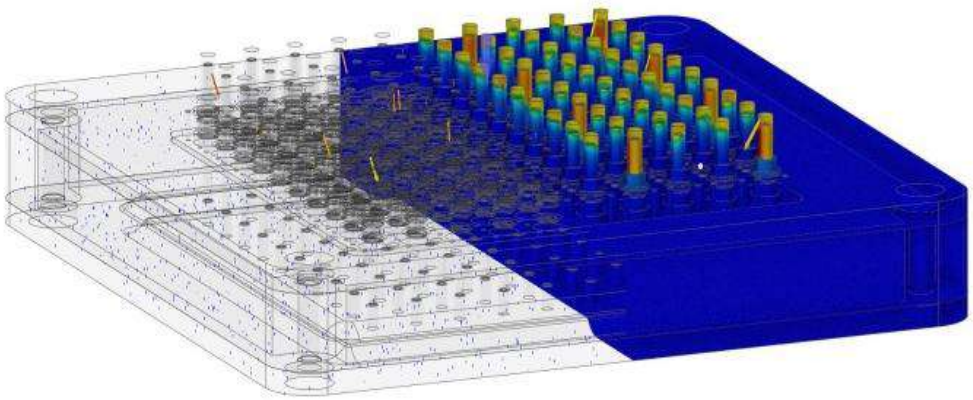

Fig. 5. – Fastening the tooling with the thread of the sliding screw

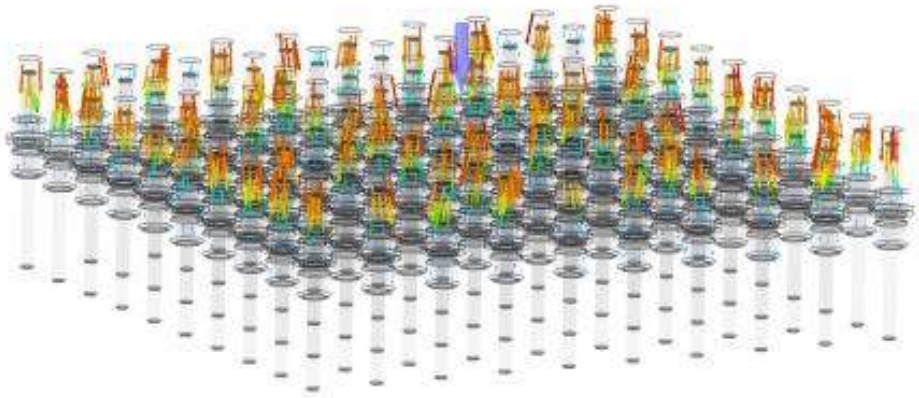

Fig. 6. - Load application across the entire surface of the fixture pins

The load-bearing capacity of the new adaptive tooling design was determined based on the calculation of the safety factor [21]:

$$n = \frac{\sigma_y}{\sigma_{eq}} \quad (1)$$

σ_y – yield strength, MPa;
σ_{eq} – equivalent stresses, MPa.

For objects ensuring load-bearing capacity, the safety factor must be $n \geq 1.5$.

2. Results and discussion

As a result of the adaptive tooling strength simulation, the following parameters were obtained:
- displacements (Figure 7);
- principal stresses (Figure 8);
- equivalent von Mises stresses (Figure 9);
- pin reaction force (Figure 10).

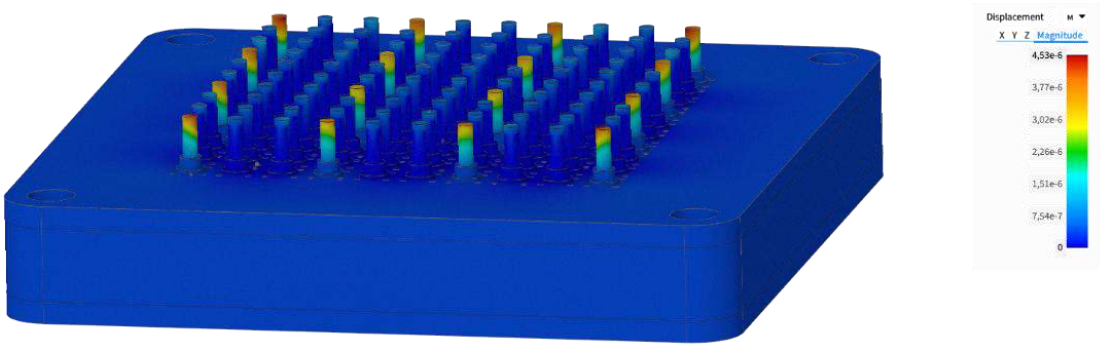

Fig. 7. – Displacements in adaptive technological equipment

According to the visualization of the results in Figure 5, the maximum displacement in the system is approximately 4.53 µm. This value is localized at the top of the telescopic pins, which were directly subjected to a distributed load of 100,000 N. The minimum displacement is 0, corresponding to the areas of rigid fixation of the tool base along the threads of the retractable screws. The maximum displacement of less than 5 µm under a colossal load of 10 tons indicates the extremely high rigidity of the system. Under real metalworking conditions, such deformations have virtually no effect on the dimensional accuracy and surface quality of the part. Displacements of a few microns at the tops of the S275N steel pins indicate elastic deformation of the elements. This confirms that the telescopic mechanism is capable of withstanding technological cutting forces without residual deformation or loss of positioning accuracy. The use of polymer concrete (epoxy-based) instead of traditional metals ensures not only geometric stability but also effective vibration damping. Figure 5 shows that the massive base remains virtually motionless (dark blue), serving as a reliable foundation for the pin matrix.

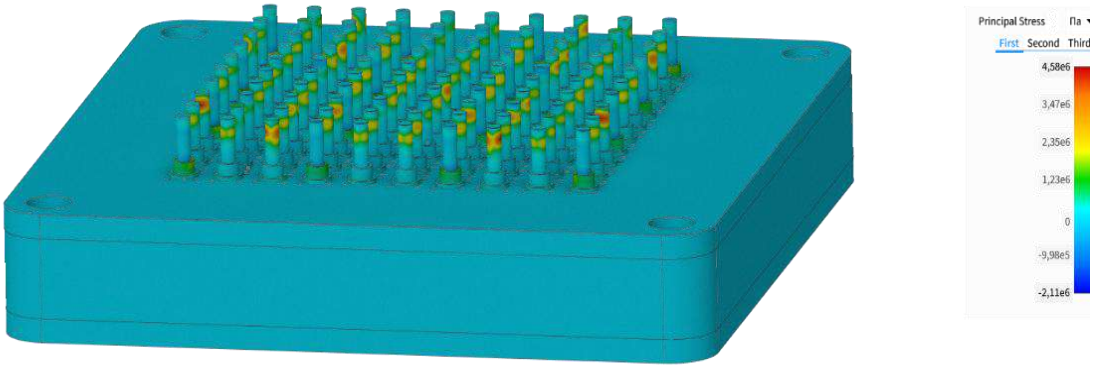

Fig. 8. – Principal stresses in adaptive technological equipment

When a total force of 100,000 N is applied to the pin surface, internal forces are generated in the metal (S275N steel), which tend to return the structure to equilibrium. The pins act as intermediate links, absorbing the pressure from the workpiece and transferring it to the polymer concrete base. Since the Young's modulus of steel (2.1 × 10 Pa) is significantly higher than that of polymer concrete (3.5 × 10 Pa), the steel matrix of the pins bears the primary structural stresses. An analysis of the principal stresses allows us to determine the risk of material failure. The fact that the maximum stress (4.58 MPa) is significantly lower than the yield strength of steel (237 MPa) and the strength of polymer concrete confirms the high safety margin of the structure under the given load. The stress distribution in the polymer concrete base confirms its role as a damper; low stress values with a high base mass contribute to the effective damping of dynamic loads.

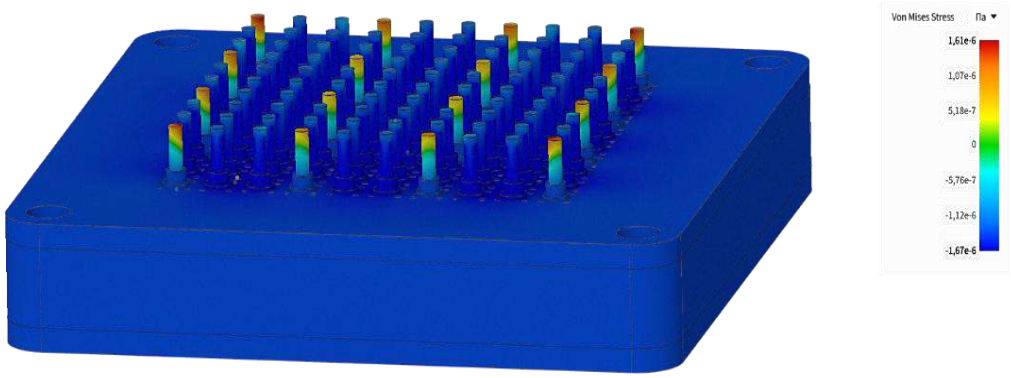

Fig. 9. – Equivalent stresses according to von Mises

An analysis of the von Mises equivalent stresses shows that the telescopic pins are the most heavily loaded elements of the system. The image clearly shows that the maximum stress values are at the top of the pins, which directly contact the workpiece, as well as in the areas where they interface with the upper platen guides. The symmetrical distribution is due to the geometry of the fixture itself-a matrix of pins arranged in a 400 x 550 mm table working area. Since the load is applied to the entire surface of the pins, the stress pattern exhibits a pronounced regularity. The uniformity of the color spectrum on most pins confirms that the adaptive system effectively distributes forces, minimizing the risk of critical stress concentrators at individual points. The polymer concrete base, meanwhile, remains in the zone of minimal stress (≈1.6 Pa), demonstrating its high rigidity and ability to absorb the resulting loads without significant deformation. The use of S275N steel for pins is justified because it withstands specified forces without the risk of plastic deformation, maintaining the positioning accuracy of the part. Uniform von Mises stress distribution ensures that during machining, thin-walled housing parts are not subject to localized overloads that cause deflection or microcracks.

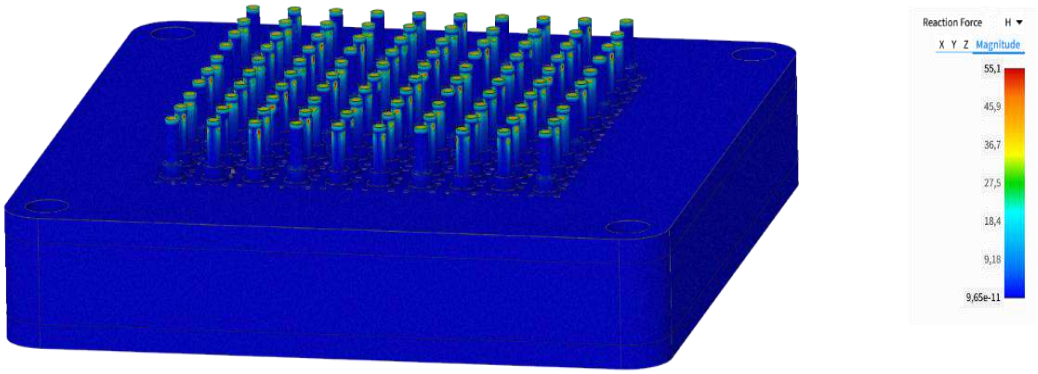

Fig. 10. - Pin reaction force

The reaction force on the pins reaches a maximum value of 55.1 N. Figure 10 shows that the greatest load is concentrated at the upper ends and the mating surfaces of the extended pins, indicated by the red and orange colors on the spectrum. In the areas of the base and elements not in contact, the reaction force approaches zero (approximately 9.65×10^{-11} N), which corresponds to the blue color on the scale.

The pins (the matrix of telescopic pins) form a support surface for the specific geometry of the part. Consequently, reaction forces arise precisely at the points of contact between the fixture and the workpiece in response to an applied external force of 100,000 N. Using the matrix of pins allows the total clamping force to be distributed across multiple support points. The polymer concrete base in which the pin guides are installed has higher internal damping compared to metal. The distribution of reaction forces through a solid polymer concrete slab effectively dampens vibrations arising during machining. The maximum reaction values at the pin ends confirm that the drive mechanism and threaded locking provide the rigid hold necessary to maintain dimensional accuracy.

To determine the maximum workpiece weight that the adaptive tooling can support, simulations of loading with various static loads were conducted, after which a safety factor was determined. The safety factor for various loading forces is shown in Figure 11.

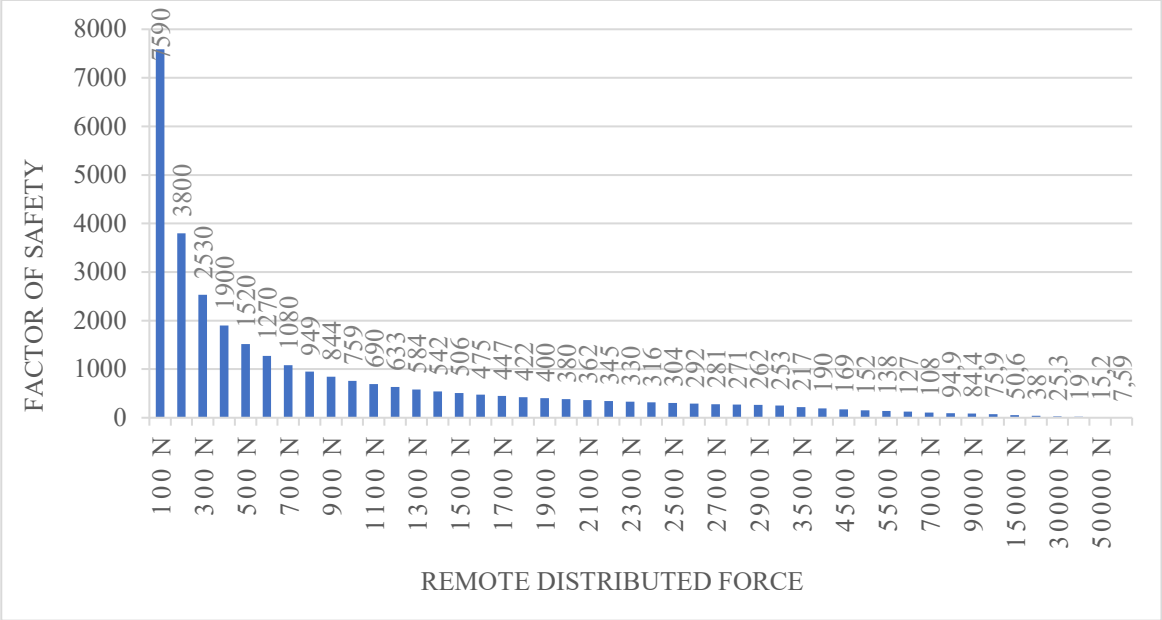

Fig. 11. – Dependence of the safety factor of the equipment on the remote distributed force

The graph in Figure 11 demonstrates an inverse relationship between the magnitude of the applied remote distributed force and the safety factor. As the load on the tool pins increases, the safety factor naturally decreases. According to the graph, this factor corresponds to a load of 100,000 N. This is equivalent to a workpiece weight of approximately 10,197 kg (approximately 10.2 tons). Extrapolating the graph data, one can assume that the safety factor becomes critical (below 1.5) when the load exceeds 550,000–600,000 N. This corresponds to a workpiece weight of over 56–61 tons.

Conclusions

The following results were obtained from the simulation:

1) A finite element analysis (FEM) performed in Ansys Discovery demonstrated the sufficient structural strength of the developed adaptive tooling. When applying a static load of 100,000 N, the maximum displacements in the system were only 4.53 μm. These deformations were localized exclusively at the tips of the steel pins and were elastic in nature. Under real-world production conditions, such microscopic displacements do not affect the dimensional accuracy or surface quality of the machined part, confirming the tooling's suitability for precision machining.

2) The use of polymer concrete (epoxy-based) as the base material proved to be a successful choice. Due to its lower Young's modulus compared to steel, the base acts as an effective damper, absorbing vibrations and dynamic loads. The massive base remains virtually motionless under load, ensuring geometric stability and high vibration resistance, which is critical for reducing tool wear and preventing microcracks in components.

3) The use of a matrix made of S275N steel effectively absorbs process forces. Maximum von Mises equivalent stresses are concentrated in the contact zones of the pins with the workpiece and guides, but their peak value (4.58 MPa) is many times lower than the yield strength of steel (237 MPa). The regular structure of the pin table ensures uniform distribution of forces, eliminating the formation of dangerous stress concentrators, which is especially important when clamping thin-walled and complex body parts prone to deformation.

4) Calculation of the safety factor (n) confirmed the high reliability of the design. Under a standard load of 10 tons, the system maintains a multiple safety factor. Extrapolation of simulation data shows that the critical safety factor ($n > 1.5$) will only be achieved for loads exceeding 550–600 kN (56–61 tons). This allows the tooling to be used for a wide range of heavy components without risk of failure.

5) The proposed adaptive tooling is a promising solution for modern mechanical engineering, combining high load-bearing capacity.

6) Future research will focus on assessing the vibration resistance of the adaptive tooling.

References

[1] Ali S.F. The Future of Mechanical Engineering: Trends and Technologies in Machine and Equipment Development //International Journal of Multiphysics, Volume 18, No. 4, 2024. – P. 313-333
[2] Berg A., Nurzhanova O., Vytautas T., Vitushenko D. Improvement of Base Sets for Complex Configuration Parts when Assessing their Manufacturability within Industry 4.0 //Material and Mechanical Engineering Technology, 2, 2024. - P. 25 - 35 DOI:10.52209/2706-977X_2024_2_25
[3] Hans-Christian Möhring, Dirk Biermann, Friedrich Bleicher, Shreyes Melkote, Gregor Kappmeyer,
Fixtures and workpiece clamping systems in machining //CIRP Annals, Volume 74, Issue 2, 2025. - P. 945-969, https://doi.org/10.1016/j.cirp.2025.04.096.
[4] Castanie B., Azoti W., Crouzeix L., Bello A., Taborda R.P., Mahmood A., Viste A. Review of monolithic composite laminate and stiffened structures in aeronautic applications // Composites Part C: Open Access,Volume 17, 2025, 100585
[5] Krawczuk M., Palacz M. Applications of Finite Element Modeling for Mechanical and Mechatronic Systems // Appl. Sci, 2021, 11, 5170. https://doi.org/ 10.3390/app11115170
[6] Ma S.L., Huang T., Wiercigroch M., Yan Y., Zhang X.M., Ding H. Effect of workpiece vibration on dynamic cutting force in thin-walled plates trimming //CIRP Journal of Manufacturing Science and Technology, Volume 61, 2025. – P. 35-50 https://doi.org/10.1016/j.cirpj.2025.05.013.
[7] Xing Y., Wang S., Xinyong M., Hongqi L., Zhaoshun L., Qiushuang G., Rong Y. Forced vibration mechanism and suppression method for thin-walled workpiece milling //International Journal of Mechanical Sciences, 2022, 230. 107553. 10.1016/j.ijmecsci.2022.107553.
[8] Haibo L., Wang C., Te L., Qile B., Kuo L., Yongqing W. Fixturing technology and system for thin-walled parts machining: a review //Frontiers of Mechanical Engineering, 2023, 17. 10.1007/s11465-022-0711-5.
[9] Anh N.T., Tung T.T. Methodical approach to fixture design in the milling of thin-walled mechanical components //Results in Engineering, Volume 27, 2025,106518, https://doi.org/10.1016/j.rineng.2025.106518.
[10] Kang X., Peng Q. Recent Research on Computer-Aided Fixture Planning //Recent Patents on Mechanical Engineering 2009, 2. - P. 8-18
[11] Siddharth A., Vijay N., Srushti D. Design and Deployment of Fixture on Assembly Line to Improve Productivity //Journal of Physics: Conference Series, 2021, 1803. 012025. 10.1088/1742-6596/1803/1/012025.
[12] Vasić M., Blagojević M., Dizdar S., Tuka S. The Influence of Thermal Stresses on the Load Distribution and Stress–Strain State of Cycloidal Reducers //Appl. Sci., 2025, 15, 9607. https://doi.org/10.3390/app15179607
[13] Ozden M.C., Simsek U., Ozdemir M., Gayir C.E., Sendur P. Innovative Vibration Control of Triply Periodic Minimum Surfaces Lattice Structures: A Hybrid Approach with Constrained Layer Damping Silicone–Viscoelastic Layer Integration //Adv. Eng. Mater. 2024, 26, 2401851 DOI: 10.1002/adem.202401851
[14] Gameros A., Lowth, S., Axinte D., Nagy-Sochacki A., Craig O., Siller H. State-of-the-art in fixture systems for the manufacture and assembly of rigid components: A review //International Journal of Machine Tools and Manufacture, 2017, 123. doi:10.1016/j.ijmachtools.2017.07.004.
[15] Lu S., Ahmad Z., Zoppi M., Ding X., Zlatanov D., Molfino R. Design and Testing of a Highly Reconfigurable Fixture with Lockable Robotic Arms //Journal of Mechanical Design, 2016. doi:10.1115/1.4033037
[16] Zharkevich O., Yurchenko V., Nikonova T., Zharkevich O. The development of the computer-aided design system for production processes of component part maching for single-piece production and repair conditions //Journal of applied engineering science, 2019, 17(4). – P.599-609
[17] Marcinkiewicz J., Spadlo, M., Staszak Ż. Strength analysis by the Finite Element Method (FEM) of a modular line //Material and Mechanical Engineering Technology, 2, 2024 doi:10.52209/2706-977X_2024_2_44.
[18] Fazlar R., Mohammad M. Fundamental of Finite Element Analysis (FEA) and Solving Stiffness Matrix By Newton-Raphson Method //Material and Mechanical Engineering Technology, 2023, 2 51, 10-14. DOI: 10.52209/2706-977X_
[19] Zharkevich O., Nikonova T., Gierz Ł., Reshetnikova O., Berg A., Warguła Ł., Berg A., Wieczorek B., Łykowski W., Nurzhanova O. Improving the Design of a Multi-Gear Pump Switchgear Using CFD Analysis // Applied Sciences (Switzerland), 2024, 14(13), 5394
[20] Vasendina E., Plotnikova I., Levitskaya A., Kvesko S. Detection and defect correction of operating process // IOP Conference Series: Materials Science and Engineering, 2016, Vol. 110 doi.org/10.1088/1757-899X/110/1/012070
[21] Nurzhanova O., Zharkevich O., Berg A., Zhukova A., Mussayev M, Buzauova T., Abdugaliyeva G., Shakhatova A Evaluation of the Structural Strength of a Prefabricated Milling Cutter with Replaceable inserts During Machining //Material and Mechanical Engineering Technology, No. 4, 2023. – P.10-17

Information of authors

Nurzhanova Oxana Amangeldyevna, PhD, acting associate professor, Abylkas Saginov Karaganda Technical University
e-mail: nurzhanova_o@mail.ru

Zharkevich Olga Mikhailovna, c.t.s., professor, Abylkas Saginov Karaganda Technical University
e-mail: zharkevich82@mail.ru

Bakenov Adilkhan Amangeldievich, m.t.s., design engineer, "Maker" LLP, Abylkas Saginov Karaganda Technical University
e-mail: bakenov.work@yandex.kz

Berg Alexandra Sergeevna, PhD, Abylkas Saginov Karaganda Technical University
e-mail: kibeko_1995@mail.ru

Zakirov Karshiga, m.t.s., KazTechInstrument LLP doctoral student, Abylkas Saginov Karaganda Technical University
e-mail: kzakirov@kazti.kz

DOI 10.52209/2706-977X_2026_1_31 **IRSTI 55.03.33** **UDC 621.822.2**

Modeling and Analysis of Interactions in the Rotor–Bearing–Housing System under Variable Loads

Makhmudova Sh.*
Tashkent State Transport University, Tashkent, Uzbekistan
*corresponding author

Abstract. Vibration arising in industrial settings significantly influences the durability and functionality of machinery, particularly those operating under high speeds and heavy loads. Despite ongoing technological improvements, sectors such as textiles continue to experience intensified vibration, impulsive noise, and broadened frequency emissions due to the integration of more potent machinery. Devices like shuttle looms and cotton-processing equipment exemplify systems that contribute to vibrational challenges. This research explores the dynamics of the "rotor–bearing–housing" assembly as a key factor in mitigating such issues. Given that rolling bearings frequently develop defects that compromise mechanical performance, the study introduces an advanced dynamic model considering deformation, misalignment, and fluctuating contact stresses under vibration. Emphasis is placed on the influence of bearing design, stiffness, and applied loads on overall system stability. The paper also reviews modern vibroacoustic diagnostic techniques for early failure detection and service life forecasting, promoting more efficient and resilient vibration control solutions in industrial environments.

Keywords. Shaft bending, saw cylinder, seed roller, shaft deformation, linter machine, transverse force, bending moment, equations of equilibrium, support reaction.

Introduction

In real industrial practice, vibration is one of the main factors that quietly but steadily reduces the reliability and service life of equipment. Even with the adoption of modern, high-speed and energy-efficient machines, the problem has not disappeared. On the contrary, more powerful drives and higher speeds often create stronger oscillations, wider frequency bands, and additional impulsive noise. These effects are especially noticeable in textile production, where machines such as looms, combing systems, and cotton-gin units operate almost continuously under heavy and variable loads.

Such conditions make it clear that conventional design measures are no longer sufficient. What is needed are advanced diagnostic tools and vibration-control strategies that are both technically sound and practical for industry. Among the most sensitive components are rolling bearings, which serve as critical supports for rotating shafts. Even small surface defects or misalignments can increase vibration levels dramatically, leading to accelerated wear and reduced safety. For this reason, the development of refined dynamic models of the rotor-bearing-housing system has become an important research direction. These models not only support more accurate detection of faults but also provide guidance for designing vibration-resistant structures.

The purpose of this study is to develop and numerically investigate a dynamic model of a rotor-bearing-housing system with elastic-damping (polyurethane) inserts, in order to evaluate their influence under variable loading conditions and to provide engineering recommendations for vibration reduction in textile machinery.

Researchers over several decades have shown that the behavior of bearing assemblies is strongly shaped by imperfections in their geometry and the development of faults. One of the most common ways to study these effects is through analysis of vibration and acoustic signals collected during machine operation. Methods such as Fourier transforms, wavelet analysis, and statistical techniques are widely applied [1-5]. They are useful for identifying early stages of damage, yet in practice their accuracy is limited by strong background noise and the complex, non-stationary form of real signals. Thus, while these tools are valuable, they often fail to give clear information about the actual magnitude and distribution of contact forces in bearings.

To go beyond signal analysis, many researchers have turned to analytical and numerical modeling [6-8]. These works have advanced our understanding of stresses and deformations in bearing elements, but most of them simplify reality by assuming rigid components or static conditions. Such simplifications leave open questions about the true influence of structural flexibility and load variation. Experimental studies on sliding effects in rolling elements are also rare, which means an important part of bearing behavior under real conditions is still not well understood.

In engineering practice, bearing defects are usually grouped into two broad categories: distributed (waviness, misalignment, dimensional deviations) and localized (cracks, spalls, pits) [10-12]. This classification is convenient, but in reality the vibration signatures of different faults can overlap, making diagnostics more difficult. Distributed defects are often the result of manufacturing tolerances or gradual wear, whereas localized damage is mainly caused by fatigue crack initiation and propagation. Localized faults are the most dangerous, because they lead to sudden changes in stress

distribution and generate short high-energy impulses. At the same time, many studies do not consider how these fault mechanisms can interact.

More recent investigations have used finite element analysis and advanced simulations to study shaft deflection, contact stresses, and dynamic response under realistic loads [13-16]. Results from these works show that design improvements - such as adding elastomeric inserts or hybrid support structures - can reduce shaft bending, suppress critical vibrations, and extend machine life. However, the benefits strongly depend on the type of machine and its working conditions. In textile equipment, for instance, shafts are slender and heavily loaded, making damping inserts a promising but not yet fully explored solution.

Comprehensive reviews, such as those by McFadden and colleagues [17-18], confirm the importance of vibration-based monitoring for bearing diagnostics. At the same time, they reveal a clear imbalance: most existing models focus on distributed defects, like raceway waviness, while only a few provide detailed simulations of localized faults. This gap shows the need for integrated approaches that combine advanced signal-processing methods with dynamic modeling. Only such combined methods can provide both qualitative and quantitative evaluation of bearing health.

Recent studies emphasize the importance of accurate numerical modeling for predicting stress–strain behavior and structural response under operational loads [7, 19]. In rotor dynamics, the introduction of elastic support layers has been shown to significantly reduce vibration levels and improve system stability [20], highlighting the role of structural modifications in enhancing mechanical reliability [21-22].

Based on these observations, the present study focuses on the influence of elastic-damping inserts in rotor-bearing-housing systems. Unlike many earlier models that assume rigid supports, this work explicitly incorporates polyurethane layers as damping elements and evaluates their role in vibration reduction. This approach not only develops theoretical understanding but also offers practical recommendations for improving the reliability of rotating machinery.

Thus, adequate analysis of the condition of rotor systems with bearings requires comprehensive modeling that takes into account interactions and possible defects, making dynamic models a key tool in the study and prediction of the technical condition of such assemblies.

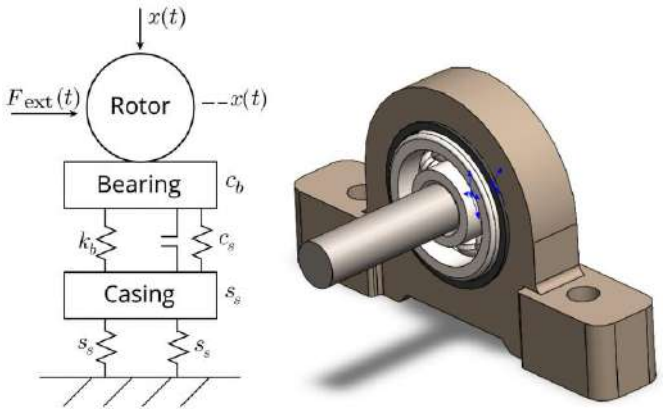

Fig.1. - The system consists of two bodies: the rotor and the housing, connected by elastic-damping elements (spring and damper). Rotor displacement is denoted by x(t); Housing displacement is denoted by $x_s(t)$; An external harmonic force F(t) acts on the rotor, simulating a disturbance

1. Research methodology

To analyze the dynamic response of the system shown in Figure 1, a mathematical model was developed that describes the interaction of components through a system of second-order ordinary differential equations. The model includes the mass of the rotating shaft and the housing, as well as the elastic and damping connections between them and the base. As a result, the system takes the following form:

$$\begin{aligned} m_1\ddot{x}+c_b(\dot{x}-\dot{x}_s)+k_b(x-x_s)&=F(t)\\ m_2\ddot{x}_s-c_b(\dot{x}-\dot{x}_s)-k_b(x-x_s)+c_s\dot{x}_s+s_sx_s&=0 \end{aligned} \quad (1)$$

where x(t) - rotor displacement;

$x_s(t)$- displacement of the housing;

$\dot{x}$-velocity (first derivative of displacement with respect to time);

$\ddot{x}$- acceleration (second derivative of displacement with respect to time);

m_1, m_2 -the masses of the rotor and the housing.

The physical and mechanical parameters used in the numerical simulation are summarized in Table 1. These values were selected to represent typical operating conditions of medium-scale textile rotor systems and ensure reproducibility of the computational results.

Table 1. Parameters used in numerical simulation

№	Parameter	Description	Value	Unit	№	Parameter	Description	Value
1	m_1	Rotor mass	25	kg	5	ks	Support stiffness	1.5×10^5
2	m_2	Housing mass	40	kg	6	cb	Bearing damping	850
3	h	Polyurethane thickness	4	mm	7	cs	Support damping	1200
4	kb	Bearing stiffness	10^5	N/m				

For numerical analysis, the given model was transformed into a vector-matrix form:

$$x(t) = \begin{bmatrix} x(t) \\ x_s(t) \end{bmatrix}, \dot{x}(t) = \begin{bmatrix} \dot{x}(t) \\ \dot{x}_s(t) \end{bmatrix}, \ddot{x}(t) = \begin{bmatrix} \ddot{x}(t) \\ \ddot{x}_s(t) \end{bmatrix} \quad (2)$$

$$M\ddot{x}+C\dot{x}+Kx=F(t) \quad (3)$$

mass matrix:

$$M = \begin{bmatrix} m_1 & o \\ 0 & m_2 \end{bmatrix} \quad (4)$$

damping matrix:

$$C = \begin{bmatrix} c_b & -c_b \\ c_b & c_b + c_s \end{bmatrix} \quad (5)$$

stiffness matrix:

$$K = \begin{bmatrix} k_b & -k_b \\ -k_b & k_b + s_s \end{bmatrix} \quad (6)$$

vector of external forces:

$$F(t) = \begin{bmatrix} F(t) \\ 0 \end{bmatrix} \quad (7)$$

By substituting expressions (1), (3), (4), (5), (6), and (7) into equation (2), the final matrix equation of motion is obtained:

$$\begin{bmatrix} m_1 & o \\ 0 & m_2 \end{bmatrix} \begin{bmatrix} \ddot{x}(t) \\ \ddot{x}_s(t) \end{bmatrix} + \begin{bmatrix} c_b & -c_b \\ c_b & c_b + c_s \end{bmatrix} \begin{bmatrix} \dot{x}(t) \\ \dot{x}_s(t) \end{bmatrix} + \begin{bmatrix} k_b & -k_b \\ -k_b & k_b + s_s \end{bmatrix} \begin{bmatrix} x(t) \\ x_s(t) \end{bmatrix} = \begin{bmatrix} F(t) \\ 0 \end{bmatrix} \quad (8)$$

The equations (8) were solved numerically using time discretization. The equations were solved using time discretization and the explicit Euler method. In addition to the harmonic excitation $F(t) = F_0 \sin(\omega t)$, an impulsive load case was also considered in the form of a short-duration force pulse to simulate sudden load variation typical for textile machinery start-up or material impact. The comparison showed that damping inserts significantly reduced peak acceleration under impulsive excitation (by approximately 30%), confirming their effectiveness under variable loading conditions.

The resulting graphs clearly demonstrate the interrelation between structural elements and allow for the identification of vibration characteristics, amplitude response, phase lag, and the level of damping in the system. Such visualization is essential for engineering assessment of the stability, reliability, and vibration activity of the structure.

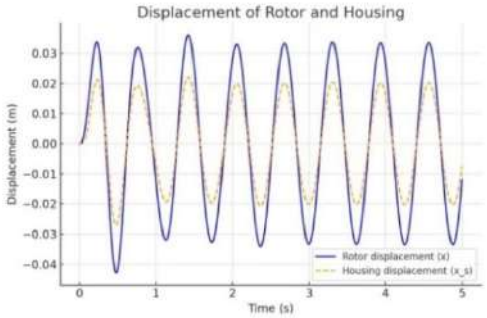

The displacement plot illustrates the relative motion of the rotor and the housing over time under the influence of a harmonic excitation force. The blue curve represents the rotor's response, while the orange dashed line corresponds to the housing. The difference in amplitude and phase between the two elements indicates the elastic interaction and the dynamic decoupling due to the bearing and foundation compliance.

Fig. 2. - Time-dependent displacement of the rotor and the housing

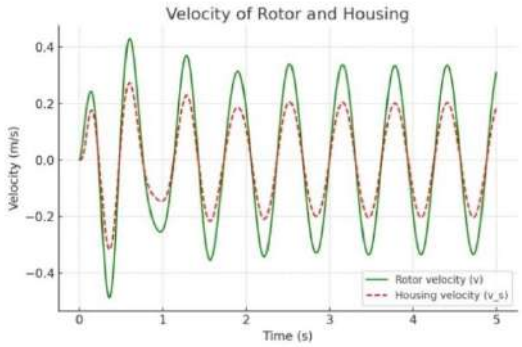

The velocity response of both components is shown in the second graph. As expected, the velocity of the housing is smoother due to the higher mass and damping, while the rotor exhibits more rapid fluctuations. This provides insight into the energy transfer between the rotating shaft and the support structure.

Fig. 3. - Time history of rotor and housing velocity

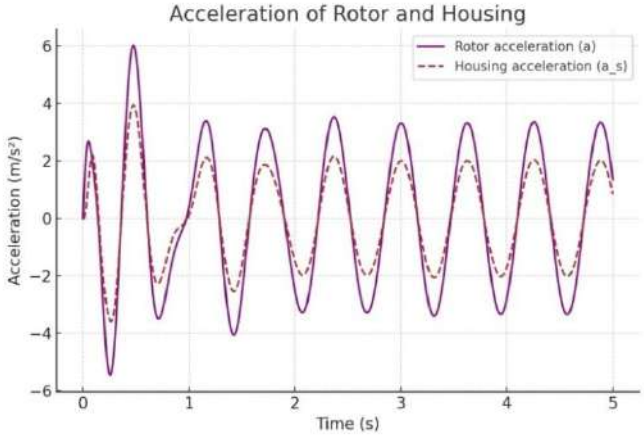

The graph shows the acceleration time of the rotor and housing in detail. These high-frequency oscillations are especially important when assessing fatigue, impact loads or when designing shock-absorbing systems. The distinct acceleration peaks reflect the smallest moments of force transmission through the flexible elements (polyurethane).

Fig. 4. - Time history of rotor and housing acceleration

2. Results and discussion

To assess the dynamic characteristics of the system, a mathematical representation was constructed considering the elastic links between the bearings and housing. The model, based on Lagrange's equations of the second kind, accounted for internal damping and stiffness forces, along with external influences such as gravity and torque. Polyurethane elements, with a stiffness k_{pu} =10^5 N/m and a thickness of 4 mm, were employed as damping components.

Simulations were executed using Mathcad, and outcomes revealed that incorporating these damping layers reduced the rotor's vibration amplitude by 35-50% on average. The time-domain responses (as seen in Figure 2) demonstrate a notable attenuation of oscillations in the damped configuration. Frequency domain analysis also confirmed diminished amplitude peaks at resonance. In Figure 5, the Y-axis labeled "Amplitude" represents displacement amplitude in meters (m), obtained from Fourier transformation of the steady-state response. Consequently, utilizing polyurethane inserts at the bearing supports effectively minimizes vibrational stresses, enhancing the durability and operational reliability of the entire rotor system.

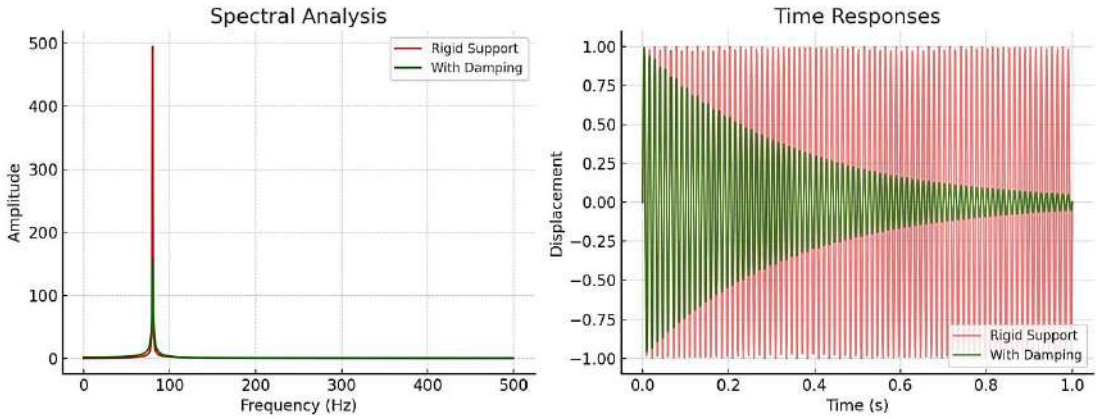

Fig. 5. - Comparison of two Support variants based on modeling results

The left-hand plot presents the results of spectral analysis comparing two configurations of the bearing support system: a rigid mounting and a damping-enhanced support. The spectrum for the rigid support (red) shows a dominant resonance peak at a specific natural frequency, indicating a pronounced response to harmonic excitation. In contrast, the configuration with damping (green) significantly suppresses the amplitude of the resonant peak, effectively broadening the response spectrum and reducing vibrational energy concentration at the critical frequency. This demonstrates the damping system's effectiveness in mitigating resonance phenomena and improving the dynamic stability of the structure. The right-hand diagram displays the time-dependent displacement response for both support configurations under identical excitation. The red curve corresponds to the rigid support, while the green curve represents the system with added damping. As seen in the plot, the rigidly mounted system maintains high-amplitude oscillations with persistent undamped behavior. In contrast, the damped system exhibits reduced amplitude and visible energy dissipation over time. This time-domain analysis confirms that damping not only lowers the peak response but also facilitates quicker stabilization, making it more favorable for applications requiring vibrational control.

Conclusion

The computational modeling provided insights into how the rotor and housing interact when bearings are supported with elastic elements. It was observed that both masses oscillated in synchrony, indicating a significant dynamic connection. Nevertheless, the housing exhibited lower vibration amplitudes, highlighting its role in absorbing excess energy.

The inclusion of polyurethane damping layers not only reduced steady-state vibration amplitude by 35-50%, but also decreased resonance peaks in the frequency spectrum and improved transient stability under impulsive loads. This confirms that elastic-damping supports effectively redistribute dynamic stresses and prevent excessive energy concentration at critical frequencies.

From a diagnostic perspective, the developed dynamic model can serve as a reference (baseline) model for filtering background noise in vibration monitoring systems. By comparing measured signals with simulated dynamic responses, it becomes possible to distinguish structural vibration components from external acoustic interference, thereby improving fault detection reliability.

Therefore, the proposed approach contributes both to theoretical modeling of rotor-bearing systems and to practical vibration-control strategies in textile machinery and other high-speed rotating equipment. Future work should include experimental validation and extension to nonlinear contact models.

References

[1] Zhang Y., Li H. Dynamic modeling and vibration response analysis of rotor-bearing systems with flexible supports //Journal of Sound and Vibration, 2020, Volume 486, Article 115563.

[2] Liu, C., Zhao M., Lin J. Rolling bearing fault diagnosis under variable speed conditions using adaptive time–frequency analysis //Mechanical Systems and Signal Processing,2021, Volume 148

[3] Rubini R. et al. Application of the Envelope and Wavelet Transform Analyses for the Diagnosis of Incipient Faults in Ball Bearings //Mechanical Systems and Signal Processing, 2001, Volume 15, Issue 2. - P. 287-302.

[4] Harsha S. Nonlinear dynamic analysis of an unbalanced rotor supported by roller bearing //Chaos, Solitons and Fractal, 2005, Volume 26, Issue 1. - P. 47-66.

[5] Kumar, P., Singh, A., & Verma, N. Influence of damping materials on resonance suppression in rotating machinery //Journal of Mechanical Engineering Science, 2023,Volume 237(8). - P. 3625-3641.

[6] Kang Y. et al. «A modification of the Jones-Harris method for deep-groove ball bearings». Tribology International. November 2006, Volume 39, Issue 11, Pages 1413-1420.

[7] Adilov F., Makhmudova S. Boundary element method for numerical solution to two-dimensional problems of fracture mechanic // AIP Conference Proceedings. 2024, Volume 3119, 040001.

[8] Kumar J P., Singh A., Verma N. Influence of damping materials on resonance suppression in rotating machinery». Proceedings of the Institution of Mechanical Engineers, Part C: Journal of Mechanical Engineering Science, 2023, Volume 237, Issue 8.- P. 3625-3641.

[9] Li T., Zhou D., Gao R. Integrated dynamic modeling and vibration-based health assessment of flexible rotor systems //Journal of Sound and Vibration, 2025, Volume 565, Article 117895.

[10] Hassan M., Abdelrahman A. Hybrid analytical-numerical modeling of rotor-bearing systems under impulsive loads // Mechanical Systems and Signal Processing, 2024, Volume 203, Article 110812.

[11] Tandon N. et al. A review of vibration and acoustic measurement methods for the detection of defects in rolling element bearings //Tribology International, 1999, Volume 32, Issue 8. - P. 469-480.

[12] Ocak H. et al. Estimation of the running speed and bearing defect frequencies of an induction motor from vibration data //Mechanical Systems and Signal Processing, 2004, Volume 18, Issue 3. - P.515-533.

[13] Khamzaev I., Umarov E., Khaydarova O., Muminov J., Ortiqaliyev B. Consideration of shear deformation in the calculation of bent structural elements //EPJ Web of Conferences, 318, 04011, 2025, P. 34 - 42

[14] Avdeeva A., Mamaev Sh., Bakyt G. Determination of the resource of wheel pairs of locomotives during operation on the railways of Uzbekistan //Vibroengineering Procedia Conference Paper, 2025. - P.347 -353.

[15] Yunusov S., Maxmudova Sh., Kasimova D., Agzamov M. The Influence of Changes in Technological Loads on the Deflection of the Saw Cylinder Shaft of a Linting Machine //Material and Mechanical Engineering Technology, 2025. – P. 2-13.

[16] Adilov F., Makhmudova S., Abirov R., Toshmatov E., Maxmudova I. To assessment of stress-strain state in rock continua // IOP Conference Series: Materials Science and Engineering, 2020, Volume 869, No. 7, 072019.
[17] McFadden P.D. et al. The vibration produced by multiple point defect in a rolling element bearing //Journal of Sound and Vibration, 1985, Volume 98, Issue 2. - P. 263-273.
[18] N. Tandon et al. «An analytical model for the prediction of the vibration response of rolling element bearings due to a localized defect», Journal of Sound and Vibration. August 1997, Volume 205, Issue 3, Pages 275-292.
[19] Adilov F., Turdibekov J., Makhmudova S., Abirov R. On Reliable Solution of Plasticity Problems // AIP Conference Proceedings,. 2022, Volume 2637, 030010.
[20] Makhmudova S., Tursunov N., Avazova G. Planar dynamic modeling of a rotor-bearing-housing system with polyurethane support layer // Vibroengineering Procedia, 2025, Volume 60. - P. 1-7
[21] Azimov S., Toirov O., Xalmurzayev B., Tursunov S., Khujakhmedova K. Using a cooling hole to improve the performance of transport brakes // Problems in the Textile and Light Industry in the Context of Integration of Science and Industry and Ways to Solve Them (PTLICISIWS-2) //AIP Conference Proceedings, 2024, Volume 3045, 060016.
[22] Bekmurzaev N., Nurmetov K., Alimukhamedov S. Creation of a wear-resistant bimetallic coating for the track treadmill of a crawler // Vibroengineering Procedia, 2025, Volume 60. - P. 370-377.

Information of the author

Makhmudova Shakhnosa Abduvaliyevna, PhD, associate professor, Tashkent State Transport University
e-mail: maxmudovash88@mail.ru

DOI 10.52209/2706-977X_2026_1_37 **IRSTI 81.09.07** **UDC 504.65**

Studying Radiation-Radon Safety of Building Materials and Residential Buildings of the Karaganda Region

Pak D. [1], Pak Yu.[1], Ibragimova D.[1], Matonin V.[2], Tebayeva A.[1]
[1]Abylkas Saginov Karaganda Technical University, Karaganda, Kazakhstan
[2] Ecoexpert LLP, Karaganda, Republic of Kazakhstan

Abstract. The objective of the study is to assess the radiation and radon safety of building materials and structures and to develop material science recommendations to reduce radon hazard. The study included 78 residential buildings in the Akchatau settlement of the Karaganda region that were built in different periods and using various materials: brick, natural stone, cinder blocks, foam blocks and concrete. The methodology included determining specific activity of natural radionuclides (Ra-226, Th-232, K-40) by gamma spectrometry using a high-resolution detector, as well as measuring radon emanation with Alfarad Plus and Ramon-Radon devices. The mineral composition of materials and their porosity that affect radon permeability were analyzed. The results showed that in a number of houses, the equivalent equilibrium concentration of radon in the premises exceeded sanitary and hygienic standards by tens of times, while the maximum values were recorded in buildings made of brick and stone quarried in areas of granite massifs. It was found that increased porosity and cracking of materials, as well as the presence of uranium-containing minerals, significantly increase radon emission. Based on the analysis, measures to reduce radon hazard were proposed: the use of concrete mixtures with low radioactivity, barrier membranes, sealing coatings and effective ventilation.

Keywords: radon, building materials, specific activity, Ra-226, radiation safety, porosity.

Introduction

Radon (222Rn) is a radioactive noble gas formed as a result of the decay of radium-226 in the uranium-238 chain. Radon (Rn222 and Rn220) and their daughter products (isotopes Po, Pb, Bi) make the main contribution to the radionuclide background of residential and industrial premises [1-3]. It is the second leading cause of lung cancer after smoking, according to the World Health Organization (WHO). Radon and its daughter products emit alpha radiation, which, when inhaled, can cause damage to respiratory cells [4, 5]. The main characteristics of radon and its daughter products are shown in Figure 1.

In a number of regions of Kazakhstan, including the Karaganda region, geological conditions contribute to increased radon emissions from soil and building materials. Particular danger are materials made of rocks with high uranium and thorium content, as well as materials with a developed pore structure that promotes gas migration into the premises.

The negative impact of radon on human health has led to the introduction of permissible radon levels in such countries as the United States (148 Bq/m^3), Canada, Norway (100 Bq/m^3), and the EU countries (300 Bq/m^3). In Kazakhstan, the permissible level is 200 Bq/m^3. In addition to the level of radon exposure, countries need to identify areas that are most susceptible to radon, to identify those areas where the predicted radon concentration in most buildings will exceed the permissible level.

Radon is recognized by the World Health Organization and the International Agency for Research on Cancer (IARC) as a class I carcinogen. Experience in foreign countries shows that radon is one of the key threats to radiation safety in residential premises. Many countries have implemented strict building codes (Finland, Czech Republic, Germany), large-scale housing stock inspection programs (USA, UK), engineering protection technologies (under-foundation ventilation systems, sealing) [5, 18, 19]. Differences in radon hazard in some countries are presented in Table 1 [18, 20, 21].

There are a significant number of studies in the world practice that deal with the impact of building materials on the radon level in rooms [7-9]. Work [6] presents a collection of data on radon emanation and exhalation rate of about 2000 samples of building materials used in Europe. Concrete is the most consumed material in the world after water. The authors of [7] measured radon gas in concrete, the concentration of which varied in the range of 100–400 Bqm^{-3} in houses and 100–3700 Bqm^{-3} in workplaces. System analysis of models for describing radon transport inside porous materials and its release from structures showed the importance of taking them into account when transferring and generating radon in building materials [8]. Cement-based materials made of rocks and soils emit radon that is a carcinogen and affects indoor air quality. Alkaline cement-based materials neutralize carbon dioxide in the air with acid gas, reducing its pH value [9]. Being an inert gas, radon can easily penetrate highly porous materials, such as building materials, due to their characteristic microstructure. Table 2 provides a comparative analysis of building materials by radon emanation [10].

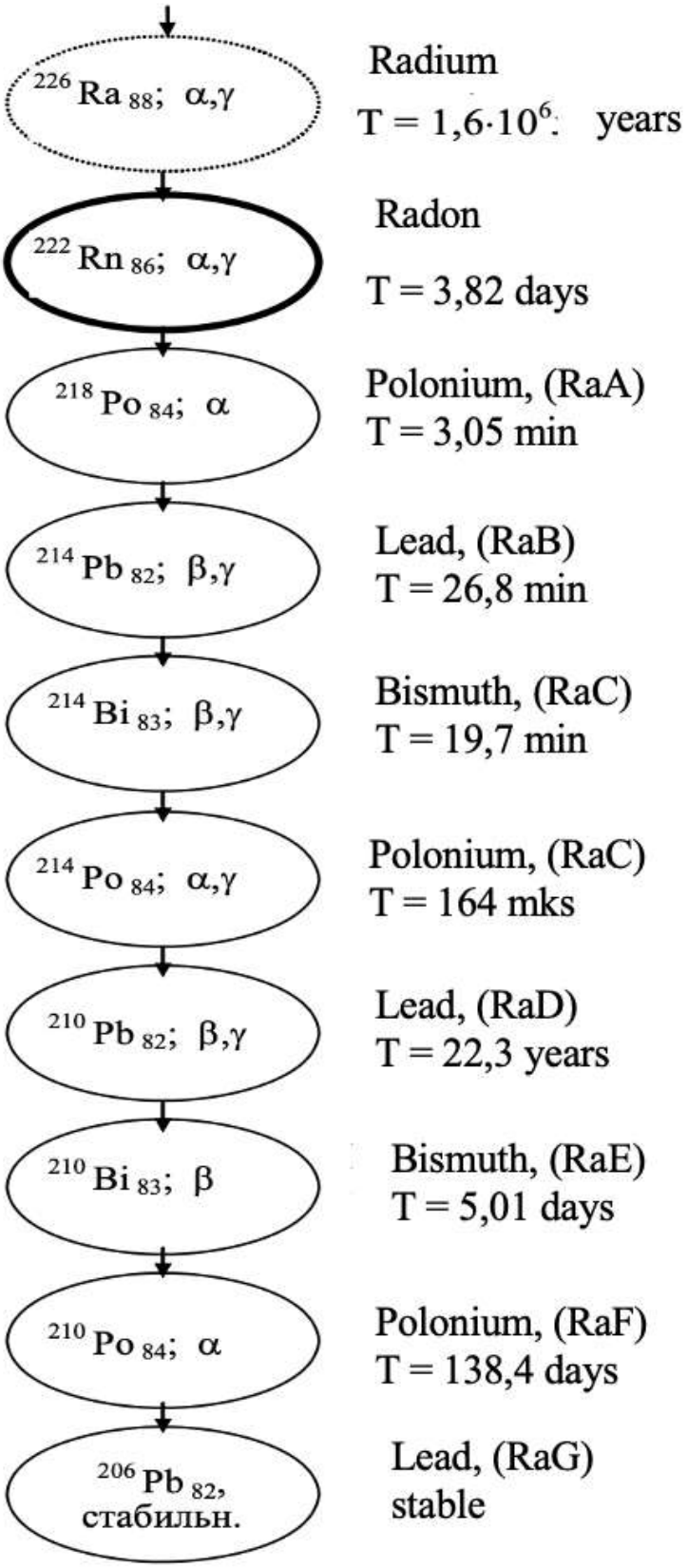

Fig. 1. - Radon isotopes and their daughter products in decay chains (symbol, decay path (α-, β, γ-radiation), name, half-life T) [20]

Table 1. Comparative data on radon in residential buildings in different countries

Country	Average values, Bq/m ³	Maximum values, Bq/m³	Measures taken
Finland	100–150	to 10 000	Standard ≤200 Bq/m³ for new buildings; ≤800 Bq/m³ for old buildings
Sweden	~100	to 10 000	In 10% of houses >100 Bq/m³, in 1% >400 Bq/m³; strict control during construction
Great Britain	40–60	to 2000+	Identified >20 thousand houses with high radon; rehabilitation programs
Germany	40	to 600	Federal law StrlSchG (2018), reference level 300 Bq/m³
USA	55	до 800	Indoor Radon Abatement Act (1988), EPA limit of 150 Bq/m³
Ukraine	150–250	>1000	High levels in crystalline massif areas; average annual dose of 4.2 mSv
Russia	30–100	to 2500	Standard ≤200 Bq/m³, radon maps and building material controls

Table 2. Comparative analysis of building materials by radon emanation

Material	Emanation coefficient (%)	Activity Ra-226 (Bq/kg)	Structural features	Source of data
Concrete	10–25	20–50	Low porosity, cement stone, fly ash	Kovler, 2005; Wu et al., 2019
Granite	15–40	80–200	Crystalline structure, quartz, feldspar, biotite	Pillai et al., 2014; Shabek et al., 2024
Brick (ceramic)	5–15	15–40	Porous baked clay, possible feldspar impurities	Chao, 1999; Sabbarese et al., 2022

Continuation of the Table 2

Material	Emanation coefficient (%)	Activity Ra-226 (Bq/kg)	Structural features	Source of data
Marble	1–5	5–20	Dense calcite structure, low porosity	Kuzmanović et al., 2022
Phosphogypsum	20–50	200–800	Fine-grained structure, residual phosphate minerals	Campos et al., 2017; Ferranti et al., 2013
Gas concrete (AAC)	25–60	30–60	High open porosity, autoclaved	Wu et al., 2019

The highest emanation coefficients are characteristic of materials with high open porosity and significant radionuclide content, such as phosphogypsum and aerated concrete. Granite demonstrates moderate emanation but has high Ra-226 activity, which makes it a significant source of radon in rooms. Concrete and ceramic brick have moderate indicators, while marble is characterized by minimal emanation due to its dense structure.

In Serbia, studies have shown that aerated concrete with high porosity requires mandatory sealing before use [11]. In Iran, it has been found that covering walls with travertine significantly reduces radon levels in hospital rooms [12]. In Peru, it has been found that cement with uranium-containing additives can significantly increase radon emanation, which requires the introduction of standards for the content of Ra-226 in cement [13].

In Kazakhstan, the problem of radon hazard remains poorly understood. Despite the presence of geological and material science prerequisites (granitoid massifs, brick housing construction, groundwater), there are no systematic studies and a national program for radon regulation yet. This study is aimed at filling this gap and developing recommendations for reducing the radon load on the population. Studying radon hazard has been conducted, where the main factors causing high radon concentrations in the houses of the village are: high exhalation from the soil surface; radioactivity of building materials; low air exchange in the premises [14].

1. Materials and methods

In 2023–2024, the studies were conducted in different seasons (winter, spring, summer) in residential buildings and educational premises of the Akchatau settlement. The increased concentration of radon in a number of areas is associated with the Akchatau tungsten-molybdenum mine. The geological source of radon is acidic leucocratic granites in the northwestern and southeastern parts of the studied area. All the measurements were carried out in heated rooms at the temperature of 18–25 °C. Both active and passive methods were used to record the volumetric activity (VA) and equivalent equilibrium concentration (EEC) of radon. Active measurements were carried out using the Alfarad-Plus complex (Russia) and the Ramon-Radon radiometer (Kazakhstan) (Figures 2 and 3). The devices are equipped with an electrostatic chamber, a built-in microprocessor and the ALFA AR software, which provides automatic recording, processing and storage of data. Built-in sensors recorded temperature, humidity and atmospheric pressure. The time of one measurement was 20–40 min. The operating principle is based on the deposition of charged daughter products of radon decay on the detector, which allows for the instantaneous assessment of the ERC. Passive measurements were performed using carbon sorption detectors "Kamera-01" (Republic of Kazakhstan) containing sorbent SK-13. These devices were installed indoors for 1–6 days at the temperature of 12–30 °C and a relative humidity of up to 95%. The method is based on the adsorption of radon by activated carbon, followed by measurement of the activity by gamma or beta radiation of short-lived daughter products of decay (Pb-214, Bi-214).

Fig. 2. - Radon radiometer Alpharad Plus

Fig. 3. - Radon radiometer Radon-Ramon

To determine the radionuclide composition of building materials, a gamma-spectrometric complex with a high-purity semiconductor HPG detector manufactured by the NTC Aspect (Russia) with the SpectraLine software was used.

The energy resolution was 1.8 keV (on the 1.33 MeV line), the relative registration efficiency was 21.8%. Measurements were carried out in 1-liter Marinelli vessels, the sample fraction was 0–5 mm, the measurement time was 30–40 min. The detection limit for 226Ra and daughter products was no worse than 2 Bq/kg. The measurement error did not exceed 20%.

The obtained values of specific activity were compared with the sanitary standard of 370 Bq/kg for building materials. The ambient dose equivalent rate (ADER) of gamma radiation was measured using dosimeters DKS-AT1121 and DKS-AT1123 with the relative error of ±15%. The sensors were placed at the height of 1 m from the floor and no closer than 0.5 m from the walls. Integrating methods were used to take into account the effect of ventilation on radon concentration.

In each room, at least four ADER measurements were taken under different air exchange modes: closed windows, slot ventilation, cross ventilation, and typical operating mode.

In the winter season, 10 paired ADER and average radon VA measurements were taken.

To analyze their interrelationship, a linear dependence was constructed, which revealed a weak positive correlation (correlation coefficient of 0.282), indicating a weak positive relationship between these parameters. The equilibrium factor between radon and its decay products was 0.4, which corresponds to typical values for unventilated indoor environments. The reduction factor of the equivalent equilibrium concentration (EEC) of radon during daytime relative to the daily average was 0.705, which is most likely associated with natural ventilation and a decrease in radon concentration during daylight hours. At the same time, the indoor radon concentration is determined not only by the

activity of Ra-226, but primarily by emanation and exhalation processes and gas transport conditions, including material porosity and fracturing, moisture content, pressure gradients, temperature regime, and ventilation. Therefore, gamma radiation from walls does not always correspond to the rate of radon release into indoor air: under similar gamma background levels, significantly different radon fluxes may occur, and vice versa.

The calculation of the effective annual dose of radon radiation was carried out according to the methodological guidelines (the Committee of State Sanitary - Epidemiological Supervision of the RK MH (CSSES) order No. 94 dated 09/08/2014) using the conversion factor of 5.1 10^{-9} Sv/(Bq m^{-3} h) and the structure of the time of stay: 0.8 years indoors and 0.2 years outside.

The annual volume of inhaled air for an adult was taken to be 8100 m^3.

$$D_{Rn} = 0.8 \cdot 8100 \cdot 5.1 \cdot 10^{-9} \cdot \text{EEC av. year} . \quad (1)$$

Differentiated values of radon concentration were obtained in cases where daily and seasonal observations were carried out. In 43.1% of premises, the effective dose varies from 6.6 mSv/year to 33 mSv/year, and for 9.4% of premises from 33 mSv/year to 680 mSv/year. The increased radon concentration is due to high exhalation from the soil surface, radioactivity of building materials and low air exchange in the surveyed premises. Gamma surveying identified 11 anomalous zones and 12 point anomalies with exposure dose rate (EDR) values exceeding 0.3 μSv/h against a background level of 0.18 μSv/h. In the northwestern part of Akchatau, anomalous zones were found where the exposure dose rate of gamma radiation exceeded 0.6 μSv/hour. The elevated EDR values are attributed to the presence of leucocratic granite outcrops exposed at the surface in the southeastern part of the studied settlement, as well as a closed mine and the occurrence of geological fault zones.

Such an integrated approach made it possible to take into account both the radionuclide characteristics of building materials and the actual operating conditions of the premises. Radiation safety standards must be calculated regardless of whether the irradiation occurs from natural or man-made sources of ionizing radiation. Hence, the systematic monitoring of radon should not only have independent significance but also be part of a complex of rehabilitation measures for surveying areas subject to man-made impacts.

2. Results and discussion

The conducted seasonal studies (winter, spring, summer 2023-2024) showed that the levels of equilibrium equivalent concentration (EEC) of radon in residential buildings of the Karaganda region varied widely. The average annual values of radon EEC in the surveyed buildings ranged from 35 to 380 Bq/m^3, while the maximum concentrations in individual rooms exceeded the permissible level for residential buildings of the Republic of Kazakhstan (200 Bq/m^3) and reached 1200-1900 Bq/m^3.

The highest values of radon EEC were recorded in winter (up to 1200 Bq/m^3), which is associated with a low air exchange rate and the operation of heating systems. In summer, concentrations were significantly lower and decreased by 2-4 times due to natural ventilation. The highest concentrations were noted in the northern part of the region (Figure 4).

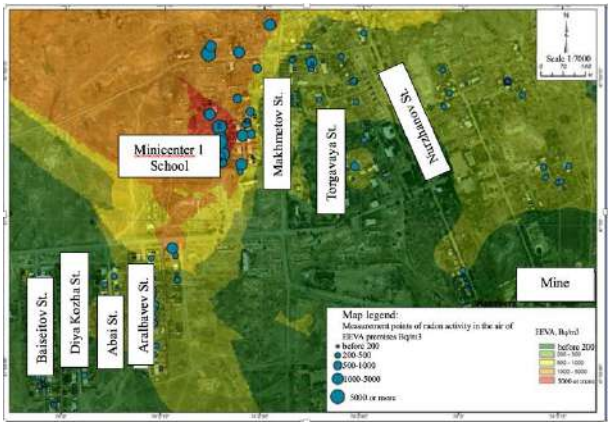

Fig. 4. - Map of the average annual radon EEC values

Additionally, an assessment of the radiation characteristics of the most common building materials (brick, concrete, granite, foam blocks) was carried out. For this, data from gamma-spectrometric studies and literature data were used [15]. The results are presented in Table 3.

Table 3, Radon activity of building materials

Material	Specific activity, Bq/kg (Ra-226)	Volume activity in premises, Bq/m³	Structural features
Brick	50–120	to 19 000	Porosity, clay base
Granite	80–150	to 10 000	High U, Th content
Concrete	30–80	to 1500	Low porosity, cement matrix
Foam block	40–90	to 3000	Increased sorption capacity
Wood	< 30	Lower that 200	Organic structure, low emanation

The highest radon levels are recorded in brick and granite buildings. It is due to the porosity and mineralogical composition, as well as the increased content of Ra-226. Concrete structures and foam blocks are characterized by lower emanation, which makes them preferable from the point of view of radiation hygiene. Wood is practically not a source of radon, which explains the low concentrations in wooden buildings.

It has been established that regular ventilation of premises reduces the radon concentration by 30-50%. The use of waterproofing of floors and walls in basements significantly reduces the ingress of radon from the soil. The use of forced ventilation systems allows maintaining EEC levels below sanitary standards.

In Lithuania and Poland, comparable radon values were recorded in brick and stone buildings (up to 15-20 thousand Bq/m³) [16]. In Finland and the Czech Republic, strict building codes have been introduced limiting the use of granite in residential construction. In Germany, mandatory design of ventilation systems is practiced in areas with increased radon hazard [17].

Thus, the obtained results confirm the importance of taking into account the radiation characteristics of building materials when designing buildings. Materials with low emanation (concrete, wood) are preferable, while the use of brick and granite requires mandatory engineering measures for sealing and ventilation. Under the sharply continental climatic conditions of the Karaganda region, it is advisable to use the following radon protection barriers: polyethylene membranes as a continuous gas-impermeable layer over the soil, and polymer-modified bituminous materials that combine gas impermeability with high adhesion and resistance to temperature-induced deformations and aging. The key condition for their effectiveness is the airtight sealing of overlaps, junctions, and service penetrations, since radon ingress is mainly associated with leakage through cracks and gaps rather than diffusion through the membrane itself.

Conclusions

1. The conducted studies of radon concentrations in residential buildings of the Akchatau settlement of the Karaganda region showed that the values of the equivalent equilibrium concentration (EEC) of radon varied significantly: from minimum values of the order of tens of Bq/m³ to maximum values exceeding the permissible sanitary standard (200 Bq/m³).

2. The highest radon concentrations were recorded in the winter, which is associated with reduced ventilation of the premises and accumulation of radon inside the buildings. In the summer, the values of radon activity are significantly reduced due to ventilation and temperature conditions.

3. A dependence of radon levels on the type of building materials was established: buildings made of brick and natural stone were characterized by increased radon emission, while concrete and foam block structures showed significantly lower values.

4. The results obtained confirm the need to take into account radon hazard in the design and operation of residential buildings. Particularly relevant is the task of developing and implementing building materials with low radon emission potential, as well as the use of engineering solutions (effective ventilation, waterproofing of foundations and walls), which is directly related to the problems of materials science.

5. Methodological recommendations are needed to ensure radiation safety of housing in radon-hazardous areas of Kazakhstan.

Funding: This research was funded by the Science Committee of the Ministry of Science and Higher Education of the Republic of Kazakhstan (grant no. AP26199353).

References

1. Fialova E., Otahai P. Determination of the Radon Progeny Activity Size Distribution in Laboratory Conditions //Atmosphere, 2024, 15(11), 1262. https://doi.org/10.3390/atmos15111262
2.Bekman I.N. Ecological radiochemistry and radioecology. Study guide. Volume VI. – M.: Publisher Markhotin P.Yu., 2015. - 400 p. ISBN 978-5-00038-184-7.
3. Leshukov T., Legoshchin K., Larionov A. A Case Study of the Radon Hazard at the Boundary of a Coal Minefield// applied sciences, 2023, 13(24),13188. https://doi.org/10.3390/app132413188.
4. Papaefthymiou H., Mavroudis A., Kritidis P. Indoor radon levels and influencing factors in houses of Patras, Greece// Journal of Environmental Radioactivity, 2003б V. 66(3). - P. 247-260. https://doi.org/10.1016/S0265-931X(02)00110-8.
5. UNSCEAR (United Nation Scientific Committee on the Effects of Atomic Radiation Report), Vol. II: Sources-to-Effects Assessment for Radon in Homes and Workplaces; UNSCEAR, United Nations: New York, NY, USA, 2006.
6. Nuccetelli C., Leonardi F., Trevisi R. Building material radon emanation and exhalation rate: Need of a shared measurement protocol from the european database analysis // Journal of Environmental Radioactivity, 2020, 226:106438. DOI: 10.1016/j.jenvrad.2020.106438
7. Bulut H.A., Şahin R. Radon, concrete, buildings and human health - A Review Study //Buildings, 2023, 14(2), 510. https://doi.org/10.3390/buildings14020510
8. Carlo C. Di, Maiorana A., Ampollini M., Antignani S., Caprio M., Carpentieri C., Bochicchio F. (2023) Models of radon exhalation from building structures: General and case-specific solutions //Science of the Total Environment, V.885(10):163800, 2023 https://doi.org/10.1016/j.scitotenv.2023.163800
9. Yang R., Wang J., Zhang X., Li J., Chen M. Radon exhalation from cement-based materials under accelerated carbonation// Environmental Science and Pollution Research, 30(17):50610-50619, 2023 doi: 10.1007/s11356-023-25831-x
10. Hassan, N. M., Ishikawa, T., Hosoda, M., Iwaoka, K., Sorimachi, A., Sahoo, S. K., et al. The effect of water content on the radon emanation coefficient for some building materials used in Japan//Radiat. Meas., 46(2), 2011. - P.232–237. doi:10.1016/j.radmeas.2010.11.006. https://www-pub.iaea.org/MTCD/Publications/PDF/trs474_webfile.pdf
11. Kuzmanović P., Miljević B., Todorović N., Forkapić S., Čeliković I., Filipović Petrović L., Knežević Radić J. (2022) The influence of building material structure on radon emanation// Journal of Radiological Protection, V. 42, №4. DOI 10.1088/1361-6498/aca59d
12. Pirsaheb M., Najafi F., Haghparast A., Hemati L., Sharafi K., Kurd N. () The Influence of Internal Wall and Floor Covering Materials and Ventilation Type on Indoor Radon and Thoron Levels in Hospitals of Kermanshah, Iran //Iranian Red Crescent Medical Journal (IRCMJ), 18(10):e25292, 2016, doi: 10.5812/ircmj.25292
13. Liza R., Pereyra P., Muñoz D., Viera V., Herrera L.M.E., Rojas J., Palacios D., Díaz,F., Cerna N., Rojas S.; et al. Comprehensive Study of Natural Radioactivity in Building Materials: A Case Study in Ica, Peru //Atmosphere, 2024, 15, 279. https://doi.org/10.3390/atmos15030279
14. Pak Y., Pak D., Matonin V., Ibragimova D., Timoshenko P., Barkov Y., Tebayeva A., Medvedev P. Study of Radon Radiation in the Area of the Akchatau Polymetallic Mine, Republic of Kazakhstan //Atmosphere, 2025, 16, 769. https://doi.org/10.3390/atmos16070769
15. Soroka Yu.N., Molchanov A.I. Survey of the radiation situation in the area of operation of the Kaztungsten Production Association // Non-ferrous Metallurgy, 1992, No. 2. – P. 62-66.
16. Wysocka M. Radon problems in mining and post-mining areas in Upper Silesia region, Poland // Nukleonika, 2016, V. 61(3). DOI:10.1515/nuka-2016-0051
17. Dehnert J., Altendorf D., Trabitzsch R., Grunewald H., Geisenhainer R., Oeser V., Streil T., Weber L., Schonherr B., Thomas J., Forner K., Alisch-Mark M., Weiss H. Radon protection in apartments using a ventilation system wireless-controlled by radon activity concentration// Journal of Radiological Protection, 2021, 41(3) doi: 10.1088/1361-6498/abfc97
18. Protection against Radon-222 at Home and at Work-Annals of the ICRP, № 65. - Oxford: Pergamon, 1994.
19. Schmier H., Koenig K., Schmitt-Hannig A., Schwibach J. Results of radon-measurements in buildings and recommended action in the Federal Republic of Germany/ /High Levels of Natural Radiation, 1993. -Vienna: IAEA. - P. 353-363.
20. Tikhonov M. N. Radon radiation: sources, doses and unresolved issues // Ecology of industrial production, 2008, No. 1. - P. 35-51. EDN JXRIPH.
21. Holmgren O., H. Arvela H., Collignan B., Jira´nek M., Ringer W. Radon remediation and prevention status in 23 European countries //Radiation Protection Dosimetry, 2013. – P. 1-5. doi:10.1093/rpd/nct156

Information of the authors

Pak Dmitri Yuryevich, c.t.s., ass. professor, Abylkas Saginov Karaganda Technical University
e-mail: d.pak@ktu.edu.kz

Pak Yuri Nikolayevich, d.t.s., ass. professor, Abylkas Saginov Karaganda Technical University
e-mail: yu.pak@ktu.edu.kz

Ibragimova Diana Andreevna, PhD, research fellow, Abylkas Saginov Karaganda Technical University
e-mail: podgornaya1992@mail.ru

Matonin Vladimir Viktorovich, director, Ecoexpert LLP
e-mail: matoninvov@mail.ru

Tebayeva Anar Yulayevna, master lecturer, Abylkas Saginov Karaganda Technical University
e-mail: tebaeva@ktu.edu.kz

DOI 10.52209/2706-977X_2026_1_46 **IRSTI 81.09.03** **UDC 621.791.927.5**

Effect of Nickel Content on Tensile, Hardness Properties and Dry Sliding Wear Behaviour of Austempered Ductile Iron

***Subramanya Raghavendra[1*], Arun Kumar Rudrappa [2], Manjunatha Kuntanahalli Narayanappa [3], Suresh Suraiah [4], Shivaramakrishna Aere[5]**

[1]Department of Mechanical Engineering, Sai Vidya institute of Technology, Bangalore, India
[2]Department of Mathematics, Sai Vidya institute of Technology, Bangalore, India
[3]Department of Mechanical Engineering, S.J.C Institute of Technology, Chikaballpura, India
[4]School of Mechanical Engineering, Reva University, Bangalore, India
[5]Department of Mechanical Engineering, Ballari Institute of Technology and Management, Ballari, India
*corresponding author

Abstract. The increasing interest in the development of austempered ductile cast irons has led to a great deal of study being done on their physical metallurgy and mechanical properties. The exceptional strength and hardness of these cast irons are well recognised. In this study, samples of permanent moulded toughened austempered ductile iron (PMADI) that are subjected to an austempering heat treatment are used to investigate the effects of nickel content on their tensile strength and hardness strength. PMADI samples were developed using Casting and samples with 1% nickel 2% Nickel content were prepared. The characteristics of PMADI samples were compared with those of samples that had been hardened and subjected to normal austempering heat treatment. Investigations were conducted on mechanical characteristics, such as tensile and hardness tests. ADI samples have shown higher levels of hardness and tensile strength. The findings showed that the mechanical characteristics of PMADI samples with 2.0% nickel were noticeably better. The scanning electron microscopy images revealed both ductile and brittle mode of fracture. Wear testing was conducted utilising a pin-on-disk machine in dry sliding method. Large quantities of austenite, which are produced at higher austempering temperatures, help to increase wear resistance through martensitic transformation. The coarse ausferrite structure in ADIs experiences adhesion, delamination, and mild abrasion in addition to oxidational wear, according to an analysis of worn surfaces and the kind of wear debris. An increase in mechanical strength seems to be correlated with an increase in retained austenite content.

Key words: nickel, austempered ductile iron, tensile, hardness, wear.

Introduction

Through heat treatment, ADI, a grade of iron, is transformed into austenite, a metastable face-centred-cubic (FCC) matrix solid solution that is stable at room temperature due to its saturation with 1.8–20% carbon [1]. The unique microstructure of ADI is composed of carbon-stabilized austenite and acicular ferrite.

Austempered Ductile Iron (ADI) is created when ductile iron undergoes the isothermal heat treatment procedure known as "Austempering." Compared to ductile iron, it offers superior characteristics. The microstructure that results from austempering ductile cast iron is called "Ausferrite" and is made up of stabilised austenite that has been enhanced with carbon and fine acicular ferrite. Compared to several ferrous and aluminium alloys, the novel microstructure produces outcomes with greater capabilities. For a given degree of ductility created by traditional heat treatment procedures, Ausferrite displays double the strength as compared to pearlitic, ferritic, or martensitic structures. The ausferrite microstructure affects the austempered ductile iron's mechanical characteristics. Compared to other grades of ductile iron, the austempered matrix provides a superior tensile strength to ductility ratio [2]. Due to its ausferrite microstructure, that is influenced by alloyed components and heat treatment parameters, austempered ductile iron can have a wide range of combined characteristics.

Even though there has been a lot of research done on the aforementioned topics by many researchers, more research is needed in this area to better understand alloyed and un-alloyed PMADI samples. This is because PMADI alloys are used to make critical parts for mining, power plants, and automobiles, and these alloys extend component life by increasing fracture toughness [3]. The following are some of the literatures analysed on Austempered Ductile iron subjected to austenitization Table 1.

Table 1. List of literatures on Austempered Ductile iron.

Ref	Investigation details	Outcome
[4]	Investigation of nickel content and austempering temperature effects. XRD analysis for retained austenite content estimation.	Nickel content improves strength and hardness, peaking at 0.8%. Retained austenite increases with higher austempering temperatures.
[5]	Experimental investigation of microstructures and mechanical properties. Characterization of hardness, compressive strength, and wear resistance.	Vanadium increases hardness and compressive strength in ductile iron. Optimal austempering time is 2 hours for V-containing iron.
[6]	Austempered at different temperatures: 240 ℃, 280 ℃, 320 ℃. Analyzed microstructure, mechanical properties, and wear resistance.	The morphology of bainite changes from needle to featheriness with increasing austempered temperature. The optimal austempered temperature is 280 ℃, resulting in improved impact toughness and wear resistance
[7]	The research aims to study the influence of austempering temperature on the microstructure and properties of austempered ductile iron with carbides, specifically focusing on how these factors affect abrasive resistance	The study demonstrated that the austempering temperature significantly affects the microstructure and properties of CADI, with higher temperatures leading to thicker and larger acicular ferrite, increased impact toughness, and decreased hardness.
[8]	The research aims to investigate the effect of austempering temperature on the microstructure of Carbidic Austempered Ductile Iron (CADI).	Also, CADI consists of bainite, retained austenite, and carbides, with nodular graphite dispersed throughout the matrix.

The application of ADI in marine conditions has been made easier by the PMADI sample's superior mechanical capabilities and enhanced fracture toughness characteristics. The use of alloying materials, changes in critical heat treatment parameters such as austenitization, temperature and length of austempering, and the use of permanent moulds all contribute to the enhancement of ADI's fracture toughness qualities [9]. Studies that use unalloyed PMADI samples to look at how various austempering temperatures affect important mechanical properties as hardness, tensile strength, and fracture toughness over an extended length of time [10]. During austenitizing, the cast iron is essentially heated between 850 and 950 degrees Celsius. The eutectic grain development and homogeneity of components, the input structure of cast iron prior to quench hardening, graphite emissions, temperature and duration of warming, and the matrix's chemical structure all affect the austenitizing procedure. [11][12].

Ausferritie transformation research is the primary focus of ADI cast iron investigations. This is a very logical attitude given that the microstructure of the metal matrix mostly influences the development of the cast iron's high strength, excellent plasticity, and impact strength [13].

This work is focused on improving mechanical parameters, such as ultimate tensile strength and ductility, in Nickel-added Permanent Moulded Toughened Austempered Ductile Iron. This research is expected to provide key insights and approaches for developing next-generation steels.

The conditions of isothermal heat treatment, particularly the temperature of austenite's isothermal transition, can have a significant impact on the microstructure and mechanical characteristics of ADI. This research is being conducted to develop austempered alloyed ductile iron since huge rollers and automotive components are becoming more and more in need of high strength and hardness resistance qualities. In this specific case, the goal of the research is to determine the ideal austempering conditions based on microstructural control and evaluation of many attributes including tensile strength and hardness.

The impact of nickel addition on austempered ductile iron's microstructure, tensile strength, and wear resistance was investigated. Austenitization and austempering temperatures, austenitization and austempering durations, and cooling rate are some of the heat treatment process factors that are crucial to the ADI microstructure that is produced in ductile iron. Understanding the mechanical properties and wear characteristics of ausferritic cast irons under wear and friction behaviour environments was the primary goal of the investigations discussed in this article. Specifically: An analysis was conducted on the impact of the nickel concentration in ADI on wear resistance.

1. Materials and methods

The current study aims to evaluate the feasibility of improving the mechanical characteristics of ductile cast iron by heat treatment of a permanent mould casting. In the current investigation, two classes of ductile cast iron samples have been taken and processed through the Austempering procedure.

For the experimentation, an electric induction furnace with a 500 kg crucible furnace capacity was utilised. High-temperature metallic charge material, up to1530°C. The samples that were received were machined and cut in accordance with EN1563.

The following table 2. Shows the details of sample designation along with Nickel percentage and Austenitization Temperature and time.

Table 2. Sample details with its composition and processing parameters

S/No	Test Sample Designation	Nickel (%)	Austenitization Temperature	Austempering Temperatures	Austempering Time (Minutes)
1	A (Unalloyed PMADI)	0	780°C	350°C	150
2	B	1	780°C	350°C	150
3	C	2	780°C	350°C	150

To perform the austempering method, ductile cast iron specimens were created from the melt. There were two phases to the heat treatment process. The samples were first heated to an austenitization temperature of 780°C for 110 minutes. After that, they were immediately transferred to a salt bath that contained 50% $NaNO_3$ and 50% KNO_3 and was kept at a 350°C austempering temperature. The same techniques were used, based on earlier research by Wieczorek A.N [14].

The material was kept at this temperature for a variety of periods of time before being quenched to preserve the microstructure that existed at each stage of the transformation. The composition details of PMADI received samples are shown in Table 3.

Table 3. Final chemistry of the received sample (wt %)

Sample	C	Si	Mn	S	P	Cr	Ni	Mo	Cu	Mg
A	3.49	2.70	0.4	0.006	0.013	0.017	0	0.32	0.598	0.044
B	3.68	2.22	0.16	0.011	0.026	0.02	1.03	0.02	0.003	0.048
C	3.68	2.22	0.16	0.011	0.026	0.02	2.02	0.02	0.003	0.048

2. X – Ray Diffraction (XRD) Analysis

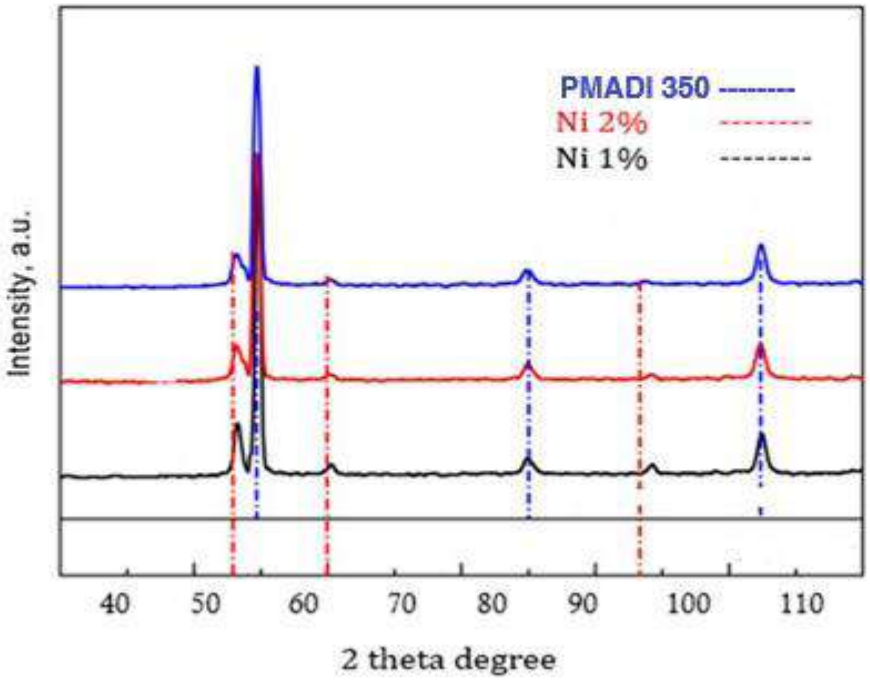

Fig. 1. - X – Ray Diffraction (XRD) Analysis of unalloyed PMADI, 1% Ni PMADI and 2%PMADI samples

The crystalline material's phase is identified using a common technique known as X – ray diffraction (XRD) analysis [9].

A Cu target diffractometer was used to perform XRD investigation on an un-alloyed PMADI sample at 40 kV and 25 mA (Bruker make). Scanning was performed over an angle range of 10° – 90° at a scanning speed of 1° min-1. XRD study of an unalloyed PMADI sample austempered for 150 minutes at 350°C. Peak locations and (shown in Fig 1) intensities of the 1 - (110) 44° - 45°, 2 - (200) 66° - 68°, and 4 - (211) 86° - 87° planes of BCC ferrite, and the 3 - (220) 78° – 79° and 5 - (311) 89° – 90° planes of FCC Austenite, were investigated. The volume fraction of retained austenite was calculated using the integrated intensities of distinct ferrite and austenite planes. The volume fraction of retained austenite was calculated based on the integrated intensity of the peaks of FCC-phase, as well as the peaks of BCC phase.

The existence of retained austenite was verified by X-ray analysis. Retained austenite is calculated using following equation (1) [15].

$$V\gamma = \frac{1.4I\gamma}{I\alpha + 1.4I\gamma} \quad (1)$$

where $V\gamma$ - retained austenite;

$I\gamma$ and $I\alpha$ are the integrated intensities of austenite and ferrite, respectively.

3. Microstructure of Nodular and cast Ductile Iron

Figure 2 shows the microscope image details of the as-cast Nodular Iron and Nickel alloyed ADI and verifies the presence of graphite in the form of nodules. The figure 2 microstructure demonstrates that the isothermal shift at 350^{0}C is to blame for this. The amount of austenite that has been kept is at 150 minutes. When chilled to room temperature, austenitic portions that are not sufficiently stabilised with carbon transform into martensite. As the treatment duration rises, more austenite is isothermally converted to acicular ferrite, which enriches the residual austenite due to carbon rejection. Cooling the austenite to room temperature has no effect on it but the effect of carbon rejection on stabilising the residual austenite becomes much greater. Samples that were subjected to an austempering temperature of 350^{0}C for 150 minutes also exhibited improved residual austenite.

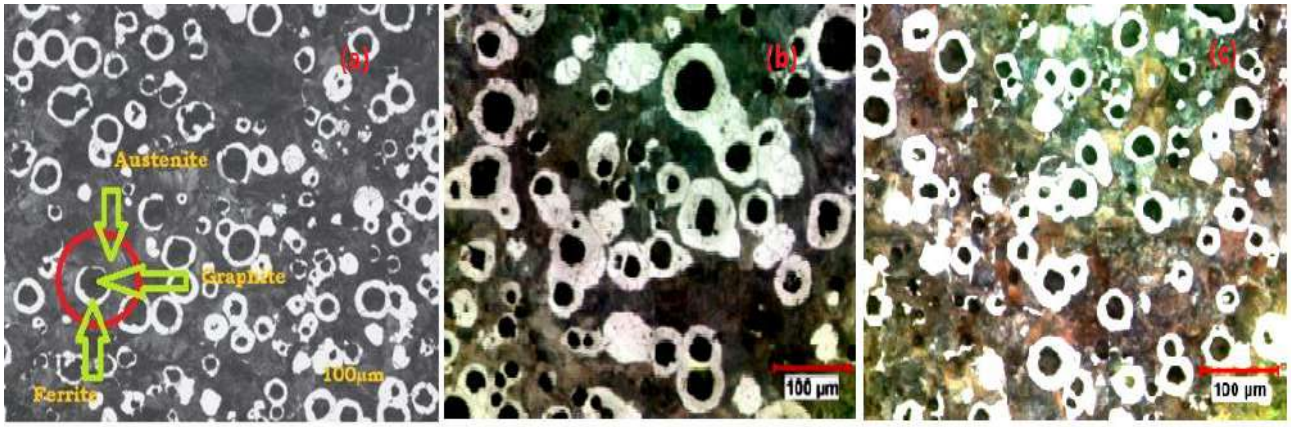

Fig. 2. - (a-c) As-cast structure of 0 %, 1%, and 2% Nickel bearing permanent molded ductile iron

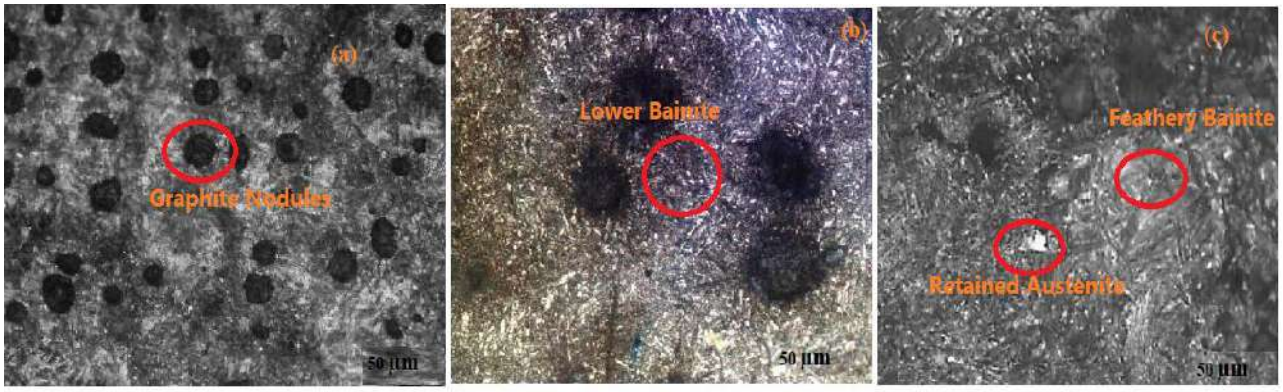

Fig. 3. - (a-c) Micrographs of PMADI 350– Austentizing temperature – 900°C for 120 minutes, Austempering temperature – 350°C for 150 minutes time duration

Fig 3 a - c clearly shows the micrographs of as cast PMADI samples alloyed with 0%, 1%, and 2% Nickel in condition – etched using 2% Nital solution. The graphite nodules are surrounded by ferrite in the form of Bull‘s eye structure along with pearlite and iron carbide (Fe3C) and the same was confirmed from the photomicrograph of Nickel alloyed PMADI samples. From the observation, It is clear that, the pearlite content in the matrix increased and the ferrite content decreased as the nickel additions were increased. Nickel is referred to as an austenite-stabilizing element because it shifts the pearlite knee to greater time intervals in solid state transformation. Traces of iron carbide were seen in all the samples. Also clearly displays the microstructural observations such as nodule size of 4-7µm for 0% PMADI sample, 6-8 µm for 1% Ni-PMADI and 7-9 µm for 2% Ni-PMADI samples (Nodule Count of 128, 150 and 180 number/mm^2 for PMADI , 1% Ni-PMADI and 2% Ni-PMADI samples).Fig 3 (c) displays the photomicrograph of PMADI - 350 sample austempered at 350ºC for 150 minutes With a maximum degree of retained austenite of 26%, duration validates the presence of a feathery dispersion of Bainite. Pearlite and cementite were converted to ferrite and graphite by low temperature graphitisation annealing; otherwise, their presence would significantly enhance the iron's brittleness, which has a negative effect on toughness.

5. Hardness Test

A Brinell hardness tester was used to evaluate both an unalloyed PMADI sample and PMADI that had been alloyed with nickel. Three mean values were obtained. A 5 mm diameter ball is utilised as the indenter, 250 kgf is applied as the load. The BHN values of tested samples are shown in figure 4.

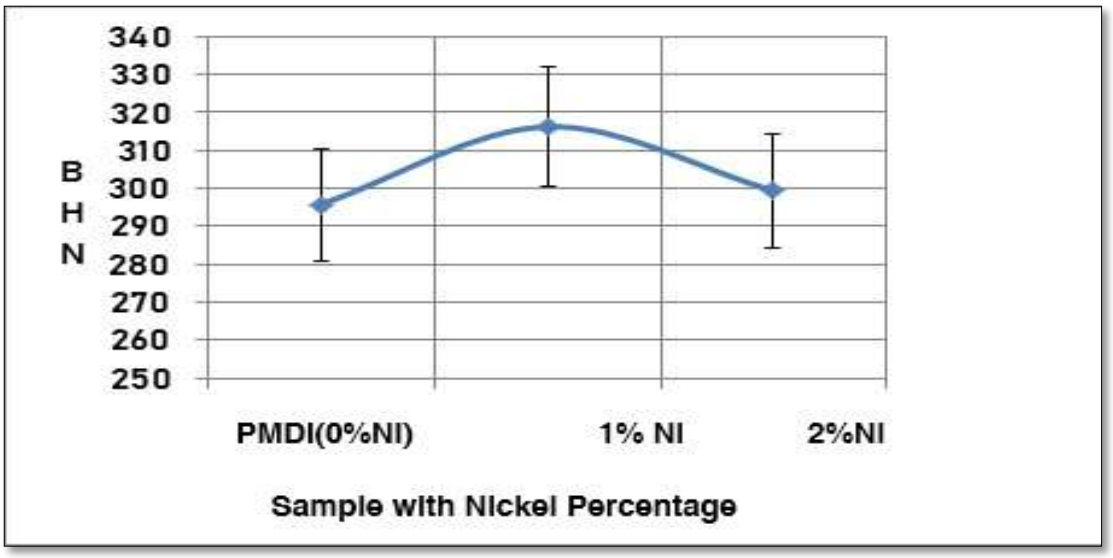

Fig. 4. - Results of Hardness Test

The results of the hardness test showed that the PMADI's 1% Ni PMADI sample had the highest hardness, while the unalloyed PMADI sample had the lowest. This might very well be explained by the ideal composition of ausferrite. As the austempering temperatures rose, the extent of retained austenite increased while the amount of acicular ferrite decreased gradually. Hardness was decreased by both ferrite coarsening and retained austenite [16]. As the temperature of austempering increases, there is a corresponding rise in the quantity of austenite and microstructure coarsening. As the proportion of the softer austenite phase increases, the hardness of the austempered ductile irons falls. Furthermore, the coarsening of the grain also results in a decrease in hardness [17].

6. Tensile Test

The tensile parameters of PMADI sample include ultimate tensile strength (UTS), yield strength and percentage (percent) elongation, which were tested using a computerised FIE manufacture universal testing equipment (UTM). The average readings of three samples in PAMDI-350, 1%Ni and 2%Ni specimens were taken and recorded. The evaluated details are shown in table 4.

Table 4. Tensile strength results of Unalloyed P PMADI, 1%Ni PMADI and 2%PMADI

		UTS MPa	% Elongation	YS MPa
PMADI	Sample 1	986.21	4.81	805.12
	Sample 2	983.54	4. 76	805.08
	Sample 3	969.47	4.71	806.41
A 1%Ni	Sample 1	995.65	3.88	812.24
	Sample 2	989.38	3.71	814.36
	Sample 3	981.19	3.82	818.27
B 2%Ni	Sample 1	1089.32	5.11	1084.16
	Sample 2	1088.91	4.92	1084.12
	Sample 3	1087.63	5.16	1084.18

The Ultimate tensile strength, Yield strength and % elongation results are clearly displayed in table 4. The highest tensile strength of 1089.32 MPa was discovered to be for 2% Nickel alloyed PMADI sample and the minimum of 969.47 MPa for 0% Nickel alloyed PMADI sample. The highest % elongation of 5.16% was found in 2%Ni PMADI samples and lowest % elongation of 3.82% discovered in 1% Ni PMADI Samples.

Finer acicular ferrite is found at 350^0C. Tensile strength is higher at 350^0C as a result. The microstructure confirms that acicular ferrite increases at austempering temperature, and the tensile strength also declines. Tensile strength drops with increasing ferrite cell size. Similar trend were witnessed in the work of Dakre et et,al.,[18].

The high tensile elongation of these is attributed largely to the substantial volume percentage of residual austenite than to martensite production during plastic deformation [19].

According to research findings, ductility and toughness increase with rising austempering temperatures, whereas ultimate tensile strength (UTS) and hardness decrease. The ideal temperature is found to be 350°C. When the 150-minute austempering period is taken into account, the amount of retained austenite stabilises in each sample, with the PMADI 350 sample having the highest amount. The importance of nickel as an alloying element helps to stabilise the austenite phase and reinforce the Bainitic matrix. An austenite and ferrite-based ausferrite matrix is created during the austempering process from the pearlite matrix. The mechanical characteristics were impacted by the temperature that was austere [20]. Elevating the retained austenite and decreasing the acicular ferrite might be the cause. The area proportion of retained austenite increased and acicular ferrite decreased when a greater austempering temperature was applied, according to earlier studies [21].

7. Scanning electron microscope

Figure 5 show the tensile fracture surface of the broken specimen which is witnessed under scanning electron microscope (SEM; Model: JSM-7001F). As cast samples show brittle fracture. Intergranular fracture is viewed under the SEM. The fracture surface has a ‘‘rock candy’’ appearance that reveals the shapes of the individual grains. Thus, the fracture takes place between the grains [21].

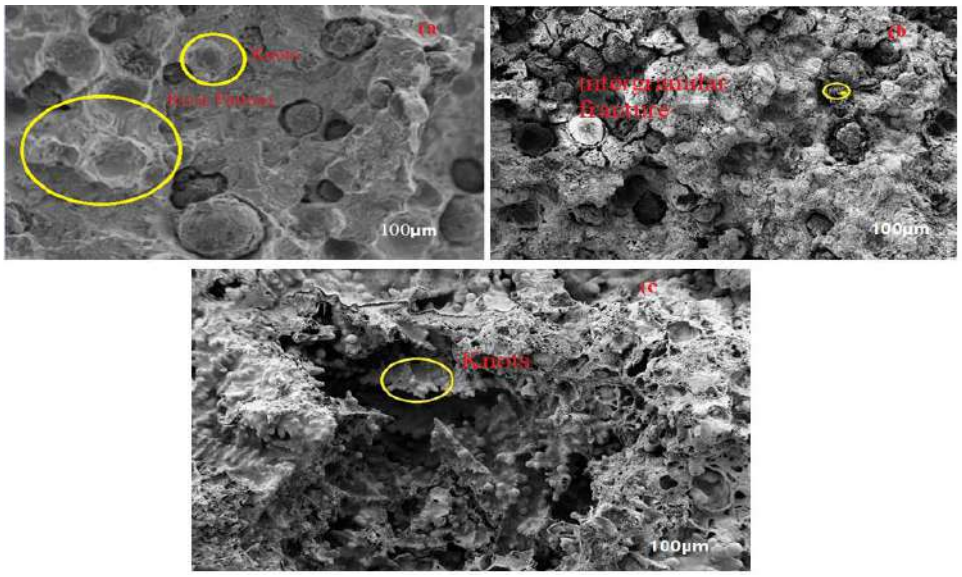

Fig.5. - (a) SEM photomicrograph of fractured Un alloyed PMADI samples; (b)PMADI samples with 1% Nickel content; (c) PMADI samples with 2% Nickel content, austempered at 350°C for 150 minutes

Mix type i.e. ductile as well as brittle fracture mode is observed in austempered samples. A significant number of dimples, a sign of ductile fracture, were seen in the nickel-alloyed samples. The samples showed unmistakable signs of dimple fracture between the nodular ligaments. Also, several of the nodules showed signs of graphite particle breakage. Additionally, nickel alloyed samples showed ductile void coalescence followed by de cohesion. Figure 5c illustrates that the 2.0% Ni PMADI samples showed ductile fracture because of the many knots present and the resulting significant elongation prior to fracture.

As per Ravishankar et al.,[22] The samples that underwent lengthier austempering durations in the first phase, such as 60 minutes, had fine austenite that was maintained as thin films between ferrite sheaths, together with a relatively high carbon content. Consequently, the austenite that remained exhibited exceptional stability. The constancy of the retained austenite is a key factor contributing to the enhanced fracture toughness observed in samples subjected to either low temperature conventional austempering or prolonged durations of first step austempering in the two-step austempering process.

The specimens displayed brittle fracture characteristics due to cleavage ductile cracks throughout the surfaces. This is characterised by the formation of relatively large cavity widths in relation to the sizes of the nodules. The stress-induced martensitic transition seems to have contributed to the development of brittle fractures, resulting in a decrease in fracture toughness [23].

The effective utilisation of permanent moulds has also contributed to the enhancement of nodule morphological characteristics, including counts and size [24]. The efficient dispersion of Bainite inside the ultimate microstructure is also accountable for the enhancement of the maximum load-bearing capacity.

The hardness and tensile properties of Al/Si3N4 nanocomposites were examined by Md Tanwir Alam et al. The study observed that the physical characteristics of nanocomposites, such as density and porosity, exhibited a linear improvement similarly in this work addition of nickel in ADI increased mechanical properties [25]. It is commonly known that producing dynamically loaded parts requires a combination of high ductility and high strength values.The effects of nickel alloying vary depending on the form of cast iron, and several researchers have studied this material to see how little nickel additions influenced different forms of cast iron alloys. These outcomes highlight the importance of the solidification cooling rate in ductile iron, which could affect the final material's hardness and tensile strength. The outcomes evidently show that all attributes increase with nickel content up to 2%. This is visible in the number of nodules and the amount of retained austenite in the matrix. Nickel, as a solute element dissolved in the matrix, interacts with dislocations and elements separated near dislocations to create Cottrell atmosphere, which may be the cause of this.

8.Wear analysis

Wear tests were performed out using a pin-on-disc wear testing machine with cylindrical samples of 10 mm diameter and 20 mm height against a 60 mm hardened M2 steel ring.This study examined wear rate as a function of sliding velocity while maintaining a constant applied load of 50 N. Track radius of 60 mm was taken into account for sliding velocities of 1.57 m/s, 2.57 m/s, and 3.77 m/s.

The specimen's surface temperature and characteristics may be impacted by the change in the generation of heat caused by the speed increase. As the sliding speed rises, higher surface temperatures may accelerate oxidation and alter the wear process to a softer wear. It was discovered that specimens tested at greater loads had a higher wear factor. Although martensite is known to be brittle and prone to breaking, the change of austenite to martensite strengthens the surface, enabling it to sustain the high contact load [26].

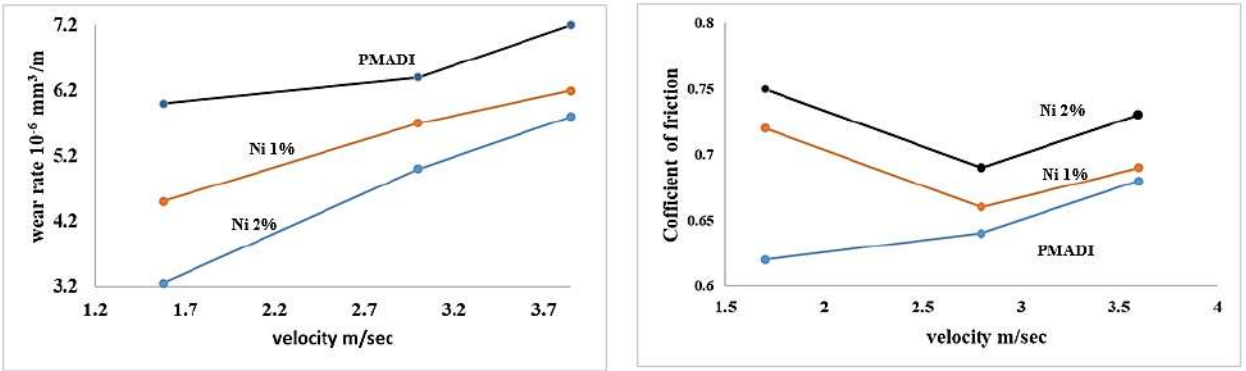

Fig. 6. - (a) wear rate as a function of sliding speed; (b) coefficient of friction as a function of sliding speed

The main factors that influence of wear rate are temperature, hardness, velocity, and environmental factors. Because temperature increases together with velocity and load, temperature has a significant impact on wear rate.

COF rises as load and sliding velocity increase (fig 6.). The contact surfaces heat up while sliding as a result of friction, and wear particles and hard asperities plough the flat areas of the sliding surfaces. Because there is not enough

time for heat dispersion, the frictional heating occurs continuously when the counter surface is moving relative to the surface. The sliding action rises with the material's flow ability, which also lowers the coefficient of friction by reducing frictional heating.

The COF marginally rises in each composition as a result of mass loss decreasing and Ni% increasing, while the velocity and load increase as mass loss increases. The physical phenomena of wear at low austempering temperatures were adhesive and abrasive wear, whereas at high austempering temperatures it was adhesive wear through the creation of an intermediate or mixed layer, as the friction coefficient rose with rising austempering temperature.

In addition to lowering the wear rate and lowering the coefficient of friction, the presence of a tribo mechanically mixed layer changes the wear way from two body to three body wear. The amount of metal removed during the wear test decreased significantly as a result. Without adding Ni, it is suggested that there is more worn debris, which accelerates the rate of wear. In another way, the presence of hard, pulled-out Ni particles on the steel disc creates an obstruction and changes the adhesive wear mode into an abrasive one. A lower number of cracks and scratches is associated with optimal wear rates.

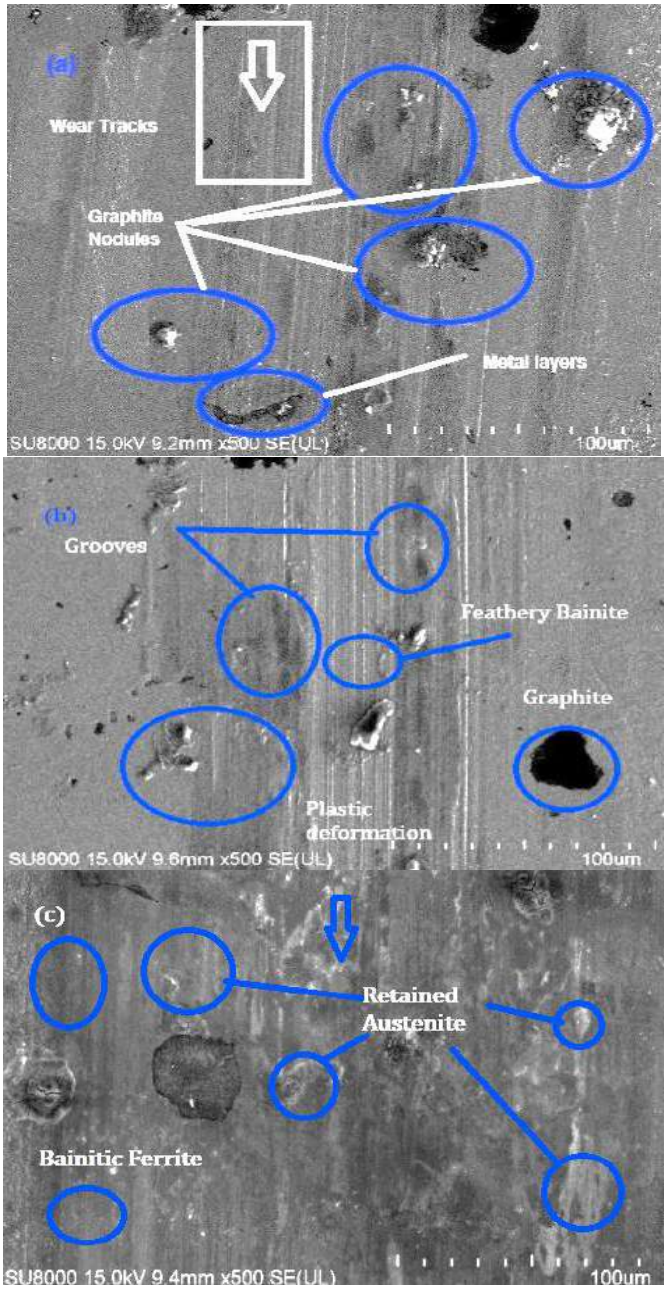

Fig. 7. - Worn morphology of the ADI tested samples. (a) PMADI (b) Ni 1% added ADI and (c) Ni 2% added ADI sample

This micrograph revealed a smooth surface with some wear traces due to ductility. There was a smearing of the material across the nodules, indicating a more ductile structure, although the black one on the worn surface was graphite-

shaped and noduled. Because graphite nodules function as porosity flaws, this micrograph also showed that certain graphites had been distorted from the pin surface and altered shape.

From Figure 7. It has been demonstrated that the depth of the scratches seemed to increase as the abrasive particles approached the leading edge of the graphite nodule. Additionally, edge chipping was observed in this case along with plastic deformation. Owing to a greater number of grooves and microchips created by plastic deformation at the contact areas between the sample and abrasive particles, Fig. b shows a rougher surface. Because the shape of the particle and the increase in ductility affected the penetration depth, it varied. In this instance, wear caused the majority of the groove volume to be lost without staying at the groove sides.

Conclusions

The following are the primary conclusions drawn from this investigation:

By adding nickel by weight 1% and 2%, respectively, to austempered ductile cast iron, the material's mechanical properties such as its hardness and tensile strength were enhanced. The iron was then austempering at a variety of temperatures, including 350 °C.This was a result of the specific combination of alloying elements utilised and a well-formed microstructure mostly composed of acicular ferrite and austenite.

The PMADI sample, alloyed with 2 percent Nickel, has superior yield strength qualities. This may be attributed to the effective utilisation of permanent moulds, a greater volume percentage of retained austenite, and the dispersion of Bainite.

The precise combination of heat treatment parameters, which includes ideal nodule count and size, effective austenite management, and proper Bainite dispersion, leads to an enhancement in both tensile and hardness properties for both the PMADI – 350 samples and the nickel alloyed PMADI samples. Considering these factors, PMADI samples might be utilised as a substitute material for applications that need enhanced yield strength qualities. The 2 % Nickel carrying PMADI sample exhibited a 12.36% improvement in its highest ultimate tensile strength compared to the unalloyed PMADI sample when both were subjected to equal austempering conditions.

The addition of 1 percent Nickel to a PMADI sample resulted in a 6.92% increase in its maximum hardness strength when compared to an unalloyed PMADI sample that underwent comparable austempering conditions. Severe adhesive wear, plastic deformation, and surface delamination were the most common wear processes identified on worn surfaces at low loads in both materials. The enhanced wear resistance of ADI under normal loads was connected with the deformation-induced transition of austenite to martensite and the resulting increase in hardness. Nickel presence of 2 wt% in ADI strengthened the material's hardness and wear resistance at low loads.

Compared to other alloys, ADI alloys, when appropriately heat-treated, have the ability to replace more expensive alloys in the construction of industrial products like as rolling mills. This substitution can result in cost savings.

Disclosure statement. No potential conflict of interest was reported by the author.

Funding. No funding received for this research study.

References

[1] K.Narasimha Murthy, P. Sampathkumaran, S. Seetharamu, Abrasion and erosionbehaviour of manganese alloyed permanent moulded austempered ductile iron //Wear, 267, 2009, P.1393 - 1398.doi.org/10.1016/j.wear.2008.12.033.

[2] Gundlach. R. and Janowak. J.F, Austempered ductile iron combines strength withtoughness and ductility //Metal progress, Vol. 128, No. 2, PP 19-26, 1985.

[3] Y. Sahin, O. Durak,Abrasive wear behaviour of austempered ductile iron //Materials & Design,Vol 28, Issue 6,2007, P. 1844-1850,doi.org/10.1016/j.matdes.2006.04.015.

[4] Sellamuthu P., Samuel D. G. H., Dinakaran D., Premkumar V. P., Li, Z., Seetharaman S. Effect of nickel content and austempering temperature on microstructure and mechanical properties of austempered ductile iron (ADI), 2018, 383(1), 012069. https://doi.org/10.1088/1757-899X/383/1/012069

[5] Cui J., Chen L. Influence of austempering process on microstructures and mechanical properties of V-containing alloyed ductile iron //Journal of Iron and Steel Research International, 201825(1), 81–89. https://doi.org/10.1007/S42243-017-0010-2

[6] Xu X. Effects of Austempered Temperature on Microstructure and Properties of CAD, 2011 https://en.cnki.com.cn/Article_en/CJFDTOTAL-ZZZZ201101011.htm

[7] Liu J. H., Li G. L., Zhao X., Hao X. Y., Zhang J. Effect of Austempering Temperature on Microstructure and Properties of Carbidic Austempered Ductile Iron //Advanced Materials Research, 2011, 1085–1088. https://doi.org/10.4028/WWW.SCIENTIFIC.NET/AMR.284-286.1085

[8] Chen Z. Effect of Austempering Temperature on Microstructure and Mechanical Properties of CADI, 2008 https://en.cnki.com.cn/Article_en/CJFDTOTAL-ZZZZ200803020.htm

[9] Bingxu Wang, Gary C. Barber, Feng Qiu, Qian Zou, Hongyu Yang A review: phase transformation and wear mechanisms of single-step and dual-step austempered ductile irons //Journal of Materials Research and Technology,Vol 9, Issue 1,2020, P. 1054-1069, doi.org/10.1016/j.jmrt.2019.10.074.

[10] Wilk-Kołodziejczyk D., Regulski K., Giętka T. et al. The Selection of Heat Treatment Parameters to Obtain Austempered Ductile Iron with the Required Impact Strength //J. of Materi Eng and Perform, 2018, 27, 5865–5878 doi.org/10.1007/s11665-018-3714-y.

[11] Grech M., Young J. M. Effect of austenitising temperature on tensile properties of Cu–Ni austempered ductile iron //Materials Science and Technology, 1990, 6:5, 415-421, DOI: 10.1179/mst.1990.6.5.415

[12] Mallia J., Grech M. Effect of silicon content on impact properties of austempered ductile iron, Materials Science and Technology, 1997, 13:5, 408-414, DOI: 10.1179/mst.1997.13.5.408.
[13] Giętka T., Szykowny T., Dymski S. The influence of saturation of cast iron austenite with carbon on the ausferrite transformation //Archives of Foundry Engineering, 2007, 7(3), 241-246.
[14] Wieczorek A.N. The role of operational factors in shaping of wear properties of alloyed Austempered Ductile Iron. Part I. Experimental studies abrasive wear of Austempered Ductile Iron (ADI) in the presence of loose quartz abrasive //Arch. Metall. Mater. 2014, 59, 1665–1674. doi.org/10.2478/amm-2014-0281.
[15] Li Z., Wu D. Effects of hot deformation and subsequent austempering on the mechanical properties of Si–Mn TRIP steels //ISIJ international, 2006, 46(1), 121-128
[16] Rao P.P., Putatunda S.K. Dependence of fracture toughness of austempered ductile iron on austempering temperature //Metall Mater Trans A 29, 1998, 3005–3016 doi.org/10.1007/s11661-998-0208-9
[17] Putatunda S. K., Kesani S., Tackett R., Lawes G. Development of austenite frees ADI (austempered ductile cast iron). Materials science and Engineering: A, 2006, 435, 112-122.
[18] Dakre V., Peshwe D.R., Pathak S.U. et al. Mechanical Characterization of Austempered Ductile Iron Obtained by Two Step Austempering Process //Trans Indian Inst Met 2017, 70, 2381–2387 https://doi.org/10.1007/s12666-017-1099-5
[19] Bendikiene R. et al. Influence of austempering temperatures on the microstructure and mechanical properties of austempered ductile cast iron //Metals (Basel), 2021, vol. 11, no. 6, p. 967
[20] Wang B., Barber G. C., Tao C., Sun X., Ran X.Characteristics of tempering response of austempered ductile iron //J. Mater. Res. Technol., 2018, vol. 7, no. 2, pp. 198–202,
[21] Wulpi D.J. Understanding How Components Fail. 2nd ed. Materials Park OH: ASM International; 1999. http://www.books24x7.com/marc.asp?bookid=42688. Accessed December 18 2023.
[22] Ravishankar K. S., Rao P. P., Udupa K. R. Improvement in fracture toughness of austempered ductile iron by two-step austempering process //International Journal of Cast Metals Research, 2010, 23:6, 330-343, doi: 10.1179/136404610X12693537270091
[23] Bendikiene R., Ciuplys A., Cesnavicius R., Jutas A., Bahdanovich A., Marmysh D., Nasan A., Shemet L., Sherbakov S. Influence of Austempering Temperatures on the Microstructure and Mechanical Properties of Austempered Ductile Cast Iron //Metals, 2021, 11(6):967. https://doi.org/10.3390/met11060967
[24] Subramanya Raghavendra, J. V. Raghavendra, Manjunatha Kuntanahalli Narayanappa, Chandra Shekar Anjinappa, K. G. Srinivas B. Manjunatha An influence of nickel with heat treatment on the microstructure and fracture toughness of austempered ductile iron //Canadian Metallurgical Quarterly, 2023, 62:2, 221-231, DOI: 10.1080/00084433.2022.2088172
[25] Md Tanwir Alam, Md Azhar, Yasser Rafat Physical Mechanical and Morphological Characterization of A356/Si_3N_4 Nanoparticles Stir Casting Composites //Journal of Engineering research, 2022,doi.org/10.36909/jer.16205
[26] Ramkumar T., Madhusudhanan S., Rajendran I. Effect of nickel on the microstructure, mechanical and tribological properties of austempered ductile cast iron for steering knuckle applications //Arch. Metall. Mater, 2020, 65, 15–25.

Information of the authors

Subramanya Raghavendra, Department of Mechanical Engineering, Sai Vidya institute of Technology
e- mail: rvs.sdly@gmail.com

Arun Kumar Rudrappa, Department of Mathematics, Sai Vidya institute of Technology
e -mail: arun.kumarr@saividya.ac.in

Manjunatha Kuntanahalli Narayanappa, Department of Mechanical Engineering, S.J.C Institute of Technology
e-mail: bangaloreju@gmail.com

Suresh Suraiah, School of Mechanical Engineering, Reva University
e-mail: sureshpoojar95@gmail.com

Shivaramakrishna Aere, Department of Mechanical Engineering, Ballari Institute of Technology and Management
e-mail: areshivark@gmail.com

DOI 10.52209/2706-977X_2026_1_56 **IRSTI 55.03.03** **UDC 539.3**

Stability of a Cantilever Rod with Variable Bending Stiffness

Akhmediyev S.K., Filippova T.S., Oryntayeva G.Zh., Tazhenova G.D.*
Abylkas Saginov Karaganda Technical University, Karaganda, Kazakhstan
*corresponding author

Abstract. This article deals with a rather complex problem of the rod system stability, the solution of which is complicated by the inconstancy of the bending stiffness along the length of a cantilever rod compressed by a concentrated axial force. The original fourth-order differential equation is split into a system of two second-order differential equations that, under given boundary conditions at the ends of the rod, are solved by the numerical finite difference method. The transition from the fourth-order equation to the second-order equations made it possible to eliminate the need to record the "second" contour nodes outside the material part of the structure under study, which made it possible to obtain a more "correct" (a physically determined value) of critical forces. Reliability of the presented theoretical provisions and applied results is confirmed by comparison with the known exact solutions of the other authors. In the course of the study, along with the values of critical forces, four forms of loss of stability are presented due to the corresponding "standing" waves along the length of the considered cantilever rods of variable bending stiffness. The scientific and applied results presented in this article will be useful in developing methods of strength calculations in the mechanics of deformable solids, and will also serve as a methodological guide for practicing engineers and designers.

Keywords: cantilever rod, variable bending stiffness, numerical finite difference method, critical force, mode of loss of stability.

Introduction

The problem of stability of various mechanical systems (including rod systems) has been facing scientists and engineers for a long time (starting with the stability theory of Euler, Yasinsky, Lyapunov) [1].

At present, this issue is the subject of quite a lot of scientific works that, along with the well-known problems of the stress-strain state (SSS) of structures, also solve stability issues. Thus, in work [2], stability of the "SSS" is considered by the vibration method (based on the analysis of the values of the natural frequencies of the structure oscillations) for a clamped rod with a non-circular cross-section.

Work [3] studies the dynamic behavior of flexible beam systems of the Euler-Bernoulli "beam" type, taking into account geometric nonlinearity factors; in this case, the method of "smoothing" the model is used based on the filtering (sampling) of higher-order frequencies. Stability of columns and rod systems in a compressed-bent deformable form in the elastic stage is studied using the analytical method [4], the physically linear stability of a cantilever rod from the action of an axial force is considered both in the static and dynamic formulation [5]; in this case, the compressive force is “connecting”, i.e. its direction is associated with the form of bending deformation; the results are compared with the results of classical stability theory.

In work [6] the strength and stability of a pipe-concrete column of a high-rise building are studied; on the basis of a rod model the longitudinal and bending stiffness of such a structure are determined, taking into account the joint work of the concrete and steel components. The problem of bending stability of a cantilever tubular rod with a hinged end is studied using the numerical method [7]. On the basis of a finite element rod model with five degrees of computational nodes the problem of stability of flat rod systems is solved taking into account the combination of their curvature and axial deformation; the geometric nonlinearity of the problem is taken into account, the corresponding finite element matrices are obtained [8]. The problem of optimization of steel flat rod systems with control of their overall stability taking into account the initial deflections in two main planes is solved and obtained on the basis of the finite element method with flat nodal displacements [9]; a tangent matrix is developed taking into account the use of small fictitious forces by a self-balanced system; an iterative cycle is applied.

Work [10] reflects the issues of structural stability of mechanical systems (columns, beams, arches, rings, plates) based on modernized analytical methods taking into account plastic deformation and initial deflections; the issues of structural analysis in design, material fatigue and probable failures are also considered.

In articles [11, 12, 13] a nonlinear bending one-dimensional model of elastic flat rods for solving the stress-strain state of thin Föppl-von Karman shells without taking into account membrane stresses based on the Koiter model was studied; buckling (loss of stability) of composite rods made of hybrid carbon fiber was studied based on the multiscale finite element method; a 3D model (for a brick rod) and a 2D model (for a beam with a square and circular cross-section) were used; mathematical modeling of displacement functions for compressed elastic rods was considered taking into account the properties of materials, the shape of the "diameter", the magnitude of the compressive force and its eccentricity; the experimental results were processed using the Minitab program. The presented experimental results were estimated based on the theoretical results of the Euler's theory.

The plane stability of an elastic and plastically deformable beam was studied for its different values of tensile and compressive resistance (brittle-fracturable materials: ceramics, copper, cast iron, polymers, composite materials); based on the corresponding studies, the boundaries of the elastic and plastic deformation regions were established [14].

To study the stability of rods, a comparison of numerical methods is considered: the finite element method, the Galerkin method, and the difference method. The dependence of the solution to the stability problem on the discretization parameters of these numerical methods is studied [15]. In [16], a solution to stability problems of planar rod systems using the finite element method, based on stresses, is presented. The proposed method is based on a combination of the additional energy functional and the principle of feasible displacements. To solve stability problems, the functional takes into account the additional energy from longitudinal deformations arising from rod bending. The buckling mode in the finite element domain is approximated by a linear function.

Having lost stability, the rod is subjected to two bendings and torsion. Large lateral displacements often lead to various accidents. Therefore, the problem of preventing such phenomena remains relevant. Article [17] presents a sequence of actions for solving the boundary value problem of plane-flexural stability of mechanical structures. A system of two differential stability equations for the indicated structural elements – circular arches – has been integrated. Fundamental orthonormal functions for differential stability equations for a circular rod are presented in two versions. It is proposed to solve stability problems using the boundary element method.

As important components of lifting equipment, tie rods have been the subject of research into their compressive strength. Axial compression tests were conducted on two types of lattice tie rods with different cross-sectional dimensions. The tests provided comprehensive data, including the damage pattern, axial pressure-displacement curves, axial compression capacity, and axial pressure-strain curves. These data, in particular, revealed the presence of stress concentrations at the joints of lattice elements in the tie rods [18]. The study [19] details the results of full-scale experimental investigations conducted on spatial composite columns with transverse bracing. Two different analytical approaches were used to determine the overall critical buckling load. The results showed minimal influence of shear effects on the tested columns, suggesting that the critical buckling load can be accurately determined using existing analytical formulas.

1. Methods

The focus of this article is on the stability of rod systems, a problem that is rendered more intricate by the variable bending stiffness EI_x encountered along the length of a cantilever rod under axial compression by an axial force P (Figure 1, a). These types of constructions find extensive application across numerous technological fields, including building, aviation, and naval engineering.

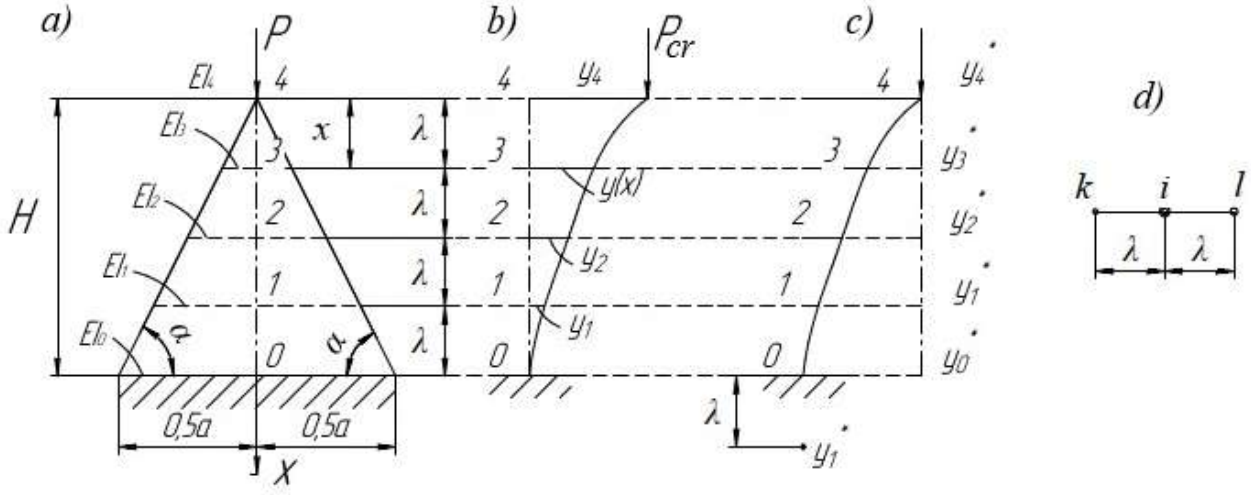

Fig. 1. – Towards the calculation of a cantilever rod for stability

The state of indifferent equilibrium of straight elastic rods is described by the following system of ordinary differential equations [20]:

$$M^{//} - P(x)Y^{//} - P(x)Y^{//} = 0; \quad (1)$$

$$Y^{//} + \frac{M}{EI(x)} = 0; \quad (2)$$

$$P^{/} = P(x), \quad (3)$$

where $Y(x)$is the displacement (deflection) of the rod in the indifferent equilibrium;

$M(x)$ is the bending moment arising in the same state;

$P(x)$ is the intensity of the distributed longitudinal axis;

$EI(x)$ is the variable bending stiffness of the rod.

To solve this problem (in the case of a cantilever rod) (Figure 1, a), it is advisable to proceed from the resolving equation (2) in moments. Taking the origin of coordinates at point "4", the bending moment from the concentrated force "P" can be written down as $M(x)= P \cdot Y\ (x)$.

Then, based on equation (2), there is obtained the following resolving differential equation:

$$\frac{d^2y(x)}{dx^2} + \frac{P \cdot y(x)}{EI_x} = 0; \tag{4}$$

$$k^2 = \frac{P_{cr}\lambda^2}{EI_0}, \tag{5}$$

where k^2 is the critical load parameter.

Then, taking into account (5), equation (4) will take the form:

$$\frac{d^2y(x)}{dx^2} + \frac{k^2}{\alpha_i\lambda^2} y(x) = 0, \tag{6}$$

where ($\alpha_i = EI_i / EI_0$) are stiffness coefficients along the rod length.

Given the value of k^2, the value of the desired critical force is determined using formula (5):

$$P_{cr} = k^2 \frac{EI_0}{\lambda^2} = k^2 n^2 \left(\frac{EI_0}{H^2}\right), \tag{7}$$

where n=H/4 is the number of the linear grid steps along the grid length.

For the *i*-th node of the linear grid (Figure 1, d), equation (6) in finite differences will take the form:

$$(k^2\alpha_i - 2)y_i + (y_k + y_l) = 0. \tag{8}$$

2.Solutions

When writing the finite difference equation (8) for cantilever rods, the problem of eliminating deflections of the "contour" nodes of the linear grid arises; in this regard, there is used the following technical method (Figure 1, c): node “4” is conditionally fixed from displacement by placing the origin of coordinates in it, then a conditional displacement will appear in node "0", and instead of the actual deflections y_i (i = 1, 2, 3, 4) (Figure 1, b), conditional deflections y_i^* (i = 0, 1, 2, 3) are used. According to (Figure 1, c), the resolving finite difference equations for nodes 0, 1, 2, 3 are written down as follows [21]:

a) node “0” (i= “0”; $\alpha_0 = 0.44$):

$$(0.44k^2 - 2)y_0^* + 2y_1^* = 0; \tag{9}$$

b) node “1” (i= 1; $\alpha_1 = 0.75$):

$$(0.75k^2 - 2)y_1^* + (y_0^* + y_2^*) = 0;\ y_0^* + (0.75k^2 - 2)y_1^* + y_2^* = 0; \tag{10}$$

c) node “2” (i= 2; $\alpha_2 = 0.5$):

$$(0.5k^2 - 2)y_2^* + (y_1^* + y_3^*) = 0;\ y_1^* + (0.5k^2 - 2)y_2^* + y_3^* = 0; \tag{11}$$

d) node “3” (i= 3; $\alpha_3 = 0.25$):

$$(0.25k^2 - 2)y_3^* + y_2^* = 0;\ y_2^* + (0.25k^2 - 2)y_3^* = 0. \tag{12}$$

By combining equations (9-12) together into a system of four linear algebraic equations (SLAE), and equating the determinant to zero at the corresponding displacements y_i^*(i =0, 1, 2, 3), there is obtained D=0.

	y_0^*	y_1^*	y_2^*	y_3^*
1)	$(0.44k^2 - 2)$	2	0	0
2)	1	$(0.75k^2 - 2)$	1	0
3)	0	1	$(0.5k^2 - 2)$	1
4)	0	0	1	$(0.25k^2 - 2)$

(13)

Expanding the fourth-order determinant (13), we obtain:

a) eigenvalues of matrix (13):

$$k_1^2 = 0.264;\ k_2^2 = 3.015;\ k_3^2 = 6.365;\ k_4^2 = 9.569. \tag{14}$$

b) eigenvectors:

$$V_1 = \begin{vmatrix} - & 8.198 \cdot 10^{-13} \\ - & 4.278 \\ - & 14.0 \\ - & 10.076 \end{vmatrix} \begin{matrix} 1 \\ 2; \\ 3; \\ 4 \end{matrix} \quad V_2 = \begin{vmatrix} 0.553 \\ -2.101 \cdot 10^{-8} \\ -0.516 \\ -0.751 \end{vmatrix};$$

$$V_3 = \begin{vmatrix} 0.604 \\ 0.232 \\ 2.343 \cdot 10^{-8} \\ -0.153 \end{vmatrix} \begin{matrix} 1 \\ 2; \\ 3; \\ 4 \end{matrix} \quad V_4 = \begin{vmatrix} 0.63 \\ 0.31 \\ 0.164 \\ -4.678 \cdot 10^{-9} \end{vmatrix} \begin{matrix} 1 \\ 2 \\ 3 \cdot \\ 4 \end{matrix} \tag{15}$$

Using formula (7) and the results (14), there is calculated the value of the critical force "P" for a rod with variable bending stiffness (Figure 1, a), assuming that $k_{min}^2 = k_1^2 = 0/264$ (n=4):

$$P_{cr} = 0.264\ (Y_0)^2 \left(\frac{EI_0}{H^2}\right) = 4.224 \left(\frac{EI_0}{H^2}\right);\ P_{cr} = 4.224 \left(\frac{EI_0}{H^2}\right). \tag{16}$$

The exact value of the critical force for a cantilever rod of variable stiffness with a reduced (average) value of bending stiffness ($\mathrm{E}I_x = 0.5\mathrm{E}I_0$) is equal to [22]:

$$P_{cr}^* = \frac{\pi^2 EI_x}{4e^2} = 2.4674\ \frac{EI_0}{0{,}5H^2} = 4.9348 \frac{EI_0}{H^2};\ P_{cr}^* = 4.9348 \frac{EI_0}{H^2}. \tag{17}$$

Comparing the values (16, 17), we establish that the error of this calculation with the exact one is 14.4%. This error can be reduced by increasing the density of the "linear grid", i.e. by taking n>4.

Based on the values of the eigenvectors (15), the forms of the rod stability loss are constructed (Figure 2).

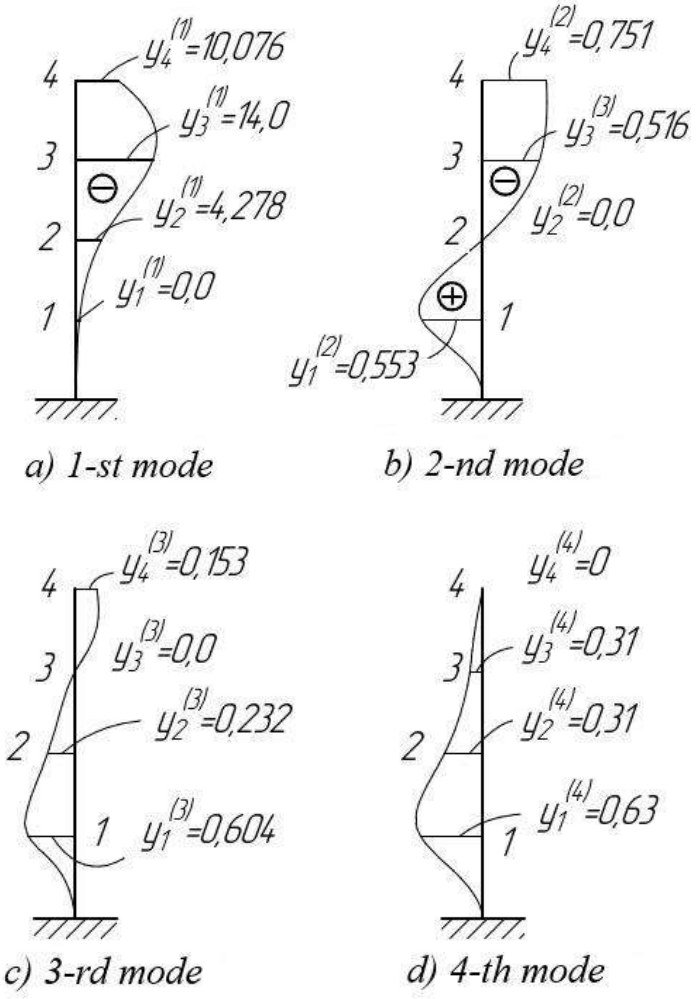

Fig. 2. – The forms of the rod stability loss with variable bending stiffness loss

Figure 2 shows that the higher the stability loss mode, the greater the number of half-waves in the natural vibration modes.

Based on formula (16), a study was conducted of the dependence of the critical load value P_{cr} on changing the ratio of geometric parameters (H/a) (Figure 3).

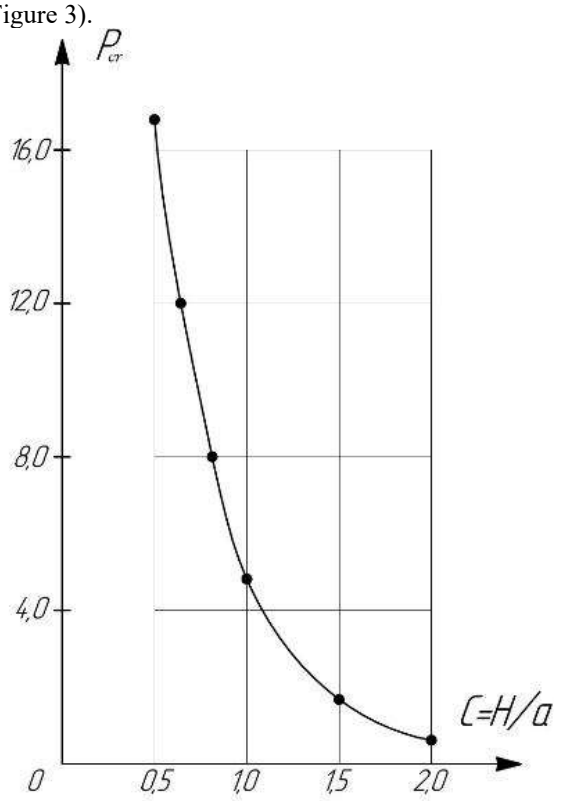

Fig. 3. – Critical load dependence on changing the ratio of geometric parameters

According to Figure 3: with an increase in the height of the rod, the magnitude of the critical load P_{cr} decreases according to a curvilinear relationship.

Conclusions

In this paper, a study is carried out to determine the value of the concentrated force applied to the apex of a triangle for a cantilever rod with variable bending stiffness; the known problem of the uncertainty zone at the apex of the triangle (at the end of the cantilever) is solved in an original way: the original diagram of the rod with real displacements (Figure 1, a) is replaced by a conditional diagram (Figure 1, c), in which the end of the cantilever (node "4") is fixed against displacements.

When using the finite difference method, this approach allows excluding the presence of contour nodes (outside node "4") in the structure of resolving finite difference equations. As an illustrative example, a rod with linearly variable bending stiffness (Figure 1, a) with the number of divisions n = 4 is considered.

The numerical finite difference method was used to determine the critical force (P_{cr}) value and to construct four modes of buckling; the following was established based on the research results:

– the odd (1st and 3rd) modes of buckling have two half-waves; the even (2nd and 4th) modes of buckling have one half-wave; the largest deflections during buckling occur with the 1st mode (Figure 2, a);

– the graph of the critical force P_{cr} dependence on the ratio of geometric parameters (H/a) (Figure 3) shows that with increasing the value of (H/a), the critical force value decreases monotonically, approaching a very small value (for plates with a large height, i.e. those having large bending stiffness).

References

[1] Handbook for designers of industrial and public buildings and structures. Calculation and theory, book 2; edited by A.A. Umansky. - M.: Stroyizdat, 1973. - 416 p.

[2] Fang J., Chen Jen-San Deformation and vibration of a spatial clamped elastica with noncircular cross section //European Journal of Mechanics, 2014, Volume 47, P. 182 – 193.

[3] Zhuo Y., Wang G., Qi Zh., Zhang J. A Spatial Geometric Nonlinearity Spline Beam Element With Nodal Parameters Containing Strains // Applied Mathematics and Mechanics, 2022. Volume 43, Issue 9, P. 987 – 1003.

[4] Shvets A., Murawski K., Fedorov Y. Analytical determination of critical forces during buckling of systems consisting of two pinned connected rods // Meccanica, 2025. 60(2), P. 441-455. DOI 10.1007/s11012-025-01941-3

[5] Ilgamov M. A. Bending and stability of a cantilever bar under the action of pressure on its surface and longitudinal force // Mechanics of Solids, 2021. Volume 56, Issue 4. - P. 495 – 504.
[6] Kozhanov, D.A., Khazov, P.A., Shkoda, I.V., Likhacheva, S.Yu.// Strength and stability of a pipe-concrete column of a high-rise building // Magazine of Civil Engineering, 2024, 17(2),12601. DOI 10.34910/MCE.126.1
[7] Sergey A. Astakhov, Vasiliy I. Biryukov Buckling under the action of loading by aerodynamic and inertial forces during ground track tests of aviation equipment // INCAS Bulletin, 2021. Volume 13 P. 5-12, DOI: 10.13111/2066-8201.2021.13.S.1
[8] Tyukalov Yu.Ya. Refined finite element of rods for stability calculation // Magazine of Civil Engineering, 2018.Volume 79, Issue 3. - P. 54 – 65.
[9] Serpik I. N., Alekseytsev A. V., Balabin P. Yu., Kurchenko N. S. Flat rod systems: Optimization with overall stability control // Magazine of Civil Engineering, 2017.Volume 76, Issue 8, P. 181 – 192.
[10] Simitses G.J., Hodges D.H. Fundamentals of Structural Stability, 2006. - 389 P. DOI 10.1016/B978-0-7506-7875-9.X5000-2.
[11] Brunetti M., Favata A., Vidoli S. Enhanced models for the nonlinear bending of planar rods: localization phenomena and multistability // Proceedings of the Royal Society A: Mathematical, Physical and Engineering Sciences, 2020. Volume 476, Issue 2242.
[12] Ahmadi M., Ansari R., Rouhi H. Studying buckling of composite rods made of hybrid carbon ber/carbon nanotube-reinforced polyimide using multi-scale FEM // Scientia Iranica, 2020. Volume 27, Issue 1 B, P. 252 – 261.
[13] Hasanov A., Rzayev N.S., Gahramanov N.F., Salmanov V. // Experimental and theoretical analysis of rod deflection under compressive loading // International Journal on Technical and Physical Problems of Engineering, 2025. Volume 17, Issue 1, P. 330 – 336.
[14] Rzayev N.S., Aliyev R.D. Planar stability of an elastic, plastic beam differently resisting to tension and compression // International Journal on Technical and Physical Problems of Engineering, 2024. Volume 16, Issue 3, P. 1 – 7.
[15] Yazyev B.M., Yazyev S.B., Grinev A.P., Britikova E.A. // The definition of a critical deflection of compressed rods with the creep by the method of Bubnov-Galerkin //Materials Science Forum, 2018, 931 MSF, P. 127-132. DOI10.4028/www.scientific.net/MSF.931.127
[16] Tyukalov Y.Y. Stability Analysis Method of Flat Rod Systems, Based on Forces Approximations //Lecture Notes in Civil Engineering, 2022. Vol 168, pp. 3-12. DOI 10.1007/978-3-030-91145-4_1
[17] Orobey V., Lymarenko O., Bazhanova A., Khamray V., Ponomarenko A. // Stability of Arched Rod Structural Elements of Machines //Lecture Notes in Mechanical Engineering, 2025. pp. 557-566. DOI10.1007/978-3-031-82746-4_49
[18] Xie, Y., Han, X., Chen, B., Ai, H., Wang, Z. // Study of axial compressive stability of lattice-type attached support // Journal of Constructional Steel Research, 2025. Vol 226, 109311. DOI 10.1016/j.jcsr.2024.109311
[19] Bastos C.C.D.O., Batista E.M. Buckling of spatial laced columns composed of built-up cold-formed channel members // Stability and Ductility of Steel Structures - Proceedings of the International Colloquia on Stability and Ductility of Steel Structures, 2019. pp. 155-163.
[20] Karamanski T.D. Numerical methods of structural mechanics. - M.: Stroyizdat, 1987. - 436 p.
[21] Collection of problems on strength of materials / Edited by Kachurin V.K. - M.: Nauka, 2012. - 368 p.
[22] Akhmediyev S.K., Filippova T.S, Oryntayeva G.Zh., Tazhenova G.D. // Strength Calculation of Variable Bending Rigidity Rods in the Presence of Initial Cambers along Their Axes // Material and Mechanical Engineering Technology, 2024. №4, Vol. 4, P. 51-57.

Information of the authors

Akhmediev Serik Kabultaevich, c.t.s., Associate Professor, Abylkas Saginov Karaganda Technical University
e-mail: s.ahmediev@kstu.kz

Filippova Tatyana Silinyevna, c.t.s., Professor, Abylkas Saginov Karaganda Technical University
e-mail: tsxfilippova@mail.ru

Oryntayeva Gulzhaukhar Zhunuskhanovna, senior lecturer, Abylkas Saginov Karaganda Technical University
e-mail: oryntaeva70@mail.ru

Tazhenova Gulzada Dauletkhanovna, c.t.s., Associate Professor, Abylkas Saginov Karaganda Technical University
e-mail: g.tazhenova@ktu.edu.kz

DOI 10.52209/2706-977X_2026_1_62 **IRSTI 81.09.07** **UDC 611.018.4-089.84**

A Review of Modeling and Preparation of Functionally Graded Materials for Bone Tissue Engineering

Oda Z.A.* , Radhi N.S.
Metallurgical Engineering department, college of Materials Engineering, University of Babylon, Iraq
*corresponding author

Abstract. Functional gradient materials (FGMs) are contemporary materials that mimic the hierarchical and gradient structures of natural systems while performing various functions. Because biomedical implants frequently replace bone tissues, advanced materials are required to replicate the complex structure and mechanical behavior of natural bone. Given that bone is an organic, natural FGM material, it seems reasonable to apply the FGM concept in these applications. FGMs offer numerous benefits, including the ability to customize mechanical and biological responses through composition, porosity, and size. They also reduce stress-shielding effects, improve osseointegration, and enhance electrochemical behavior and wear resistance. Despite these benefits, there is still a need for more detailed norms and standards. This report aims to provide a detailed evaluation of the current state of FGM metallic materials in the biomedical field, specifically their dental and orthopedic applications. The article discusses the influence of various processing technologies, particularly additive manufacturing, on FGM production, including its prospects and potential applications. FGMs have the potential to change the trajectory of both industry and biomedicine. FGMs have the potential to change the trajectory of both industry and biomedicine. Advancements in FGM understanding and technology can lead to improved implant designs that are more biocompatible and comparable to natural tissues, thereby improving human quality of life.

Keywords: functionally graded material (FGM), manufacturing, applications, fabrication, Ti

Introduction

Niino and coworkers proposed the original idea of Functionally Graded Materials (FGMs) in 1987 while working on a space aircraft at Japan's National Aerospace Laboratory. Where a mixture of materials is utilized to create a thermal barrier that can tolerate a surface temperature of 2000 K and a temperature differential of 1000 K over a 10mm section. FGM, also known as "gradient material," is distinguished by a progressive change in material qualities with location. The material's property gradient is caused by its position-dependent chemical composition, microstructure, or atomic order. The geographical extent of the gradients may vary: in a mass FGM, the characteristic change spreads over a large part of the material, whereas in a grade coating or joint, it is restricted to the surface of the material or a small interfacial region. Although FGMs sparked scientific interest toward the close of the twentieth century, these materials are not novel. Living creatures have been exploiting shifts in the structure of materials for millions of years. In many plant structures, microstructural gradients are generated to provide optimal architectural and functional performance with minimal material use contin [1, 2].

The material's selection is critical since it must meet a variety of stringent specifications. It must, among other things, be corrosion-resistant, extremely durable, interact well with tissue cells, have no immunological or allergic reactions, and possess mechanical properties similar to those of human bone. According to these criteria, the most common materials used to make this device are polymers, ceramics, metals, and their alloys [3]. Functionally graded materials are a type of innovative technology that emerged in the twenty-first century. They are composed of a two-component composite whose characteristics are determined by the compositional gradient of one or both components.

In contrast, traditional composites have a homogeneous composition, which means that the composition possesses the ideal characteristics of its constituent components. The need to compromise on qualities is avoided, as the key properties of FGM include the pure structure of each component. Furthermore, the qualities of FGM components can be fully utilized; for example, the refractoriness of ceramic can be combined with the toughness of metal without needing to sacrifice either the toughness of the metal side or the refractoriness of the ceramic side [3].

Mechanical parameters, such as elastic modulus, Poisson's ratio, shear modulus, material density, and thermal expansion coefficient, vary smoothly and continuously in preferred FGM orientations. Due to their diverse qualities, functionally graded materials are utilized in biomedical applications, with several examples of natural functionally graded materials, including bones, teeth, skin, and bamboo trees.

Accidents happen, and important components of our bodies need to be replaced or repaired. At other times, as witnessed on a global scale, the same parts become worn out after a lifetime of service to their host. Thanks to the tireless efforts of several medical experts, scientists, and engineers. However, biocompatible materials, surgical methods, drugs, and antibiotics have been created to successfully treat this condition, dramatically enhancing the quality of life for millions of individuals. Nonetheless, the intricacy of our biological system, including its deep symbiotic interactions with microorganisms, can lead to materials, surgical operations, or therapies failing. These issues, along with longer life spans

and increased societal demands, have led to a compelling need for improvements and the creation of more enhanced products and technologies [5].

The first and most important prerequisite for selecting a biomaterial is its suitability to the live organism. The implanted material should not induce any undesirable consequences, such as allergy, inflammation, or toxicity, either immediately following surgery or throughout the postoperative period. Second, biomaterials must have sufficient mechanical strength to withstand the forces to which they are subjected, preventing them from fracturing. More importantly, a bioimplant should exhibit very high corrosion and wear resistance in a highly acidic body environment and under varying loading conditions, in addition to fatigue strength and fracture toughness [6,7].

The success of a biomaterial or implantation is highly dependent on three major factors: (i) the properties (mechanical, chemical, and tribological) of the biomaterial in question, (ii) the implant's biocompatibility, and (iii) the recipient's health and the surgeon's competency [6,7]. Biomedical material is defined as any substance that has been created to interact with biological structures for medical use, which might be therapeutic (i.e., to treat, enhance, repair, or replace defective tissue in the body) or diagnostic. Metallic materials are commonly employed in biomedical applications due to their strong load-bearing capacity, favorable wear and friction properties, and acceptable biocompatibility [8].

1.Types of Biomaterials

A biomaterial is any natural or artificial material that constitutes all or part of a living building or biomedical device that performs, augments, or substitutes the function of nature [9]. These biomaterials are particularly constructed using the following material classes: polymers, ceramics, metals, and composite materials. Most biomaterials accessible today are produced either alone or in combination with materials from these classes. These types of materials exhibit varied atomic arrangements, resulting in diverse structural, physical, chemical, and mechanical properties, and thus offer a range of potential applications in the body. The sorts of materials are shown in the following parts [10].

Biomaterial is defined as "a nondrug substance suitable for use in systems that enhance or restore the function of body tissues or organs" [11]. Biomaterials are divided into three primary groups based on biocompatibility: bioinert, active, and bioresorbable.

i. Bioinert: These are materials that have limited contact with the surrounding tissue, resulting in osteogenesis. A few examples are steel made from stainless steel, titanium, zirconium, alumina, and ultra-high molecular weight polyethylene.[11]

ii. Bioactive: These are compounds that, once deposited in the mouth cavity, react with both hard and soft tissues. Examples include synthetic hydroxyapatite, glass ceramics, and bioglass.[11]

iii. Bioresorbable: Upon installation, these materials begin to resorb and are gradually replaced with bone. Examples include tricalcium phosphate, polylactic-polyglycolic acid copolymers, calcium oxide, calcium carbonate, and gypsum [12].

Bioinert and bioactive materials are dubbed "osteoconductive" materials because they can function as "scaffolds" for bone formation on their surfaces. [12]. Biomaterials can also be classed chemically into metals, ceramics, and polymers, as follows:

i. Materials: titanium, which is titanium alloys, stainless steel, cobalt chrome alloys, gold alloys, and tantalum.

ii. Ceramics include alumina, hydroxyapatite, beta-tricalcium phosphate, carbon, carbon/silicon, bioglass, zirconium, and zirconia-toughened alumina [13].

iii. Polymers include polymethyl methacrylate, polytetrafluoroethylene, polyethylene, polysulfone, polyurethane, and polyether ketone ether [13].

2. Titanium and titanium alloys

Titanium and titanium alloys. Titanium and titanium alloys are among the most commonly used implant materials in biomedical applications due to their exceptional properties, which include excellent biocompatibility, resistance to bodily fluid effects, high tensile strength, flexibility, and corrosion resistance [14]. Titanium and its alloys possess a unique combination of strength and biocompatibility, rendering them suitable for various medical applications. For example, a key problem in orthopedic biomaterials is designing material surfaces that offer excellent osseointegration while also promoting implant longevity. After more than 50 years of employing biomaterials as implant materials [15] (metals: stainless steel, cobalt alloys, titanium alloys; ceramics: aluminum and zirconium oxides, calcium phosphates, synthetic and natural polymers), titanium and titanium alloys continue to be regarded as one of the most appealing and significant materials due to exceptional features like as resistance to bodily fluid effects, high tensile strength, flexibility, and corrosion resistance. This unique combination of strength and biocompatibility makes them ideal for medical applications [16,17]. In dental implants, commercially pure titanium (c.p. Ti) is prevalent, whereas Ti-6Al-4V is more commonly used in orthopedics. When assessing the desired biomedical use, the alloy composition must be examined to provide both biocompatibility and mechanical strength. Dental titanium alloys include Ti-6Al-7Nb, Ti-6Al-4V, Ti-13Cu-4.5Ni, Ti-25Pd-5Cr, and Ti-20Cr-0.2Si [18].

Ti-6Al-4V alloy was replaced in permanent implants with Ti-6Al-7Nb, Ti-13Nb-13Zr, and Ti-12Mo-6Zr [17] due to the potentially harmful consequences of vanadium or aluminum leaching. Extensive research has been conducted to determine the optimal surface topography for use in biotechnological applications [19]. In recent years, research on

materials for biomedical applications has shifted from microtopography to nano topography [20-22]. As a result, the current focus is on the application or testing of nanotechnology for biomedical purposes. A recent study found that titanium implants with rough surface topography and free energy promote osteoblast adhesion, maturation, and eventual bone formation [18].

Furthermore, the surface properties of titanium implants impact the adherence of various cell types. Titanium, namely topography, charge distribution, and chemistry [23, 24]. As the focus of biomaterials shifted to tissue engineering, complex medical applications, and biotechnology, it became necessary to identify and analyze the unique interactions between biomaterials and tissue components. Following a thorough examination of the biomaterials sector at the time, Williams [16] presented a unified notion of biocompatibility. This unified concept is as follows: "Biocompatibility refers to the ability of a biomaterial to perform its desired function about medical treatment, without producing any not desirable systemic or local effects in the recipient or beneficiary of that therapy, but generating the most appropriate beneficial cellular or tissue response in that particular scenario, and optimizing the clinically relevant performance of that therapy [16]. Titanium and its alloys are physiologically stable or inert [25], meaning they remain virtually unchanged when implanted in human bodies. However, titanium has limited wear and abrasion resistance because of its low hardness, which may result in a shorter service life for the implants. This difficulty can be significantly alleviated by using an appropriate surface modification approach [18].

One important factor to consider is that the fate of the implant material is determined by both the bulk of the material (which is critical in determining biological performance) and its surface properties (including surface chemistry and structure), with the latter being a crucial factor in the material's interactions with the surrounding tissue. The bulk material should be able to sustain high stress (too high for ceramic and polymeric materials, but possible for metallic materials). Nonetheless, the biomaterial's surface qualities do not allow for a permanent attachment between the implant surface and surrounding tissue. In that case, a fibrous layer may form, undermining load transfer at the bone-implant interface. In that case, micro-movements will be preferred, which can lead to implant failure [26].

The reaction of the titanium biomaterial is entirely dependent on its biocompatibility and surface characteristics. As a result, to enhance the performance of these biomaterials in biological systems, their surfaces need to be modified [27]. Improvements can be represented by: i) morphological modifications (increasing roughness, shifting topography from micro- to nanoscale, and tailoring the nanoscale morphology) caused by mechanical [28], chemical, and physical methods [27-30]; ii) modification with coatings based on hydroxyapatite, biomimetic calcium phosphate coatings, or hybrid coatings. Organic components and calcium phosphate minerals), or biomolecule functionalized coatings; or iii) a mixture between morphological changes and coatings for a combined synergistic effect.

The overall objective is to enhance the bioactivity, biocompatibility, blood compatibility, wear resistance, and corrosion resistance of titanium and titanium alloys for their intended applications. Of the aforementioned strategies, nanoscale surface tailoring produced breakthrough results, namely that roughness alone affects osteoblast cell adherence, spreading, and proliferation on titanium nanostructures [22,31]. The high surface energy of nanoscale surfaces enables an elevated initial amount of protein adsorption, which is critical for controlling cellular interaction at the implant surface. Surface characteristics influence cell adhesion, and charge distribution and material chemistry [32,33] may have an additional impact. With the rise of the tissue engineering and nanotechnology sectors, surface modification of implants has become necessary to promote tissue adhesion and implant integration while minimizing bacterial adhesion and inflammation. Response, or avoid the foreign body response. Summary and remarks concluding.

3.Functionally Graded Materials (FGMs)

Two distinct criteria are utilized to classify functionally graded materials. The first is based on material structure, while the second is based on the size of functionally graded materials. Figure 2 illustrates that functionally graded materials can be categorized into two broad classes based on their material structure: FGMs exhibit both continuous and discontinuous structures. Continuous FGM has a continuous gradient from one material to another. However, in the case of discontinuous FGM, the material gradient is stacked. FGMs are divided into two categories based on their material size: thin FGM and bulk FGM. Thin FGMs have relatively thin parts, such as surface coatings, whereas bulk FGMs are complete. Volume of materials. Thin FGM is manufactured using technologies like physical vapor deposition (PVD), chemical vapor deposition (CVD), and self-propagating high-temperature synthesis (SHS). Bulk FGMs are produced utilizing processes such as powder metallurgy, centrifugal casting, and solid freeform/additive manufacturing procedures.

Functionally graded materials have established themselves as a prominent category among contemporary, sophisticated materials. They were fierce competitors in a wide range of applications, particularly in the energy, military, aviation, and medical sectors. The growing interest in FGMs in the scholarly and industrial areas necessitates the establishment of many classifications from various perspectives. These provide more insight into the link between FGM qualities, processing approaches, level of control, and cost. This publication provided a critical assessment of several classification methods. Used in the field of FGM. These examined the merits and limits of the classified groupings from several engineering perspectives. Designers and manufacturers proposed new classifications for FGM production methods based on product form and wall thickness, control over gradient properties, residual stresses, equipment and manufacturing costs, energy consumption, and environmental impact over the entire life cycle. Some areas were identified as obstacles for FGMs on an industrial scale, including material modeling, numerical simulation, systematic selection and

design procedures, and an FGM data bank. The adaptability to mass manufacturing, process repeatability, dependability, and cost-effectiveness are among the future frontier for FGMs. Types of Functionally Gradient Materials (FGMs)

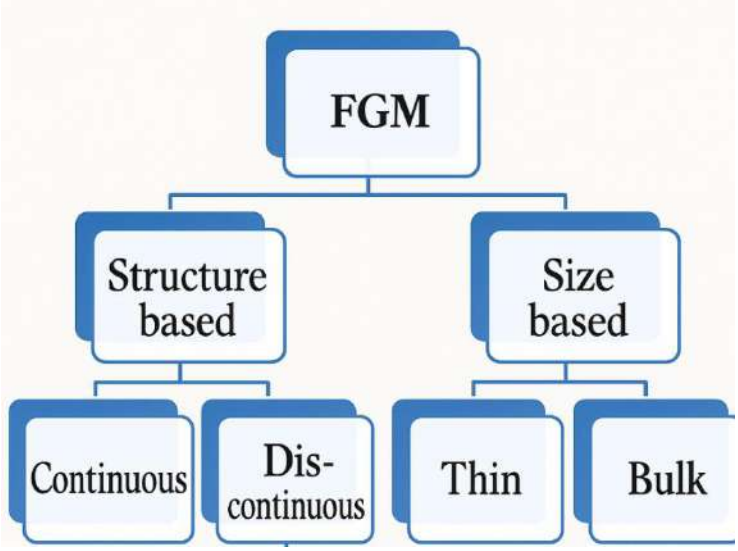

Fig. 1. - Classification of Functionally Gradient Materials [34].

4. Methods of producing FGM

There are several approaches for producing functionally graded materials (FGMs). A few of these are discussed in further depth below.

1. Vapour deposition technique

Vapor deposition techniques refer to a range of vacuum deposition procedures used to form thin films on base materials. All of these procedures may be utilized to create thin FGMs exclusively. There are two types of vapor deposition techniques: physical vapor deposit (PVD) and chemical vapor deposition (CVD). These are energy-intensive and create hazardous byproducts [35]. Other deposition-based processes capable of depositing thin, functionally gradient coatings include electrostatic deposition (ED), ion beam deposition (IBD), and self-propagating high-temperature synthesis (SHS) [36]. All of the aforementioned methods are uneconomical to produce bulk-type FGMs.

2. Powder metallurgy

Powder metallurgy-based techniques can be utilized to create bulk-type FGMs with a discontinuous (stepwise) structure. The process is carried out in several steps, including weighing and mixing powder according to a pre-designed spatial distribution based on functional requirements, stacking and ramming premixed powders, and, finally, sintering [37].

3. Centrifugal technique.

The centrifugal process is capable of producing continuously structured bulk-type FGMs. It produces functionally graded materials by spinning a mold using gravity [38]. FGMs are formed when material densities differ and a mold is spun. There are two drawbacks to this method: it can only manufacture cylindrical-shaped FGMs and has a restriction on the sort of gradient that can be formed.[38].

4. Techniques for additive manufacturing (AM) and solid free-form fabrication

Solid freeform fabrication (SFF)/Additive manufacturing (AM), often referred to as 3D printing, is a technique that involves connecting materials to create items from 3D model data, typically layer by layer, as opposed to subtractive manufacturing technology [39]. This toolless manufacturing process can make completely dense metallic pieces quickly and precisely. Metal AM methods are widely categorized into two types: Powder Bed Fusion (PBF) and Directed Energy Deposition (DED) technologies. Both of these technologies can be further divided according to the energy source employed. Thermal energy is utilized in PBF-based technologies to fuse portions of the powder bed selectively. The two primary typical methods are select laser sintering/melting (SLS/SLM) and electron beam melting (EBM). PBF-based technology. DED-based technologies utilize concentrated heat energy to melt and fuse materials (in powder or wire form) as they are deposited. Some of the most prominent DED-based technologies include Laser Engineered Net Shaping (LENS)/Direct Metal Deposition (DMD), Electron Beam Free Form Fabrication (EBFFF), and arc-based Additive Manufacturing (AM). Most of the SFF/AM processes discussed above may generate functionally gradient materials (FGMs), ranging from thick coatings to complex FGM bulk pieces.[39] The advantages of AM methods, including improved material utilization, faster production, design flexibility, the ability to produce complex components, and lower energy intensity, are generating significant interest in producing FGMs for various purposes. Powder bed fusion (PBF)--based AM methods such as selective laser melting (SLM) and electron beam melting (EBM) are extremely popular. Methods for producing complicated parts owing to their high accuracy and surface finish as compared to directed energy

deposition (DED) based technologies. However, PBF-based technologies are less flexible than DED-based technologies in terms of functionally gradient material manufacturing because it is not possible to vary the material gradient by changing the chemical composition of the powder. However, these technologies may enable bulk FGMs by regulating porosity or incorporating various forms of lattice structures into the components to be manufactured. Directed energy deposition (DED) based additive manufacturing (AM) techniques are the most convenient for producing functionally graded materials (FGMs) because they can manufacture FGMs from thick coatings to bulk sections with continuous or discontinuous gradients. These techniques can create FGMs with superior adhesion and mechanical properties compared to powder bed technologies. Laser metal deposition (LMD) and electron beam free form deposition (EBFFF)/electron beam additive manufacturing (EBAM) are prominent technologies based on DED-based additive manufacturing (AM) equipment that can be utilized to produce various functionally graded materials (FGMs) [39].

5.Laser Metal Deposition (LMD)

The primary techniques based on DED technology are laser-engineered net shaping (LENS) and direct metal deposition (DMD), which employ a laser beam as a power source and powder as the raw material. The LENS method was developed by Sandia National Laboratories in 1997 and later licensed to Optomec (USA), whereas the DMD technique was jointly developed by the POM group and the University of Michigan [40, 41]. In this method, a high-power laser beam is used to form a molten pool on the base material and powder material is fed into the molten pool through nozzles. Powder delivered to the laser beam point is absorbed into the melt pool, resulting in a deposit on the surface. Figure 3 illustrates that the worktable can be moved in the x-y direction to obtain a desired cross-section of the sliced model, and subsequent layers can be deposited by incrementing the deposition head in the z-direction to complete the object. Deposition of layers is repeated until the desired three-dimensional component has been additively formed. Metal powder is delivered through nozzles and distributed around the circumference of the deposition head either by gravity or by using an inert carrier gas. The entire process is conducted under a controlled argon atmosphere where oxygen levels are maintained below 10 ppm [40, 41].

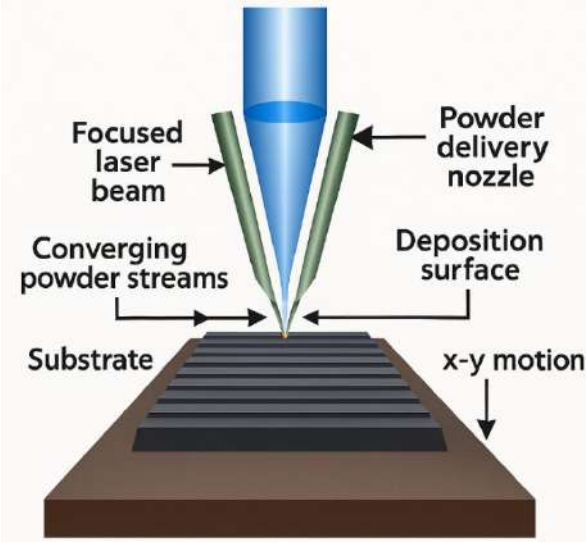

Fig. 2. - Basic laser-engineered net shaping procedure [42].

The laser-based Directed Energy Deposition (DED) approach in metal additive manufacturing (AM) is the most suitable technology for producing Functionally Graded Materials (FGMs). All varieties of FGMs, including continuous/discontinuous structured and thin/bulk types, may be readily fabricated using laser metal deposition (LMD). Pre-alloyed powders can be used to create discontinuous FGM. At the same time, elemental powders may be fed in exact proportions to the melt zone via different feeders to produce various alloys and composite materials in a continually graded method. With the use of this approach, the number of FGMs can be manufactured into complicated forms, as the rate of elemental powder deposition can be regulated for each feeder during fabrication for each layer. The final product can be obtained within hours [43].

6.Direct production using electron beams

Electron Beam Direct Deposition (EBDM) is another directed energy deposition (DED) process that employs an electron beam as a power source and wire as the raw material. Sciaky (Chicago, USA) developed this method, also known as electron beam additive manufacturing (EBAM). This technology can manufacture medium to large-sized near-net-shaped components within a vacuum chamber that are directly used as deposition material. The basic electron beam

system includes a Sciaky 60 kW/60 kV welder. The electron beam is electrically focusable, and the output power is scalable across a wide range, which allows for a wide range of deposition rates to be obtained with the same apparatus. The typical deposition rates of EBAM systems range from 3 to 9 Kgs/hrs, depending on the material used and part complexity. Additionally, the EBAM system features a closed-loop control system in which the melt pool size is continuously monitored, and parameters are adjusted to maintain a constant size, ensuring consistent part geometry, uniform microstructure, and mechanical properties.

Fig. 3. - Electron beam additive manufacturing using twin wire deposition [44].

EBAM technology may also manufacture a variety of functionally graded materials (FGMs) by connecting numerous wire feed nozzles to a single EB gun. Two or more wires of various metal alloys can be controlled individually and fed into a single molten pool to generate graded materials. Both coating and bulk FGMs can be generated in a continuous or discontinuous way.

FGMs are created using arc deposition technology. A wide range of arc-based additive manufacturing technologies are available, using arc (plasma, TIG, MIG) as the power source and material in the form of powder or wire. Plasma transferred arc (PTA) and plasma arc welding (PAW) are free from additive manufacturing (AM). Methods that employ plasma arc as a power source and raw material in the form of powder and wire, respectively. Shaped metal deposition (SMD) is another additive manufacturing (AM) technology that employs tungsten inert gas (TIG) or metal inert gas (MIG) welding with wires to create free-form fabrications. Because most of these systems involve wire-fed, they are also known as wire-assisted additive manufacturing (WAAM) systems. A wide range of system configurations can be created by combining traditional welding methods with robots, manipulators, or gantries for automation. All of these techniques, with suitable inert gas shielding, offer a high potential for producing near-net-shaped medium to large-sized components at a far cheaper cost than laser and electron beam-based procedures.

Several welding-based additive manufacturing (AM) techniques have been developed to deposit functionally graded materials. In this example, two filler wires are controlled independently and fed into the arc (TIG or MIG) for deposition. Several experiments have been conducted to establish the efficacy of arc-based additive manufacturing (AM) setups for producing functionally graded materials (FGMs). Sajan Kapil et al. [45] effectively synthesized an Al-Si alloy with varying thermal conductivity. It was built utilizing a hybrid layered manufacturing machine (HLM), which combines a three-axis CNC with a gas metal arc welding (GMAW) deposition technology. S. Suryakumar et al. [46] proposed two methods for fabricating functionally graded materials using weld deposition. FGMs can be created by altering process parameters or by employing a twin-wire feeder that can be guided and controlled independently.

Processing Techniques for FGMs

The manufacturing process of an FGM is typically separated into two stages: constructing the Gradation, which involves transforming an inhomogeneous structure into a bulk substance, also known as consolidation, and then forming the Gradation. Gradation processes are categorized into three types: constitutive, homogenizing, and segregating. Constitutive processes begin with precursor materials or powders and gradually develop into a graded structure. [47]

Automation advancements in recent decades have made constituent grading methods more highly advanced. Economically feasible. Homogenizing processes transform a sharp contact between two materials into a gradient by material transfer. Segregating processes begin with a homogenous substance that is transported to a graded state by an external source, such as gravity or electricity. Homogenizing and segregating processes result in continuous gradients, but they have their limits. Different gradients can be made. After grading, the material is often dried, sintered, or solidified. Consolidation techniques for FGMs require careful consideration of processing conditions to prevent uncontrolled destruction or alteration of the gradient.[47]

FGMs may shrink unevenly during free sintering. To optimize sintering behavior, it is important to consider factors such as porosity, particle size, shape, and content of the powder mixture. Each material combination and gradient type should be addressed separately, taking into account the current understanding of sintering mechanisms [47].

Surface coatings are often used for thin, functionally graded materials, with many deposition techniques available. Service requirements vary based on the procedure.[47] There are many applications for functionally graded materials (FGMs), and below are some of them:

1. Aerospace

(FGMs) are used in aerospace industries due to their ability to withstand high thermal gradients, making them suitable for structures such as airplane bodies, rocket motor components, and other space applications [48].

2. Medical

The human body contains many tissues that are classified as natural functionally graded materials, such as teeth and bones. During accidents, human tissues suffer damage, and in most cases, these damages are irreversible, necessitating the use of alternative parts to replace them. According to [49], functionally graded materials may be used in the medical field to replace damaged tissues, such as teeth and bones, with biomedical materials [50-52].

3. Defense

The qualities of functionally graded materials are widely recognized, and they have an exceptional capacity to prevent fractures from propagating. These properties enable the use of these materials in defense, particularly to shield soldiers from firearms through the production of armor plates and bullet-proof vests [53].

4. Energy

According to [(Müller et al., 2003) and (Niino et al., 2005), functionally graded materials (FGMs) are used to generate energy because they are used to produce solar power, devices for energy conversion, and as thermal protection to protect the coating of the turbine blades in gas turbine motors [54-55].

5. Optoelectronic

Due to their graded refractive index, functionally graded materials can be utilized in the field of optoelectronics, such as low-threshold current edge lasers (GRINSCH), storage media, notably magnetic discs (audio-video), and tunable photodetectors [56].

6. Construction

The construction sector faces several issues related to material performance, material costs, and environmental impacts. Additionally, the variation in building structure functionality with location opens the door to the use of functionally graded materials (FGMs) in the construction sector [57]. When employing (FGMs), the structure and content of materials will progressively vary across the volume, resulting in diverse material characteristics [58].

7. Other applications

Furthermore, (FGMs) might be used as foundation materials in a variety of industries, including cutting tool coating [59]. Components of vehicle engines, components of nuclear reactors, turbine blades, heat exchangers, fire sensors, tribology (advanced materials), fire retardant doors, and many more applications. All of these applications are emerging as a result of lower manufacturing costs and the ability to regulate and improve the characteristics of FMGs [60].

IN (2016) A. Kumar et al. [61] This article explores the link between method, structure, and property in implantable biomaterials utilizing additive manufacturing-based rapid prototyping techniques. Traditional procedures, such as freeze casting and sintering, are limited due to adaption difficulties and incompatibilities with host tissues. Additive manufacturing provides the benefit of Creating patient-specific designs. The article examines 3D printing scaffolds for tissue regeneration, focusing on their biocompatibility and mechanical properties. It also covers functionally graded scaffolds and the vascularization of 3D porous scaffolds to fulfill biomedical industry standards. Functionally graded 3D structures with excellent strength and energy absorption are appealing.

In 2017, Dalia Mahmoud et al. [62] This research examined the use of additive manufacturing (AM) technology to create orthopedic implants from lattice structures and functionally graded materials. It investigates the benefits of these technologies, their design flexibility, and the obstacles associated with their implementation. It also examines current case studies and proposes future research areas to improve their usage in orthopedic implants.

In (2018) Ezgi Onal 1, et al. [63]. Functionally graded lattice structures from additive manufacturing show promise for bone tissue engineering. However, the relationship between mechanical qualities and biological reactions remains unclear. Creating continuous gradient structures and examining their mechanical and biological properties may help enhance orthopedic implant design and establish standards for these materials. The best gradient structures must have small pores in the core for increased strength and large pores for enhanced cell penetration and proliferation.

In 2019, Qifeng Jiang et al. [64] This article assessed the biomechanical response and stress distribution of a new disc prosthesis made from functionally graded polymers (FGP). The kinetics of FGP parameters are based on experimental data from linear ethylene copolymers. The findings suggest that FGP parameters can be customized to manage stiffening, non-linear behavior, inelastic effects, and stress distribution, thereby paving the way for patient-specific FGP prostheses utilizing 3D printing technology.

(2020), Syed Saad Bin Qasim et al. [65]. Researchers are working on innovative treatment ways to restore damaged tissue structure and function. Current synthetic biomaterials are basic when compared to natural ones; however, the capacity to include biologically inspired features has improved. Functionally graded materials mimic natural tissue shapes, resulting in a more pronounced reaction.

On targeted tissue. This review provides an overview of spatiotemporal arrangement in clinical dentistry, ranging from additive manufacturing to conventional techniques.

In 2021, Douglas Fabris et al. [66] employed the finite element technique (FEM) to compare the biomechanical behavior of one-piece zirconia implants with a functionally graded bioglass (BG) layer to that of monolithic zirconia and BG-coated implants. Zirconia disks were infiltrated with bioglass S53P4 and examined morphologically using a scanning electron microscope (SEM). The study found that BG coating resulted in a 30% reduction in stress in the implant body compared to monolithic zirconia implants. The BG-graded system demonstrated improved overall biomechanical behavior, indicating that these enhancements should be paired with the osseointegration benefits of bioactive glasses.

In (2022) Ganesh Kumar Sharma et al. [67]. Biomechanics employs mechanical principles to simulate biological tissues, and recent advances in additive manufacturing (AM) have enabled the production of functionally graded biomaterials for orthopedic bone replacements and implants. However, no functionally graded buildings have been 3D printed using biodegradable materials. This work utilizes computational and analytical tools to calculate the mechanical behavior of biomaterials composed of repeating unit cells, with a focus on the bi-pyramid hexagonal lattice structure. The Timoshenko beam theory was discovered to be closer to numerical values.

In (2023), Amir Najibi et al. [68]. This study investigates the application of Functionally Graded Materials (FGMs) and coatings in orthopedic implants to mitigate stress shielding and prevent loosening. It proposes two areas of research: 1) FGM manufacturing technologies and 2) design and optimization of knee and hip arthroplasty components. The study emphasizes the importance of optimal design for long-span goods and recommends incorporating 2D and 3D FGMs into the design of TKA and THA.

In 2024, Mohaddeseh Fatemi et al. [69] investigated the use of functionally graded materials (FGM) in dental implants to increase biocompatibility, fracture toughness, and wear resistance. Porous FGM implants are proposed to minimize stress shielding while improving bone ingrowth properties. To investigate material characteristics and stress transmission, the researchers employ ABAQUS software's UMAT subroutines and parametric analysis. The study discovered that porous FGM implants can achieve early stability when compared to pure titanium implants. This study fills a gap in FGM implant research and may be beneficial in dental implant design.

Conclusion

In conclusion, Functionally Graded Materials (FGMs) represent a promising class of advanced materials with significant potential in biomedical and engineering applications. Their ability to tailor mechanical and biological properties makes them particularly suitable for bone tissue engineering. Although production costs remain a limitation, advances in additive manufacturing - especially Directed Energy Deposition (DED) technologies -offer practical pathways toward cost reduction and large-scale implementation. Future research should focus on material modeling, optimization, and clinical translation to fully exploit the capabilities of FGMs.

References

[1] Yamanouchi M., Hirai T., Shiota I., “Proceedings of First International Symposium on Functionally Gradient Materials”, FGM Forum, Tokyo, 1990, Japan.
[2] Lannutti J., Compos. Eng. 4 (1994) 81
[3] Hao Y., Zhang W., and Ji X., Nonlinear Dynamic Response of Functionally Graded Rectangular Plates under Different Internal Resonances. Mathematical Problems in Engineering, 2010, pp.1-12, 2010.
[4] Koizumi, M. and Niino, M., Overview of FGM research in Japan. Mrs Bulletin, 20(1), pp.19-21, 1995.
[5] T Albrektsson, P.I. Brånemark, Hans-Arne Hansson and Lindström JJ Osseointegrated titanium implants. Requirements for ensuring a long-lasting, direct bone-to-implant anchorage in man. 1981. 52(2): p. 155-170.
[6] Manivasagam, G., D. Dhinasekaran, and A.J.R.p.o.c.s. Rajamanickam, Biomedical implants: corrosion and its prevention-a review. Materials Science, 2010.
[7] Bedi, R.S., et al., Biocompatibility of corrosion-resistant zeolite coatings for titanium alloy biomedical implants. Acta Biomaterialia, 2009. 5(8): p. 3265- 3271.
[8] Tsou, H.K. and P.Y.J.A.o. T.D. Hsieh, Anticorrosive, antimicrobial, and bioactive Titanium Dioxide coating for surface-modified purposes on biomedical material. 2017: p. 103-22.
[9] Priyadarshini, B., Bioactive coating as a surface modification technique for biocompatible metallic implants: a review.Journal of Asian Ceramic Societies, 2019. 7(4): p. 397-406.
[10] Lorenzetti, M., The influence of surface modification on bacterial adhesion to titanium-based substrates. ACS Applied Materials & Interfaces, 2015. 7 :)3(p. 1644-1651.
[11] Heness, G. and B. Ben-Nissan, Innovative bioceramics. In Materials forum, 2004, VOL. (27) 104 – 11.
[12] Osman, R.B. and M.V.J.M. Swain, A critical review of dental implant materials with an emphasis on titanium versus zirconia. Journal Materials (Basel), 2015, 11(3): p. 932-958.
[13] Muddugangadhar, B., et al., Biomaterials for dental implants: An overview. International Journal of Oral Implantology and Clinical Research, 2011. 2(1): p. 13-24 [14] Roy P, Berger S and Schmuki P 2011 Angew. Chem. Int. Ed. 50 2904
[14] Mihov D and Katerska B 2010 Trakia J. Sci. 8 119
[15] Williams D 2008 Biomaterials 29 2941
[16] Elias C N, Lima J H C, Valiev R and March M M A 2008 JOM 60 46
[17] Geetha M, Singh A K, Asokamani R and Gogia A K 2009 Prog. Mater. Sci. 54 397

[18] Anil S, Anand P S, Alghamdi H and Jansen J A 2011 Dental implant surface enhancement and osseointegration Implant Dentistry—A Rapidly Evolving Practice (Rijeka: InTech) p 83
[19] Park J and Lakes R S 2007 Biomaterials 3rd ed (New York: Springer)
[20] Bauer S, Park J, Faltenbacher J, Berger S, Von der Mark K and Schmuki P 2009 Integr. Biol. 1 525
[21] Park J, Bauer S, Von Der Mark K and Schmuki P 2007 Nano Lett. 7 1686
[22] Gongadze E and Iglič A 2012 Bioelectrochemistry 87 199
[23] Gongadze E, Velikonja A, Perutková Š, Kramar P, Maček-Lebar A, Kralj-Iglič V and Iglič A 2014 Electrochim. Acta 126 42
[24] Williams D 2001 Titanium for Medical Applications ed D M Brunette, P Tengvall, M Textor and P Thompson (Berlin and Heidelberg: Springer-Verlag) p 13
[25] Mas-Moruno C, Espanol M, Montufar E, Mestres G, Aparicio C, Javier G F and Ginebra M 2013 Bioactive ceramic and metallic surfaces for bone engineering Biomaterials Surface Science (New York: Wiley) pp 337–74
[26] Li Y, Yang C, Zhao H, Qu S, Li X and Li Y 2014 Materials 7 1709
[27] Liu X, Chub P and Dinga C 2004 Mater. Sci. Eng. 47 49
[28] Bagno A and Di Bello C 2004 J. Mater. Sci. Mater. 15 935
[29] Kim K and Ramaswani N 2009 Dent. Mater. J. 22 28 20
[30] Bauer S, Schmuki P, von der Mark K and Park J 2013 Progress in Materials Science 58 261
[31] Puckett S, Taylor E, Raimondo T, and Webster T 2010 Biomaterials 31 706
[32] Dale G, Hamilton J, Dunlop P, Lemoine P, and Byrne J 2009 J Nanosci. Nanotechnol. 9 4215.
[33] Mahamood R, Akinlabi E, Shukla M, and Pityana S 2012 Functionally graded materials: An overview Proceedings of the World Congress on Engineering 2012 Vol.3, WCE, London, U.K.
[34] J. F. Groves, and H. N. G. Wadley 1997 Functionally graded materials synthesis via low vacuum directed vapor deposition Composites Parts B 28B, (1997), 57-69.
[35] R. Knoppers, J. W. Gunnink, J. Van den Hout, and W. VanVliet The reality of functionally graded material products TNO ScienceandIndustry, The Netherlands, pp 38-43.
[36] Zhu J, Lai Z, Yin Z, Jeon J, and Lee S Fabrication of ZrO2–NiCr functionally graded material by powder metallurgy Materials Chem. Phys. 68 130. Crossref.
[37] Watanabe Y, Inaguma Y, Sato H, and Miura-Fujiwara E 2009 Novel fabrication method for functionally graded materials under centrifugal force: the centrifugal mixed-Powder method Materials, Vol. 2, No. 4, pp.2510-2525.
[38] Bhavar V, Kattire P, Patil V, Khot S, Gujar K, Singh R 2014 A Review on Powder bed fusion technology of metal additive manufacturing AMSI Conference 2014, Banglore, India.
[39] Ruan J, Sparks T, Fan Z, Stroble J, Panackal A and Liou F 2006 A Review of Layer Based Manufacturing Processes for Metals Solid freeform fabrication symposium, January 2006.
[40] Thymianidis M, Achillas C, Tzetzis D, Iakovou E, Pariente F, Guagliano M. 2012 Modern Additive Manufacturing Technologies: An Upto-Date Synthesis and Impact on Supply Chain Design", 2nd International conference on supply chains, October -2012.
[41] Hedges M., Calder N 2006 Near Net Shape Rapid Manufacture & Repair by LENS Cost Effective Manufacture via Net-Shape Processing, pp. 13-1 – 13-14. Meeting Proceedings RTOMP-AVT-139, Paper 13. Neuilly-sur-Seine, France: RTO. Available from: http://www.rto.nato.int/abstracts.asp
[42] Popoola P, Farotade G, Fatoba G, and Popoola O, Zlatanovic M 2016 Laser Engineering Net Shaping Method in the Area of Development of Functionally Graded Materials (FGMs) for Aero Engine Applications - A Review, from "Fiber Laser", book edited by Mukul Chandra Paul, ISBN 978-953-51-2257-9Chapter 17
[43] (2014) SLM Solution website [online], available at www.sciaky.com, accessed January 2017.
[44] Kapil S, Kulkarni P, Karunakaran K, Joshi P 2014 Development and Characterization of Functionally Graded Materials Using Hybrid Layered Manufacturing 5th International & 26th All India Manufacturing Technology, Design and Research Conference (AIMTDR 2014)
[45] Suryakumar S, Somashekara M 2013 Manufacture of functionally gradient materials using weld-deposition Solid Free. Fabr. Symp. (2013) 1-36
[46] Bhaskar K, Varadan TK. Assessment of the self-consistent scheme approximation: conductivity of composites. ASME J Appl Mech 2001;68(4):660–2
[47] Marin, L., Numerical solution of the Cauchy problem for steady-state heat transfer in two-dimensional functionally graded materials. International Journal of Solids and Structures, 42(15), pp.4338-4351, 2005.
[48] Radhi N.S., Preparation, Characterization, and Modeling Functionally Graded Materials in Bioapplication. PhD thesis. University of Technology. Iraq, 2015.
[49] MATSUO, S., WATARI, F. and OHATA, N., Fabrication of a functionally graded dental composite resin post and core by laser lithography and finite element analysis of its stress relaxation effect on tooth root. Dental materials journal, 20(4), pp.257-274, 2001.
[50] Pompe, W., Worch, H., Epple, M., Friess, W., Gelinsky, M., Greil, P., Hempel, U., Scharnweber, D. and Schulte, K., Functionally graded materials for biomedical applications. Materials Science and Engineering: A, 362(1-2), pp.40-60, 2003.
[51] Watari F., Yokoyama, A., Omori, M., Hirai, T., Kondo, H., Uo, M. and Kawasaki, T., Biocompatibility of materials and development to functionally graded implant for bio-medical application. Composites Science and Technology, 64(6), pp.893-908, 2004
[52] Lu, L., Chekroun, M., Abraham, O., Maupin, V. and Villain, G., Mechanical properties estimation of functionally graded materials using surface waves recorded with a laser interferometer. NDT & E International, 44(2), pp.169-177, 2011.
[53] Müller, E., Drašar, Č., Schilz, J. and Kaysser, W.A., Functionally graded materials for sensor and energy applications. Materials Science and Engineering: A, 362(1-2), pp.17-39, 2003.
[54] Niino, M., Kisara, K. and Mori, M., Feasibility study of fgm technology in space solar power systems (ssps). In Materials Science Forum (Vol. 492, pp. 163-170). Trans Tech Publications, 2005.

[55] Bharti, I., Gupta, N. and Gupta, K., Novel Applications of Functionally Graded Nano, Optoelectronic and Thermoelectric Materials. International Journal of Materials, Mechanics and Manufacturing, pp.221-224, 2013.
[56] Craveiro, F., de Matos, J.M., Bártolo, H. and Bártolo, P., An innovation system for building manufacturing. In ASME 2012 11th Biennial Conference on Engineering Systems Design and Analysis (pp. 175-179). American Society of Mechanical Engineers, 2012 July.
[57] Craveiro F., Matos J.M., Bártolo H. and Bártolo P.J., September. Automation for building manufacturing. In Innovative Developments in Virtual and Physical Prototyping: Proceedings of the 5th International Conference on Advanced Research in Virtual and Rapid Prototyping, Leiria, Portugal, 28 September-1 October, 2011 (p. 451). CRC Press, 2011.
[58] Xing, A., Jun, Z., Chuanzhen, H. and Jianhua, Z., Development of an advanced ceramic tool material—functionally gradient cutting ceramics. Materials Science and Engineering: A, 248(1-2), pp.125-131, 1998.
[59] Malinina, M., Sammi, T. and Gasik, M.M., Corrosion resistance of homogeneous and FGM coatings. In Materials Science Forum (Vol. 492, pp. 305-310). Trans Tech Publications, 2005.
[60] Kumar, A., Nune, K. C., Murr, L. E., & Misra, R. D. K. (2016). Biocompatibility and mechanical behaviour of three-dimensional scaffolds for biomedical devices: process–structure–property paradigm. International Materials Reviews, 61(1), 20-45.
[61] Mahmoud, D., & Elbestawi, M. A. (2017). Lattice structures and functionally graded materials applications in additive manufacturing of orthopedic implants: a review. Journal of Manufacturing and Materials Processing, 1(2), 13.
[62] Onal, E., Frith, J. E., Jurg, M., Wu, X., & Molotnikov, A. (2018). Mechanical properties and in vitro behavior of additively manufactured and functionally graded Ti6Al4V porous scaffolds. Metals, 8(4), 200.
[63] Jiang, Q., Zairi, F., Frederix, C., Yan, Z., Derrouiche, A., Qu, Z., ... & Zairi, F. (2019). Biomechanical response of a novel intervertebral disc prosthesis using functionally graded polymers: a finite element study. Journal of the Mechanical Behavior of Biomedical Materials, 94, 288-297.
[64] Qasim, S. S. B., Zafar, M. S., Niazi, F. H., Alshahwan, M., Omar, H., & Daood, U. (2020). Functionally graded biomimetic biomaterials in dentistry: an evidence-based update. Journal of Biomaterials Science, Polymer Edition, 31(9), 1144-1162.
[65] Fabris, D., Fredel, M. C., Souza, J. C., Silva, F. S., & Henriques, B. (2021). Biomechanical behavior of functionally graded S53P4 bioglass-zirconia dental implants: Experimental and finite element analyses. Journal of the Mechanical Behavior of Biomedical Materials, 120, 104565.
[66] Sharma, G. K., & Kukshal, V. (2022). Assessment of mechanical behaviour of functionally graded biomaterials using finite element method. Materials Today: Proceedings, 62, 7487-7493.
[67] Elleuch, S., Jrad, H., Wali, M., & Dammak, F. (2023). Finite element analysis of the effect of porosity on biomechanical behaviour of functionally graded dental implant. Proceedings of the Institution of Mechanical Engineers, Part E: Journal of Process Mechanical Engineering, 09544089231197857.
[68] Fatemi, M., Bahrami, Z., Bahraminasab, M., & Nabizadeh Chianeh, F. (2024). Optimizing functionally graded tibial components for total knee replacements: a finite element analysis and multi-objective optimization study. Computer Methods in Biomechanics and Biomedical Engineering, 1-19

Information of the authors

Oda Zahraa Abbas, Metallurgical Engineering department, college of Materials Engineering, University of Babylon
e-mail: mat214.zahraa.abbas@student.uobabylon.edu.iq

Radhi Nabaa Sattar, Metallurgical Engineering department, college of Materials Engineering, University of Babylon
e-mail: mat.nabaa.sattar@uobabylon.edu.iq

DOI 10.52209/2706-977X_2026_1_72 **IRSTI 55.03.14** **UDC 621.771**

Stress State and Contact Pressure during Asymmetrical Rolling of Thick Sheets

Ashkeyev Z.A.[1], Andreyachshenko V.A.*[2], Abishkenov M.Zh.[1], Kamarov A.U.[1]
[1] Karaganda Industrial University, Temirtau, Kazakhstan
[2]Abylkas Saginov Karaganda Technical University, Karaganda, Kazakhstan
*corresponding author

Annotation. Asymmetrical rolling is one of the modern methods of stabilizing the microstructure during the rolling process. The implementation of this process ensures an increase in the mechanical properties of rolled products, reduces texture and contributes to obtaining a more uniform microstructure. In this work, the stress state during asymmetrical rolling of thick sheets is studied and the contact pressure is determined by calculation methods. To study the stress state, the slip line method and velocity hodograph were used. Contact pressure was calculated using the slip line method. and joint solution of differential equations of equilibrium and plasticity conditions. It was revealed that in the zone of plastic deformation, compressive stress components prevail, in contrast to the traditional method of rolling in cylindrical rolls, where tensile stresses arise in the axial central zone, which can lead to destruction and elongation of grains in the rolling direction. Analysis of the calculation of contact pressures shows that the relative difference in the values of the specific contact pressures of the metal on the rolls during asymmetric rolling, calculated by the slip line method and the joint solution of differential equilibrium equations and plasticity conditions is insignificant, i.e. does not exceed 6%, which indicates the reliability of the results obtained. During asymmetrical rolling of a strip with a wide deformation zone, due to the occurrence of shear deformations, the neutral height shifts to the exit from the deformation zone, and it is even possible that there is no neutral zone.

Key words: deformation, stress state, slip lines, strain force, severe plastic deformation.

Introduction

For metallurgical production, improving product quality is of paramount importance. The production of thick plate steel is a multi-stage production process, which mainly includes steelmaking, continuous casting, hot rolling and cooling. The quality of the final product must meet the requirements for chemical components, profile, size, etc. It is determined by the technological parameters of each production stage and the quality of intermediate products. To control many factors, mechanisms such as machine learning [1], [2] and genetic algorithm [3], [4] are currently used. At the same time, the success of the production process remains directly related to the technologies used [5] - [9]. Many laboratories developing steels have focused on new high-alloy steels in which the composition and / or heat treatment dominate over the properties [10]. Another approach to improving the quality of the metal is the use of severe plastic deformation [11] - [14]. In this study, we focused on the hot rolling process. In [15], it is noted that the deformation trajectory during asymmetric rolling consists of two parts: first, the main rolling occurs, followed by a simple shear process. As is known [16] - [18], asymmetric rolling allows for the uniformity of deformation, improving the mechanical properties and microstructure of the processed workpieces [19], [20]. The first studies on the implementation of asymmetric rolling were carried out in 1948 by Sachs and Klinger [21] to develop a model of homogeneous deformation. Now the principles of asymmetric rolling are used both for steel production [22], [23] and for the processing of non-ferrous metals [24], [25], in addition, asymmetric rolling is successfully used as a basic process in accumulated rolling by joining [26], [27]. Asymmetry can be provided by the difference between the rotation speeds of the upper and lower rolls [28], different roll diameters [29], a specific roll shape leading to asymmetry [30], as well as other technological methods.

Despite the increased attention to the asymmetric rolling process, the stress-strain state during asymmetric rolling, as well as the values of contact pressure, which are necessary for the correct design of the rolling process, remain insufficiently studied. Thus, in [31], the configuration zones of deformation in the process of asymmetric rolling were analyzed, the authors [32] performed a modeling of friction forces in two-roll modules, where asymmetry is provided by the arrangement of rolls of different diameters. Despite the use of asymmetric rolling as a heterogeneity regulator, asymmetric rolling itself is also accompanied by a heterogeneous stress-strain state [33], and the magnitude of asymmetry can affect the magnitude of the shift [34].

The aim of the work: to study the stress state during asymmetric rolling of thick sheets and to determine the contact pressure using calculation methods.

1. Experimental part

The process of asymmetric strip rolling has a positive effect on the quality of the metal, i.e. on the mechanical and geometric properties of the resulting rolled metal products and the power parameters of the process. Let us consider the stress state and change in contact pressure of thick strips during asymmetric rolling.

The production of thick strips and blanks occupies a significant place in the national economy, as they are widely used in the oil and gas industry, shipbuilding, bridge building, mechanical engineering and other industries. Therefore, the quality of the resulting rolled metal products is increasingly demanding. One of the ways to solve this problem is the process of asymmetric rolling of blanks in conical rolls with different variable diameters along the length of the roll barrel. Asymmetric rolling can also be used in the processing of composite materials to ensure the required quality.

To study the stress state, the slip line (SL) method and the velocity hodograph were used. The contact pressure was calculated using the SL method and the joint solution of the differential equations of equilibrium and the plasticity condition. When determining the stress state using the slip line method, the following properties are used:

1 Slip lines form two mutually perpendicular families of curves α and β;

2 Slip lines must be continuous;

3 Slip lines must be orthogonal;

4 Slip lines must intersect the direction of the principal normal stresses at an angle of π/4;

5 The change in the average normal stress σcp when moving along the slip line is equal to the product of its angle of rotation by 2k.

Let us consider one of the options for asymmetric rolling of thick strips, adopting the following main parameters that characterize the proposed process:

1. The diameter of the larger roll D = 980 mm, the strip reduction $\Delta h = h_0 - h_1 = 10$ mm, where h_0 is the initial strip thickness, h_1 is the final strip thickness, the degree of reduction $\varepsilon_h = \Delta h/h_0 = 10/40 = 0.25$ and the length of the contact arc $l_D = \sqrt{R\Delta h} = \sqrt{490 \cdot 10} = 70$ mm, where R is the radius of the larger roll.

2. The diameter of the smaller roll d = 720 mm, the length of the contact arc $l_d = \sqrt{r\Delta h} = \sqrt{360 \cdot 10}$=60 mm, the length of the roll barrel L_b = 1500 mm, the taper of the rolls, $\frac{(D-d)}{2L_b}$= 0.04924, i.e. γ = arctg(0.04924) = 4.95 ≈ 5°, which is the most optimal value, since with increasing taper, the feeding and gripping of the strip by the rolls becomes more difficult.

3. The angle of gripping the strip, respectively, from the side of the larger diameter and the length of the contact arc: $\alpha_D = arccos[1-(\frac{\Delta h}{2R})]$=8°192, $l_D = \frac{\pi R \alpha_D}{180} = \frac{\pi \cdot 490 \cdot 8{,}192}{180}$ =70,02 mm.

4. The angle of capture from the side of the smaller diameter and the length of the contact arc, $\alpha_d = arccos[1-(\frac{\Delta h}{2r})]$=9°56, $l_d = \frac{\pi r \alpha_r}{180} = \frac{\pi \cdot 360 \cdot 9.56}{180}$ =60.04 mm.

The obtained values of the length of the contact arc from the side of the larger and smaller diameters, calculated by two expressions are identical and practically coincide, accordingly they can be considered correct.

A distinctive feature of the proposed process of asymmetric rolling of thick strips from the known ones [30] is that the shape of the deformation zone is wide, i.e., the ratio of the average contact arc length to the mean strip thickness is $\frac{(l_D+l_d)}{(h_0+h_1)}$= 1.85, in contrast to conventional processes, where the deformation zone is narrow and does not exceed $\frac{(l_D+l_d)}{(h_0+h_1)}$ ≈1,0.

Therefore, it is of interest to determine the stress state and contact pressure during asymmetric rolling of thick sheets with a wide shape of the plastic deformation zone *abcd* (Fig. 1), since the use of thick sheets in production is increasing (armor, shipbuilding, etc.). The field of slip lines (SL) during rolling of thick strips is shown in Fig. 1.

The construction of the slip-line field is carried out from the strip exit side of the plastic deformation zone, where the slip lines intersect the principal *x*- and *y*-axes at the nodal point 0.0′ at an angle of 45° (Fig. 1).

The construction of the SL grid is performed from the side of the strip exit from the plastic deformation zone, where the SL must intersect with the principal axes x and y at the nodal point 0.0' at an angle of 45°. Taking the step of change of LS equal to Δθ'=2Δθ=20°, or π/9 rad, and drawing from points *b* and *d* arcs with radii: /*b* 0.0′/ and /*d* 0.0′/ at an angle of 2Δθ=20°, we obtain nodal points 0.1' and 1.1'. By replacing the obtained arcs with chords, perpendiculars are drawn from the resulting points (0.1′ and 1.1′) to the chords until they intersect the x-axis; as a result, the intersection point 2.4 is obtained (Fig. 1).

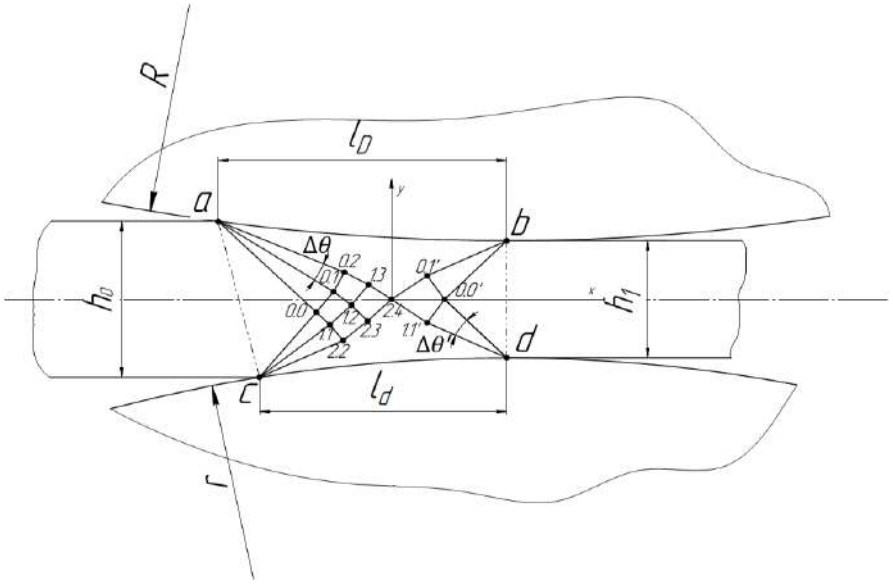

R – radius of the larger roll; r – radius of the smaller roll; l_d, l_D – the length of the contact arc ; h_0, h_1 – initial and final strip thickness

Fig. 1 – Field of slip lines during asymmetric rolling of thick strips

When constructing, we strictly used the basic properties of the LS, for example, the orthogonality property, i.e. the property of the LS intersection with the main axes at a right angle, etc. Using the LS properties, we construct the SL grid by analogy from the side of the entrance to the plastic deformation zone, up to the intersection with the nodal point 2.4. From the constructed SL grid, it can be seen that the number of nodal points from the side of the entrance to the plastic deformation zone is greater than from the exit side. This can be explained by the fact that closer to the exit, the plastic deformation process is completed and the strip moves as an absolutely rigid body. The correctness of the SL grid can be verified by constructing the velocity field. Figure 2 shows the velocity hodograph. The velocity plan was also constructed using the basic properties of the SL, i.e. the orthogonality property. On the y-axis, vertically, we plot the roll speed $\dot{u}_0$, equal to the value of strip compression per unit time t, i.e. $\dot{u}_0 0=\Delta h/t$. We construct from the side of the strip exit from the plastic deformation zone to the nodal point 0.0', observing the orthogonality condition. Hence, if we neglect the change in width during rolling, we can write the incompressibility condition for a unit of strip width.

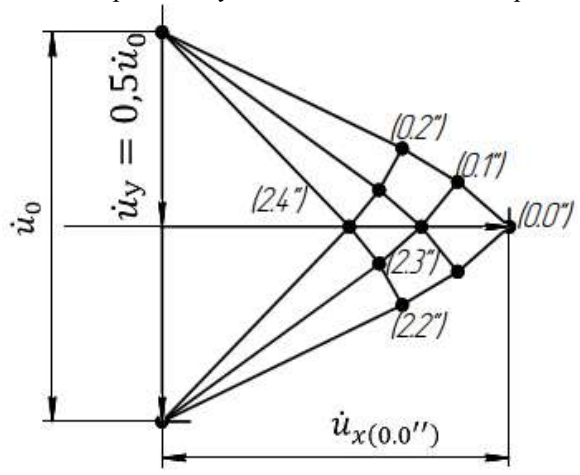

Fig.2 – Speed hodograph for rolling in conical rolls

The incompressibility condition can be written as follows:

$$\dot{u}_0 \cdot l_{mean} = \dot{u}_{x(0.0'')} \cdot h_{mean}, \text{ hence, } \frac{l_{mean}}{h_{mean}} = \frac{\dot{u}_{x(0.0'')}}{\dot{u}_0} = \frac{(l_D+l_d)}{(h_0+h_1)} = \frac{\dot{u}_{x(0.0'')}}{\dot{u}_0} \approx 1.850.$$

It can be seen that taking into account the error, the incompressibility condition is satisfied, which indicates the correctness of the constructed LS grid. Next, we can proceed to calculating the stresses in the plastic deformation zone *abcd*. From the condition of equilibrium of forces at the exit from the plastic deformation zone, we can write the following,

$$\int_{0.0'}^{b} \sigma_{0.0'}\, dy + kx_b = 0,$$

$$\sigma_{0.0'}\,(y_{0.0'} - y_b) + kx_b = 0,$$

$$\sigma_{0.0'}\,(-y_b) = kx_b, \text{ as } y_{0.0'} = 0, \text{ thence,}$$

$$\sigma_{0.0'} = -k = -\frac{\sigma_T^*}{2},$$

since $x_b = y_b$, where σ_t^* is the deformation resistance depending on the temperature-speed and deformation parameters of the rolling process. Assuming that a strip of Steel 45 is rolled at a temperature of 1000 °C, with a thickness reduction of ε_h = 25% and a strain rate of $\dot{u}$=1s^{-1}, the deformation resistance is σ_T^*= 85 MPa.

Knowing the average stress at the nodal point 0.0', from the Hencky relation one can determine the average stress at the neighboring nodal point 1.1', i.e.,

$$\sigma_{1.1'} = \sigma_{0.0'} - 2k\Delta\theta',$$

$$\sigma_{1.1'} = -k - 2k\frac{\pi}{9} = -\frac{\sigma_t^*}{2}\left(1 + 2\frac{\pi}{9}\right) = -1{,}7\frac{\sigma_t^*}{2}.$$

The average stress at the nodal point 1.1' increases by 1.7 times compared to the value at the nodal point 0.0', which once again proves the advantage of asymmetric rolling.

From the condition of equilibrium of forces from the larger and smaller roll diameters, the average stresses at the nodal points 1.1' and 0.1' will be equal. From the condition of symmetry and equilibrium of forces relative to these axes, similar values of the average stresses will also be at the nodal points 0.2. and 1.2. Given the metal deformation resistance σ_T^*= 85 MPa, the mean stress at the nodal points $0.0'$and 0.0, is determined as k=- $\frac{\sigma_T^*}{2}$ = -42,5 MPa. From the symmetry of the points and the orthogonality of the LS at the nodal points 0.2, 2.2, 0.1' and 1.1' will be equal to:

$$\sigma_{1.1'} = \sigma_{0.1'} = \sigma_{0.2} = \sigma_{2.2} = 1.7\frac{85}{2} = -72.25, \text{ MPa.}$$

It will be slightly lower at the intermediate nodal points 0.1 and 1.1, determined through the rotation angle of the hp $\Delta\theta$=10° (π/9 rad), as follows:

$$\sigma_{1.1} = \sigma_{0.1} = -k - k\frac{\pi}{9} = -\frac{\sigma_t^*}{2}\left(1 + \frac{\pi}{9}\right) = -57.327 \text{ MPa.}$$

The voltage components at the corresponding nodal points are determined using the following expressions:
At the nodal point 0.0',

$$\sigma_{x0.0'} = \sigma_{0.0'} + k\sin 2\theta_{0.0'} = -k + k = 0;$$
$$\sigma_{y0.0'} = \sigma_{0.0'} - k\sin 2\theta_{0.0'} = -k - k = -2k = -85 \text{ MPa};$$
$$\tau_{xy0.0'} = -k\cos 2\theta_{0.0'} = 0,$$

where θ_(0.0') is the angle of inclination of the hp to the principal axes at the nodal point 0.0', which at this point is equal to 45°.

At the adjacent nodal point 0.1',

$$\sigma_{x0.1'} = \sigma_{0.1'} + k\sin 2\theta_{0.1'} = -72.25 + 72.25\sin 2\cdot(45+20) = -16.904 \text{ MPa};$$
$$\sigma_{y0.1'} = \sigma_{0.1'} - k\sin 2\theta_{0.1'} = -72.25 - 72.25\sin(2\cdot 65) = -127.596 \text{ MPa};$$
$$\tau_{xy0.0'} = -k\cos 2\theta_{0.1'} = 27.318 \text{ MPa.}$$

At the intermediate nodal point 0.1 and 1.1,

$$\sigma_{x0.1} = \sigma_{0.1} + k\sin 2\theta_{0.1} = -57.327 + 57.327\sin 2\cdot(45+10) = -3.457 \text{ MPa};$$
$$\sigma_{y0.1} = \sigma_{0.1} - k\sin 2\theta_{0.1} = -57.327 - 57.327\sin(2\cdot 55) = -111.197 \text{ MPa};$$

$$\tau_{xy0.0'} = -k\cos 2\theta_{0.1} = 14.535 \text{ MPa}.$$

Analysis of the distribution of stress components shows that all values of stress components increase from the center to the contact surface. By summing the stress components along the y axis, we can calculate the average contact stress p_{mean} and the rolling force, i.e.,

$$p_{mean} = \frac{(85+111,197+127,596)}{3} = 107.931 \text{ MPa}.$$

It should be noted that in the plastic deformation zone *abcd* the stress components are compressive, unlike the traditional rolling method in cylindrical rolls, where tensile stresses arise in the axial central zone, which can lead to destruction and stretching of grains in the rolling direction.

When rolling a wide strip, the compressive stresses acting in the plastic deformation zone are more significant, compared to a narrow shape of the plastic deformation zone. This is due to the fact that with a low shape of the deformation zone, the coverage is denser, which does not allow the development of tensile stresses. Especially in the axial central zone of the strip, where during symmetrical rolling in cylindrical rolls, significant tensile stresses arise, which lead to the destruction of the metal in the rolling direction.

Therefore, to prevent this phenomenon, it is advisable to roll in conical rolls with different diameters along the length of the roll barrel.

To determine the specific contact pressure of the metal on the rolls, we use the method of jointly solving the differential equations of equilibrium and the plasticity condition. To do this, let us consider the equilibrium condition of the element a'b'c'd', located at a distance x from the center p of the *x* and *y* coordinate axes (Fig. 3).

The following forces act on the selected element a'b'c'd':

From the side of the entrance to the plastic deformation zone, $(\sigma_x+d\sigma_x)\frac{h_x}{cos\beta}$;

From the side of the exit from the plastic deformation zone, $\sigma_x(h_x-dh_x)$;

The component of the contact pressure p along the x axis from the side of the larger diameter of the rolls, $p\sin\varphi_x\frac{dx}{cos\varphi_x}$;;

The component of the contact pressure p along the x axis from the side of the smaller diameter of the rolls, $p\sin\varphi_{x1}\frac{dx_1}{cos\varphi_{x1}}$;

The contact friction forces from the side of the larger diameter rolls, $t_x\cos\varphi_x\frac{dx}{cos\varphi_x}$;

Contact friction forces from the side of the smaller diameter rolls, $t_x\cos\varphi_{x1}\frac{dx_1}{cos\varphi_{x1}}$.

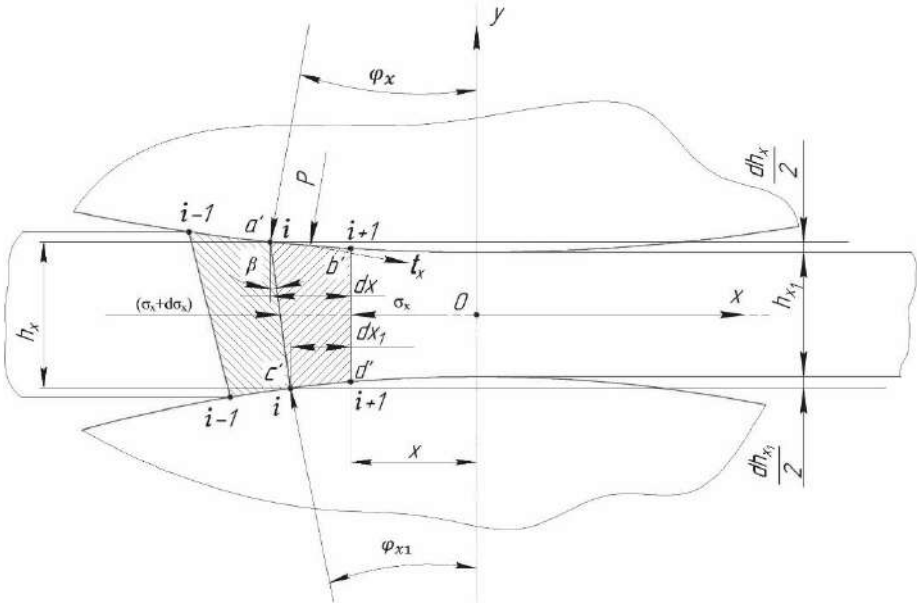

Fig.3 – The equilibrium condition of the element a'b'c'd' and the step of changing the nodes of the grids *i-1*, *i*, *i+1* in the center of plastic deformation during asymmetric rolling of thick sheets

From the condition of equilibrium of the element, a'b'c'd' we can write the following:

$(\sigma_x+d\sigma_x)\frac{h_x}{cos\beta}-\sigma_x(h_x-dh_x)+t_x cos\varphi_x\frac{dx}{cos\varphi_x}+t_x cos\varphi_{x1}\frac{dx_1}{cos\varphi_{x1}}-psin\,\varphi_x\frac{dx}{cos\varphi_x}-psin\,\varphi_{x1}\frac{dx_1}{cos\varphi_{x1}}=0$, or,

$(\sigma_x+d\sigma_x)\frac{h_x}{cos\beta}-\sigma_x(h_x-dh_x)+t_x(dx+dx_1)-ptg\,\varphi_x dx-ptg\,\varphi_{x1}dx_1)=0.$

Using the following relationships, i.e. $tg\varphi_x=\frac{dh_x}{2dx}$ and $tg\varphi_{x1}=\frac{dh_{x_1}}{2dx_1}$, as well as the Coulomb-Amontons law in the following form, $t_x=\mu p$, then the differential equation can be represented as follows:

$\sigma_x\frac{h_x}{cos\beta}+d\sigma_x\frac{h_x}{cos\beta}-\sigma_x h_x+\sigma_x dh_x+\mu p\frac{dh_x}{2}\left(\frac{1}{tg\varphi_x}+\frac{1}{tg\varphi_{x1}}\right)-pdh_x=0,$

where $dh_x=\frac{dh_x}{2}+\frac{dh_{x_1}}{2}-$ elementary strip compression.

In the case under consideration, the angle β≈14°, then cosβ=0.97≈1.0, the differential equation is simplified to the following form:

$d\sigma_x h_x+\sigma_x dh_x+\mu p\frac{dh_x}{2}\left(\frac{1}{tg\varphi_x}+\frac{1}{tg\varphi_{x1}}\right)-pdh_x=0$, after reducing by h_x, we get:

$d\sigma_x+\sigma_x\frac{dh_x}{h_x}-p\left(1-\frac{\mu}{2tg\varphi_x}-\frac{\mu}{2tg\varphi_{x1}}\right)\frac{dh_x}{h_x}=0.$

Using the plasticity condition $p-\sigma_x=\sigma_т^*$ or $\sigma_x=p-\sigma_т^*$, by $\sigma_т^*$=const $dp=d\sigma_x$, we will receive,

$dp+[(p-\sigma_т^*)-p\left(1-\frac{\mu}{2tg\varphi_x}-\frac{\mu}{2tg\varphi_{x1}}\right)]\frac{dh_x}{h_x}=0.$

$dp+[p\left(\frac{\mu}{2tg\varphi_x}+\frac{\mu}{2tg\varphi_{x1}}\right)-\sigma_т^*]\frac{dh_x}{h_x}=0.$

To solve the obtained differential equation, we will use the numerical method of finite differences or the grid method, where for the grid points we compose a finite difference analogue in the following form:

$$\Delta p_i=[\sigma_т^*-p_i\left(\frac{\mu}{2tg\varphi_x}+\frac{\mu}{2tg\varphi_{x1}}\right)]\frac{\Delta h_{xi}}{h_{xi}}. \quad (1)$$

Then, at the corresponding grid nodal points, this expression can be expanded as follows:

$$(p_{i-1}-p_i)=[\sigma_т^*-p_i\left(\frac{\mu}{2tg\varphi_{xi}}+\frac{\mu}{2tg\varphi_{x1i}}\right)]\frac{h_{xi-1}-h_{xi}}{h_{xi}}, \quad (2)$$

for example, when i=1,

$$(p_0-p_1)=[\sigma_т^*-p_1\left(\frac{\mu}{2tg\varphi_{x1}}+\frac{\mu}{2tg\varphi_{x11}}\right)]\frac{h_0-h_1}{h_1}, \quad (3)$$

for example, when i=2,

$$(p_1-p_2)=[\sigma_т^*-p_2\left(\frac{\mu}{2tg\varphi_{x2}}+\frac{\mu}{2tg\varphi_{x12}}\right)]\frac{h_1-h_2}{h_2}, \quad (4)$$

etc. from the initial height of the strip $h_{i-1}=h_0$=40 mm, from the side of the entrance to the deformation zone (lag zone) and to the neutral height of the strip $h_{i-1}=h_n$, where the contact pressures from the lag and lead zones must be equal.

For step-by-step calculation of the contact pressure p_i, the section of the deformation zone length is divided into n steps, respectively from the side of the larger and smaller diameters of the rolls, i.e.: $\Delta x_i=\frac{l_D}{n}$ and $\Delta x_{i1}=\frac{l_d}{n}$, where n – number of steps. For this case under consideration, we first take n=10, then, $\Delta x_i=\frac{70}{10}=7$ mm and $\Delta x_{i1}=\frac{60}{10}=6$ mm. Accordingly, the step of changing the elementary compression of the strip will be equal to, $\Delta h_{xi}=\frac{10}{10}=1{,}0$ mm. Then, the step of changing the angles, respectively, from the side of the larger and smaller diameters, respectively, will be equal to: $tg\varphi_{x1}=\frac{1}{2*7}=0{,}0714$, $tg\varphi_{x11}=\frac{1}{2*6}=0.0833$, the step of change of which is unchanged, and remains constant during further step-by-step calculation.

At both ends of the plastic deformation zone, the values of normal pressure pi and pi+1 are known and equal, i.e., $p_0=p_{10}=\sigma_t^*=85$ MPa. Taking into account the accepted values and designating the values in brackets in equations (1-4) with the letter $\delta=\left(\frac{\mu}{2tg\varphi_x}+\frac{\mu}{2tg\varphi_{x1}}\right)=3.25$, (μ – coefficient of contact friction) equation (1) can be represented as follows:

$$\frac{\Delta p_i}{(\sigma_t^*-p_i\delta)}=\frac{\Delta h_{xi}}{h_{xi}}. \quad (5)$$

Thus, knowing the initial values and the step of changing the elementary length of the deformation zone, the angles of capture and the height of the strip, it is possible to calculate the corresponding values of p_i at the corresponding nodal points plotted on the grid of the plastic deformation zone (Fig. 3) step by step.

Let us make the first step to determine the contact pressure p1: at n = 10, i = 1, Δh_x = 1 = 1.0 mm, h_{xi} = 1 = 39 mm, at the average value of the contact friction coefficient μ = 0.25. We will start the calculation from the side of the entrance to the deformation zone, i.e. from the lagging zone to the neutral height of the strip

$h_n = h_{xi=5}$=35 mm:

$(85 - p_1) = [\,85 - p_1(3.25)]\frac{1}{39}$, from here p_1 =90.35 MPa.

We perform the calculation in the next step at i=2,

$(90.35 - p_2) = [\,85 - p_2(3.25)]\frac{1}{38}$, from here p_2=96.35 MPa.

We perform similar calculations when i=3,

$(96.35 - p_3) = [\,85 - p_3(3.25)]\frac{1}{37}$, from here p_3 =103.11 MPa, etc. up to the neutral height of the strip, where the contact pressures should be equal. Further assuming that it is in the middle of the plastic deformation zone, i.e. $h_n = h_{xi=5} \approx 35$ mm, we get it p_5 =119.40≈120 MPa.

A similar differential equation of equilibrium, changing the sign, can be written from the side of the exit from the plastic deformation zone, i.e. from the side of the advance zone. For this, we use the obtained finite-difference analogue (2), representing it as follows:

$$(p_{i+1} - p_i) = [\,\sigma_t^* - p_i(3.25)]\frac{h_{xi} - h_{xi+1}}{hx_i}$$

We will also similarly perform the first step of calculating the contact pressure pi, from the exit side of the plastic deformation zone. *abcd* i.e. when i=9,

$$(85 - p_9) = [\,85 - p_9(3.25)]\frac{1}{31}, \text{ from here } p_9 = 91.9 \text{ MPa.}$$

It can be seen that at the first step from the lagging zone the contact pressure was p_1 =90.35 MPa, and the difference is less than 2%.

Let's perform the next step of calculation at the nodal point i=8,

$(91.9 - p_8) = [\,85 - p_8(3.25)]\frac{1}{32}$, и p_8= 99.32 MPa.

Let's take the next counter step i=7,

$(99.32 - p_7) = [\,85 - p_7(3.25)]\frac{1}{33}$, and p_7= 107.315 MPa.

2.Discussing the results

The contact pressure values at the adopted neutral height of the strip from the lead zone side at $h_n = h_{xi}$=5=35 mm are equal to p_5 = 125.07≈125 MPa.

Based on the fact that the neutral line of the strip is presumably located between h_{x-1} and h_{x+1}, i.e. between the current height of the strip: 36÷34 mm, it should be expected that the maximum value of the contact pressure will also be between the obtained values, i.e. between 120 and 125 MPa, where the difference between the obtained values is 4%. To accurately determine the neutral height h_n, it is necessary to reduce the step of changing the adopted values. With a further decrease in the adopted values, to Δx_i=70/20=3.5 mm, Δx_{i1}=60/20 =3 mm, Δh_{xi}=10/20 = 0.5 mm, i.e. taking the number of steps n=20, at $h_n = h_{xi}$=10≈34.5 mm, the contact pressure from the lagging zone side will be 122.65 MPa, and from the leading side: ~120.0 MPa, i.e. the difference will already be about 2%.

Similarly, as in the previous case, summing up the value of the contact pressure along the contact surface, we obtain the average value, which will be equal to p^*_{mean}≈ 101.94 MPa. Approximately the same value was obtained above by the hp method (p_{mean}=107.93 MPa), i.e. the difference does not exceed 6%.

The slip-line method, on the other hand, offers a clear analytical framework and allows for a transparent visualization of the stress and strain fields. Therefore, while both methods yield close results, the combined differential-equation approach can be considered slightly more accurate for detailed local stress predictions, whereas the slip-line method is valuable for understanding the overall physical behavior and for parametric studies.

Analysis of the calculation of contact pressures shows that the relative difference in the values of specific contact pressures of metal on the rolls during asymmetric rolling, calculated by the hp method and the joint solution of the

differential equations of equilibrium and the plasticity condition, is insignificant, i.e. does not exceed 6%, which indicates the reliability of the results obtained.

It should be noted that, in asymmetric strip rolling with a wide deformation zone, the neutral plane shifts (rotates) toward the exit of the plastic deformation region due to the development of shear strains. Determining the position of this surface therefore constitutes the next principal task, which must be considered separately. Relative to the neutral height of the strip during symmetrical rolling, tensile stresses arise in the direction of rolling, which can lead to ruptures and cracks in the direction of rolling. Therefore, to transform these undesirable phenomena, it is effective to use asymmetrical rolling to ensure the required quality of rolled metal.

Conclusions

In asymmetric rolling of strips with a wide deformation zone, the compressive stresses are significantly higher compared to a narrow deformation zone. This is due to the denser contact between the rolls and the strip in the wide deformation zone, which prevents the development of tensile stresses. This effect is particularly important in the central axial zone of the strip, where symmetric rolling in cylindrical rolls can generate considerable tensile stresses that may lead to cracks and material failure.

The contact pressures calculated using the slip-line method and the combined solution of the differential equilibrium equations with the plasticity condition differ by no more than 6%. This confirms the correctness of the obtained results and allows accurate determination of rolling forces and torques, which is critical for evaluating the strength and durability of the main components of the rolling mill during the production of thick strips.

It should be noted that the numerical solution of the differential equations provides higher local accuracy, while the slip-line method offers a clear and convenient visualization of the stress distribution across the strip. The shift of the neutral line toward the exit of the plastic deformation zone due to shear deformations is an important factor affecting the stress distribution and requires separate investigation.

Future research may focus on refining the neutral line position, accounting for strain hardening, variable friction, and temperature gradients to improve predictive accuracy and optimize the asymmetric rolling process.

Acknowledgement

The work was carried out within the framework of the state budget research work AP19677907 “Study of the influence of micro/nanoparticles, industrial waste and shear on the quality of metal blanks for mechanical engineering”.

References

[1] Ji Yi., Liu Sh., Zhou M., Zhao Z., Guo X., Qi L. A machine learning and genetic algorithm-based method for predicting width deviation of hot-rolled strip in steel production systems //Information Sciences, 2022, 589. - p. 360-375. https://doi.org/10.1016/j.ins.2021.12.063.

[2] Pan Q.-K., Gao L., Wang L. A multi-objective hot-rolling scheduling problem in the compact strip production //Applied Mathematical Modelling, 2019, 73. – p. 327-348. https://doi.org/10.1016/j.apm.2019.04.006.

[3] Liu X., Xiao H. Theoretical and experimental study on the producible rolling thickness in ultra-thin strip rolling //Journal of Materials Processing Technology, 2020, 278 – p. 116537. https://doi.org/10.1016/j.jmatprotec.2019.116537.

[4] Muntin A.V. Advanced Technology of Combined Thin Slab Continuous Casting and Steel Strip Hot Rolling //Metallurgist, 2019, 62. – p. 900–910. https://doi.org/10.1007/s11015-019-00747-5.

[5] Mekhtiev A.D., Yurchenko A.V., Neshina E.G., Al’kina A.D., Madi P.Sh. Physical Principles of Developing Pressure Sensors Using Refractive Index Changes in Optical Fiber Microbending //Russian Physics Journal, 2020, 63.2. – p. 323–331 https://doi.org/10.1007/s11182-020-02038-y.

[6] Mekhtiev A., Alkina A., Neftissov A., Kazambayev I., Kirichenko L. Intelligent Systems for Monitoring the Integrity of Technical Objects Based on Distributed Fiber-Optic Sensors. CEUR Workshop Proceedings, 2022, 3347. – p. 290-306.

[7] Yurchenko A.V., Mekhtiyev A.D., Bulatbaev F.N., Neshina Y.G., Alkina A.D. Investigation of Additional Losses in Optical Fibers Under Mechanical Action //IOP Conference Series: Materials Science and Engineering, 2019, 516.1 – p. 012004. https://doi.org/10.1088/1757-899X/516/1/012004.

[8] Yurchenko A., Alkina A., Mekhtiev A., Bulatbayev F., Neshina E. The Questions of Development of Fiberoptic Sensors for Measuring Pressure with Improved Metrological and Operational Characteristics //MATEC Web of Conferences, 2016, 79. – p. 01085. DOI: 10.1051/matecconf/20167901085.

[9] Mekhtiev A., Bulatbaev F.N., et all. Use of reinforcing elements to improve fatigue strength of steel structures of mine hoisting machines (MHM) //Metallurgija, 2020, 59.1 – p.121-124.

[10] Zhu Y., et al. Rapid alloy prototyping for strip steel development: DP800 steel case study //Ironmaking & Steelmaking, 2021, 48.5 – p. 493-504.

[11] Andreyachshenko V., Naizabekov A.B. Microstructural and mechanical characteristics of AlSiMnFe alloy processed by equal channel angular pressing. Metalurgija, 2016, 55(3). – p. 353–356.

[12] Andreyachshenko V.A. Evolution of the AA2030 alloy microstructure in the ECAP process //.Kovove Materialy, 2022, 60(2). – p. 79-87. doi: 10.31577/km.2022.2.79.

[13] Andreyachshenko V.A. Finite element simulation (FES) of the fullering in device with movable elements //Metalurgija, 2016.55(4) – 829–831.
[14] Sachs G., Klingler, L.J. The Flow of Metals Through Tools of Circular Contour //ASME. J. Appl. Mech., 1947, 14(2) – pp. A88–A98. https://doi.org/10.1115/1.4009656.
[15] Ren X., Zhang X., Huang Yu., Liu Yu, Zhao L., Zhou W. Evolution of shear texture during the asymmetric rolling and its annealing behavior in a twin-roll casting AA6016 sheet: an ex-situ electron backscatter diffraction study //Journal of Materials Research and Technology, 2020, 9, 3. – p. 6420-6433. https://doi.org/10.1016/j.jmrt.2020.04.026.
[16] Fu B., Pei C., Pan H., Guo Y., Fu L., Shan A. Hall-Petch relationship of interstitial-free steel with a wide grain size range processed by asymmetric rolling and subsequent annealing. Materials Research Express, 2020, 7(11). – p. 116516. DOI 10.1088/2053-1591/abc79f.
[17] Dhinwal S.S, Toth L.S., Lapovok R., Hodgson P.D. Tailoring One-Pass Asymmetric Rolling of Extra Low Carbon Steel for Shear Texture and Recrystallization //Materials, 2019, 12(12) – p. 1935. https://doi.org/10.3390/ma12121935.
[18] Ashkeyev Z.A., Andreyachshenko V.A., Bukanov Z.U. Research of the asymmetric rolling of workpieces // PNRPU Mechanics Bulletin, 2020, 4. – p. 27–35.
[19] Vincze G., Simões F.J.P., Butuc M.C. Asymmetrical Rolling of Aluminum Alloys and Steels: A Review. Metals, 2020, 10(9). – p.1126. https://doi.org/10.3390/met10091126.
[20]Zhu J., Liu Sh., Long D., Zhou Sh., Zhu Yu., Orlov D. The evolution of texture and microstructure uniformity in tantalum sheets during asymmetric cross rolling // Materials Characterization, 2020, 168. – p. 110586. https://doi.org/10.1016/j.matchar.2020.110586.
[21] Magalhães D.C.C., Sordi V.L., Kliauga A.M. Microstructure evolution of multilayered composite sheets of AA1050/AA7050 Al alloys produced by Asymmetric Accumulative Roll-Bonding //Materials Characterization, 2020, 162. – p. 110226. https://doi.org/10.1016/j.matchar.2020.110226.
[22] Magalhães D.C.C., Cintho O.M., Rubert J.B., Sordi V.L., Kliauga A.M. The role of shear strain during Accumulative Roll-Bonding of multilayered composite sheets: Pattern formation, microstructure and texture evolution //Materials Science and Engineering: A, 2020, 796 – p. 140055. https://doi.org/10.1016/j.msea.2020.140055.
[23] Vincze G., Pereira A.B., Lopes D.A.F,. Yánez J.M.V., Butuc M.C. Study on Asymmetric Rolling Process Applied to Aluminum Alloy Sheets. Machines, 2022, 10(8). – p.641. https://doi.org/10.3390/machines10080641.
[24] Choi C.H., Kim K.H., Lee D.N. The effect of shear texture development on the formability in rolled aluminum alloy sheets. //Mater. Sci. Forum, 1998, 273–275. – p. 391–396. https://doi.org/10.4028/www.scientific.net/MSF.273-275.391.
[25] Pustovoytov D., Pesin A., Tandon P. Asymmetric (Hot, Warm, Cold, Cryo) Rolling of Light Alloys: A Review. Metals, 2021, 11(6) – p. 956. https://doi.org/10.3390/met11060956.
26. Wang J., Liu X., Sun X. Study on the relationship between asymmetrical rolling deformation zone configuration and rolling parameters // International Journal of Mechanical Sciences, 2020, 187. – p. 105905. https://doi.org/10.1016/j.ijmecsci.2020.105905.
[27] Khurramov Sh.R., Abdukarimov A., Khalturaev F.S., Kurbanova F.Z. Modeling of friction forces in an asymmetric two-roll module //IOP Conference Series: Materials Science and Engineering, 2020, 916, No. 1 – p. 012051. DOI 10.1088/1757-899X/916/1/012051.
[28] Mavlonov T., Akhmedov A., Saidakhmedov R., Bakhadirov K. Simulation modelling of cold rolled metal strip by asymmetric technology In IOP Conference Series: Materials Science and Engineering //International Scientific Conference Construction Mechanics, Hydraulics and Water Resources Engineering (CONMECHYDRO – 2020), 23-25 April 2020, Tashkent, Uzbekistan, 883 – p. 012194. DOI 10.1088/1757-899X/883/1/012194.
[29] Wang X., Liu H., Tang X., Wang Y., Guo M., Zhuang L. Influence of asymmetric rolling on the microstructure, texture evolution and mechanical properties of Al–Mg–Si alloy //Materials Science and Engineering: A, 2022, 844 – p. 143154. https://doi.org/10.1016/j.msea.2022.143154.
[30] Khurramov Sh.R. Some questions of the contact interaction theory in two-roll modules //J. Phys.: Conf. Ser., 2020, 1546. – p. 012132. DOI 10.1088/1742-6596/1546/1/012132.

Information of the authors

Ashkeyev Zhassulan Amanzholovich, c.t.s., ass. professor, docent, Karaganda Industrial University
e-mail: jashkeev@mail.ru

Andreyachshenko Violetta Alexandrovna, PhD, associate professor, head of the test laboratory of engineering profile «Complex development of mineral resources», Abylkas Saginov Karaganda technical university
e-mail: v.andreyachshenko@ktu.edu.kz

Abishkenov Maxat Zharylgasynovich, PhD, senior lecturer of the department of "Technological machines and transport", Karaganda Industrial University
e-mail: m.abishkenov@tttu.edu.kz

Kamarov Aman Uakhitovich, doctoral student of the department of "Technological machines and transport", Karaganda Industrial University
e-mail: a.kamarov@tttu.edu.kz

DOI 10.52209/2706-977X_2026_1_81 **IRSTI 81.09.03** **UDC 004.942**

Comparative Mechanical Performance of Cylindrical and Cuboid Pore Geometries in Additively Manufactured ABS Bone Scaffolds

Modi Yashwant Kumar*
Jaypee University of Engineering and Technology, Guna, India
*corresponding author

Abstract. Synthetic bone scaffold must possess a good balance of porosity and mechanical strength for success of the tissue engineering process. With availability of additive manufacturing (AM) technology, it is possible to fabricate porous scaffolds with customised porosity, pore shape and size; which was rather difficult for the traditional processes. This paper presents design, analysis and additive manufacturing of ABS porous bone scaffolds. It also compares mechanical behaviour of the porous scaffolds with different pore geometry. Initially, two CAD models with same porosity but different pore geometry were created in Solidworks®2016. Then, finite element analysis (FEA) of both the scaffolds was conducted in ANSYS® Workbench for von-Mises stress, elastic strain and total deformation by applying a compressive load of 500N. On comparing, stress-strain curve of scaffold with cylindrical channels found to be steeper than scaffold with cuboid channels. Moreover, Young's modulus of scaffold with cylindrical channels (2587 MPa) was found greater than the scaffold with cuboid channels (2512 MPa). Stress-strain curve obtained via physical testing of specimens also found to follow similar tends. This result leads to conclude that scaffolds with cylindrical channels can withstand more loads in comparison with scaffolds with cuboid channels for the same porosity.

Keywords: additive manufacturing; compressive strength; finite element analysis; porosity; porous bone scaffold; fuse deposition modelling.

Introduction

Additive Manufacturing (AM), originally introduced in 1980s with the name rapid prototyping, is an umbrella term for a host of manufacturing processes, which can fabricate physical part directly from a CAD model in additive manner [1]. ASTM International has classified AM technologies into seven major categories; namely, vat photo-polymerisation, material extrusion, binder jetting, material jetting, powder bed fusion, sheet lamination and directed energy deposition [2]. AM has been maturing day by day for more than past 35 years and today with increased technological knowhow and range of materials, it has become capable of producing even end-use functional components in metal, polymer and ceramics [3-5]. One of the key advantages of AM is the ability to produce complex shapes and geometries such as pre-designed lattice structures to reduce weight, that are very difficult or even impossible for other manufacturing processes [6-8]. To fabricate a part via AM process, initially, one need to have a CAD model in STL (**ST**ereo**L**ithography or Standard Triangulation Language) format, which is then converted into sliced model and finally one slice at a time is sent to the AM machine, where part gets fabricated in layer by layer manner [9, 10].

Bone tissue engineering (BTE) is one of the fastest growing technologies, which is capable of developing implantable bone substitutes for large sized bone defects that cannot heal on their own [11-12]. The success of BTE depends on a supporting structure known as scaffold. This scaffold is expected to possess adequate porosity so that new tissues can grow properly and nutrients can flow inside it without any obstruction [13]. Moreover, it should also possess adequate mechanical strength so that it can withstand the pressure exerted by the growing tissues (for *in vitro* applications) as well as skeletal pressure in case of *in vivo* applications [14-16]. In addition to existing auto and allograft procedures, surgeons have been trying synthetic bone grafts for past few years. Synthetic bone graft employs a porous scaffold to seed, proliferate and mature the stem cells. Traditional scaffold making methods such as salt leaching, freeze drying, electro spinning suffer by several limitations, like difficulty in creating customised porosity, pore size, shape etc. [17-18]. In recent years, AM has emerged as a promising alternative to traditional methods for fabricating such customised scaffolds for BTE applications. A synthetic scaffold must have a good balance of porosity and mechanical strength so that it can allow free flow of nutrients and oxygen through proliferating stem cells as well as withstand the pressure exerted by the sprouting cells. Customized porosity, pore size and shape in scaffold can be designed during CAD model development. The objective of this study is to evaluate and compare the mechanical properties of acrylonitrile butadiene styrene (ABS) porous scaffolds with different pore geometry but same porosity by simulating their behaviour under compressive loading via FEA and physical testing of the additively manufactured specimens.

2.Material and Methods

2.1 Material

Acrylonitrile butadiene styrene (ABS) is one of the biocompatible materials processed by different AM processes [19]. It is an impact resistant thermoplastic polymer of three different monomers. Polymerization of different monomers imparts excellent physical, mechanical, chemical and electrical properties to ABS. It has been employed for making of variety of items such as pipe, telephone bodies, kitchen appliances, automotive components, wheel cover, helmet, toys, show-pieces etc. for past several years [20]. In recent years, it has been used in medical field also. Apart from manufacturing respiratory, auto-injection and infusion devices, it has also been applied to print miniature prosthetic implants, such as middle ear prostheses [21-23]. However, ABS can be used in medical applications when supplied in certified medical-grade formulations. These grades comply with ISO 10993 and often meet USP Class VI requirements, including cytotoxicity, sensitization, and irritation testing. These grades are suitable for non-implantable components such as device housings and surgical instrument handles. Regulatory acceptance typically requires compliance with agencies, such as U.S. Food and Drug Administration or EU MDR guidelines, along with material traceability and risk assessment. Standard ABS is generally not recommended for long-term implantable applications due to limited long-term bio-stability and potential additive leaching.

2.2 Methodology

Methodology adopted to conduct this study is presented in Figure 1. Initially, a suitable specimen shape and size was chosen for ABS material. The dimensions of the specimen were chosen according to ISO-604 standard. Then, CAD models with two different pore geometries were created with almost same porosities by hit and trial method. Then the CAD model was imported into ANSYS® Workbench to perform static structural analysis and compare von-Mises stress, elastic strain and total deformation using finite element method. After that, porous specimens were additively manufactured via fused deposition modelling (FDM) technology. Finally, results obtained via FEA and physical test were compared for both the pore geometries.

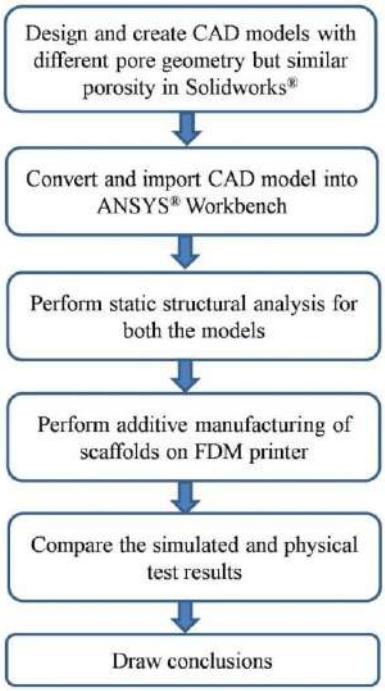

Fig. 1. - Methodology

2.3 CAD Modelling

A cuboid shaped specimen (25.4 mm × 12.7 mm × 12.7 mm), according to ISO 604 standard for compression testing was chosen for this study [24]. Two different CAD models of porous scaffolds were prepared with cuboid and cylindrical shaped pore channels using Solidworks®2016 software. Initially, several designs were prepared with slightly different sized channels to obtain the equal porosity. Initial designs were investigated with increasing number of channels (from 1, 2, 4, 8, 9 and 18) in three mutually perpendicular directions. Figures 2(a) and 2(b) show the CAD model of the porous scaffolds with cuboid and cylindrical channels.

Table 1. Specifications of CAD models of porous scaffolds

Characteristics	Cuboid channel	Cylindrical Channel
CAD model dimensions (mm) (L×B×H)	25.4 x 12.7 x 12.7	25.4 x 12.7 x 12.7
Cross section of channel (mm)	0.73 x 0.73	Φ 0.83
No. of channels along x,y and z-axis	18 x 9 x 9	18 x 9 x 9
Vol. of solid CAD model (mm^3)	4096.77	4096.77
Volume of porous CAD model (mm^3)	1941.97	1936.22
Porosity (%)	52.60	52.74

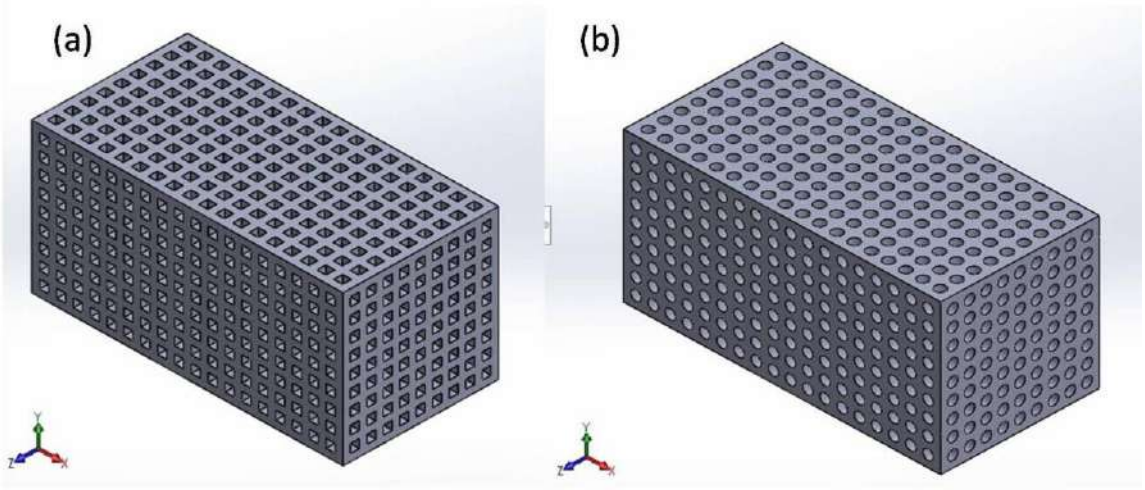

Fig. 2. - CAD model of porous scaffolds with (a) cuboid channels, (b) cylindrical channels

2.4 Finite Element Analysis

The behaviour of both the porous scaffold models under compressive loading has been simulated via finite element analysis using ANSYS® Workbench. The material properties of ABS plastic were used from the software itself (Poisson ratio = 0.35, Young's modulus = 2000 MPa). Initially, the model from Solidworks®2016 was imported in ANSYS® Workbench. For applying boundary conditions, one side (square face i.e. 12.7 mmx 12.7 mm) of the scaffold model was fixed and compressive load of 500 N was applied on other side of the scaffold. The load was applied along the length of model. The model was compressed at about 5% of its height and 1s time period at an increment of 0.01s was set. Then, static structural analysis under compression loading was performed on both CAD models. The results for von-Mises stress, elastic strain and total deformation were recorded. Simulated results were rendered in different colours to indicate the safety level of the models. The values of equivalent stress and strain were recorded to plot the stress-strain curve and calculate the Young's modulus for both the structures.

2.5 Additive Manufacturing

Porous specimens used in this study were printed using FDM process. In FDM process, a solid wire filament is passed through a heated extruder head, wherein it gets melted, extruded and finally deposited onto a substrate in layer by layer manner [25]. The extruder head is moved in xy-plane according to data obtained from the sliced model. Data of one slice is sent at a time to printer, which results in one layer. The substrate moves down by one layer thickness after printing each layer. Printing continues until full part is printed. Pratham 6.0, an FDM printer, shown in Figure 3(a), has been used to print the porous specimens. It is a heavy duty, industrial grade printer with a build volume of 600 mm x 600 mm x 600 mm. The specimens were printed on the following parameters, layer thickness: 0.2 mm and printing speed: 20 mm/sec. Three specimens of each type were printed. Photographs of the printed specimens are shown in Figure 3(b) and 3(c).

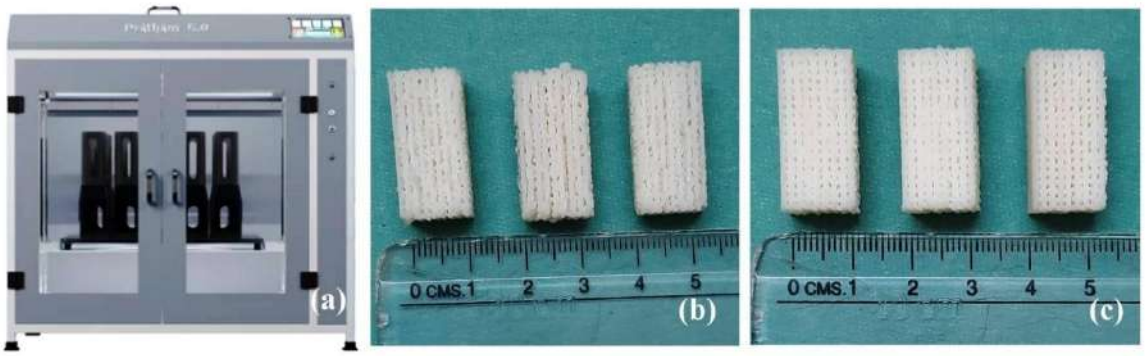

Fig. 3. - Photograps of a) FDM printer Pratham 6.0, b) scaffolds with cylindrical channels, c) scaffolds with cuboid channels

2.6 Testing of Compressive Strength

Compressive strength of printed porous specimens was tested on Tinius Olsen H5KL, a computerized compression testing machine with 5 kN load-cell and a cross-head loading rate of 2 mm per minute.

3. Result and Discussions

The simulated results for both the scaffold structures i.e. cuboid and cylindrical channels were obtained using ANSYS® Workbench. The rendered images with colour coded scale of both the structures for von-Mises stress, elastic strain and total deformation are shown in Figures 4, 5 and 6 respectively. In all the cases, load is applied on the top surface and bottom surface is fixed. The area where maximum and minimum stress and strain developed is shown in Figures 4 and 5 respectively.

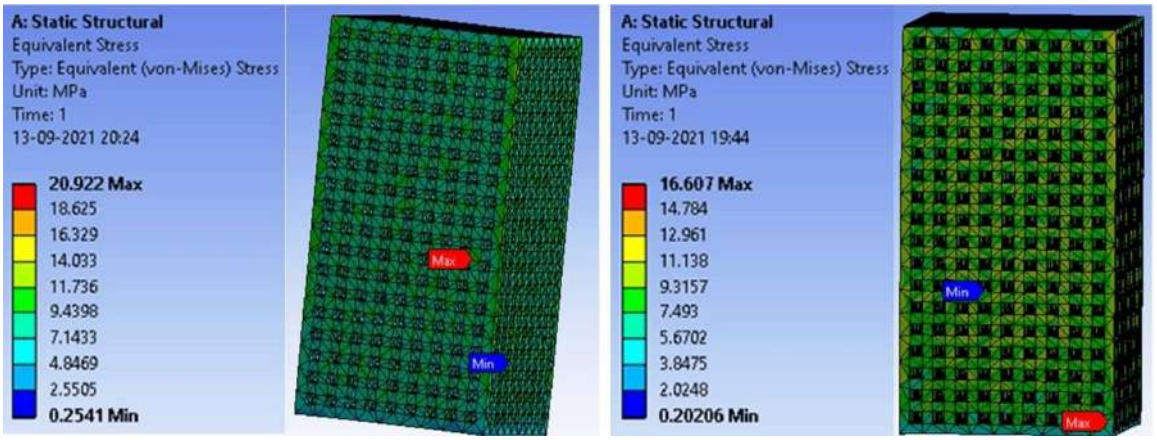

Fig. 4. - ANSYS results for von Mises stress of scaffolds with (a) cylindrical channels (b) cuboid channels

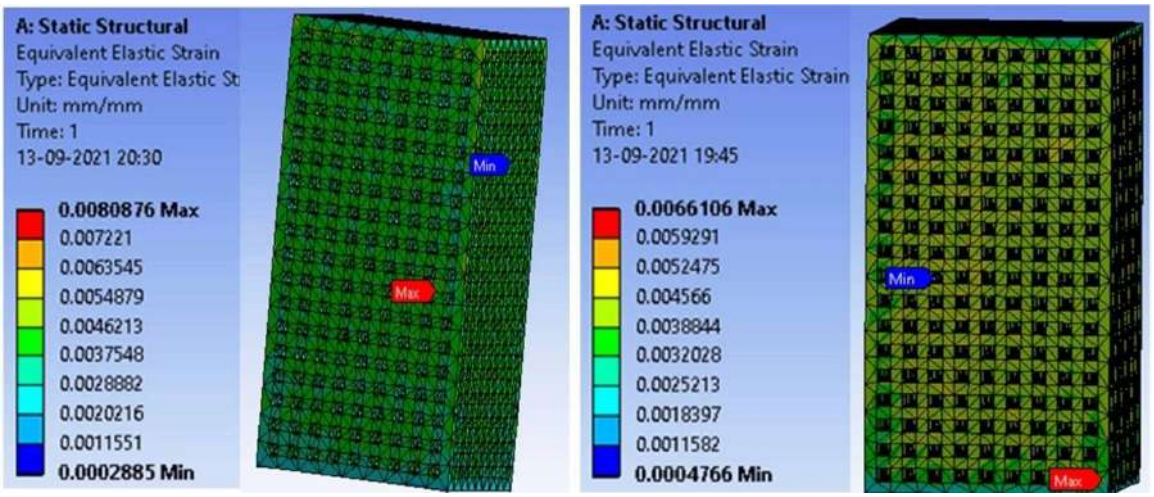

Fig. 5. - ANSYS results for equivalent elastic strain of scaffolds with (a) cylindrical channels (b) cuboid channels

Similarly, the amount of deformation can be seen with the help of rendered image and corresponding scale in Figure 6. Maximum deformation occurs at the face where compressive load is applied; which gradually decreases towards the fixed end and becomes the minimum at the fixed surface.

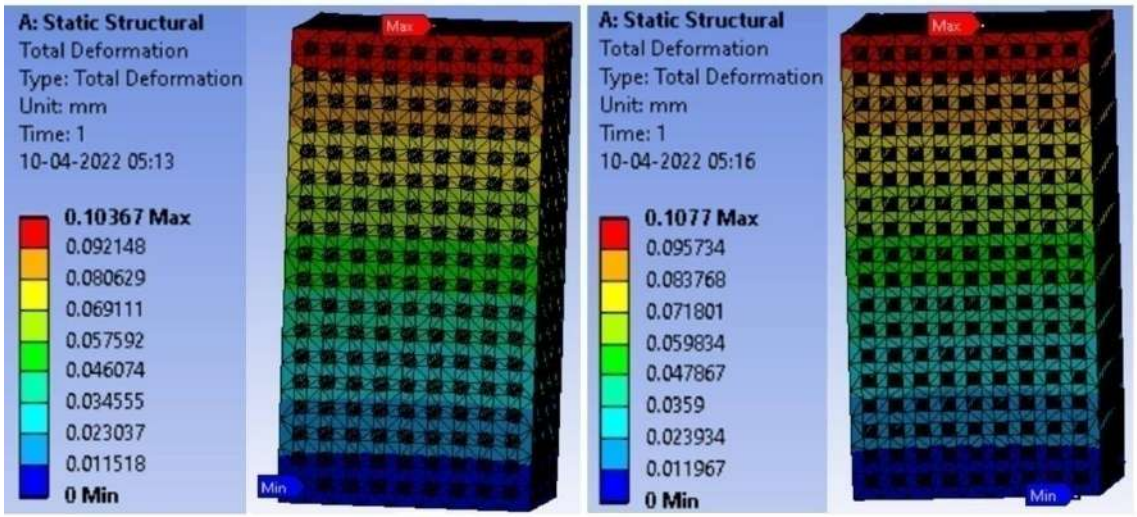

Fig. 6. - ANSYS results for total deformation of scaffolds with (a) cylindrical channels (b) cuboid channels

In Figure 7, stress-strain diagram obtained from linear static simulation for both the structures is shown. It can be seen that stress-strain curve of scaffold with cylindrical channels is steeper than the cuboid channels. This indicates that more force is required to compress the cylindrical channels than cuboid channels. The cylindrical channel consistently exhibits higher stress values at the same strain levels, demonstrating superior structural stiffness. From the slope of the curves, the effective elastic modulus of the cylindrical channel is approximately 25–30% higher than that of the cuboid channel. The cuboid channels consist of sharp edges, where stress concentration occurs that is responsible for lower elastic modulus. Therefore, it can be concluded that structure with cylindrical channels offers better elastic modulus and stiffness in comparison with cuboid channels.

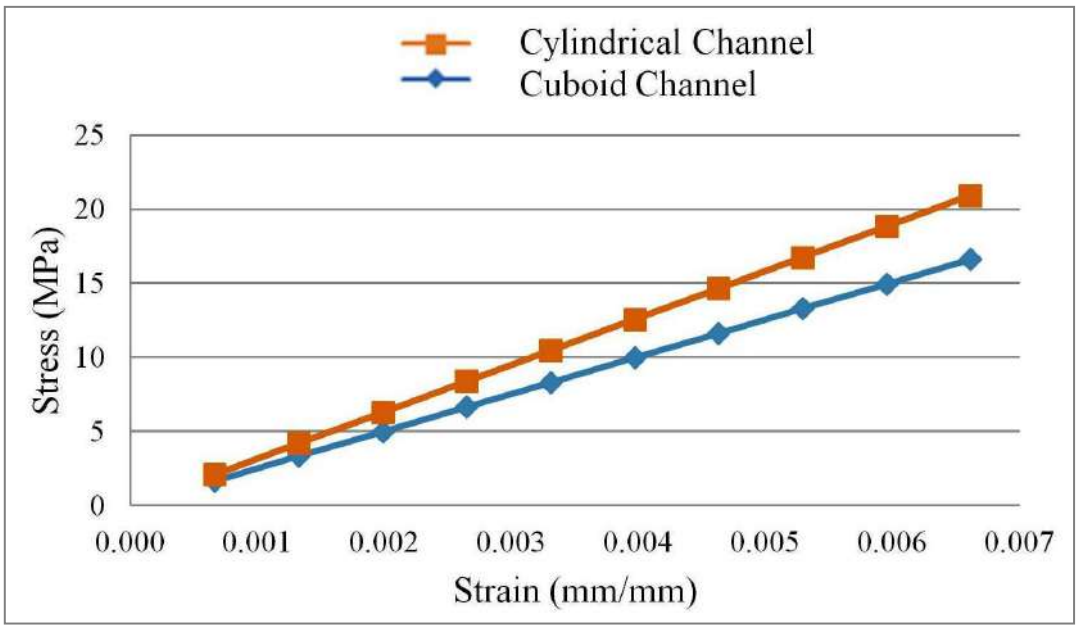

Fig. 7. - Stress-Strain curve for scaffolds with cylindrical and cuboid channels via FEA

Figure 8, presents a comparison of Young's modulus of scaffolds with both the structures. Young's modulus of scaffold with cylindrical channels is 2587 MPa, which is greater than the scaffold with cuboid channels (2512 MPa). This is because the strut region of the cylindrical channels is larger than the cuboid channels and offers more resistance. Moreover, sharp edges present in cuboid structure also make it slightly weaker. There is a difference in total deformation

of both the structures as well, as can be seen from the Figure 9. For cylindrical structure, it is 0.1036 mm; whereas for cuboid structure, it is 0.1077 mm. This also indicates that cylindrical structure possesses better compressive strength.

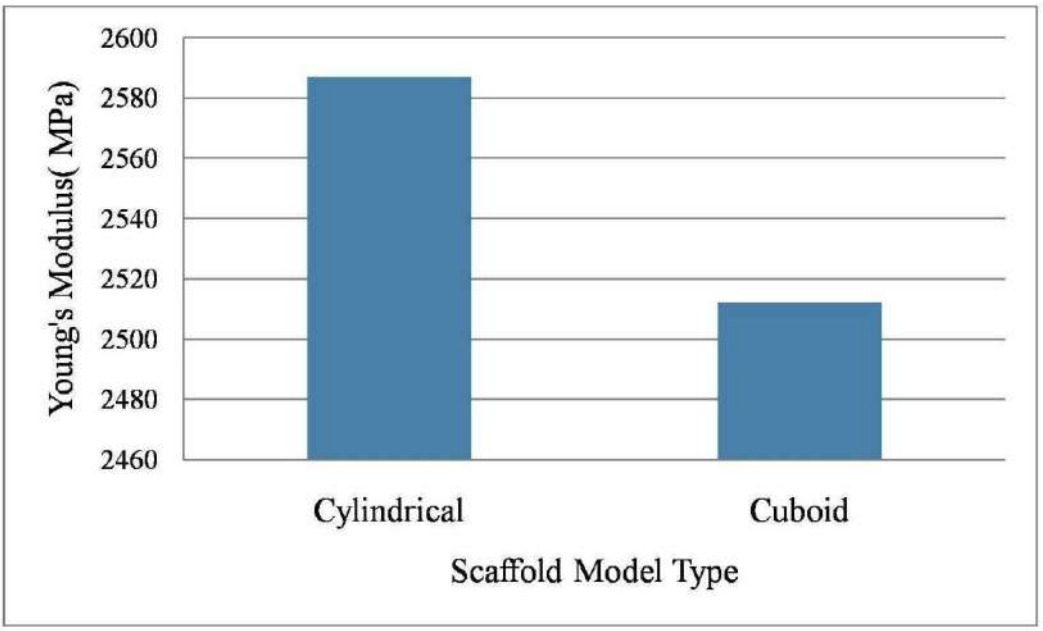

Fig. 8. - Young's modulus of scaffolds with cylindrical and cuboid channels

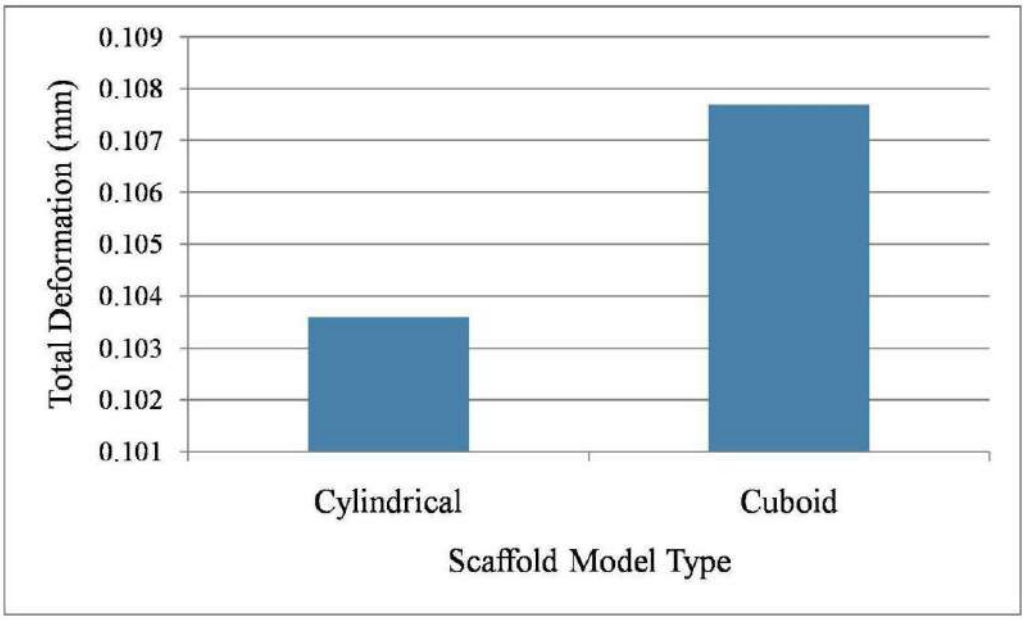

Fig. 9. - Total deformation of scaffolds with cylindrical and cuboid channels

The stress-strain curves obtained via compressive testing of physical specimens are shown in the Figure 10. It is clear from the Figure that scaffolds with cylindrical channels exhibit better mechanical performance in comparison with scaffold with cuboid channels.

On comparing Figure 7 and Figure 10, it can be observed that physical testing confirms results of FEA to some extent. The simulated and actual stress-strain curves show similar trend in elastic region. However, slight difference in stress and strain values in simulated and actual results may be due to the fact that Figure 7 represents an ideal linear static simulation, where the material and geometry are assumed to be perfectly elastic and free from imperfections. In contrast, Figure 10 is based on experimental results, where factors such as machine compliance, specimen alignment, surface contact effects, and minor geometric imperfections slightly reduce the initial stiffness, causing small deviations from perfect linearity. Moreover, slight variation in structural details between CAD model and actual fabricated specimens may also be responsible for introducing slight variation in results.

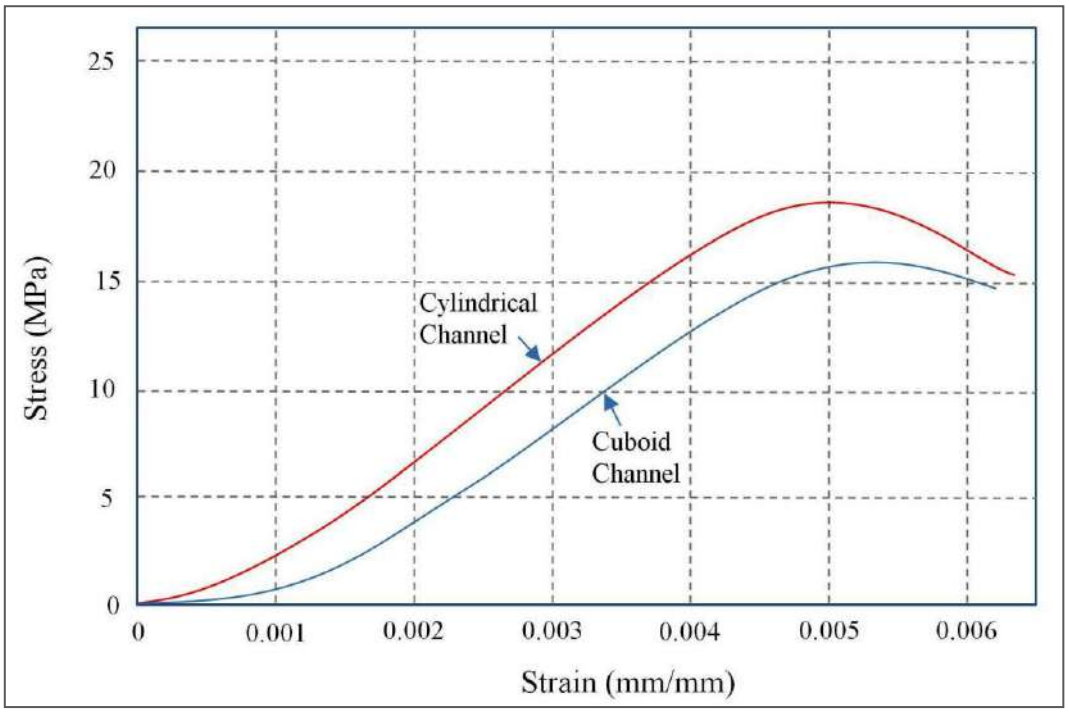

Fig. 10. - Stress-strain curves of porous scaffolds via physical testing

Conclusions

This study investigated the design, modeling, finite element analysis (FEA), and 3D printing of two distinct porous bone scaffolds, one featuring cylindrical channels and the other with cuboid channels. The CAD models for both scaffolds were created using SolidWorks® 2016 software, and their porosity was kept identical to ensure a fair comparison of their mechanical performance. The mechanical properties of the scaffolds were initially assessed using FEA in ANSYS® Workbench, where both scaffolds were subjected to a 500 N compressive load. The FEA results were carefully analyzed, focusing on total deformation, equivalent stress, and strain, which were then validated through experimental compression testing of the additively manufactured specimens. The stress-strain curves obtained from the experimental data were found to be consistent with the FEA predictions, further validating the computational approach. Notably, the scaffold with cylindrical channels exhibited superior strength under the same porosity compared to the cuboid-channel scaffold, highlighting its potential as a more robust design for bone tissue engineering applications. These findings provide valuable insights for researchers in the field, suggesting that cylindrical-channel scaffolds may offer enhanced mechanical properties.

Furthermore, this study paves the way for future research, with opportunities to explore a broader range of structural designs, varying pore shapes, porosity levels, and materials to optimize scaffolds for diverse bone regeneration applications [26-27]. From a BTE perspective, such geometrical optimization becomes particularly relevant when applied to widely used biodegradable materials such as polycaprolactone (PCL) and polylactic acid (PLA), which are extensively employed in additively manufactured scaffolds due to their biocompatibility and tunable degradation behaviour [28]. Therefore, cylindrical-channel architectures fabricated using PCL or PLA may offer improved mechanical reliability for load-bearing bone regeneration applications.

References

[1] Murr L.E. Frontiers of 3D printing/additive manufacturing: from human organs to aircraft fabrication. //Journal of Materials Science & Technology, Vol. 32, Issue 10, 2016. – p. 987-995.

[2] Salmi M. Additive manufacturing processes in medical applications. //Materials, Vol. 14, Issue 1, 2021. – p. 191.

[3] Najmon J.C., Raeisi S., Tovar A. Review of additive manufacturing technologies and applications in the aerospace industry. Additive Manufacturing for the Aerospace Industry, Elsevier, 2019. – p. 7-31.

[4] Lakhdar Y., Tuck C., Binner J., Terry A., Goodridge R. Additive manufacturing of advanced ceramic materials. //Progress in Materials Science, Vol. 116, 2021. – p. 100736.

[5] Gibson I., Rosen D., Stucker B., Khorasani M. Materials for additive manufacturing. //Additive Manufacturing Technologies, Springer Nature, Switzerland, 2021. – p. 379-428.

[6] Aslan B., Yıldız A.R. Optimum design of automobile components using lattice structures for additive manufacturing. //Materials Testing, Vol. 62, Issue 6, 2020. – p. 633-639.

[7] Tang Y., Dong G., Zhou Q., Zhao Y.F. Lattice structure design and optimization with additive manufacturing constraints. //IEEE Transactions on Automation Science and Engineering, Vol. 15, Issue 4, 2017. – p. 1546-1562.

[8] Tao W., Leu M.C. Design of lattice structure for additive manufacturing. //International Symposium on Flexible Automation (ISFA), IEEE, Cleveland, USA, 2016. – p. 325-332.
[9] Zhang Z., Joshi S. An improved slicing algorithm with efficient contour construction using STL files. //The International Journal of Advanced Manufacturing Technology, Vol. 80, 2015. – p. 1347-1362.
[10] Anastasiou A., Tsirmpas C., Rompas A., Giokas K., Koutsouris D. 3D printing: Basic concepts mathematics and technologies. //International Conference on BioInformatics and BioEngineering, IEEE, Chania, Greece, 2013. – p. 1-4.
[11] Chen S., Wang M. Fabrication, properties, and applications of scaffolds for bone tissue regeneration. //Advanced Materials Technologies, 2026. – p. e01877.
[12] Haleem A., Javaid M., Khan R.H., Suman R. 3D printing applications in bone tissue engineering. //Journal of Clinical Orthopaedics and Trauma, Vol. 11, 2020. – p. S118-S124.
[13] Lee S.S., Du X., Kim I., Ferguson S.J. Scaffolds for bone-tissue engineering. //Matter, Vol. 5, Issue 9, 2022. – p. 2722-2759.
[14] Bose S., Vahabzadeh S., Bandyopadhyay A. Bone tissue engineering using 3D printing. //Materials Today, Vol. 16, Issue 12, 2013. – p. 496-504.
[15] Sahu K.K., Modi Y.K. Investigation on dimensional accuracy, compressive strength and measured porosity of additively manufactured calcium sulphate porous bone scaffolds. //Materials Technology, Vol. 36, Issue 8, 2021. – p. 492-503.
[16] Wang C., Huang W., Zhou Y., He L., He Z., Chen Z., He X., Tian S., Liao J., Lu B., Wei Y. 3D printing of bone tissue engineering scaffolds. //Bioactive Materials, Vol. 5, Issue 1, 2020. – p. 82-91.
[17] Modi Y.K., Sahu K.K. Process parameter optimization for porosity and compressive strength of calcium sulfate based 3D printed porous bone scaffolds. //Rapid Prototyping Journal, Vol. 27, Issue 2, 2021. – p. 245-255.
[18] Gibbs D.M., Vaezi M., Yang S., Oreffo R.O. Hope versus hype: what can additive manufacturing realistically offer trauma and orthopedic surgery? //Regenerative Medicine, Vol. 9, Issue 4, 2014. – p. 535-549.
[19] Ziąbka M., Menaszek E., Tarasiuk J., Wroński S. Biocompatible nanocomposite implant with silver nanoparticles for otology – In vivo evaluation. //Nanomaterials, Vol. 8, Issue 10, 2018. – p. 764.
[20] Harper C. Handbook of Plastics, Elastomers and Composites. New York: McGraw-Hill, 2002.
[21] Elix Polymers. Products for Medical Applications. Tarragona: Elix Polymers, 2016. – Available at: http://www.elix-polymers.com (Accessed: 15/09/2025).
[22] Ziąbka M. A review of materials used in middle ear prosthetics. //Materiały Ceramiczne (Ceramic Materials), Vol. 70, Issue 1, 2018. – p. 65-85.
[23] PJ J.F., Arun K.J., Navas A.A., Joseph I. Biomedical applications of polymers – An overview. //Macromolecules, Vol. 28, Issue 4, 2018. – p. 939-944.
[24] ISO 604:2002. Plastics – Determination of Compressive Properties. Geneva: International Organization for Standardization, 2016. – Available at: https://www.iso.org/standard/31261.html (Accessed: 15/09/2025).
[25] Gorana F., Modi Y.K. Process parameter optimization for fabrication of acrylonitrile butadiene styrene parts. //Materials Today: Proceedings, Vol. 103, 2024. – p. 109-114.
[26] Gorana F., Modi Y.K. Optimization of porosity and strength of selective laser-sintered polyamide porous scaffolds useful in bone tissue engineering. //Rapid Prototyping Journal, Vol. 31, Issue 6, 2025. – p. 1141-1155.
[27] Gorana F., Modi Y.K. Multi-objective optimization for porosity and strength of selective laser sintered porous scaffolds useful in bone tissue engineering. //Iranian Journal of Science and Technology, Transactions of Mechanical Engineering, Vol. 49, Issue 3, 2025. – p. 1345-1360.

Information of the author

Modi Yashwant Kumar, PhD, Dr., associate professor, Jaypee University of Engineering and Technology
e-mail: yashwant.modi@juet.ac.in

DOI 10.52209/2706-977X_2026_1_89 **IRSTI 55.03.31** **UDC 621.313.333**

Influence of the Seed Shaft Parameter of the Linter Machine on the Dynamics and Load of the System

Yunusov S.Z.[1], Kasimova D. A.[2]
[1]Tashkent State Transport University, Tashkent, Uzbekistan
[2]Andijan State Technical Institute, Andijan, Uzbekistan
*corresponding author

Abstract. This paper deals with the dynamic study of a machine unit with the mechanism of the seed shaft of a linter machine designed for cleaning cotton fibre from seed residues. Taking into account that the working bodies of the machine operate under variable loads, the authors carry out a comprehensive analysis of the influence of inertial, elastic and dissipative properties of the system on the transient and steady-state modes of its operation. Particular attention is paid to moments of inertia, resistance of the technological environment and the influence of belt transmission parameters. The mathematical model is formulated on the basis of Lagrangian equations of the second kind taking into account the moments of resistance arising in the process of linting. The drive is investigated as a two-mass system, and the model also takes into account the oscillations of the process resistance moment described by a sinusoidal function. For numerical solution of the system of nonlinear differential equations the Runge-Kutta method in Mathcad environment is applied. Calculations at different values of stiffness, viscous friction and resistance amplitude coefficients determining the dynamic behaviour of the system have been carried out. Graphs of change of torque, angular velocity of rotor and seed shaft, as well as dependence of start-up time on the level of technological resistance were obtained. It is established that the increase of the moment of technological resistance leads to the decrease of the torsional oscillation range, but increases the angular velocity of the motor, contributing to the reduction of the steady-state time. The results of the research allow optimising the parameters of the machine unit, increasing the stability of its operation and energy efficiency. The work is of interest to developers and researchers of machines in the cotton processing industry, as well as specialists in the field of applied mechanics.

Key words: linear machine, seed shaft, dynamics of machine unit, transition mode, belt transmission, torque fluctuations, angular velocity, asynchronous electric motor, modelling, Mathcad, technological resistance, torsional vibrations, stability of mechanical system, cotton processing equipment.

Introduction.

Currently, about 100 cotton processing enterprises operate in Uzbekistan. The enterprises are working on modernizing machines and equipment. The main goal of modernizing the factories is to increase machine productivity and produce high-quality products, including lint, that meet the requirements of the global market [1, 2]. The cotton ginning industry produces three types of lint. The first type of lint contains fibres with a masslength of 13/14 mm or more, the second type - from 7-8 to 12-13 mm, and the third type - 6-7 mm or less. In addition, the lint is also characterised by its grade, which is determined according to the grade of the seeds to be processed [3-5]. The process of linting of cotton seeds originated as a preparatory process necessary to maximise the compression of oil from the cotton seeds. The resulting lint had no industrial value. Seed linting was performed on lintering machines developed similar to saw gins in the United States of America [6, 7]. In the creation of machines for cotton ginning industry with high parameters can be realised only on the basis of deep knowledge of physical processes occurring in machines in different loading modes and development of new, more perfect methods of calculation of acting loads, which are the basis for calculation of machine parts and units for strength and endurance. Especially urgent are the issues of development and refinement of methods of calculation of drives and shafts of machines of large capacity or importance for production. This would make it possible to carry out production tests to refine the adopted parameters. One such machine in the cotton processing industry is the linter machine. The lintering process is carried out on linter machines, where the main working organ is the saw cylinder. It is the drive of the saw cylinder of linter machines 18.5 kW that consumes a significant amount of power in the machine.

In the majority of production processes, including lintering process, the load on the motor of machine units is variable. As it is known, the main structural elements of machine units used in technology for driving the working organ are: engine; clutch; gearbox or gearbox (or variator); working organ drive mechanism (belt gears). It has been found that due to varying loads, many machine units operate at varying energy inputs to the engine and varying engine speeds [8].

Usually, the working shafts of machine units in the cotton industry are affected by the parameters (weight, moisture, etc.) of the processed raw material (raw cotton, fibre, seeds) [9]. In [10] it is noted that the maximum load modes in the drive of cotton processing machines are characteristic in the acceleration mode, which is performed either by changing the operating mode of the machine unit at a constant speed of movement, or by changing the speed of the

machine unit without changing the operating mode. At the same time, the dynamics of the machine unit at each stage of its movement (acceleration, steady-state movement, gear shifts, stops) have peculiarities in the load modes of both the electric motor and the drive.

In order to overcome such a load without a significant drop in the average speed of operation, it is necessary to use motors with a higher power than would be required if only the external load and the given time of its execution were taken into account, without taking into account the work required for transients in the motor and for the recovery of the kinetic energy of the moving masses of the machine unit lost in the drop in speed after overcoming each recurring peak of the variable load. The greater the frequency and amplitude of load variation and the higher the required average operating speed, the greater the motor power required and the greater the proportion of its work lost to transients. And so, in the process of linting effective work of the seed shaft depends mainly on the dynamic parameters of the machine unit, including the moments of inertia of the masses, elastic, dissipative properties of the belt transmission and the nature of technological loads from raw cotton. To substantiate these parameters it is necessary to investigate the dynamics of transient and steady-state modes of operation of the machine unit of the seed shaft of the seed shaft of the linter machine [11].

During the operation of the linter machine drive, the inertial characteristics of the working bodies of the machine unit change within wide limits. Since the drive includes elements with belt and chain transmissions, as well as variators of unequal angular velocities with non-linear characteristics [12].

1. Main theoretical part

In this case, the nonlinear dynamic model of the drive is represented by the coupling of the moments of inertia of centred masses (*Ji*) and stiffnesses (*C*). The dynamic model of the machine unit with the seed shaft mechanism of the seed shaft of the linter machine is presented in Fig. 1. In this case, the machine unit is a two-mass system, the first mass - the rotor of the electric motor, the second mass - the mass of the seed shaft - the masses of discs and bars of the seed shaft. All discs and slats are counted as one mass.

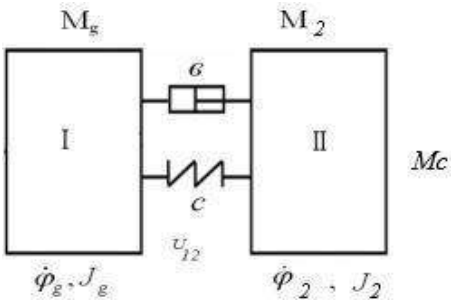

Fig. 1. - Dynamic model of a machine unit with the mechanism of the seed shaft mechanism of the linter machine seed shaft.

The dynamic study of the machine unit with the mechanism of the seed shaft of the linter seed shaft will be considered in the following modes of motion - the transitional mode of the system start; - the established mode of operation of the system. At the same time, the fluctuations of the angular velocity of the seed shaft and the load on the drive are mainly considered.

At researches the asynchronous motor was considered in the form of dynamic mechanical characteristic, offered by I.S.Pinchuk [13,14,16]

$$\dot{M}_{\mathrm{g}} = 2\,M_k\,\omega_c - 2M_k\,\mathrm{p}\,\dot{\phi}_{\mathrm{g}} - \omega_c\,S_k\,M_{\mathrm{g}} \qquad (1)$$

where M_g, M_k - driving and critical moments of the motor;

ω_c- angular frequency of the network;

ϕ_g- angular displacement of the motor rotor;

S_k- critical slip of the motor.

We will use the Lagrange equation of the second kind [15-17] to formulate the differential equations of motion of this linter machine system:

$$\frac{d}{dt}\left[\frac{\partial T}{\partial \dot{\phi}_i}\right] - \frac{\partial T}{\partial \phi_i} + \frac{\partial \Pi}{\partial \phi_i} + \frac{\partial \Phi}{\partial \dot{\phi}_i} = M_i(\phi_i) \qquad (2)$$

where, T - kinetic energy of the system;

Π - potential energy of the system;

Φ - dissipative Rayleigh function;

φ_i - generalised coordinate;
$\dot{\phi}_i$ - generalised velocity;
$M_i(\phi_i)$ - generalised force.

The seed shaft drive consists of an electric motor and a belt transmission, by means of which the movement is transmitted to the working shaft. The following kinematic relations are valid for this drive system:

$$U_{12} = \frac{\dot{\phi}_g}{\dot{\phi}_2} \tag{3}$$

where, $\dot{\phi}_g, \dot{\phi}_2$ - angular velocities of the motor rotor, seed shaft, s^{-1};
U_{12}- transmission ratio of the belt transmission.

For generalised coordinates we take angular displacements of rotating masses of the machine unit, $\dot{\phi}_g, \dot{\phi}_2$. The kinetic energy of the considered system has the form:

$$T = \frac{J_g \dot{\phi}_g^2}{2} + \frac{J_2 \dot{\phi}_2^2}{2} \tag{4}$$

The potential energy of the system is a homogeneous quadratic form of the generalised coordinates and is written in the following form:

$$\Pi = \frac{1}{2}\left[c \cdot \left(\phi_g - U_{12} \cdot \phi_2\right)^2\right] \tag{5}$$

The dissipative Rayleigh function for this system is expressed as:

$$\Phi = \frac{1}{2}\left[b \cdot \left(\dot{\phi}_g - U_{12} \cdot \dot{\phi}_2\right)^2\right] \tag{6}$$

Next, we define the terms of the Lagrangian equations:
(a) derivatives of the kinetic energy of the machine unit

$$\frac{d}{dt}\left(\frac{\partial T}{\partial \dot{\phi}_g}\right) = J_g \ddot{\phi}_g; \frac{d}{dt}\left(\frac{\partial T}{\partial \dot{\phi}_2}\right) = J_2 \ddot{\phi}_2 \tag{7}$$

b) partial derivatives on displacements from potential energy

$$\frac{\partial \Pi}{\partial \phi_2} = c \cdot (\phi_2 - U_{12}\phi_2); \tag{8}$$

c) partial derivatives on velocities from the dissipative function

$$\frac{\partial \Phi}{\partial \dot{\phi}_g} = в \cdot \left(\dot{\phi}_g - U_{12} \cdot \dot{\phi}_2\right); \ \frac{\partial \Phi}{\partial \dot{\phi}_2} = -в\, U_{12} \cdot \left(\dot{\phi}_g - U_{12} \cdot \dot{\phi}_2\right) \tag{9}$$

e) generalised forces (moments):

$$M\left(\phi_g\right) = M_g; \quad M(\phi_2) = M_C - M_{pri}; \tag{10}$$

where M_C - is the moment of resistance from the cotton on the seed shaft, *Nm*; M_{pri} -is the moment of resistance from the rest of the drive, *Nm.*

Putting in (2) certain terms of Lagrangian equations, we obtain the differential equations of motion of the machine unit of the seed shaft of the seed shaft of the linter machine:

$$\begin{gathered} \dot{M}_g = 2M_k\omega_c - 2M_k p\dot{\phi}_g - \omega_c S_k M_g; \\ J_g\ddot{\phi}_g = M_g - c\left(\phi_g - U_{12}\phi_2\right) - в \cdot \left(\dot{\phi}_g - U_{12}\dot{\phi}_2\right) - M_{pri} \\ J_2\ddot{\phi}_2 = U_{12}c\left(\phi_g - U_{12}\phi_2\right) + U_{12}b\left(\dot{\phi}_g - U_{12}\dot{\phi}_2\right) - M_C - M_{pri} \end{gathered} \tag{11}$$

2. Main practical part

The resulting system of nonlinear differential equations (11) is difficult to solve analytically, so the solution of system (11) is performed on a PC. The Runge-Kutta method was chosen as the numerical method, in which the function is calculated sequentially by incrementing the argument under given initial conditions. The mathematical program "MathCad" was used. To do this, the following transformations need to be performed:

$$_g(t) = _1(t); _g(t) = _1(t)$$
$$_g(t) = _2(t); _g(t) = _2(t) = _3(t); \ddot{g}(t) = _3(t);$$
$$_2(t) = _4(t); _2(t) = _4(t) = _5(t); \ddot{2}(t) = _5(t) = _6(t);$$

After transformations using the mathematical software "MathCad" and taking into account the accepted designations, the mathematical model of the machine unit with the seed shaft mechanism of the linter machine will be presented as follows:

$$y := (0\ 0\ 0\ 0\ 0\ 0)^T$$

$$D(t,y) := \begin{bmatrix} 2\cdot M_k\cdot\left(W_c - P\cdot y_3\right) - W_c\cdot S_k\cdot y_1 \\ y_3 \\ \left[\dfrac{y_1 - C\cdot\left(y_2 - U_{12}\cdot y_4\right) - b\cdot\left(y_3 - U_{12}\cdot y_5\right) - M_{pri}}{J_d}\right] \\ y_5 \\ \dfrac{y_1 - \dfrac{C\cdot\left(y_2 - U_{12}\cdot y_4\right)}{U_{12}} + \dfrac{b\cdot\left(y_3 - U_{12}\cdot y_5\right)}{U_{12}} - M_c - M_{pri}}{J_2} \\ \alpha \end{bmatrix}$$

To obtain the solution, it is necessary to set the initial conditions and initial parameters of the system.

$$t_0 = 0;\ = _2 = 0; _g = _2 = 0; M_g = M_r = M_{or}$$

Drive of the executive body of the mechanism of the accelerator mechanism of the raw material roller of the saw gin is carried out by the asynchronous electric motor with squirrel-cage rotor of mark 4A90L4U3 [18] are given on Table 1.

Table 1. Parameters of the asynchronous electric motor

Parameter	Value
rated motor power	N=11 kW
nominal number of rotor revolutions of the motor rotor per minute	n=960 min^{-1}
critical (maximum) torque on the engine rotor shaft	M_k=M_n-2=218,8 Nm
nominal moment on a shaft of a rotor of the motor	M_n=9550-(N/n)=9550-(11/960)=109,4 Nm
mains frequency	*fc=50 Hz*
number of pole pairs	*P=2*

Calculation of necessary parameters and motor coefficients was made as follows [18] (Table 2).

To determine the influence of dynamic parameters of the machine unit with the seed shaft and to find the relationship between other parameters of the system and modes of its motion, we give the following variations:

- coefficient of stiffness dissipation of elastic element from technological resistance of the system c=100÷1000 Nms/rad;
- coefficient of dissipation or viscous friction b=0,5÷5 Nms/rad. This range of variation, established by the results of experiments for the elastic element;
- moment of resistance from technological load (seed shaft) on the seed shaft M_C at angular speed n=300;350;400;450;500 min^{-1}, which corresponds to M_C = 260; 245,9; 218,5; 197,5; 178,9 Nm

Table 2. Calculation of necessary parameters and motor coefficients was made

Circular frequency of the network	$\omega_S=2\pi f_S=314$ rad/sec.
Nominal angular speed of the motor rotor	$\omega_n=\pi n/30=3,14\text{-}960/30=100,5$ rad/s.
Angular velocity of ideal idling of the electric motor rotor	$\omega_O=2\pi f_S/P=2\text{-}3,14\text{-}50/2=157$ rad/s.
Moment of inertia of the electric motor rotor	$J_e= GD^2/4g=0,24/4\text{-}9,81=0,061$ Nms^2
Nominal slip value	$S_n= (\omega_O- \omega_n) / \omega_{(O)} =(157\text{-}100,5)/157=0,36$
Critical value of slip	$S_k = \lambda \cdot S_H \left(1+\sqrt{1-\frac{1}{\lambda^2}}\right) = 1,34$

Consideration of technological loads on the working body is explained by the fact that this parameter will not mediate on the load of the drive. From the known method [10] approximate function of mathematical expectation of the moment of technological resistance force from the material has the form $M1=M_C+M(0)\ (Sin\alpha t)$ where, $M0$- amplitude of fluctuations of the moment of resistance.

The range of variation of the values of the stiffness and dissipation coefficients is established by the calculation data for V-belt gears of types A and B [18-22].

The technological resistance acting on the seed roll seed shaft during linting varies widely depending on the seed shaft rotation speed as well as on the seed roll density (Table 3) [23].

Table 3. The technological resistance

n (seed shaft) ., (min^{-1})	300	350	400	450	500
M_C (N m)	260	245.9	218.5	197.5	178.9
m, (kg)	51	46	42	39	36

3. Analysis of results

As a result of realisation of the mathematical model of the machine unit, graphical dependences (laws of motion of the system) are obtained, which are shown in Fig. 2.

From Fig. 2. it can be seen that taking into account the amplitude of oscillation of the resistance moment from the seeds, the torque and angular velocity of the electric motor shaft, as well as the seed shaft changes. To determine the rational dynamic parameters carried out possible variations that are summarised in Table 4, which shows the effect of changing $M0$- the amplitude of the oscillation of the drag torque, stiffness coefficient and dissipation of the elastic transmission on the value of motor torque Mg and its angular velocity φg, as well as on the angular velocity of the seed shaft and $\varphi(g)$.

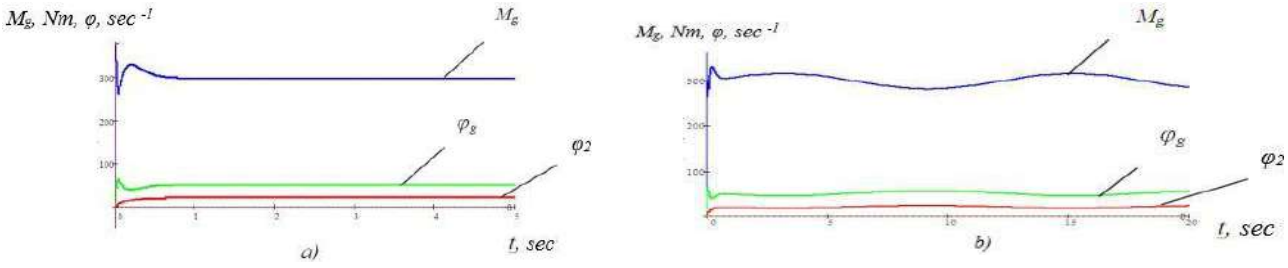

a) graphs of change of Mg and φg, $\varphi(thief)$, without taking into account the amplitude of oscillations of the seed resistance moment; b) graphs of change of M_g and φg, $\varphi thief$, at $M1=M_C+M0Sin\alpha$; $M_C=100$; $M0=10$; $\alpha=\pi/6$

Fig. 2. - Graphs of change of driving torque of induction motor and angular velocities of drive shafts

Table 4. The rational dunamic parameters

M0 = 5					M0 = 15			
C	50	100	150	500	50	100	150	500
Mg	220	220	220	220	237	237	237	237
	202	202	202	202	185	185	185	185
φg	84	84	84	84	90	90	90	90
	78	78	78	78	72	72	72	72
φ2	35	35	35	35	37	37	37	37
	32	32	32	32	30	30	30	30
M0 = 10					M0 = 20			
g	228	228	228	228	245	245	245	245
	194	194	194	194	177	177	177	177
φg	87	87	87	87	93	93	93	93
	75	75	75	75	69	69	69	69
φ2	36	36	36	36	39	39	39	39
	31	31	31	31	28	28	28	28

The analysis of the obtained data characterising the operation of the machine unit in different technological modes and at different system parameters leads to functional dependences of the range of oscillations of angular velocity *Δφg*, torque *ΔMg* on the electric motor shaft. Which are presented in Fig.3. they show that at increase of technological resistance M_C from 103,4 Nm to 115 Nm the range of motor torque ΔM_g oscillations decreases from 96,04 Nm to 76,24 N-m accordingly. A similar increase in M_S affects the angular velocity spread of the engine shaft of the machine unit $\Delta\varphi_g$ positively, that is, the spread $\Delta\varphi_g$ also increases from 6.8 rad/s.to 13.4 rad/s.

From the tabulated data, it can be seen that the values of Mg, φ_g and φ_2 at increasing the amplitude of oscillation of the resistance torque M0 from 5 to 20 decrease respectively M(g) from 202 Nm to 177 Nm, φ(g)from 78 rad/s to 69 rad/s and φthief from 32 rad/s to 28 rad/s.

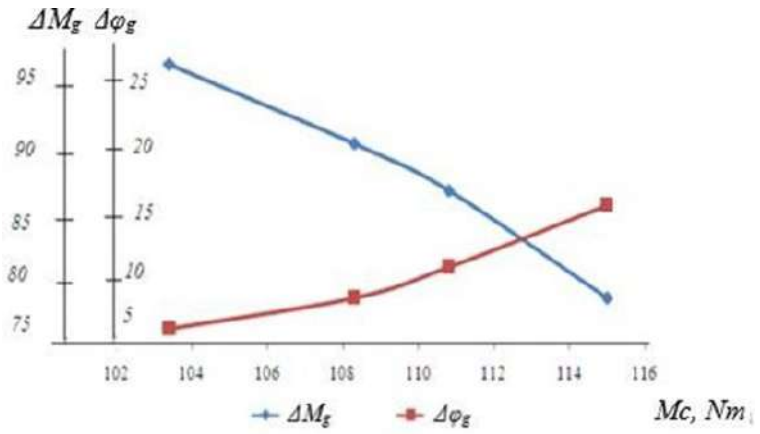

Fig. 3. - Effects of process resistance *Mc* on the variation of torque (*Mg*) and angular velocity *φ(g)* ofthe motor of the machine unit with linter machine seed shaft mechanisms

Consequently, the effects of drag torque $M1=M_C+M_0\text{Sin}\alpha$ will affect the dynamic loads of the machine. We can also consider the effects of the oscillation frequency of the drag torque α. As the oscillation frequency increases, changes in Mg, and φ(2) are observed which are shown in Fig. 4.

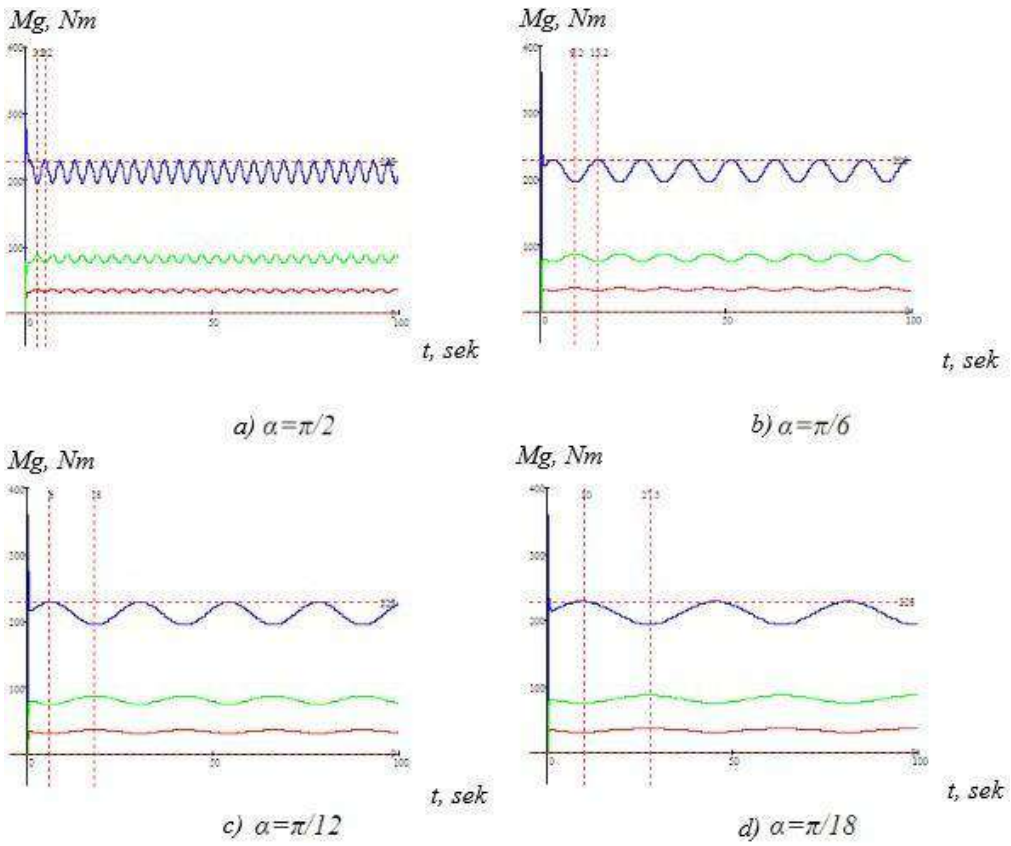

Fig. 4. - Variation of M_d and φ of the seed shaft as a function of oscillation frequency α: M_C=100; M_0=10; C=50; b=2

By solving the mathematical model of the machine unit, taking into account the seed shaft of the seed shaft, it is possible to determine the main stage of the machine unit operation, i.e. the "start-up" period.

It is known that any machine unit operates in the following stages: "Start"-entry into the established mode; "Mode"-established mode; "Stop"-from the established mode to a complete stop, which are shown in Fig. 5 [23-26].

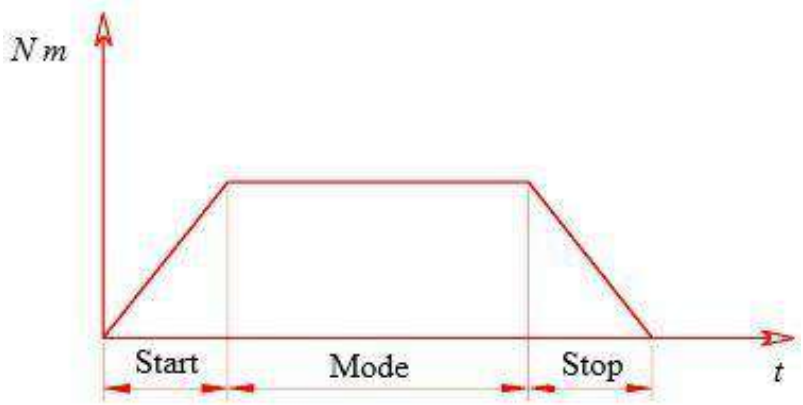

Fig. 5. - Operating modes of the machine unit

It is clear that the painless passage of the "start-up" mode directly affects the operation of the machine unit Therefore, we were interested in the question of the "start-up" time. The analysis of the data obtained when solving the problem of dynamics of the machine unit of the linter machine with a seed shaft of the seed shaft shows that when the force of technological resistance from the matershaft shaftial M_1 increases from 103 to 115 *Nm* the time of "start" *tstart*

are different. This can be seen in fig. 6. are curves where it can be clearly seen that the difference between the process resistances M1 affects the "start up" time. At values of technological resistance *M1* from 103 *Nm* to 115 *Nm*, the start-up time for the motor shaft is from 1.7 *sec*. to 1.5 *sec*. respectively for the seed from 1.5 *sec*. to 1.3 *sec*. This is due to the fact that the mass of the seed shaft dampens the peak stage of the start-up mode and thus the transition to the set mode takes place.

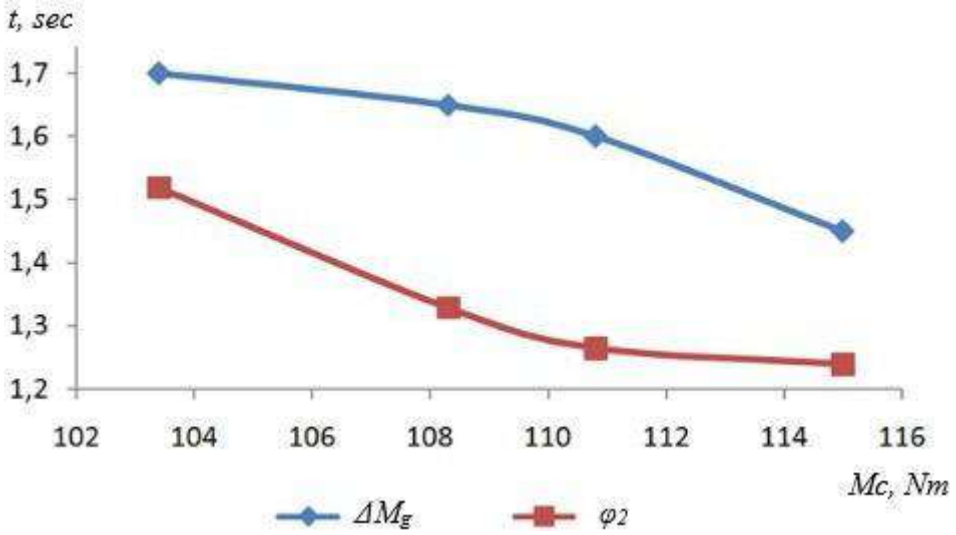

Fig. 6. - Changes in the start-up time of the seed shaft machine depending on the technological resistance

Conclusion

It is revealed that with the increase of the moment of technological resistance affects the range of torque fluctuations (decreases) and the range of angular velocity (increases).

This indicates that the moment of technological resistance affects the process of "start-up" of the system. The difference between peak and nominal values is reduced, and the decrease in the start-up time confirms this.

If we take into account that the moment of technological resistance overestimate from the angular speed of the seed shaft of the seed shaft of the linter machine, we can conclude that the growth of the angular speed of the seed shaft leads to a faster start-up process, which is important in the operation of the machine unit.

References

[1] Sulaimonov R.Sh. et al. Improvement of the main units of the working chamber linter // Universum: technical sciences : electronic scientific journal, 2022, 3(96).
[2] Azamatovich O., O'g'li A., Akramovich Q. Determining the optimal parameters of an advanced linter machine // Engineering, 810-820. doi: 10.4236/eng.2023.1512057.
[3] Bittenbinder I.A. Productivity of linter machine, Collection of works. // All-Union Congress of ITR, 1982.
[4] Yunusov, S.Z., Kenjayev, S.N., Makhmudova, Sh.A. Shafts of technological machines with combined supports // E3s Web of Conferences, 2023, 401, 01059.
[5] Yunusov S.Z., Kenjayev S.N., Makhmudova Sh.A., Islamova G.X. Full factorial experiment in research the parameters of a combined shaft of technological machines // E3S Web of Conferences, 2023, 401, 03043.
[6] Metalworker's Handbook in five volumes. Mashgiz - 1959.
[7]Mukhammadiev D., Ibragimov F., Abzoirov O. Experimental study of the bending of the linter machine saw blade // E3S Web of Conferences 390, AGRITECH-VIII, 2023.
[8] Kozhevnikov S.N. Dynamics of machines with elastic links – Kiev: 1961. - C.160.
[9] Dzhuraev A. Rotational mechanisms of technological machines with variable transmission ratios. – Tashkent: Mekhnat 1980. - 215 p.
[10] Dzhuraev A. Dynamics of working mechanisms of cotton processing machines. - T.: Fan, 1987. 168 c.
[11] Yunusov S.Z., Makhmudova Sh.A., Kasimova D.A. Increasing the efficiency of the seed shaft of the linter machine //Technology and Quality, 2024, № 3(65). - C. 37-41. doi.org/10.34216/2587-6147-2024-3-65-37-41.
[12] 5LP Linter Machine-Building Passport of Tashkent Cotton Cleaning Research Institute, 1981;18.
[13] Den-Gartog D.P. Mechanical vibrations. - M.: Fizmatgiz, 1960.-580 p.
[14] Dzhuraev A. Modelling of dynamics of machine units of cotton processing machines. - T.: Fan, 1984. - 128 c.
[15] Gao P., Xie L., Pan J. Reliability and availability models of belt drive systems considering failure dependence //Chinese Journal of Mechanical Engineering, 2019, 32, 1-12.
[16] Panovka J.G. Fundamentals of applied theory of vibration and impact, 1976, - 234 p.
[17] Targ S.M. Short Course of Theoretical Mechanics. - M.: Nauka, 1988. - 480 p.
[18] Lixin Zhang, Jean W. Zu, Zhi-chao Hou / Complex Modal Analysis of Non-Self-

Adjoint Hybrid Serpentine Belt Drive Systems // Journal of Vibration and Acoustics. 123(2), April 2001, DOI:10.1115/1.1356697
[19] Krawczyk A.E. et al.Asynchronous Motors of 4AM Series // Energoizdat, 1982. - 504 p.
[20] Li X. J., Chen, L. Q. Modal analysis of coupled vibration of belt drivesystems // Applied Mathematics and Mechanics, 2008, 29(1), 9-13.
[21] Mukhammadiev D. M., Ibragimov F. H., Abzoirov O. H. Performance analysis of a linter machine with a new design of inter-saw pad // Modern Innovations, Systems and Technologies - Modern Innovations, Systems and Technologies, 2022, 2(3), 0401-0409. https://doi.org/10.47813/2782-2818-2022-2-3
[22] Rivin E.I. Dynamics of machine tool drives. - M.: Mashinostroenie 1966.p. 204.
[23] Yunusov S.Z., MakhmudovaS.A., Kasimova D.A., Agzamov M.M. The influence of changes in technological loads on the deflection of the saw cylinder shaft of a linting machine //Material and mechanical engineering technology, 2025 (1), 10.52209/2706-977X_2025_1_8
[24] Obidov A.A., Sarimsakov O.Sh., Hamidov S.D. Dynamic problem of interaction of cotton with processing working bodies of machines //Universum: Technical Sciences: electronic scientific journal, 2020, 10(79). URL: https://7universum.com/ru/tech/archive/item/10746.
[25] Wilson A., Green T. Belt drives in modern mechanical systems: design and optimization. - Berlin: Springer, 2022. – 502 p.
[26] Feridman M.V. The moment of inertia of bodies. - M.: Mashinostroenie, 1977. - 511 p.

Information of the authors

Yunusov Salokhiddin Zunununovich, d.t.s., professor, Tashkent State Transport University
e-mail: Uzbekistanysz1979@gmail.com

Kasimova Dilafruz Alisherkizi, teacher assistant, Andijan State Technical Institute, Andijan
e-mail: Uzbekistankasimova_d@andmiedu.uz

DOI 10.52209/2706-977X_2026_1_98 **IRSTI 55.57.43** **UDC 621.927**

Determination and Optimization of Working Parameters of a Sheep House Feeding Device Based on the Discrete Element Method

Fan Zhihao[1], **Wen Baoqin**[1], **Reshetnikova O.S**[2*], **Li Jinbin**[1], **He Xiaowei**[3]
[1]School of Mechanical and Electrical Engineering, Shihezi University, Shihezi, China
[2]Abylkas Saginov Karaganda Technical University, Karaganda, Kazakhstan
[3]College of Mechanical and Electrification Engineering, Tarim University, Alar, China
[*]corresponding author

Abstract. To achieve precise feeding, this study coupled a Discrete Element Method (DEM)-based virtual test platform with the Response Surface Method (RSM) to quantitatively evaluate and optimize the effects of traveling speed (X_1), scraper rotation speed (X_2), and conveyor belt speed (X_3) on unit feeding amount (Y_1) and feeding uniformity (Y_2). A simplified core model of the feeding device was established in EDEM, and the cohesive characteristics of Total Mixed Ration (TMR) were characterized using the Hertz–Mindlin with JKR Cohesion contact model. A three-factor, three-level Box–Behnken experimental design was employed to fit quadratic regression models for Y_1 and Y_2. The results indicated that both models were statistically significant ($P < 0.0001$). The significant influencing factors for Y_1 were ranked as $X_1 > X_2 > X_3$, while those for Y_2 were ranked as $X_2 > X_3 > X_1$. Based on the analysis of interaction effects among parameters and multi-objective desirability optimization (targeting Y_1 = 10–12 kg·m^{-1} and maximizing Y_2), the optimal combination was determined as X_1 = 3.05 km·h^{-1}, X_2 = 84.9 r·min^{-1}, and X_3 = 326.5 r·min^{-1}. After rounding for engineering application, X_1 = 3 km·h^{-1}, X_2 = 85 r·min^{-1}, and X_3 = 330 r·min^{-1} yielded verification results of Y_1 = 11.49 kg·m^{-1} and Y_2 = 91.54%, with prediction deviations below 5%. Within the studied geometric and parameter ranges, the material flow remained continuous and stable, without persistent arching or blockage. Therefore, the analysis primarily focused on uniformity and throughput. This study provides executable operational parameters and a transferable parameter design approach applicable to cohesive feed systems.

Keywords: discrete element method, EDEM, response surface method, feeding uniformity, unit feeding amount, Total Mixed Ration (TMR)

Introduction

In large-scale sheep farming, the structure and control method of the feeding device are directly related to feed distribution uniformity and feeding cost [1]. At present, various mechanical feeding systems are employed in sheep houses, including belt conveyors, chain/scraper conveyors, screw augers, throwing-type distributors, and multi-mechanism composite systems [2]. These devices have been widely applied in practical production. Over the past decade, the Discrete Element Method (DEM) has gradually become one of the mainstream approaches for analyzing the flow and discharge behavior of bulk feed materials [3]. Compared with purely empirical or fully physical experiments, DEM offers advantages such as lower computational cost, the ability to observe force and velocity fields at the particle scale [4], and efficient investigation of multi-factor combinations. It is particularly suitable for materials like Total Mixed Ration (TMR), which exhibit cohesiveness and morphological diversity [5].

To achieve high-quality feeding performance, it is essential to optimize both the structural and operational parameters of the device, including the matching of scraper/chain speed and belt speed, vehicle traveling speed, feed-retaining mechanism parameters, as well as material moisture content and adhesion characteristics. DEM provides a controllable "virtual test platform" for this purpose: by configuring contact models and material parameters, it enables simulation of the coupled processes of feeding, conveying, and discharging under various operating conditions. This allows for quantitative analysis of the relationships between unit feeding amount and spatial uniformity, and facilitates parameter screening at lower risk and cost [6]. Among available models, the Hertz–Mindlin with JKR Cohesion contact model has been proven effective in characterizing the cohesive behavior of moist silage, alfalfa stems, and powder-granule mixtures, making it suitable for simulation of feeding processes in sheep houses.

Previous studies have investigated key influencing factors of feeding systems from various perspectives. For instance, the scraper (or chain plate) speed determines the advancement rhythm of the lower material layer; the belt speed, together with the outlet geometry, jointly affects the instantaneous flow rate and the spatial distribution of deposited feed strips; while the traveling speed influences the temporal window of material discharge per unit length. Some research has also focused on the structure of the feed bin and anti-arching mechanisms to reduce blockage risk and improve system stability. However, most of these studies have adopted single-factor or empirical approaches, or have used dry granular materials as substitutes for cohesive TMR, lacking quantitative coupling and systematic optimization of three factors under adhesive model constraints. Moreover, the matching mechanism among the scraper, belt, and traveling speed, the forms of their interaction terms, and their combined effects on feeding uniformity remain without a reproducible framework for statistical modeling and validation [7].

Therefore, this study aims to develop a DEM-based virtual simulation platform for a sheep feeding device to systematically quantify the effects of X_1, X_2, and X_3 on Y_1 and Y_2. Furthermore, it seeks to obtain an optimal, engineering-applicable combination of operating parameters via statistical modeling and multi-objective optimization, thereby providing methodological and data support for the structural design and operational calibration of cohesive TMR feeding systems.

To achieve these objectives, this study first develops a simplified device model in SolidWorks and imports it into EDEM. The Hertz–Mindlin with JKR Cohesion contact model is selected to characterize the adhesion properties of TMR. Building on this, the research investigates the effects of the three key operating parameters (X_1, X_2, and X_3) on Y_1 and Y_2. To obtain engineering-applicable parameter combinations, this study establishes a quadratic regression model using the Box–Behnken design (BBD) and conducts analysis of variance (ANOVA) and residual diagnostics. Finally, the multi-objective desirability function is employed to solve for the optimal parameters under given constraints, which are then validated using rounded values for practical engineering application.

1. Materials and methods

To investigate the effects of different combinations of traveling speed, scraper speed, and conveyor belt speed on feeding performance, a simplified computational domain of the feeding device was established in EDEM. Only the lower structures related to material discharge were retained, including the lower cavity of the feed hopper, the scraper conveying channel, the rotating feed-retaining roller, and the tail-end belt conveyor unit. The vehicle's traveling motion was represented by a constant speed V, implemented through a moving coordinate system to simulate the relative uniform motion of the discharge outlet with respect to the ground. Gravitational acceleration was set to 9.81 $m \cdot s^{-2}$. All walls and metallic components were modeled as rigid boundaries, and the contact interactions between the device and the material were defined as "steel–material" contacts.

The motion boundaries and operating conditions were configured as follows: the scraper, feed-retaining roller, and belt were driven as rigid bodies with prescribed rotational speeds. The level ranges of the three factors were determined based on the adjustable ranges observed in field conditions and verified through preliminary simulations. Specifically, X_1 (traveling speed), X_2 (scraper rotational speed), and X_3 (belt rotational speed) were set within 3–7 $km \cdot h^{-1}$, 65–85 $r \cdot min^{-1}$, and 200–400 $r \cdot min^{-1}$, respectively. The total simulation duration was 10 s, during which 0–2 s corresponded to the particle generation and natural accumulation stage, while 2–10 s represented the steady operating stage. The uniform simulation time step was set to 5×10^{-6} s, and the steady-state analysis window was defined within 3.5–10 s.

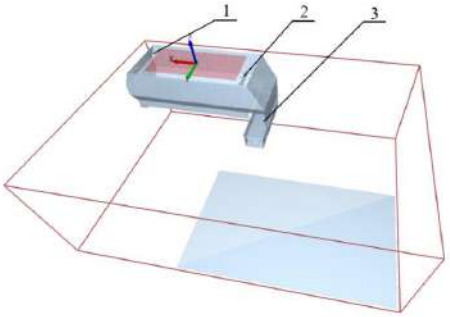

1.Stock bin 2.Material stick 3.Discharge port

Fig.1 - Sketch of EDEM feeding unit

To accurately characterize the adhesion effects among moist organic feed particles and effectively capture the cohesive behavior of the silage and alfalfa particle system, this study employed the Hertz–Mindlin with JKR Cohesion contact model to develop the Discrete Element Method (DEM) simulation framework [8]. To reduce the computational load and enhance simulation efficiency, the actual materials were simplified into equivalent spherical particles with a 5 mm radius, guided by similarity theory[9]. The surface energy parameter of the JKR model was set to 0.27 J/m^2 to reflect the actual adhesion level of the wet TMR [10]. Three representative particle types were constructed based on a mass ratio of 10:5:1 for silage, alfalfa stems, and corn flour, respectively. Their geometries are illustrated in Figure 2. The physical properties of each component are presented in Table 1 [11,12], and the inter-material contact parameters, obtained through literature review and experimental calibration, are listed in Table 2.

Alfalfa stem particles Silage particles Corn meal particles

Fig.2. - Material discrete element model

Table 1. Simulated material characteristics

Material properties	Material type		
	Silage	Corn	Alfalfa
Density(kg/m^3)	195.67	230.23	655.00
Shear modulus(Pa)	7.78×108	2.71×109	1.37×108
Poisson's ratio	0.27	0.23	0.40

Table 2. Contact parameters of materials used in the DEM simulation

Contact pair	Number		
	Static friction coefficient	Rolling friction coefficient	Restitution coefficient
Silage–Silage	0.77	0.14	0.13
Silage–Alfalfa stem	0.52	0.15	0.36
Silage–Corn meal	0.63	0.15	0.12
Silage–Steel	0.58	0.09	0.62
Silage–Ground	0.13	0.01	0.07
Alfalfa stem–Corn particle	0.42	0.19	0.32
Alfalfa stem–Steel	0.41	0.04	0.34
Alfalfa stem–Alfalfa stem	0.37	0.06	0.28
Alfalfa stem–Ground	0.15	0.02	0.10
Corn particle–Corn particle	0.62	0.08	0.11
Corn particle–Steel	0.42	0.05	0.21
Corn particle–Ground	0.10	0.01	0.10

To quantitatively evaluate the effects of the three factors on feeding performance under reproducible conditions and to obtain an engineering-applicable optimal combination, a unified experimental scheme was adopted in this study. First, along the traveling direction, the mass of deposited material on the ground or trough surface was spatially sampled at 1 m intervals . Within the steady-state time window [5, 10, 13] s, the two response indicators, Y_1 and Y_2, were statistically analyzed. Here, Y_1 is defined as the ratio of the total discharged mass during the steady-state stage to the traveling distance, while Y_2 is calculated according to Equations (1) and (2).

$$C_V = \frac{\sqrt{\frac{\sum_{i=1}^{n}(m_i - \overline{m})^2}{n-1}}}{\overline{m}} \quad (1)$$

$$M = 1 - C_V \quad (2)$$

where C_v denotes the coefficient of variation;

m_i represents the mass of the i-th sample (kg);

$\overline{m}_i$ is the average sample mass (kg);

M refers to the feeding uniformity.

Each operating condition was independently repeated three times. To separately investigate the effects of different values of X_1, X_2, and X_3 on Y_1 and Y_2 and to narrow the parameter ranges, single-factor experiments were first conducted by varying one factor while keeping the other two fixed. Subsequently, a three-factor, three-level Box–Behnken Design (BBD) was established to perform combination experiments. The number of center points was set to five or more to estimate pure error, and the experimental sequence was randomized to minimize systematic bias. Each factor was coded as [−1, 0, 1]. Quadratic polynomial models, as expressed in Equation (3), were fitted separately for Y_1 and Y_2. Analysis of variance (ANOVA), lack-of-fit tests, and residual diagnostics were then performed to identify significant factors affecting Y_1 and Y_2. Based on the constraints of experimental parameters, optimization analysis was conducted to determine the optimal combination of parameters. Verification experiments were subsequently performed, and the relative errors were calculated to evaluate the feasibility and robustness of the optimized results.

$$Y = \beta_0 + \sum_{i=1}^{3} \beta_i X_i + \sum_{i=1}^{3} \beta_{ii} X_i^2 + \sum_{i<j} \beta_{ii} X_i X_j \quad (3)$$

2. Results and their discussions

The results of the single-factor experiments for X_1, X_2, and X_3 are shown in the following figures.

Since the time interval between 7–8 s corresponded to a stable feeding stage during the simulations, multiple sampling points within this interval were selected to calculate feeding uniformity.

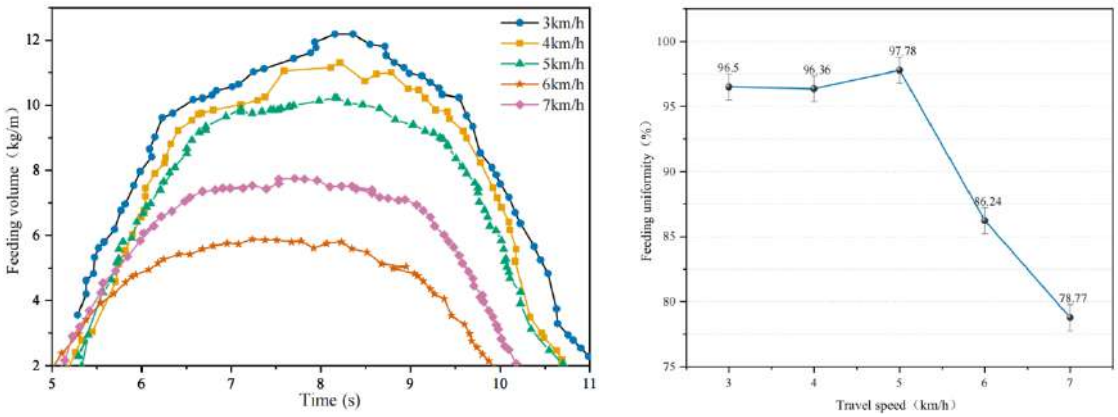

Fig.3. - Effect of X_1 on the feeding volume(Left)and feeding uniformity(Right)when X_2 and X_3 are held constant.

As shown in Fig 3, under constant X_2 and X_3, variation in X_1 affected the length of the feeding strip per unit time. The simulations indicated that as the traveling speed increased from 3–7 km·h⁻¹, the fluctuation of the discharged material intensified and the feeding amount per unit distance decreased. This occurs because particles retained their tangential velocity component from the belt when landing, resulting in greater longitudinal displacement and lateral slip, which in turn reduced feeding uniformity. When the traveling speed exceeded 5 km·h⁻¹, both the unit feeding amount and uniformity fell below acceptable standards. Therefore, the traveling speed range of 3–5 km·h⁻¹ was selected for subsequent experiments.

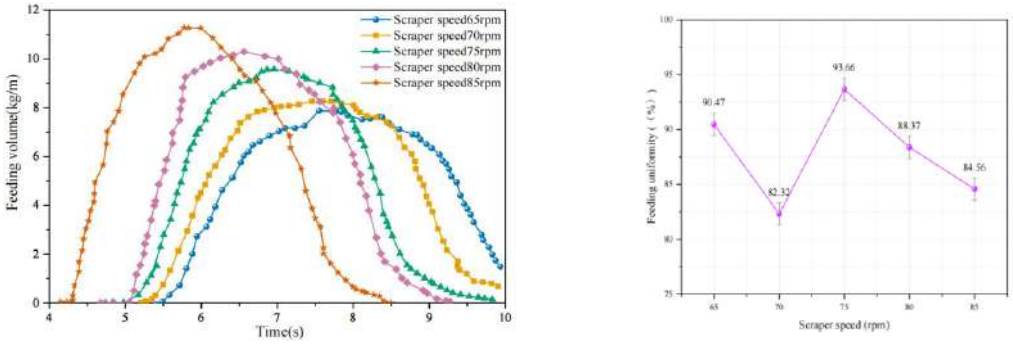

Fig.4. - Effect of X_2 on the feeding volume(Left)and feeding uniformity(Right)when X_1 and X_3 are held constant.

As shown in Fig 4, X_2 (scraper rotational speed) determines the total feeding duration and influences the longitudinal distribution pattern, exhibiting a similar effect to that of X_1. At 85 and 75 r·min⁻¹, significant fluctuations occurred between 6–8 s, whereas the unit feeding amount at 75–80 r·min⁻¹ was more consistent, resulting in improved overall uniformity. Considering the operational requirements of sheep housing, scraper speeds between 75–85 r·min⁻¹ were found to be suitable; therefore, this range was selected for subsequent tests.

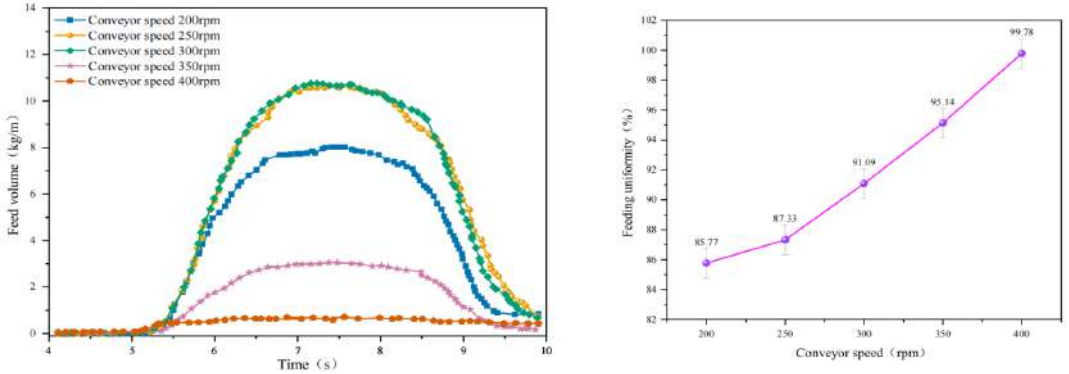

Fig.5. - Material quality chart for different scraper speeds

As shown in Fig 5, X_3 (belt rotational speed) primarily controls the throwing distance of the discharged material. Increasing the belt speed provides particles with higher initial velocity, which enhances landing dispersion and collision, thereby widening the feeding band and breaking up agglomerated particles—ultimately improving feeding uniformity. However, at 400 r·min^{-1}, the throwing distance exceeded the desired range, resulting in material waste, while speeds below 250 r·min^{-1} yielded a unit feeding amount of less than 10 kg·m^{-1}. Consequently, the belt speed range was set between 250–350 r·min^{-1}.

Interaction Effects and Optimization Analysis of Parameters

To further analyze the interactions among multiple factors, a Box–Behnken design (BBD) experiment was conducted as shown in Table 3.

Table 3. Feeding device test program and results

Number	X_1/(km/h)	X_2/(rpm)	X_3/（rpm)	Y_1/(kg/m)	Y_2/(%)
1	-1	-1	0	9.92	76.1
2	1	0	1	7.36	86.4
3	1	1	0	7.58	86.2
4	-1	1	0	12.79	93.7
5	0	1	-1	4.86	81.5
6	1	0	-1	3.42	89.9
7	0	1	1	7.09	80.1
8	0	-1	1	3.47	62.4
9	0	0	0	9.05	85.8
10	1	-1	0	5.82	79.8
11	0	0	0	9.46	86.5
12	-1	0	-1	12.20	93.4
13	0	-1	-1	4.10	69.1
14	0	0	0	9.31	85.4
15	0	0	0	9.46	86.9
16	-1	0	1	9.70	88
17	0	0	0	9.27	86.8

To analyze the influence of experimental factors on the unit feeding amount Y_1, a quadratic regression model of Y_1 with respect to X_1, X_2 and X_3 was established using Design-Expert software. The results showed that the model exhibited a high goodness of fit (R^2=0.98) and was statistically significant (P<0.0001). Regression analysis indicated that X_1, X_2, X_3, X_1X_3, and X_1^2, X_2^2 ,and X_3^2 had highly significant effects on Y^1, while X_2X_3 was significant and X_1X_2 was not significant and therefore removed from the model. The final regression equation is shown in Equation (4). The order of factor influence on Y_1 was X_1>X_2>X_3.

Table 4. Analysis of regression equations for unit feeding quantity

Term	Variance Source	Sum of squares	Degrees of freedom	Mean square	F	P
Y_1	Model	127.93	9	14.21	186.53	< 0.0001
	X_1	52.17	1	52.17	684.53	< 0.0001
	X_2	10.14	1	10.14	133.11	< 0.0001
	X_3	1.15	1	1.15	15.13	0.0060
	X_1X_2	0.3123	1	0.3123	4.10	0.0826
	X_1X_3	10.35	1	10.35	135.76	< 0.0001
	X_2X_3	2.04	1	2.04	26.83	0.0013
	X_1^2	9.53	1	9.53	125.03	< 0.0001
	X_2^2	13.42	1	13.42	176.04	< 0.0001
	X_3^2	29.43	1	29.43	386.20	< 0.0001
	Residual	0.5334	7	0.0762		
	Lack of fit	0.4203	3	0.1401	4.95	0.0782
	Pure error	0.1132	4	0.0283		

$$Y_1 = 9.31 - 2.55X_1 + 1.13X_2 + 0.38X_3 + 1.61X_1X_3 + 0.72X_2X_3 + 1.50X_1^2 - 1.78X_2^2 - 2.64X_3^2 \quad (4)$$

The analysis results of the interaction effects among the experimental parameters are shown in the following figure.

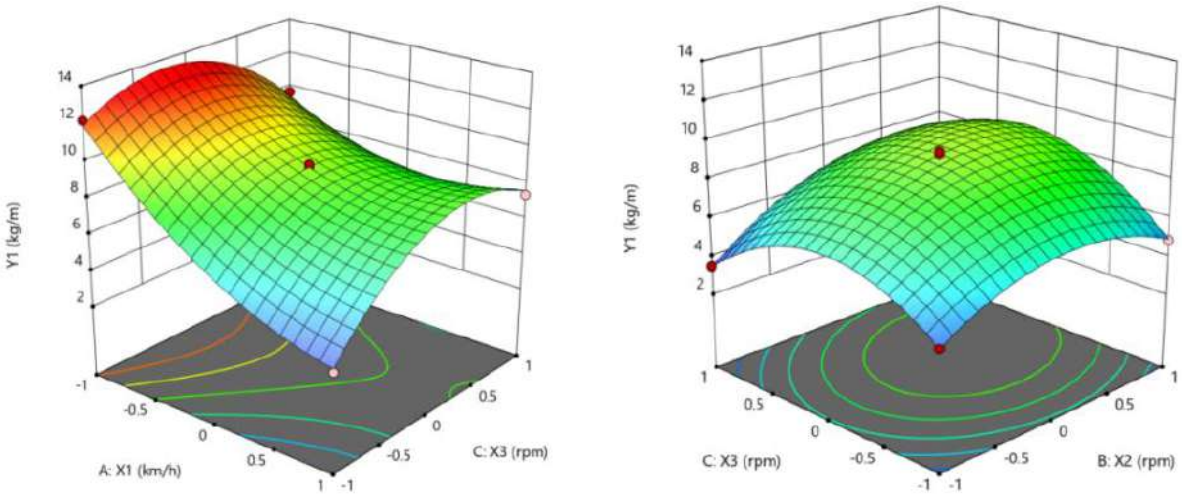

Response surface for the interaction between X_1 and X_3 on Y_1 Response surface for the interaction between X_2 and X_3 on Y_1

Fig.6. - Response surface curves for the interaction of factors on Y1

The two response surfaces show that when X_2 is at its central level (left plot), Y_1 decreases with increasing traveling speed X_1, with a steeper drop at lower levels, and first increases then decreases with belt speed X_3, rising faster at low levels. At the central level, the effect of X_1 on Y_1 is stronger than that of X_3. This occurs because a higher X_1 shortens the feeding duration, reducing the unit feeding amount, while excessive X_3 causes material to be thrown beyond the trough. When X_1 is fixed at its center (right plot), both scraper speed X_2 and belt speed X_3 show an "increase–then–decrease" trend, with X_2 having a more pronounced effect due to excessive shear within the material layer leading to arching and flow interruption. Overall, X_1 has a suppressive effect on Y_1, while X_2 and X_3 exhibit inverted U-shaped influences, with X_2 being dominant.

Similarly, a quadratic regression model of Y_2 with respect to X_1, X_2, and X_3 was constructed using Design-Expert. The model demonstrated excellent goodness of fit (R^2=0.99) and was highly significant (P<0.0001). Regression analysis revealed that X_2, X_3, X_1X_2, and the quadratic terms X_1^2,X_2^2, X_3^2 had extremely significant effects on feeding uniformity (Y^2), while X^1 and X^2X^3 were significant. The non-significant term $X_1X_3$was removed, and the final coded equation model is presented in Equation (5). The order of factor influence on Y_2 was: scraper speed (X_2) > belt speed (X_3) > traveling speed (X_1).

Table 5. Analysis of regression equations for unit feeding quantity

Term	Variance Source	Sum of squares	Degrees of freedom	Mean square	F	P
Y_2	Model	1049.11	9	116.57	122.69	< 0.0001
	X_1	9.90	1	9.90	10.42	0.0145
	X_2	365.85	1	365.85	385.08	< 0.0001
	X_3	36.13	1	36.13	38.02	0.0005
	X_1X_2	31.36	1	31.36	33.01	0.0007
	X_1X_3	0.9025	1	0.9025	0.9499	0.3622
	X_2X_3	7.02	1	7.02	7.39	0.0298
	X_1^2	201.04	1	201.04	211.61	< 0.0001
	X_2^2	359.48	1	359.48	378.38	< 0.0001
	X_3^2	59.69	1	59.69	62.82	< 0.0001
	Residual	6.65	7	0.9501		
	Lack of fit	4.94	3	1.65	3.86	0.1125
	Pure error	1.71	4	0.4270		

$$Y_2 = 86.28 - 1.11X_1 + 6.76X_2 - 2.13X_3 - 2.80X_1X_2 + 1.32X_2X_3 + 6.91X_1^2 - 9.24X_2^2 - 3.77X_3^2 \quad (5)$$

The analysis results of the interactive effects among experimental parameters are presented in the following figure.

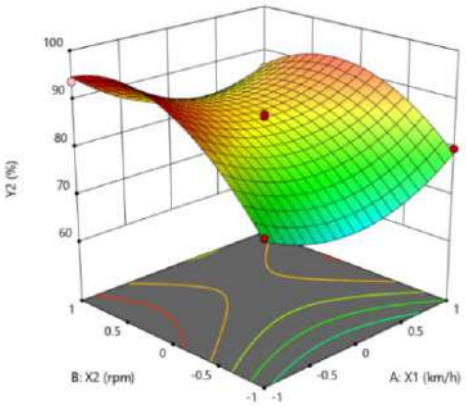

Response surface for the interaction between X_1 and X_2 on Y_2

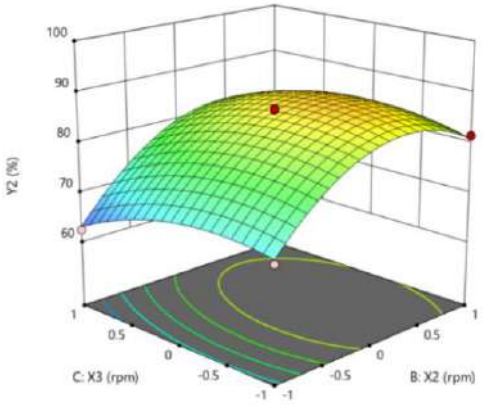

Response surface for the interaction between X_2 and X_3 on Y_2

Fig.7. - Response surface curves for the interaction of factors on Y_2

The two response surfaces indicate that when X_3 is at its central level (left figure), Y_2 (feeding uniformity) exhibits a "decrease–increase" trend with respect to the travel speed X_1, where the decline at lower levels is steeper than the subsequent rise. Its variation with scraper speed X_2 depends on X_1: when X_1 is low, Y_2 increases monotonically with X_2, with a faster rise at lower levels; when X_1 is high, Y_2 first increases and then decreases. When X_1 is fixed at the center (right figure), both X_2 and conveyor speed X_3 show a "rise–fall" effect on Y_2, featuring a faster increase at low levels and a slower decline at high levels. Mechanistically, low levels of X_1, X_2, and X_3 result in insufficient conveying and shearing, causing feed agglomeration and reduced uniformity. As X_2 or X_3 increase, the enhanced linear velocity and shear promote material dispersion through brushing and belt movement, thereby improving uniformity. However, excessive X_1 shortens operation time, overly high X_2 leads to material accumulation and re-agglomeration on the belt, and high X_3 induces similar effects, all of which ultimately reduce feeding uniformity.

Based on practical requirements, the unit feeding rate $Y_1 \in [10,12]$ kg·m^{-1}, while feeding uniformity Y_2 is set as the maximization objective. The decision variables are bounded as follows: travel speed X_1=3 − 5 km· h^{-1}, scraper speed X_2=75-85 rpm, and conveyor speed X3=250 − 350 rpm. On this basis, a constrained optimization model was formulated and Design-Expert's Numerical optimization was employed to obtain the optimal Y_1 and Y_2, as specified below.

$$\begin{cases} 3 \le X_1 \le 5 \\ 75 \le X_2 \le 85 \\ 250 \le X_3 \le 350 \\ 10 \le Y_1 \le 12 \\ maxY_2(X_1,\ X_2,\ X_3,\ X_4) \end{cases} \quad (6)$$

The optimization results indicate that the optimal feeding performance is achieved when the travel speed is 3.05 km h^{-1}, scraper speed 84.9 r min^{-1}, and conveyor speed 326.5 r min^{-1}, corresponding to a unit feeding rate of 11.85 kg m^{-1} and a feeding uniformity of 93.71%. For practical engineering application, the parameters were rounded to 3 km h^{-1}, 85 r min^{-1}, and 330 r min^{-1}, respectively. The control system was then initiated for three validation trials, and the results are summarized in Table 6.

Table 6. Comparison between model optimization value and verification test value

Item	Evaluation Metrics	
	Unit feeding amount (kg·m^{-1})	Feeding uniformity (%)
Model-optimized value	11.85	93.71
Validation (experimental) value	11.49	91.54
Relative error (%)	3.04	2.89

Conclusion

This study successfully combined the Discrete Element Method (DEM) with the Response Surface Method (RSM) to systematically optimize the operating parameters of a sheep house Total Mixed Ration (TMR) feeding device. Through single-factor simulation tests, the effective ranges of the key parameters were first determined: X_1 at 3–5 km/h, X_2 at 75–85 r/min, and X_3 at 250–350 r/min. Based on this, a Box–Behnken design was employed to establish quadratic regression models for Y_1 and Y_2. Analysis of variance (ANOVA) confirmed that both models were highly significant ($P < 0.001$), with goodness-of-fit (R^2) values of 0.98 and 0.99, respectively, indicating high accuracy and strong predictive power. Model analysis quantified the hierarchical order of factor influence: for Y_1, the significance order was $X_1 > X_2 > X_3$, whereas for Y_2, the order was $X_2 > X_3 > X_1$. The study further revealed that X_1 had a significant inhibitory effect on Y_1, while both X_2 and X_3 exhibited an inverted U-shaped influence on Y_2. With the optimization objectives set to maintain Y_1 within 10–12 kg·m^{-1} and maximize Y_2, the optimal parameter combination was determined to be X_1 = 3.05 km·h^{-1}, X_2 = 84.9 r·min^{-1}, and X_3 = 326.5 r·min^{-1}. Under these conditions, the predicted Y_1 and Y_2 were 11.85 kg·m^{-1} and 93.71%, respectively. For practical engineering application, these parameters were rounded to X_1 = 3 km·h^{-1}, X_2 = 85 r·min^{-1}, and X_3 = 330 r·min^{-1}. Subsequent validation experiments yielded a Y_1 of 11.49 kg·m^{-1} and a Y_2 of 91.54%. The relative errors between the experimental and model-predicted values were both below 5%, fully verifying the model's accuracy and the reliability of the optimization. This optimal combination also ensured stable material flow without blockage. This research not only provides executable operational parameters for cohesive feed systems like TMR but also establishes a transferable framework for parameter design and calibration. Future work will focus on investigating the system's adaptability under different operational conditions, such as varying feed formulations or moisture contents, and further enhancing its comprehensive performance.

Acknowledgments

This research was supported by the College of Mechanical and Electrical Engineering at Shihezi University, People's Republic of China. The specific project information is as follows: The agricultural projects of the Xinjiang Production and Construction Corps（NYHXGG,2023AA403; The science and technology program projects of the Xinjiang Production and Construction Corps（2024AB047; The high-level talent research startup projects of Shihezi University（RCZK202310).

References

[1] Xiao J., Sun P. Analysis on the High-end Feeding System and the Application Scenarios on the Lake Sheep Barn Feeding Scale Breeding Technology Research.

[2] Chiu Y.-C., Tsai W.-C., Wu G.-J. W. Developing an Automated Feeding System for Distributing Concentrated Goat Feed // Applied Engineering in Agriculture. American Society of Agricultural and Biological Engineers, 2020. T. 36, № 2. C. 125–140.

[3] Zhao H. и др. Applications of discrete element method in the research of agricultural machinery: A review // Agriculture. MDPI, 2021. T. 11, № 5. C. 425.

[4] Zhao J., Zhao S., Luding S. The role of particle shape in computational modelling of granular matter // Nature Reviews Physics. Nature Publishing Group UK London, 2023. T. 5, № 9. C. 505–525.

[5] Bueno A. V. I. и др. Ensiling total mixed ration for ruminants: a review // Agronomy. MDPI, 2020. T. 10, № 6. C. 879.

[6] Lu K. и др. Parameter Optimization Method for Centrifugal Feed Disc Discharging Based on Numerical Simulation and Response Surface // Machines. MDPI, 2024. T. 12, № 11. C. 799.

[7] Ma H. и др. Study on the rigid-discrete coupling effect of scraper conveyor under different chain speed-load conditions // Simulation Modelling Practice and Theory. Elsevier, 2024. T. 134. C. 102943.

[8] Tao W. U. и др. Calibration of discrete element model parameters for cohesive soil considering the cohesion between particles // Journal of South China Agricultural University. 2023. T. 38, № 3. C. 93–98.

[9] Chandratilleke G. R., Yu A. B., Bridgwater J. A DEM study of the mixing of particles induced by a flat blade // Chemical Engineering Science. Elsevier, 2012. T. 79. C. 54–74.

[10 Wu K.-C., You H.-I. Determination of solid material elastic modulus and surface energy based on JKR contact model // Applied surface science. Elsevier, 2007. T. 253, № 20. C. 8530–8537.

[11] Kaifei W., Baoqin W., Aiken Y., et al. Study on the influence of segmented helical TMR mixer auger structure on mixing performance based on discrete element method // Feed Industry. – 2020. – Vol. 41. – № 19. – pp. 35–41.

[12] Lei W., Yonglin Z., Bin L., et al. Calibration of adhesive parameters for granular feed based on discrete element method and analysis of its crushing process // Feed Industry. – 2023. – Vol. 44. – № 1. – pp. 10–17.

[13] Zharkevich O., Nikonova T., Gierz Ł., Reshetnikova O., Berg A., Warguła Ł., Berg A., Wieczorek B., Łykowski W., Nurzhanova O. Improving the Design of a Multi-Gear Pump Switchgear Using CFD Analysis // Applied Sciences (Switzerland), 2024, 14(13), 5394

Information of the authors

Fan Zhihao, MS, Graduate Student of the School of Mechanical and Electrical Engineering, Shihezi University, and the School of Mechanical Engineering, Karaganda Saginov Technical University.
e-mail:1460220250@qq.com

Wen Baoqin, PhD in Engineering, Doctoral Supervisor, Teaching Expert and Key Faculty Member of Higher Education in Xinjiang Uygur Autonomous Region.
e-mail: wendy-wbq@163.com

Reshetnikova Olga Stasisovna，PhD, acting associate professor**,** Abylkas Saginov Karaganda Technical University.
e-mail: olga.reshetnikova.80@mail.ru

Li Jingbin, PhD in Engineering, Professor (Class II), Doctoral Supervisor, Member of the Standing Committee of the Party Committee and Director of the Publicity Department of Shihezi University, Executive Deputy Director of the Key Laboratory of Modern Agricultural Machinery of XPCC, Deputy Director of the Collaborative Innovation Center for the Modernization of Cotton Production Technology (Co-established by Province and Ministry), Member of the 11th Council of the Chinese Society of Agricultural Engineering, Council Member of the China Mechanical Industry Alliance for Excellent Engineer Education, and Vice Chairman of the Industry-Education Integration Community for Modern Agricultural Machinery and Equipment in China.
e-mail: ljb8095@163.com

He Xiaowei, PhD in Engineering, Associate Professor, Master's Supervisor at Tarim University, and Secretary of the Party Branch of the Department of Agricultural Engineering, College of Mechanical and Electrical Engineering.
e-mail: Hexw_work@163.com

DOI 10.52209/2706-977X_2026_1_107 **IRSTI 55.13.01** **UDC 625.143.482**

The Reliability and Durability of Welded Joints in Steel Rails: a Methodology for Process Control at Modern Rail Welding Facilities

Abdullayev S.[1], Bakyt G.[2,*], Yelshibekov A.[3], Jakupov N.[2], Duisembayeva B.[4]

[1]Satbayev University, Almaty, Kazakhstan
[2]Mukhametzhan Tynyshpayev ALT University, Almaty, Kazakhstan
[3]Saken Seifullin Kazakh Agrotechnical University, Astana, Kazakhstan
[4]L. N. Gumilyov Eurasian National University, Astana, Kazakhstan
*corresponding author

Abstract. The objective of this study is to develop a methodology for controlling the technological process of rail joint welding at rail welding facilities, ensuring the reliability of welded joints. Based on the data obtained from rail welding enterprises, an improved methodology was developed for assessing the stability of the technological process used in the production of welded rail joints, as well as the overall quality level of welding operations at rail welding facilities (RWFs). It has been established that the continuous increase in train weight and speed imposes strict requirements on the quality of rails in operation. The developed methodology makes it possible to identify a key cause of premature rail failure - manufacturing defects, particularly welding defects arising during the production of long welded rails, as well as during the repair and welding of used rails.

Keywords: railway rails, welded rails, continuously welded rails, rail welding facilities, train traffic safety.

Introduction

The introduction of long freight trains with increased axle loads has significantly heightened the demand for smooth and stable rail track geometry. A key requirement for meeting this demand is maintaining the proper condition of rail ends and extending the length of continuously welded rail (CWR) tracks.

During railway operation, defects and damage inevitably develop in rails due to the influence of rolling stock, environmental conditions, and other factors - posing varying degrees of risk to train traffic safety. Common issues include increased head wear and bending deformations. The service life of new rail ends may range from several months to several years, depending on traffic intensity, axle loads, and the quality of routine track maintenance.

Rails represent the most critical and expensive component of the railway superstructure. Consequently, when surface defects occur, the restoration of rail ends using welding (build-up welding) is widely employed. The restoration of rail ends and CWR sections via build-up welding, followed by hardening, has become a standard and widely applied method to extend the service life of rails and other metallic track elements.

However, build-up welding is not always an economically effective solution. The deposited metal layer may delaminate from the base metal even before the end of its service life, especially on track sections with deteriorated sleepers or fastening assemblies, or where rail joints have excessive gaps.

Currently, in JSC "NC "Kazakhstan Temir Zholy" (KTZ), the monitoring and inspection of restored rail ends and CWRs is carried out by the "Track Diagnostics Center," a subsidiary of KTZ. The center utilizes non-destructive testing methods, primarily ultrasonic testing (UT), to detect internal rail flaws. Portable inspection equipment includes flaw detection trolleys such as the "KSPRUT," "Avikon-31," and "RDM-22" models. Mobile inspection systems include a flaw detection railcar and a mobile diagnostic complex equipped with track geometry, ultrasonic, and video inspection technologies integrated into a single railcar unit.

However, in areas where welding procedures were not properly followed, ultrasonic testing becomes less effective. Signal attenuation occurs in the build-up welded zone due to differences in grain structure between the deposited and base metals. This can hinder the timely detection of critical defects in rails that pose serious risks to train operations [1].

Strict adherence to the rail welding process is essential, and all restoration work must be performed by certified specialists who have undergone specialized training. Furthermore, welding repairs are only permitted when ambient temperatures are above +5 °C and in the absence of adverse weather conditions (rain, snow, fog, etc.). If blind gaps are present in rail joints, welding work is prohibited.

It is important to note that only rails of types R75, R65, and R50, categories T1, T2, and N, manufactured in accordance with GOST R 51685-2000 or corresponding technical specifications, and installed in either jointed or continuously welded tracks, may be repaired using build-up welding. These rails must have operational damage such as head deformation, delamination, plastic flow, or vertical wear as classified under surface defect criteria located in the rail head near joints.

Welding of rails of category B (highest quality category), as defined by GOST R 51685-2000, is strictly prohibited. Thus, the ability to detect critically defective rails in welded sections is primarily determined by the degree to which restoration work has complied with approved technological procedures - followed only secondarily by the qualifications of the specialist performing the monitoring.

Rails must meet the following requirements: they must be sufficiently strong, durable, and reliable in operation - that is, wear-resistant, hard, and at the same time adequately tough (non-brittle), as they are subject to impact-dynamic loads.

The main type of rail currently used in track infrastructure is the R65 rail and other rails with similar characteristics, with a mass of no less than 60 kg per linear meter. Also in use are R75, R50, R43, and lighter rails. In this study, R65 and similar rails, including R75, will be referred to as “rails with a mass of not less than 60 kg/m,” while R50 and similar types will be referred to as “rails with a mass of not less than 50 kg/m.”

Standard rail lengths are 25 and 12.5 meters; shortened rails may measure 24.92; 24.84; 12.46; 12.42; or 12.38 meters. The length of continuously welded rail strings is determined by project specifications based on local conditions.

Rails are installed with a standard inward cant of 1:20 (i.e., inclined toward the center of the track relative to the sleeper surface) both on straight and curved sections. For wooden sleepers, this inclination is achieved using steel baseplates; for reinforced concrete sleepers, the inclination is built into the rail seat design.

During comprehensive rail replacement projects on major railway lines, depending on traffic loads, two types of new rails are primarily laid: R75 and R65, both conforming to ST RK GOST R 51685-2005 (Table 1). On the tracks of industrial facilities, rails of types R50 (ST RK GOST R 51685-2005) and R43 (GOST 7173-54) are used. Railway infrastructure also contains rails of the same types but installed in earlier years (see Table 2). Rails that are reused after prior service are referred to as used rails (or second-use rails).

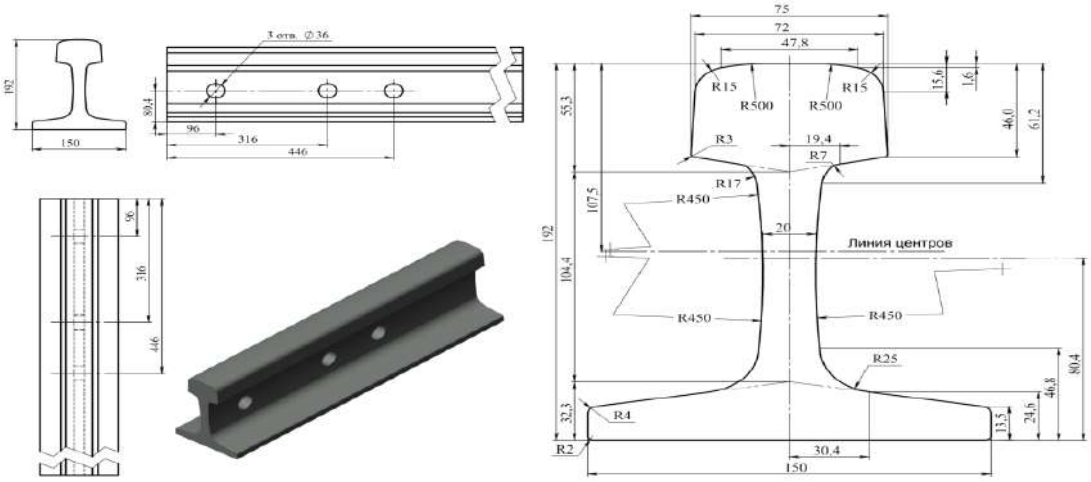

Fig. 1. - Rail type R75 according to ST RK GOST R 51685-2005

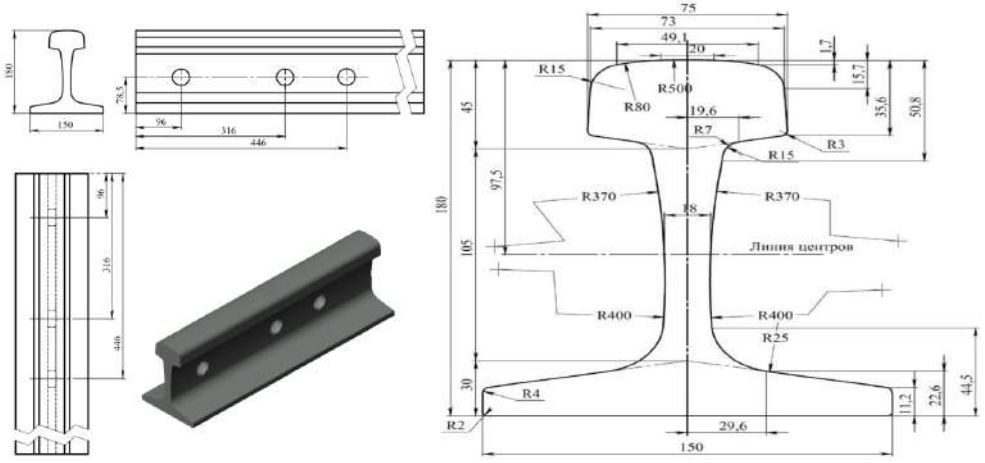

Fig. 2. - Rail type R65 according to ST RK GOST R 51685-2005

Table 1. Key Performance Characteristics of Rails

Parameter Name	Parameter Value for Rail Type				
	R43	R50	R65	R65K	R75
Figure Number in the Document	5	4	3	2	1
Cross-sectional Area of the Rail, cm^2	57,0	65,99	82,65	82,38	95,037
Distance from the Center of Gravity, mm					
to the bottom of the foot	68,5	70,50	81,30	80,60	88,20
to the top of the head	71,5	81,50	98,70	100,40	103,8
Distance from the Center of Twist, mm					
to the bottom of the foot	-	40,10	39,40	38,20	45,80
to the top of the head	-	111,90	140,60	141,80	146,20
Moment of Inertia of the Rail About the Vertical Axis, cm^4					
of the entire rail	-	375	564	557	665
head	-	91	106	103	143
foot		278	445	439	508
Moment of Inertia of the Rail About the Horizontal Axis, cm^4					
of the entire rail	1489	2011	3540	3495	4491
head	-	986	1728	1698	2198
foot	-	915	1539	1532	2005
Moment of resistance (section modulus), cm^3					
along the bottom of the flange или at the bottom of the flange	217	285	435	434	509
along the top of the head или at the top of the head	208	245	358	348	432
along the side face of the flange	45	55	75	73	89
Torsional moment of inertia of the rail, cm^4	-	201	288	285	401
Warping moment of inertia, cm^6	-	$1,0 \times 10^4$	$1,9 \times 10^4$	$1,84 \times 10^4$	$2,6 \times 10^4$
Flexural rigidity of the rail cross-section, kN/cm^2					
under pure torsion	-	$163,2 \times 10^6$	$233,5 \times 10^6$	$229,4 \times 10^6$	$325,0 \times 10^6$
under constrained torsion	-	$144,0 \times 10^6$	$180,0 \times 10^6$	$177,0 \times 10^6$	$234,0 \times 10^6$
Theoretical linear mass per meter of the rail (at a steel density of 7850 kg/m^3), kg	44,65	51,80	64,88	64,67	74,60
Area of the rail cross-section elements, % of the total area					
Head	42,8	38,12	34,11	33,52	37,42
Web	21,3	24,46	28,52	28,78	26,54
Base	35,9	37,42	37,37	37,70	36,04
Coefficient of linear thermal expansion of steel, $\alpha \cdot 10^{-6}$ °C^{-1}			11,8		

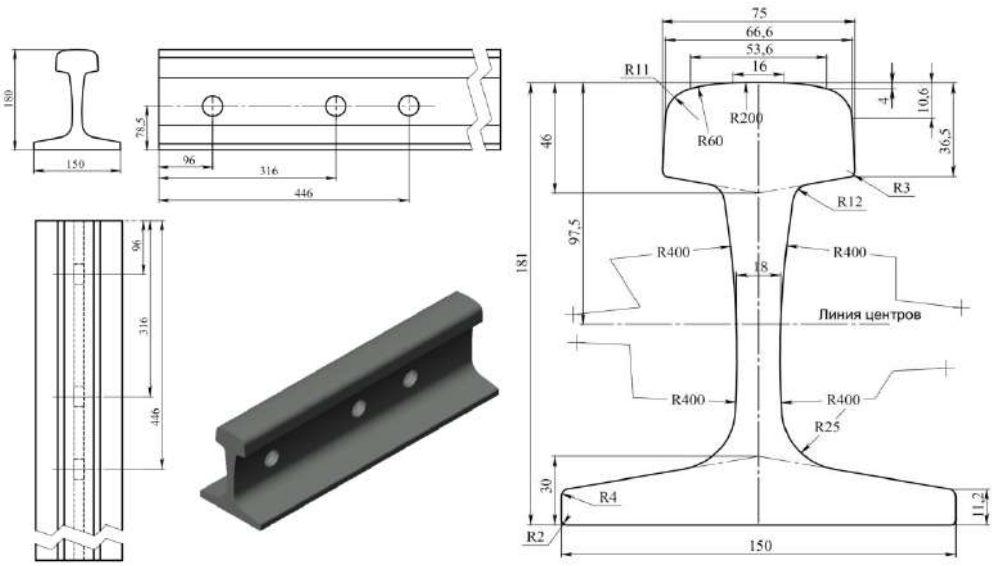

Fig. 3. - Rail type R65K according to ST RK GOST R 51685-2005

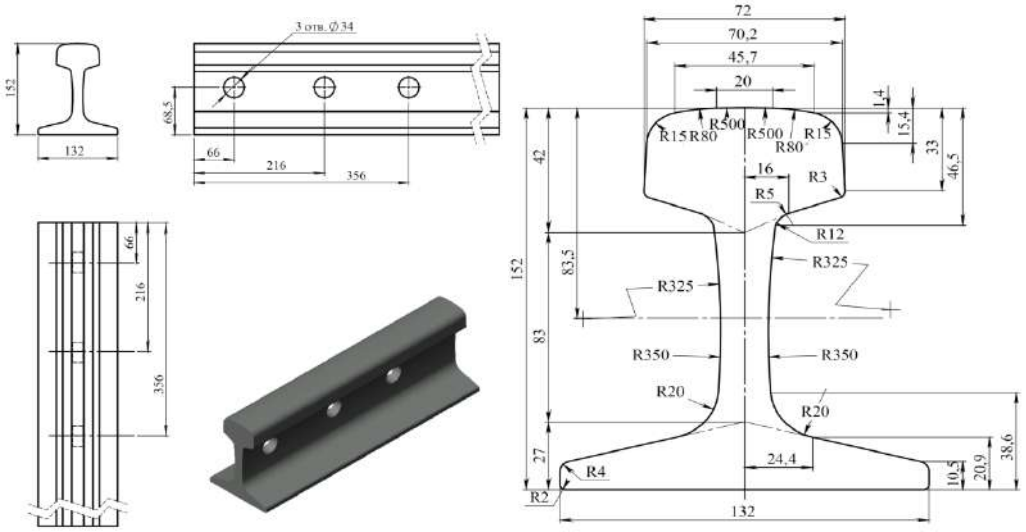

Fig. 4. - Rail type R50 according to ST RK GOST R 51685-2005

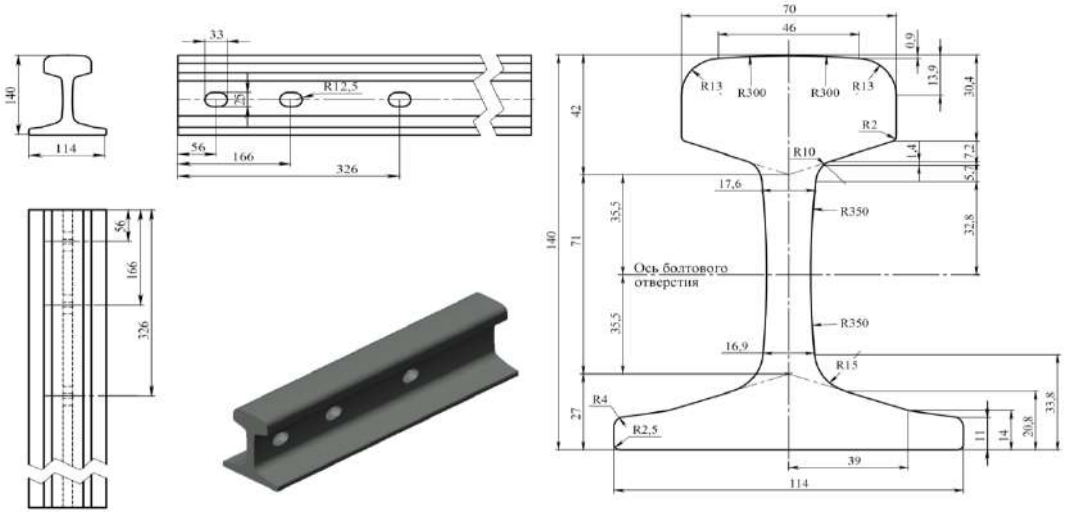

Fig. 5. - Rail type R43 according to GOST 7173-54

Table 2. Some characteristics of rails that are no longer produced but still used in track

Parameter	R75	R65		R50		R43
	GOST 16210-77	GOST 8161-63	GOST 8161-75	GOST 7174-65	GOST 7174-75	GOST 7173-54
Figure number in the document	6	7	8	9	10	11
Mass of 1 meter of rail, kg	74,4	64,64	64,72	51,63	51,8	43,61
Rail height, mm, including:	192	180	180	152	152	140
Head height	55,3	45	45	42	42	42
Web height	104,4	105	105	83	83	71
Base height	32,3	30	30	27	27	27
Rail head width, mm						
at the top	72	72,8	73	70	70	70
at the bottom	75,0	75,0	75,0	71,9	72	70
Rail base width, mm	150	150	150	132	132	114
Rail web thickness at midsection, mm	20	18	18	16	15,5	13,5
Cross-sectional area, cm²	95,04	82,6	82,9	65,9	65,8	55,7
Metal distribution over the profile, %						
Head	37,42	34,2	34,11	38,2	38,12	42,83
Web	26,54	28,4	28,52	24,4	24,46	21,31
Base	36,04	37,4	37,37	37,4	37,42	36,86
Moment of inertia about the axes, cm⁴:						
about the horizontal axis	4491	3548	3540	2018	2037	1472
about the vertical axis	665	569	564	375	377	257
Section modulus, cm³:						
at the bottom of the base	509	436	435	286	287	214
at the top of the head	432	359	358	248	251	206

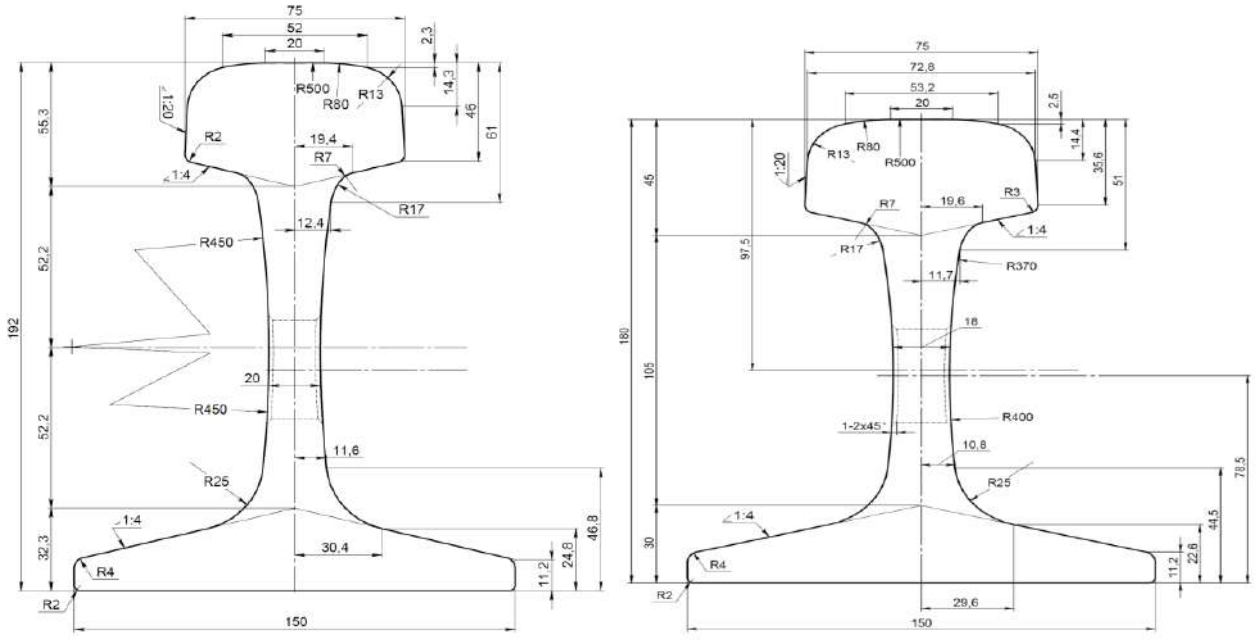

Fig. 6. - Rail type R75 according to GOST 16210-77. Figure 7. Rail type R65 according to GOST 8161-63

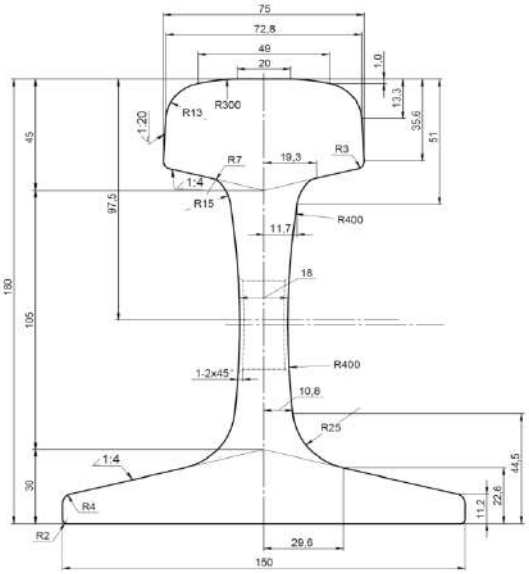

Fig. 7. - Rail type R65 according to GOST 8161-75.

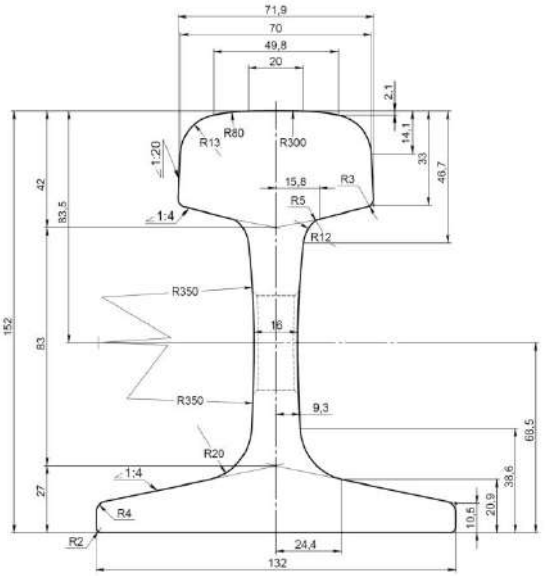

Fig. 8. - Rail type R50 according to GOST 7174-65.

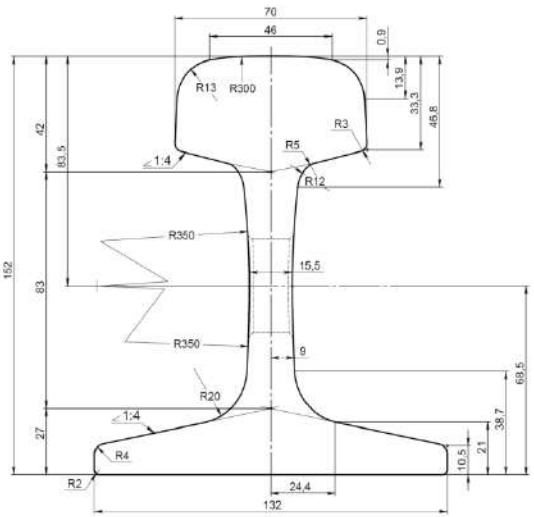

Fig. 9. - Rail type R50 according to GOST 7174-75.

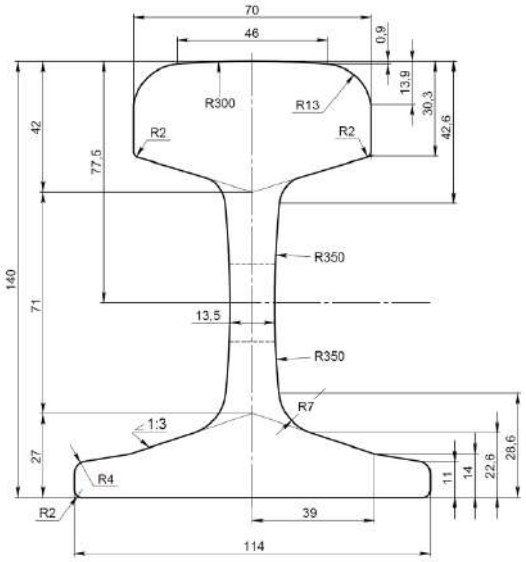

Fig. 10. - Rail type R43 according to GOST 7173-54.

Predominantly, interdendritic chemical inhomogeneity develops in weld seams. Zonal segregation is significantly less pronounced and manifests as slight enrichment in sulfur and certain other elements at the weld surface - under a wide penetration profile - and along the weld axis - under a narrow penetration profile. The degree of interdendritic inhomogeneity and zonal segregation largely depends on the cooling (solidification) conditions of the weld metal and its chemical composition.

Diffusion processes occurring in the fusion zone have a considerable influence on the quality of the welded joint. Due to the different solubilities of chemical elements in the liquid and solid phases, the chemical compositions of the boundary region of the base metal and the adjacent region of the weld metal differ substantially.

In some cases, a significant variation in chemical composition is observed along the weld length and at specific sections, i.e., macroscopic inhomogeneity of the weld. This variation is usually caused by fluctuations in the welding regime, changes in the composition of welding materials, and other technological factors.

The physical inhomogeneity observed in the weld metal is associated with the formation of so-called secondary boundaries, which occur in regions where imperfections in the metal's crystal lattice are concentrated. Physical inhomogeneity noticeably affects the weld's resistance to brittle transition, intergranular corrosion, and other mechanical and chemical properties.

1. Analysis of Statistical Data on Welded Rail Joints Quality

In accordance with the guidelines provided in the technical materials *"*Classification of Rail Defects CP-NTD/45-03", "Catalogue of Rail Defects CP-NTD/46-03", and "Indicators of Defective and Critically Defective Rails CP-NTD/47-03" [1,2], rails in which at least one defect is detected in a welded joint are classified as critically defective and are subject to immediate replacement.

To identify welding defects, all welded joints at rail welding enterprises (RWE) are subjected to visual inspection and ultrasonic testing in accordance with ST AO 39745182-044-2010 and ST AO 39745182-045-2010, following the Ultrasonic Testing Instruction for Welded Rail Joints at RWEs [4].

According to inspection data, each welded joint is evaluated using a qualitative (binary) criterion: acceptable or defective. The primary causes of defects in welded rail joints are generally attributed to malfunctions of the rail welding machines and inadequate preparation of the rail ends to be welded.

Welded joints in which defects are detected during inspection at the rail welding enterprise undergo repair; therefore, they are considered as in-plant rejects rather than finished product defects. The rail welding technological process includes: preparation of rail ends for welding, the welding itself performed according to the appropriate operational mode of a rail welding machine, and non-destructive testing of the welded joints, all carried out according to unified methodological guidelines [3].

Changes in the technological process are the prevailing factors in the formation of welding defects, as well as in the overlooking of such defects during inspection [4]. In this regard, it was necessary to improve the methodology for monitoring the rail joint welding process at JSC "NC "KTZh" RK, ensuring the reliability and durability of welded joints [5].

Since the introduction of ultrasonic testing at rail welding enterprises, the accumulation and consolidation of welded joint inspection data have been carried out. Analysis of these data has shown that, thanks to the automated welding process, the average percentage of in-plant rejects at various RWEs of JSC "NC "KTZh" over any given period is insignificant. However, it was found that in-plant rejects due to random deviations in the technological process do occur.

To promptly eliminate deviations in the technological process that lead to welding defects, it was advisable to improve the methodology for monitoring the rail joint welding process at JSC "NC "KTZh" RK, ensuring the reliability and durability of welded joints.

For this purpose, it was necessary to improve the monitoring of this process at rail welding enterprises, based on the statistical analysis of visual inspection and ultrasonic testing data. The control procedure involves calculating the average value of in-plant rejects $R_к$ over a specified preceding period for each k-th RWE, for example, over a year, and comparing this value with the average value of in-plant rejects ρ_i or the current period (month), as shown in Table 3.

For ease of comparison, rail welding control charts at RWEs are used (Figure 11), which indicate the average value over the preceding period and the control limits - upper $K_в$ and lower $K_н$, - within which changes in the current in-plant reject value are not considered indicative of deviations in the technological process. If in any month (for example, July) the in-plant reject value R_i exceeds the upper control limit $K_в$, this indicates that deviations have occurred in the technological process, leading to an increase in the number of defective joints.

Table 3. Average in-plant rejects over a year

Parameters	Month					
	I	**II**	**III**	**IV**	**V**	**VI**
Number of inspected joints *ni*	1900	2060	2210	2050	2060	1912
Number of rejected joints *mi*	9	1	2	1	4	1
Reject rate *pi = mi / ni , %*	0,05	0,10	0,05	0,20	0,20	0,05
Parameters	**Month**					
	VII	**VIII**	**IX**	**X**	**XI**	**XII**
Number of inspected joints *ni*	1500	1900	1620	1900	2030	2020
Number of rejected joints *mi*	10	5	3	2	3	4
Reject rate *pi = mi / ni , %*	0,55	0,20	0,15	0,10	0,15	0,20

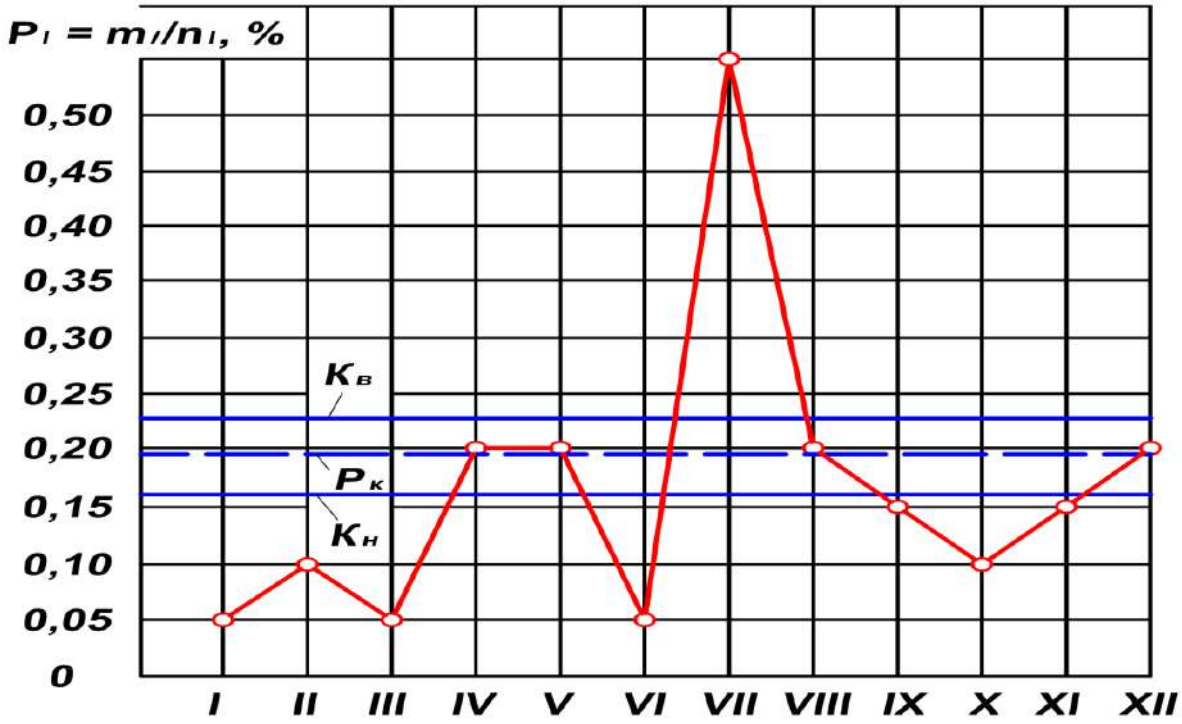

Fig. 11. – Rail Welding Control Chart at RWEs

Thus, exceeding the upper control limit indicates a deviation in the stability of the technological process and serves as a signal for intervention in the rail welding process, while falling below the lower control limit may indicate either an increase in the stability of the technological process or a possible oversight of defects, serving as a signal for an inspection of the non-destructive testing of welded joints.

If control charts allow the assessment of the stability of the rail welding process within each RWE, then comparing the average in-plant reject values for a given RWE $\overline{P}_\kappa$ with those of the other RWEs enables the evaluation of the technological level of the welding process at RWE κ Considering that practically identical rail welding machines, ultrasonic testing devices, and welding and inspection technologies are used across all RWEs, it is necessary, for the purpose of assessing the technological level of the welding process, to use charts similar to the aforementioned control charts, which should display:

- average in-plant reject values for all k-th RWEs, where $\overline{P}_\kappa$ κ-x where $\kappa = 1 \div \kappa_0$ over the preceding period, e.g., 12 months;
- $\overline{P}_\Sigma$ Average in-plant reject value across all RWEs over the preceding 12 months:

$$\overline{P}_\Sigma = \frac{\sum_{1}^{\kappa_0} \overline{P}_\kappa}{\kappa_0} \tag{1}$$

Upper $K_в$ and lower $K_н$ control limits, the exceeding of which indicates possible deviations in the welding technology or in the non-destructive testing process at the given RWE.

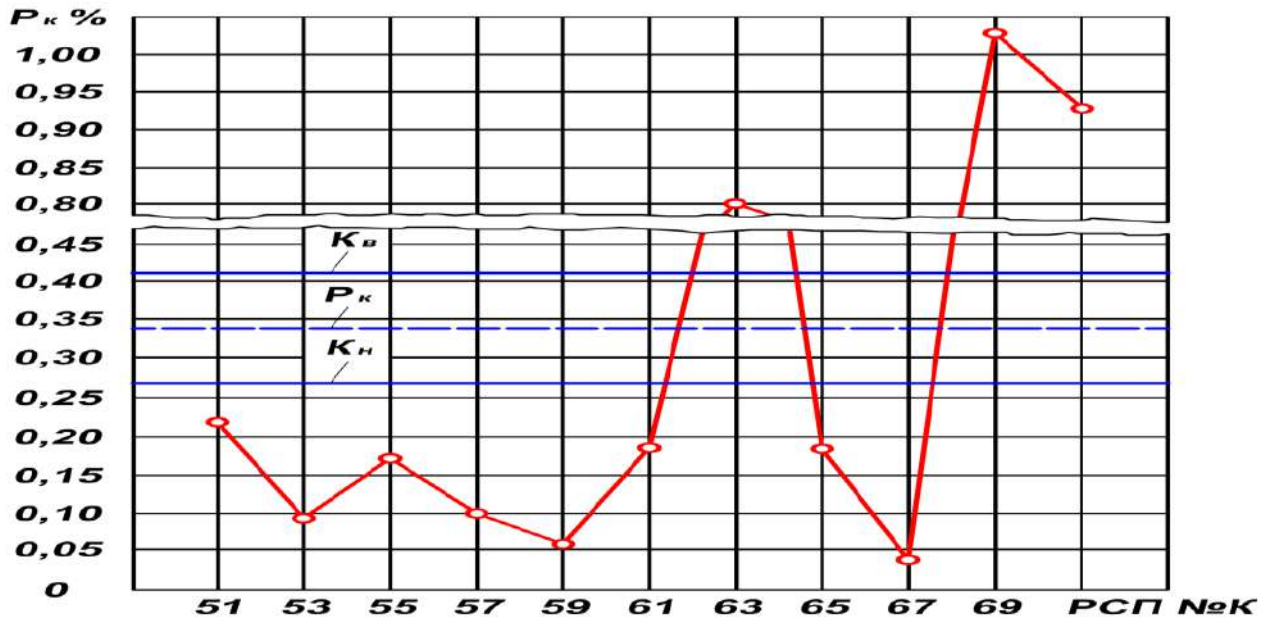

Fig. 12. – Example of a chart of average in-plant rejects for 2020 by RWEs

In addition to the annual average reject charts for all RWEs, information on the distribution of defects along the rail cross-section and by defect type over a sufficiently long period, e.g., one year, is highly useful for assessing the level of the technological process, both for individual RWEs and collectively for all RWEs, as shown in Figure 12.

The assessment of the stability of rail welding technological processes should be conducted independently at each RWE, whereas the evaluation of the technological process level should be centralized. Data collection for assessing the level of rail welding processes is carried out through Defective Joint Reports and Cards, which must be submitted quarterly to the designated data processing center.

Data accumulation and processing are performed using computers according to a specialized software program. To prevent disclosure of average in-plant reject values by RWE, each RWE is assigned a new index during data processing.

The implementation of this methodology for assessing the stability and level of the welded joint manufacturing process will contribute to improving the quality of rail welds, thereby reducing repair costs for rejected joints and minimizing the likelihood of installing welded rails with defective joints in the track.

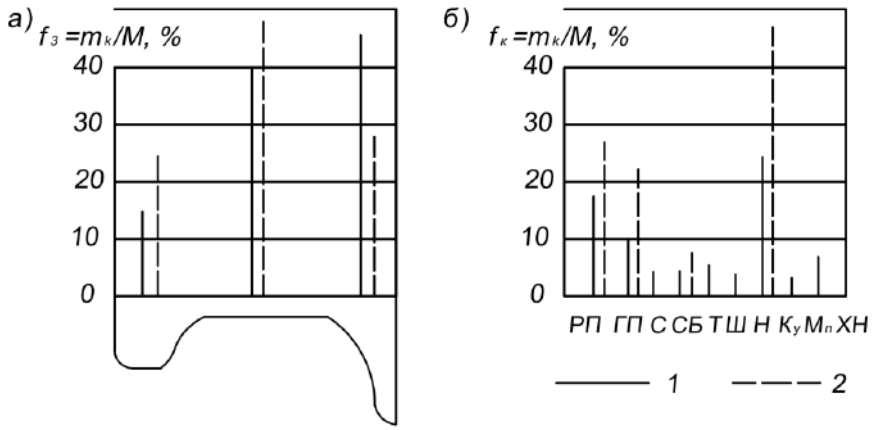

1 – for all rail welding enterprises (RWEs); 2 – for a single RWE; r_n – porosity, overburn; g_n – gas bubble s – silicate inclusion; sb – gray silicate inclusion; t – crack; sh – slag; – lack of fusion K_u – crater shrinkage; M_p – matte spot; XN – defect type not specified

Fig. 13. – Example of defect distribution for a total of M = 1000 units, detected at RWEs, by rail cross-section zones (a) and by defect types (b). Note – Each RWE is assigned a numerical code as an index

To determine weldability, methods simulating the welding process are used. For example, base metal plates are subjected to heat treatment that reproduces the changes the metal undergoes during welding.

The quality of welding is greatly influenced by the quality of welding materials. The primary type of welding materials used in assembly are electrodes for manual welding. Electrodes are delivered to construction and assembly sites by their manufacturers. Each batch of electrodes must have a certificate indicating the manufacturer, date of production, batch number and mass, standard, diameter, type and grade of electrodes, mechanical properties of the deposited metal, allowable sulfur and phosphorus content, recommended welding parameters, and drying conditions. In addition, each pack of electrodes has a label, which depending on the packaging method is either attached outside or inserted inside. The label specifies the intended use of the electrodes, their diameter, grade and type, recommended welding and drying parameters, manufacturer, production date, and batch number.

The quality of welding is also significantly influenced by the wire used in mechanized welding and as filler in gas welding. Wire is supplied in coils, equipped with metal tags indicating the standard designation, melt number, and manufacturer. The manufacturer and its quality control department also stamp the tag. Each batch of wire must be accompanied by a certificate specifying its grade and diameter, chemical composition, melt number, standard, batch mass, and the manufacturer's name.

If the strength of the welded joint is lower than that of the base metal, it is permissible to use flat and round specimens with identical cross-sections for testing. The length of the gripping part of such specimens may be chosen according to the design of the testing machine, while any changes to other dimensions are not allowed.

For testing welded joint sections, round specimens with a working part diameter of 3–10 mm are used. These specimens are cut along the weld axis in the corresponding zone of the joint for multilayer welding.

2. Improved Methodology for Assessing the Stability of the Rail Welded Joint Manufacturing Process

The assessment of the stability of the technological process is carried out at RWEs using control charts, which are prepared annually in the format shown in Figure 13(a). Based on the calculation data, the control chart displays lines corresponding to the average in-plant reject rate (in percent) and the control limits $K_в$ and $K_н$.

To calculate the average reject rate $R(\%)$, it is necessary to count the number of inspected joints N and the number of rejected joints M for the preceding year, and then compute their ratio.

$$\overline{P} = \frac{M}{N}100 \tag{2}$$

Control limits:

$$K_в = \overline{P} + 3\sqrt{\frac{\overline{P}(1-p)}{N/12}} \tag{3}$$

$$K_н = \overline{P} - 3\sqrt{\frac{\overline{P}(1-\overline{P})}{N/12}} \tag{4}$$

To assess the level of the rail welding technological process for the current month, the in-plant reject rate p_i for this month is calculated and compared with the average in-plant reject rate.

The in-plant reject rate $p_i(\%)$ for the current i-th month is calculated as the ratio of the number of rejected joints m_i during the given month to the number of inspected joints n_i for that month:

$$p_i = \frac{m_i}{n_i}100 \tag{5}$$

It is recommended that control data and in-plant reject rates for each month be recorded in the table presented above (Table 3):

1. The calculated value of p_i is marked on the control chart with a point. If the plotted point falls outside the upper control limit $K_в$, this indicates that deviations may have occurred in the technological process, causing an increase in the number of defective joints;
2. The broken line obtained by connecting the plotted points on the chart illustrates the pattern of changes in the rail welded joint manufacturing process at the RWE;
3. Filling in the table and the control chart can be performed by defect inspectors based on the data from the inspection log.

3. **Dynamic testing**

Dynamic tests include impact bending and fatigue (endurance) tests.

Impact bending tests involve determining the impact toughness of the welded joint at normal, reduced, and elevated temperatures corresponding to service conditions. The tests are conducted on specially prepared specimens with a notch, which may be located along the weld axis, the fusion line, or in the heat-affected zone on the side of the weld opening. The location of the notch depends on the purpose of the test. When testing weld metal or base metal, the notch can be made on either side of the specimen.

Tests are performed using pendulum impact testers with different maximum energy capacities. For use in laboratories of construction and assembly organizations, the MK-30A pendulum tester is recommended, which has 15 energy reserve steps and a total technical service life of 17,500 hours. After testing a welded joint, the fracture structure is examined to identify defects. Impact toughness is determined as the ratio of the work expended to fracture the specimen to the cross-sectional area at the notch prior to testing.

Fatigue (endurance) tests determine the metal's resistance to cyclic loads under bending, tension, and torsion. Variable loads are applied using symmetric, asymmetric, and pulsating loading cycles.

Axially loaded tests are conducted on cylindrical or flat specimens of special shape and specified dimensions, cut transverse to the welded joint. These tests determine the endurance limit of the specimen. A quantitative measure of fatigue strength is the number of cycles the welded specimen withstands before failure.

4. **Hardness measurement**

To evaluate changes in the weld metal and heat-affected zone, as well as to assess the degree of hardening in the welded joint zones and heterogeneity of mechanical properties, the hardness of welded joints is measured. Typically, hardness is determined on metallographic sections using three methods:

1. Indentation with a hardened steel ball of 1.568 mm diameter or a diamond cone with a 120° apex angle (Rockwell method);
2. Indentation with a square-based diamond pyramid with an angle of 136° between opposite faces (Vickers method);.
3. Indentation with a standard hardened steel ball of specified diameter (Brinell method).

Hardness measurements across the cross-section of a butt weld are carried out in two directions: along the longitudinal axis of the weld and from the center toward the base metal. Specimens are prepared to include all zones of the welded joint: base metal, weld metal, and heat-affected zones, with hardness measured in each of these three regions.

4. Improved Methodology for Assessing the Level of the Rail Welding Technological Process at RWEs

The improved assessment of the level of the rail welding technological process at RWEs is carried out centrally at the Central Track Laboratory using technological process level charts (hereinafter referred to as level charts).

Level charts are prepared twice a year, covering the preceding 12 months, in the format shown in Figure 13(b).

Based on the calculation data, lines corresponding to the average in-plant reject rate across all RWEs and the control limits K_v and K_n are plotted on the level chart.

The average in-plant reject rate is determined using formula (6).

$$\overline{P}_{\Sigma} = \frac{\sum_{\kappa=1}^{\kappa_0} \overline{P}_{\kappa}}{\kappa_0} \tag{6}$$

where $\bar{R}_k$ is the average in-plant reject rate at the k-th RWE for the studied period (12 months);

k – the RWE number;

k₀ – the total number of RWEs under investigation.

Note: The values are determined based on data received from RWEs.

The control limits are determined using the following formulas:

$$K_{\text{в}} = \overline{P}_{\Sigma} + 3\sqrt{\overline{P}_{\Sigma}(1-\overline{P}_{\Sigma})/12;} \tag{7}$$

$$K_{\text{н}} = \overline{P}_{\Sigma} - 3\sqrt{\overline{P}_{\Sigma}(1-\overline{P}_{\Sigma})/12.} \tag{8}$$

To assess the level of the rail welding technological process at a given k-th RWE for the studied period, the value for this RWE is compared with the value for all RWEs.

If the value exceeds K_v, this indicates that the RWE has potential for improving the level of the rail welding technological process.

If the value falls below K_n, this indicates that the RWE has achieved a high level of welding quality or that there may be deviations in the non-destructive testing procedures of welded rail joints at the RWE.

The improvement of the rail welded joint technology involves analyzing the condition of welded rail joints installed in the track during the studied period, which are subjected to two-stage ultrasonic testing by distance inspectors.

Additional information on the level of the rail welding technological process is presented in the form of defect distributions in the welded joints. These distributions are calculated and plotted based on the inspection data of welded joints produced during the period for which the level charts were prepared.

Macrostructural analysis is used as a preliminary method to assess the quality of welded joints obtained by different welding methods. The macrostructure of welded joints is examined either with the naked eye or at 30× magnification on the surfaces of macrosections cut from these joints. Macrostructure can also be studied on fracture surfaces of welded specimens after mechanical testing.

Macrostructural investigation allows determination of the weld shape and size, its internal structure, and the presence of various defects in the weld metal and base metal, such as lack of fusion, cracks, slag inclusions, pores, and others.

When examining the macrostructure of welded joints, templates are cut from the inspected joint in the plane of the weld cross-section to prepare sections. Sometimes, to determine the weld crystallization pattern in the welding bath, a section is prepared from a template cut along the longitudinal axis of the weld.

The section surface must include the full cross-section of the weld. To eliminate areas corresponding to unstable welding conditions, samples for sections are cut 20–30 mm away from the start or end of the weld.

For etching in microstructural studies of aluminum alloy welds, a 0.5% aqueous solution of hydrofluoric acid is used as a reagent.

For preparation of microsections of corrosion-resistant steels, electrolytic etching is used, which provides a significantly more uniform microstructure reveal than conventional etching. Electrolytic etching is also suitable for low- and medium-alloy steels. It is especially effective when high-quality surface preparation is required (for electron microscopy studies) and when work-hardening effects in the surface layer need to be removed.

The study of a microsection typically proceeds as follows. After polishing (before etching), the section is examined under a microscope at 100–500× magnification to detect pores, oxide films, and microcracks in the weld. Non-metallic inclusions appear as dark spots against the bright background of the microsection. Microcracks appear as thin, black, wavy lines. After etching, the microsection is examined under a microscope to determine the weld structure across the entire cross-section, including the types and proportions of structural components and the presence and distribution of carbides, nitrides, sulfide, and oxide inclusions.

When the study is not performed immediately after microsection preparation or is conducted multiple times with intervals, proper storage of the sections is necessary. Since the surface must be protected from oxidation during storage, a passivating solution is applied during polishing and rinsing, followed by careful washing with alcohol and drying.

Conclusion

1. To ensure the timely elimination of deviations in the technological process that lead to defects in welded rail joints, it is advisable to implement process control at rail welding enterprises based on statistical analysis of visual inspection and ultrasonic testing data.
2. Based on the obtained data, an improved methodology has been developed at rail welding enterprises for assessing the stability and level of the rail welded joint manufacturing process at RWEs. The application of this improved methodology will contribute to enhancing the quality of rail welds, thereby reducing repair costs for rejected joints and minimizing the likelihood of laying welded rails with defective joints in the track.
3. The statistical analysis of visual inspection and ultrasonic testing data involves monitoring and calculating the average in-plant reject rate for a specified preceding period for each RWE, for example, one year, and comparing this value with the average in-plant reject rate for the current period (month). It has been established that the main causes of defects in welded rail joints are malfunctions of rail welding machines and poor preparation of the rail ends to be welded.
4. To calculate the potential for improving the level of the rail welding technological process, the formulas for determining the average reject rate $R(\%)$ should be applied. This requires counting the number of inspected joints $N$and the number of rejected joints $M$for the preceding year and then computing their ratio.

References

[1] Pryakhin E.I., Sharapova D.M. Understanding the structure and properties of the heat affected zone in welds and model specimens of high-strength low-alloy steels after simulated heat cycles //CIS Iron Steel Rev. 2020, 19. – P. 60–65.

[2] Aksenov A.V., Bugrov A.V., Rezanov A.V. Improving the structural strength of rail welds. In Proceedings of the Science, Innovations and Education: Actual Problems of Development of the Transport Complex of Russia //Materials of the International Scientific and Technical Conference, Ekaterinburg, Russia, 16–17 November 2006; 77–78.

[3] Bakyt G., Abdullayev S., Suleyeva N., Yelshibekov A., Seidemetova Zh., SadvakassovaZh. Simulation of dynamic processes of interaction of car and railway track during train passage of curved sections of the track // Transport Problems International scientific journal, vol. 15, no. 2., 2020. – P. 59–70, 2020, https://doi.org/10.21307/tp-2020-020.

[4] Saita K., Ueda M., Yamamoto T., Karimine K., Iwano K., Hiroguchi Kiyoshi. Trends in Rail Welding Technologies and Our Future Approach //Technology, No. 105, 2013. - P. 84-92.

[5] Sun J., KristanJ. Gas-pressure welding: is it feasible for North American railroads, Railway Track & Structures, 2(2003).
[6] Mitsuru F. Rail flash-butt welding technology // JFE Technical Report, 2015, 20. - P. 159 – 163.
[7] Velichko D.V. Economic evaluation of the contact and the aluminothermic welding of rails // Actual problems of modern science: a collection of articles of the International scientific-practical conference: In 4 parts, 2013. – P. 93-96.
[8] Abdullayev S.S., Bakyt G.B., Aikumbekov M.N., Bondar I.S., Auyesbayev Y.T. Determination of natural modes of railway overpasses //Journal of Applied Research and Technology, 2021, 19(1). - P. 1–10.
[9] Voronin N.N. Aluminothermic welding of rails: studies. Benefit // Training Center for Education in railway transport, 2013. - 195 p.
[10] Bajic D., Kuzmenko G., Samardzic I. Welding of rails with new technology of arc welding //Metalurgija 52, 2013, 3. - P. 399-402.
[11] Sun L., Li G., Wang Y. A brief description of the application of rail welding technology on the line //Science and Technology Information, 2014, 09. – P. 84-86.
[12] Ding W., Song H., Gao Zh., et al. Development and process research of on-site heat treatment equipment for rail welded joints //Thermal Processing Technology, 2013, (01). – P.166-168.
[13] Farhangi H., Mousavizadeh S.M. Horizontal split-web fractures of flash butt welded rails //Proceedings of the 8th international fracture conference, 2007. - P. 509-517.
[14] Abdullayev, S., Kiseleva, O., Adilova, N., Bakyt, G., Vakhitova L. Key development factors of the transit and transport potential of Kazakhstan. Transport Problems, 2016, 11(2). - P. 17-26. https://doi.org/10.20858/tp.2016.11.2.2
[15] Alves L.H.D., Lagares M.L., Filho R.M.M., Tepedino T., Goldenstein H. Predictive mathematical modeling of the flash-butt welding process to optimize the properties of welds of premium and super premium rails //International heavy haul STS Conference, 2019. - P. 440-447.
[16] Porcaro R.R., et al.Microstructure and mechanical properties of a flash butt welded pearlitic rail // J Mater Process Technol, 270, 2019. - P. 20-27.
[17] Honda K., Saito S. On the formation of spheroidal cementite //J. Iron Steel Inst, 102, 1920. - P. 261-267.
[18] Abdullayev S., Bakyt G., Kamzina A., Sarsanbekov K., Abdullayeva A. Interaction of the TE33a Diesel Locomotive and the Railway Track on Curved Section with Radius 290 m. Communications - Scientific Letters of the University of Zilina, 2023, 25(4), B315-326. https://doi.org/10.26552/com.C.2023.069.

Information of the authors

Abdullayev Seidulla, d.t.s., professor, Satbayev University
e-mail: seidulla@mail.ru

Bakyt Gabit, PhD, associate professor, Mukhametzhan Tynyshbayev ALT University
e-mail: gaba_b@bk.ru

Yelshibekov Amandyk, PhD, Assistant Professor, Saken Seifullin Kazakh Agrotechnical University
e-mail: a.kz@mail.ru

Jakupov Nurbek c.t.s., assistant professor, Mukhametzhan Tynyshbayev ALT University
e-mail: pont8080@mail.ru

Duisembayeva Bakytzhamal, doctoral student, teaching assistant, L. N. Gumilyov Eurasian National University
e-mail: sharipovna27@mail.ru

DOI 10.52209/2706-977X_2026_1_120 **IRSTI 81.09.03** **UDC 621.792**

The Effect of Laser Post-Processing on NiCrMoSiBFeCuC Thermally Sprayed Coatings

Černašėjus O.*, **Rutė M., Černašėjienė R., Užtupis S., Valasevičius A.**
Vilnius Gediminas Technical University, Vilnius, Lithuania
*corresponding author

AbstractDuring the study, a nickel–chromium-based coating was formed on structural steel S235 using flame spraying technology. A NiCrMoSiBFeCuC powder mixture with the following composition was used for coating formation: ~67% Ni; 0.45% C; 4.11% Si; 3.92% B; 2.72% Fe; 15.7% Cr; 1.94% Cu; 4.69% Mo. The sprayed coatings were remelted using a gas torch at a temperature of 1100 °C in air. At the next stage of coating formation, the samples were processed with a fiber laser under four processing speed modes - without beam oscillation and with oscillation amplitudes of 1 mm and 3 mm. The aim of this study was to investigate the effect of laser processing on NiCrMoSiBFeCuC coatings formed by spraying followed by gas torch remelting. The shape and geometry of the laser-remelted tracks, microhardness of the samples, as well as tribological properties and wear resistance were investigated. The combined method of coating formation, including spraying followed by laser treatment, allows the formation of a continuous or localized NiCrMoSiBFeCuC coating layer with increased microhardness and wear resistance on the surface of the component.

Keywords: thermal spray, NiCrMoSiBFeCuC coating, laser post-processing, hardness, tribology

Introduction

The application of sprayed coatings in industry makes it possible to improve the surface properties of components both during manufacturing and repair. Thermally sprayed coatings based on nickel-chromium-molybdenum-silicon-boron (NiCrMoSiB) are one of the most popular classes of protective coatings, widely used in mechanical engineering, energy, oil and gas, and chemical industries. Their popularity is due to the combination of high wear resistance, corrosion resistance, and the ability to operate at elevated temperatures and in aggressive environments [1].

These coatings are based on a nickel matrix alloyed with chromium, molybdenum, silicon, and boron. Chromium provides high corrosion and oxidation resistance, molybdenum improves mechanical strength and wear resistance, while boron and silicon contribute to the formation of a eutectic structure and reduce the melting temperature of the alloy. This is especially important for subsequent remelting of the coating, which makes it possible to obtain a dense, low-porosity structure with good adhesion to the substrate [2].

The most common methods for producing NiCrMoSiB coatings include flame spraying, plasma spraying, and high-velocity oxy-fuel (HVOF) spraying [3–4]. After spraying, the coatings are often subjected to remelting (e.g., flame or laser remelting), which reduces porosity, eliminates interparticle bonding defects, and results in a more homogeneous structure. As a result, the mechanical and operational properties of the coating are significantly improved [5–6].
NiCrMoSiB coatings are widely used for components operating under friction and wear conditions, such as shafts, bushings, pump elements, valves, as well as components exposed to corrosive environments. Their application is particularly effective in the restoration of worn surfaces, allowing the service life of expensive components to be extended and reducing maintenance and replacement costs.

One of the key directions of modern research is the use of laser processing of sprayed coatings. Laser remelting enables localized treatment of the surface, providing high energy density and precise control of process parameters. This promotes the formation of a fine-grained microstructure, increases microhardness, and improves tribological properties. However, certain challenges arise, such as crack formation due to high thermal gradients, which requires optimization of processing parameters [7].

The prospects for the development of NiCrMoSiB coatings are associated with the improvement of deposition technologies and subsequent processing methods. Particular attention is given to combined approaches, including spraying followed by laser or electron beam remelting. In addition, modification of powder compositions through the introduction of reinforcing phases (carbides, borides) is actively investigated, which allows further enhancement of wear resistance and thermal stability of the coatings [8–13].

Thus, NiCrMoSiB-based coatings have significant potential for further application and development. Their unique combination of properties makes them promising for use under conditions of intensive wear, corrosion, and high temperatures. Further research aimed at optimizing composition, structure, and processing technologies will enable an even broader range of applications and improved efficiency of engineering systems.

1. Methodology of experimental investigation

The coatings were formed on low-carbon structural steel S235 (according to EN 10027-1) plates. The dimensions of the cut plates were 100 × 100 × 10 mm. The S235 steel plates were coated with nickel–chromium-based powders, the chemical composition of which is presented in Table 1. This coating is used in applications where corrosion and wear resistance are required.

Table 1. Chemical composition of NiCrMoSiBFeCuC powder, %

Ni–Cr–Co–Si–B–Fe–Cu–C composition							
Ni	Cr	Mo	Si	B	Fe	Cu	C
Bal.	15,7 %	4,69 %	4,11 %	3,92 %	2,72 %	1,94 %	0,45 %

Before thermal spraying, the plate surfaces were prepared by chemical and mechanical cleaning. Prior to the coating process, in order to improve coating formation conditions, the plate surfaces were preheated with a neutral acetylene–oxygen flame to a temperature of 250 °C.

A two-stage technology was used for the production of sprayed and remelted coatings: powder deposition followed by remelting of the deposited coating using a flame. In this study, spraying parameters were selected according to the equipment manufacturer's recommendations and further refined during trial spraying (Table 2). The final thickness of the sprayed coating was ensured by selecting an appropriate number of deposited layers. To ensure the stability of the technological process parameters during the experiment, an industrial robotic manipulator Motoman 100 MH6 was used.

Table 2. Main parameters of coating formation processes

Substrate preheating	Neutral flame C_2H_2/O_2 ~250°C
Thermal spray flame	Neutral flame 0,07 MPa C_2H_2/ 0,4 MPa bar O_2
Spraying distance	170 mm
Spray speed/step/layer	250 mm/s /5 mm / 8 layers
As-sprayed layer thickness	1,2– 1,4 mm
Remelted flame	Neutral flame 0,035 MPa C_2H_2/ 0,4 MPa O_2
Remelted temperature	1100^0C
Cooling	In air, at a temperature of 22°C
As-sprayed and flame remelted layer thickness	0,940–1,010 mm

For laser treatment of the flame-sprayed and remelted coating samples, a 1500 W FANUCI PRO laser with a continuous-wave fiber laser source and beam oscillation function was used. The laser beam wavelength was 1070 nm. The main parameters were as follows: laser power – 375 W; oscillation – sinusoidal with a frequency of 110 Hz; laser beam diameter – 1 mm; laser processing speed varied from 500 to 1250 mm/min; oscillation amplitude – 0, 1, and 3 mm; shielding gas – argon; shielding gas flow rate – 15 L/min. The laser processing parameters of the flame-sprayed and remelted coatings are presented in Table 3.

Table 3. The main parameters of laser processing of samples

Laser processed speed, mm/s	Laser beam oscillation, mm		
	0	1	3
500	X	X	X
750	X	X	X
1000	X	X	X
1250	X	X	X

The morphology and geometry of the tracks of the sprayed, flame-remelted, and laser-processed coatings were investigated using optical macroscopy. For this purpose, the samples were sectioned and metallographic cross-sections were prepared. The samples were ground using abrasive papers of different grit sizes from P240 to P2500. After grinding with P2500 paper, the surfaces were polished using polishing pastes with particle sizes ranging from 3 to 0,2 μm. After polishing, the samples were cleaned in an ultrasonic bath using an acetone solution and then dried with a stream of hot air.

The microhardness of the investigated samples was measured on polished cross-sections using a Mitutoyo HV-100 automated microhardness tester. The maximum measurement error was 1%. Measurements were performed using the Vickers microhardness method with a load of 200 g and a dwell time of 15 s. The optical magnification of the obtained microhardness indentations was 50X. The average microhardness of the samples was calculated from ten measurements, excluding the minimum and maximum values.

The tribological properties (coefficient of friction) and wear resistance of the investigated samples were evaluated using a dry sliding test with a Microtest tribometer. The tests were carried out using the "ball-on-disc" configuration. The following experimental parameters were used: test temperature – 21 °C, load – 30 N, sliding distance

– 100 m, rotational speed – 200 rpm, and track radius – 1 mm. A 6 mm diameter hardened AISI 52100 steel ball was used as the indenter.

The wear resistance of the samples was evaluated by comparing the mass changes before and after the wear tests. The wear resistance was calculated based on the results of two tests. To reduce inaccuracies in the friction coefficient measurements, the initial stage of the test (the first 20 m) was excluded from the analysis. The wear rate of the samples was determined using the weighing method with an analytical precision balance RADWAG AS60/220.R2, with an accuracy of ±0.01 mg.

2. Results and Discussions

To evaluate the effect of laser treatment and its parameters on the remelting process of the NiCrMoSiBFeCuC coating, a macroscopic analysis of the processed samples was performed during the experimental investigation. Metallographic cross-sections of the processed coatings were prepared for the study. The sample cross-sections were ground, polished, and cleaned in an ultrasonic bath.

The macroscopic analysis of the remelted coating structure showed that the depth and width of the remelted layer depend on the laser processing speed and the beam oscillation amplitude. The lower the laser processing speed, the deeper the coating is remelted (Fig. 1). This occurs due to a higher energy input into the coating surface during laser treatment. Increasing the laser processing speed of NiCrMoSiBFeCuC coatings from 500 to 1250 mm/s reduces the depth of the formed track in the central region by 1,24–2,0 times, depending on the laser beam oscillation (Fig. 2). The most significant reduction in remelted depth was observed when using beam oscillation amplitudes of 1 mm and 3 mm (1,85 and 2,0 times, respectively).

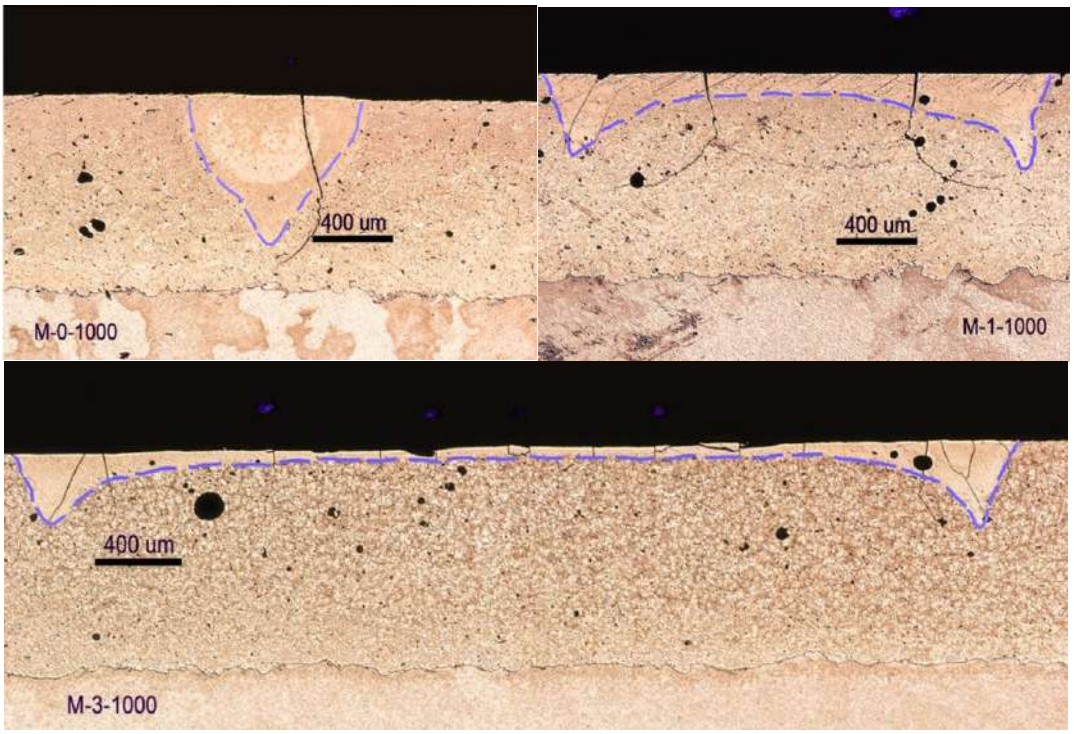

Fig. 1. - Cross-sectional micrographs of molten pools processed with 1000 mm/min laser speed and a varying oscillated amplitude between 0 and 3 mm (M-0-1000 - no oscillation; M-1-1000 - oscillation amplitude 1mm; M-3-1000 - oscillation amplitude 3 mm)

During the macroscopic analysis of laser-treated NiCrMoSiBFeCuC coatings, it was observed that when applying a laser processing mode without beam oscillation (0 mm oscillation), the shape of the remelted track is parabolic. In contrast, with beam oscillation amplitudes of 1 mm and 3 mm, the remelted track exhibits a non-uniform depth, characterized by a flatter central region of the melt pool and deeper sides following a Gaussian-type profile. It was also observed that during laser processing with beam oscillation, the depth of the remelted track in the central region is smaller than at the edges of the track (Fig. 1). This can be explained by the non-uniform distribution of laser energy on the coating surface when using processing modes with beam oscillation.

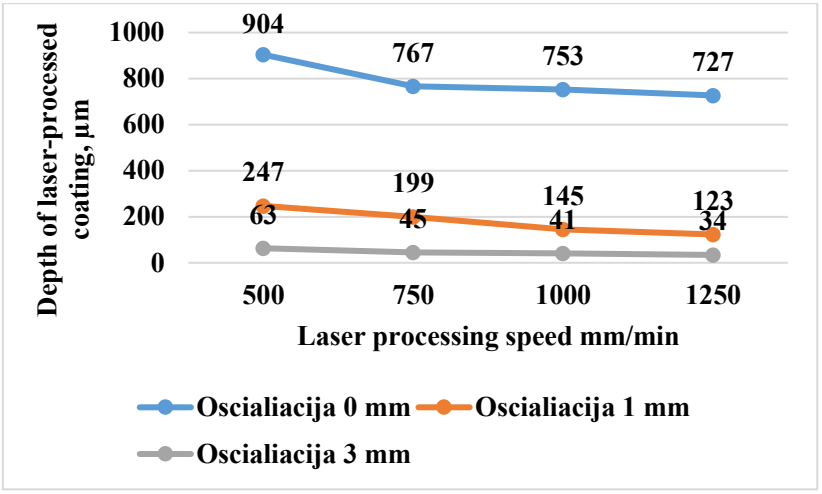

Fig. 2. - The relationship between the depth of molten pools and laser processing speed, applied oscillation amplitude (0 mm - no oscillation; 1mm - oscillation amplitude 1 mm; 3 mm - oscillation amplitude 3 mm)

During remelting of coatings both without and with beam oscillation, the width of the remelted tracks depends on the laser processing speed and the beam oscillation amplitude. Increasing the laser processing speed from 500 to 1250 mm/min reduces the width of the remelted tracks by approximately 1,06–1,88 times (Fig. 3). The most significant reduction (about 1,88 times) is observed when processing the coatings without beam oscillation (0 mm oscillation).

When beam oscillation amplitudes of 1 mm and 3 mm are applied during laser processing, the width of the remelted tracks increases by approximately 1,7–1,9 and 2,9–5,1 times, respectively, depending on the laser processing speed. The largest increase in track width (about 5,1 times) was observed when using a 3 mm beam oscillation at a laser processing speed of 1250 mm/min.

To evaluate the effect of laser processing on the mechanical properties of NiCrMoSiBFeCuC sprayed coatings, the microhardness of the substrate, the as-sprayed and remelted coating, and the laser-processed coating was measured using the Vickers method. The microhardness results showed that, during remelting of the coatings both with and without beam oscillation, the microhardness of the remelted track metal depends on the laser processing speed. Increasing the laser processing speed from 500 to 1250 mm/min increases the microhardness of the remelted tracks by 1,19 to 1,62 times, depending on the beam oscillation amplitude (Fig. 4).

The increase in microhardness of the laser-processed coating metal may be attributed to faster cooling rates, more intensive melt crystallization, a potentially finer microstructure of the remelted layer, and the formation of dispersed phases. The highest increase in microhardness of the remelted coating metal (about 38%) was observed when laser processing the NiCrMoSiBFeCuC sprayed coating without beam oscillation (Fig. 4).

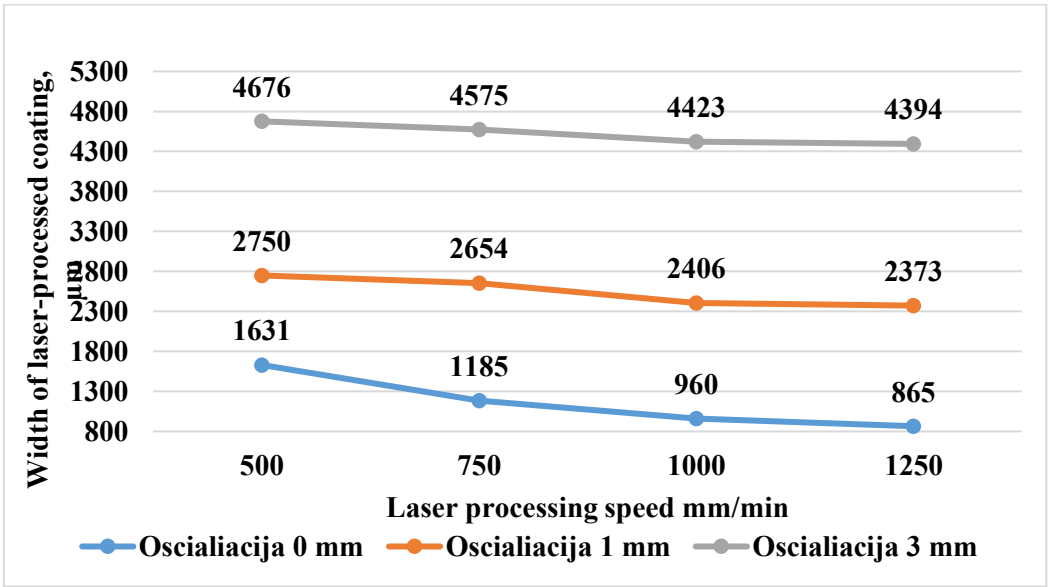

Fig. 3 - The relationship between the width of molten pool and laser operating speed, applied oscillation amplitude (0 mm - no oscillation; 1mm - oscillation amplitude 1 mm; 3 mm - oscillation amplitude 3 mm)

Analysis of the microhardness results showed that the microhardness of the as-sprayed and remelted coating is approximately four times higher than that of the S235 substrate (about 141 HV0.2). During laser processing of the NiCrMoSiBFeCuC sprayed coating, higher processing speeds and lower beam oscillation amplitudes result in higher microhardness of the remelted coating metal. The highest microhardness of the treated coating was achieved at a laser processing speed of 1250 mm/min and a beam oscillation amplitude of 1 mm, reaching 1057 HV0.2. This value is approximately 7,5 times higher than that of the substrate and about 1,9 times higher than that of the as-sprayed and remelted (non-laser-processed) coating (approximately 566 HV0.2).

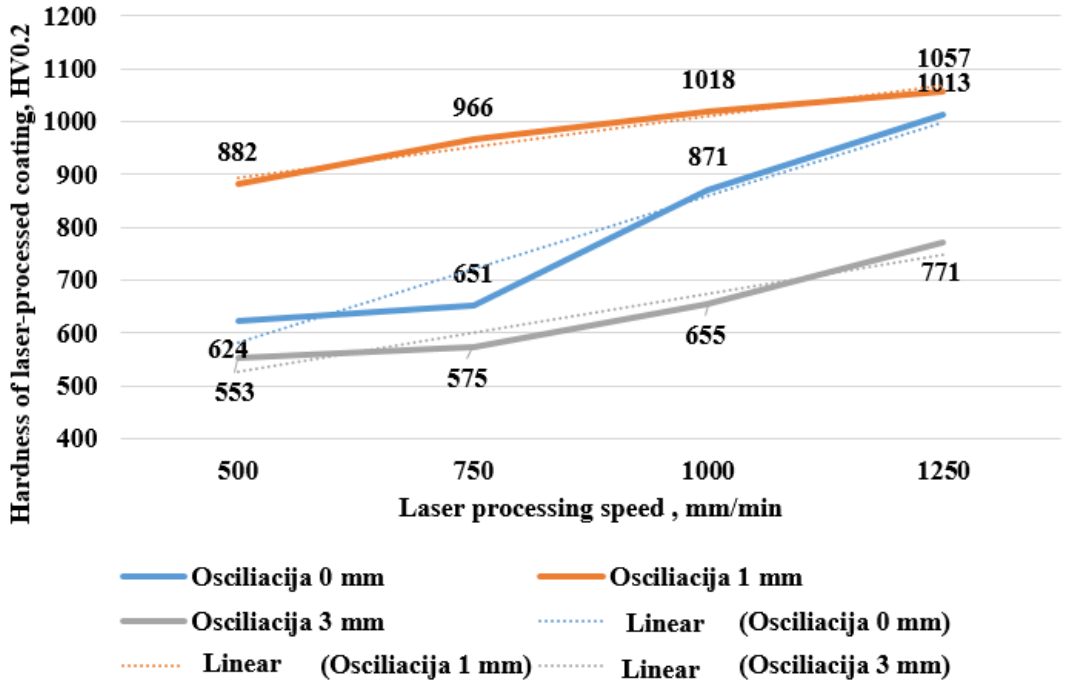

Fig. 4. - The relationship between the hardness of the coating processed at different parameters and laser operating speed, applied oscillation amplitude (0 mm - no oscillation; 1 mm - oscillation amplitude 1mm; 3 mm - oscillation amplitude 3 mm)

One of the most effective methods for evaluating the performance characteristics of a metallic surface operating under frictional conditions is wear resistance testing. To assess the tribological properties and dry sliding wear resistance of the NiCrMoSiBFeCuC sprayed coating after laser processing, a “ball-on-disc” wear test was selected. The results of the tribological and wear tests of the investigated samples are presented in Table 4.

Analysis of the tribological test results showed that the average coefficient of friction of the as-sprayed and remelted (non-laser-processed) coating is approximately 1,5 times higher than that of the substrate. Laser treatment of the coating reduced the average coefficient of friction by about 16%; however, it still remained about 1,27 times higher than that of the substrate. The lower friction coefficient values of the substrate can be explained by the lower strength and hardness of S235 steel. During wear, the softer substrate material promotes better running-in of the tribological contact surfaces.

The wear test results showed that the wear resistance of the as-sprayed and remelted NiCrMoSiBFeCuC coating is approximately 2,65 times higher than that of S235 steel, while the laser-processed coating exhibits about 8,43 times higher wear resistance compared to the substrate. Laser treatment increased the wear resistance of the remelted coating by approximately 318 %. These results indicate that laser processing of NiCrMoSiBFeCuC sprayed coatings significantly improves their operational performance.

Table 4. Results of the tribological tests

Sample	Average coefficient of friction (slip distance 20-100 m)	Sample mass loss (slip distance 100 m), µg	Sample abrasion rate, µg/m	Abrasion resistance of the specimen, m/mg
Steel S 235	0,3315	1180	118	84,7
As-sprayed and flame-remelted coating	0,4990	445	44,5	224,7
Laser processed coating	0,4205	140	14	714,2

Conclusions

The results obtained allow us to draw the following main conclusions:

1. During laser remelting of NiCrMoSiBFeCuC sprayed and flame-remelted coatings with and without beam oscillation, the width and depth of the remelted tracks depend on the laser processing speed and the beam oscillation amplitude. Increasing the laser processing speed leads to a decrease in both the width and depth of the remelted tracks. Introducing beam oscillations of 1 mm and 3 mm increased the track width by approximately 1,7–2,7 and 2,9–5,1 times, respectively, while the maximum remelted depth decreased by approximately 1,5–1,9 and 2,3–2,5 times, depending on the laser processing speed.
2. Macroscopic analysis of the laser-processed coatings showed that, without beam oscillation, the remelted track has a parabolic shape. When beam oscillation amplitudes of 1 mm and 3 mm are applied, the remelted track exhibits a non-uniform depth, with a flat central melt pool region and deeper sides following a Gaussian-type profile.
3. During laser remelting at processing speeds of 500–1250 mm/min without preheating, cracks formed in all samples. The introduction of beam oscillation during processing increased the number of cracks.
4. Microhardness measurements showed that the microhardness of the remelted tracks depends on the laser processing speed, both with and without beam oscillation. Increasing the laser processing speed from 500 to 1250 mm/min increased the microhardness of the remelted coating by 1,19 to 1,62 times, depending on the beam oscillation amplitude, due to faster cooling of the coating material. The highest microhardness of the treated coating (1057 HV0.2) was achieved at a laser processing speed of 1250 mm/min and a beam oscillation amplitude of 1 mm. This value is approximately 7,5 times higher than that of the substrate and about 1,9 times higher than that of the as-sprayed and remelted coating.
5. Analysis of the tribological test results showed that the average coefficient of friction of both as-sprayed and laser-processed coatings is higher than that of the substrate by approximately 1,5 and 1,27 times, respectively. The lower friction coefficient of the substrate can be explained by the fact that the softer substrate material promotes better running-in of the tribological contact surfaces during wear.
6. The wear test results showed that the wear resistance of the as-sprayed and remelted NiCrMoSiBFeCuC coating is approximately 2,65 times higher than that of S235 steel, while the laser-processed coating exhibits about 8,43 times higher wear resistance than the substrate. It can be concluded that laser treatment increases the wear resistance of the remelted coating and improves its service performance.

References

[1] Yu H.L., et al. Comparison of surface and cross-sectional micro-nano mechanical properties of flame sparyed NiCrBSi coating //Journal of Alloys and Compounds 672, 2016. P 137–146.
[2] Gonzalez R., Garcia, M.A., Penuelas, I., Cadenas, M., Fernandez, M.A., Hernandez Battez, A., Felgueroso, D. Microstructural study of NiCrBSi coatings obtained by different processes //Wear 263, 2007. P 619-624.
[3] Gomez-del Rio T., Garrido M.A., Fernandez J.E., Cadenas M., Rodriguez J. Influence of the deposition techniques on the mechanical properties and microstructure of NiCrBSi coatings //Journal of materials processing technology 204, 2008. P 304-312
[4] Parthasarathi, N.L., Duraiselvam, M., Borah, U. Effect of plasma spraying parameter on wear resistance of NiCrBSiFe plasma coatings on austenitic stainless steel at elevated temperatures at various loads //Materials and Design 36, 2012. P 141–151.
[5] Kim H-J., Hwang S-Y., Lee Ch-H., Juvanon P. Assessment of wear performance of flame sprayed and fused Ni-based coatings //Surface and coating technology 172, 2003. P 262-269.
[6] Liu J., Bolot R., Costil S., Planche M.-P. Transient thermal and mechanical analysis of NiCrBSi coatings manufactured by hybrid plasma spray process with in-situ laser remelting //Surface and Coatings Technology, vol. 292, 2016. P 132-143.
[7] Liu J., Wang Y., Costil, S., Bolot R. Numerical and experimental analysis of molten pool dimensions and residual stresses of NiCrBSi coating treated by laser post-remelting. Surface and Coatings Technology, vol. 318, 2017. P 341-348.
[8] Serres, N., et al. Microstructures and mechanical properties of metallic NiCrBSi and composite NiCrBSi–WC layers manufactured via hybrid plasma/laser process //Applied Surface Science 257, 2011. P 5132–5137.
[9] Škamat J., Černašėjus O., Čepukė Ž.; Višniakov N. Pulsed laser processed NiCrFeCSiB/WC coating versus coatings obtained upon applying the conventional re-melting techniques: Evaluation of the microstructure, hardness and wear properties //Surf. Coat. Technol. 374, 2019. P 1091–1099.
[10] Szajna E., Moskal G., Tupaj M., Dresner J., Dudek A., Szymański K., Tomaszewska A., Trzcionka-Szajna A., Mikuśkiewicz M., Łysiak K. The influence of laser remelting on microstructural changes and hardness level of flame-sprayed NiCrBSi coatings with tungsten carbide addition //Surface and Coatings Technology, Volume 478, 2024, 130403
[11] Praveen A.S., et al. Erosion wear behaviour of plasma sparyed NiCrSiB/Al_2O_3 composite coating //International Journal of Refractory Metals and Hard Materials 52, 2015. P 209–218.

[12] Umanski A.P., et al. Structure, phase composition, and wear mechanisms of plasma sprayed NiCrSiB-20 wt.% TiB_2 coating //Powder Metallurgy and Metal Ceramics, 53 (11–12), 2015. P 663–671.
[13] Li Y., Sun X., Du J., Li F., Qui X., Cui W., Niu J., Fan W. Effect of laser remelting treatment on the tribological properties of plasma sprayed WC–Cr_3C_2–Ni reinforced NiCrBSi coatings. Surface and Coatings Technology, Volume 494, Part 1, 2024. 131359

Information of the authors

Olegas Černašėjus, PhD, professor, Vilnius Gediminas technical university
e-mail: olegas.cernasejus@vilniustech.lt

Mindaugas Rutė, M.Sc., Vilnius Gediminas technical university
e-mail: mindaugas.rute@stud.vilniustech.lt

Raimonda Černašėjienė, PhD, associate professor, Vilnius Gediminas technical university
e-mail: raimonda.cernasejiene@vilniustech.lt

Simonas Užtupis, B.Eng., Vilnius Gediminas technical university
e-mail: simonas.uztupis@stud.vilniustech.lt

Andrius Valasevičius, B.Eng., Vilnius Gediminas technical university
e-mail: andrius.valasevicius@stud.vilniustech.lt